UNIVERSITY OF Southampton

University of Southampton Research Repository
ePrints Soton

Copyright © and Moral Rights for this thesis are retained by the author and/or other copyright owners. A copy can be downloaded for personal non-commercial research or study, without prior permission or charge. This thesis cannot be reproduced or quoted extensively from without first obtaining permission in writing from the copyright holder/s. The content must not be changed in any way or sold commercially in any format or medium without the formal permission of the copyright holders.

When referring to this work, full bibliographic details including the author, title, awarding institution and date of the thesis must be given e.g.

AUTHOR (year of submission) "Full thesis title", University of Southampton, name of the University School or Department, PhD Thesis, pagination

http://eprints.soton.ac.uk

UNIVERSITY OF SOUTHAMPTON

Some Aspects of RANS Based Jet Noise Prediction

by

Mahdi Azarpeyvand

A thesis submitted in partial fulfillment for the degree of Doctor of Philosophy

in the

Faculty of Engineering, Science and Mathematics

Institute of Sound and Vibration Research

December 2008

ABSTRACT

Title: **Some Aspects of RANS Based Jet Noise Prediction**

by Mahdi Azarpeyvand

The main objectives of this thesis are the comparison and improvement of RANS based jet noise prediction schemes. Such schemes use a RANS flow simulation to which is coupled acoustic source and propagation models allowing a prediction of far-field noise to be made. In the present work a modified RANS $k-\varepsilon$ turbulence model is used to provide the necessary CFD results. The acoustic source models discussed are a Lighthill Acoustic Analogy based method and the MGBK method. This latter allows different components of the noise sources, *i.e.* self- and shear-noise to be considered. Propagation modelling that takes account of the sound-flow interaction effect is used. This is based on the Lilley equation and both direct and asymptotic solutions are used. Different aspects of the source models are considered such as: mathematical models, source compactness, anisotropy, *etc.* Special attention will be given to the definition of parameters used in the source term, namely time-scale, length-scale and convection velocity. The relation of these parameters with the underlying physics of noise production and radiation mechanism will be studied and it will be shown that these quantities play a central and important role in the accuracy of the prediction. Moreover, the frequency dependency of these parameters will be considered using the available experimental data and also physical insights gained from the study of the turbulence. A time scale model will be introduced based on the cascade of the turbulent energy, while the length scale and convection velocity models are based on physical reasoning or experimental data. Numerical results are presented for single flow, coaxial and short-cowl nozzles at different working conditions. Comparisons will be made for sound pressure level and source distribution with experimental data obtained from the JEAN and CoJeN tests. Results generally have shown that using the turbulent energy transfer rate time scale, along with the frequency dependent length scale and convection velocity remarkably improves the prediction. However, some mismatches between the peak frequency of the prediction and data can be observed at small and large angles. Different causes for these mismatches are suggested and discussed critically.

Acknowledgements

I would like to thank my supervisor Dr. Rod Self for his guidance throughout my graduate studies. I am deeply indebted to him for his well-informed advice, encouragement, and enthusiasm. I specially thank him for his perpetual readiness to help me and for being always smiling, no matter how busy he was. I am also grateful to Professor Jeremy Astley and Dr. Philip Joseph for their support and technical advice. I would also like to thank Professor Philip Morris for serving on my PhD exam committee.

I should like to express my gratitude to Professor Philip Nelson, the former head of ISVR and the current deputy vice-chancellor of Southampton University, who initially offered me this PhD position and to Professor Jeremy Astley and Dr. Rod Self for accepting me. Among other faculty members at ISVR. I would like to thank Dr. Brian Tester, Dr. Mike Fisher, and Professor Peter Davies (died Jan. 2008), who have invaluably enriched my knowledge of jet noise. My thanks extend to the members of Flow and Acoustics group at TNO for their hospitality and providing me with a friendly environment. Financial support from TNO is also gratefully acknowledged. Special thanks to TNO for their flexibility and accepting the changes to the research subject.

I would like to thank my colleagues and officemates at FDAG/ISVR for making such a pleasant, friendly, and creative work atmosphere. In particular, I would like to thank Mr. Juan Battaner Moro for being so helpful and also for the technical discussions and providing experimental data. I would also to express my thanks to Philip Mc Laughlin, Christopher Ham, Christopher Powles, and Eugene Deane with whom I had fruitful discussions and shared some enjoyable moments. Susan Brindle, our group secretary, has always been patient and efficient, for which I am thankful. I am also grateful to my friends and the faculty members at Mechanical Engineering Department at Iran University of Science and Technology for their continuous suppor. I would also like to express my thanks to Mr. Seyyed M. Hosseini for his support and encouragement.

Lastly, but first in mind, I would like to express my gratitude to my parents, brother, sisters, and specially my wife for their never fading love and endless support, especially during the last seven years that I had been seriously involved in various research activities.

Contents

List of Figures

List of Tables

Nomenclature

Roman Symbols

a	Calibrating coefficient
b	Calibrating coefficient
c	Sound speed, m/s
c_0	Ambient sound speed, m/s
C	Convection factor $(1 - M_c cos\theta)$
D_J	Jet diameter
D_{ijkl}	Directivity factor
E	Turbulence energy spectrum
f	Frequency (Hz)
$f(r)$	Spatial part of the correlation function
$g(\tau)$	Temporal part of the correlation function
$g^2(r)$	Shielding function
I	Sound intensity
I_x	Source distribution
j	Imaginary number
k	Turbulent kinetic energy
l	Length scale $(k^{3/2}/\varepsilon)$, m
M	Mach number
M_c	Convection Mach number
M_J	Jet Mach number
$M_{\alpha\beta}$	Quadruple operator
p'	Pressure fluctuation, Pa
Pr	Production rate of turbulent kinetic energy

Q	Correlation function
r	Radial coordinate
R	Correlation function
St	Strouhal number ($St = fD_J/U_J$)
T_{ij}	Lighthill's stress tensor
T_J	Jet exit temperature, ^oC
T_∞	Ambient temperature
u	Particle velocity, m/s
U	Mean velocity, m/s
U_1	Flow speed in axis direction, m/s
U_c	Convection speed, m/s
U_J	Jet exit velocity, m/s
v	Turbulent velocity, m/s
$\bar{V}$	Sweeping velocity, m/s
x	Axial coordinate

Greek Symbols

α	Calibrating coefficient
β	Calibrating coefficient
β_c	Anisotropy level
δ	Dissipation length scale (Taylor macroscale)
δ_{ij}	Kronecker's delta
Δ	Integral length scale
ε	Turbulent dissipation rate
η	Kolmogorov length scale ($(\nu^3/\varepsilon)^{1/4}$)
θ	Observer angle
θ^*	Cone-angle
κ	Wave-number
κ_e	Peak wave-number
Λ	Eddy size
ν	Kinematic viscosity
ρ	Fluid density, kg/m^3
ρ_0	Fluid density at rest, kg/m^3

ρ'	Density fluctuation, kg/m^3
τ	Retarded time, s
τ_η	Kolmogorov time scale ($\sqrt{\nu/\varepsilon}$)
τ_τ	Turbulent energy transfer time scale (TET)
τ_d	Turbulent energy dissipation rate time scale (TDR)
τ_p	Turbulent energy production rate time scale
Υ	Length scale ratio
Ψ	Space factor
ω	Observer radian frequency
ω_0	Peak frequency
Ω	Source radian frequency

Functions

erf	Error function
erfi	Imaginary error function
Γ	Gamma function
H	Heaviside function
∇^2	Laplacian ($\nabla.\nabla$)
sech	Hyperbolic secant function

Subscripts

$()_d$	Parameters based on the dissipation rate of the turbulent kinetic energy
$()_J$	Single stream jet exit condition
$()_p$	Primary flow property
$()_s$	Secondary flow property

Abbreviations

AA	Acoustic Analogy
CAA	Computational Aero-Acoustics
CFD	Computational Fluid Dynamics
DNS	Direct Numerical Solution
LDV	Laser Doppler Velocimetry
LES	Large Eddy Simulation
LQ	Relations of form of $L(\Box) = Q$
$MGBK$	Mani, Gliebe, Balsa, and Khavaran

NCF	Non-Compactness Factor
PIV	Particle Image Velocimetry
$RANS$	Reynolds-Averaged Navier-Stokes
SPL	Sound Pressure Level
TDR	Turbulent energy dissipation rate time scale
TET	Turbulent energy transfer rate time scale
TKE	Turbulent kinetic energy
VR	Velocity Ratio
$WIND$	Flow solver; product of NASA and AEDC

Chapter 1

Introduction and Background

This thesis is concerned with methods for predicting the noise that arises from aircraft engine exhaust jets. While jet noise is only one of several noise sources on modern aircraft powered by high bypass ratio engines, it is a major contributor to the overall noise of such aircraft and there has been an ongoing interest in finding improved prediction methods for sixty years.

Aviation has an indisputable position in modern society in the 21st century. Air travel in Europe rose three-fold between 1980 and 2000, and due to the demand it is set to double by 2020. It is evident that aircraft noise is becoming an increasingly important factor in everyday life. It has become a major concern of people living around busy airports like London Heathrow. Reports are frequently published concerning the physiological and psychological effects of load and constant background noise in living areas close to airports. Public pressure on governments to act is high. For instance the UK Government recently announced spending of 5 million pounds a year over five years to help insulate schools and other public buildings under the Heathrow flight path. While such steps go some way to alleviate the problem it is unlikely that this will prevent the introduction of increasingly strick regulations that restrict the amount of noise that aircraft are allowed to generate.

Furthermore, we have to accept that air transport is a significant contributor to global and local air pollution as well as local ambient noise, and these problems are likely to become more serious if present growth trends continue. From a design point of view,

FIGURE 1.1: A380 aircraft at landing

the various problems are interlinked and it is unlikely that an optimal solution that minimises say, NOx emissions, will correspond to an optimum noise solution. There is therefore considerable pressure on engine manufacturers to develop novel noise reduction techniques. Correspondingly, there is a pressing need to develop tools that can accurately predict noise produced by a novel power plant.

1.1 Aircraft Noise in General

The broadest classifications of aircraft noise are those of airframe and engine noise. Airframe noise is part of the non-propulsive noise of an aircraft in flight. Landing gear, flaps and slats all contribute to airframe noise and are mostly used on takeoff and approach when the aircraft is near the ground. Unsteady turbulent flow from the wing and tail trailing edge, turbulent flow through or around flaps and slats, flow past landing gear and other undercarriage elements, fuselage and wing turbulent boundary layers, and panel vibrations, all contribute to airframe noise. Airframe noise is most significant during approach when the engine noise is low.

Fan, compressor, turbine and combustor, and exhaust noise (jet noise) are all categorized as the engine noise sources or propulsive noise sources. These are the four sections that a typical turbofan engine is composed of, as illustrated in figure 1.2. Air is drawn into the compressor at the front of the engine, and after it has been compressed it is mixed with fuel and burnt in the combustion system. Some of the energy in the gas

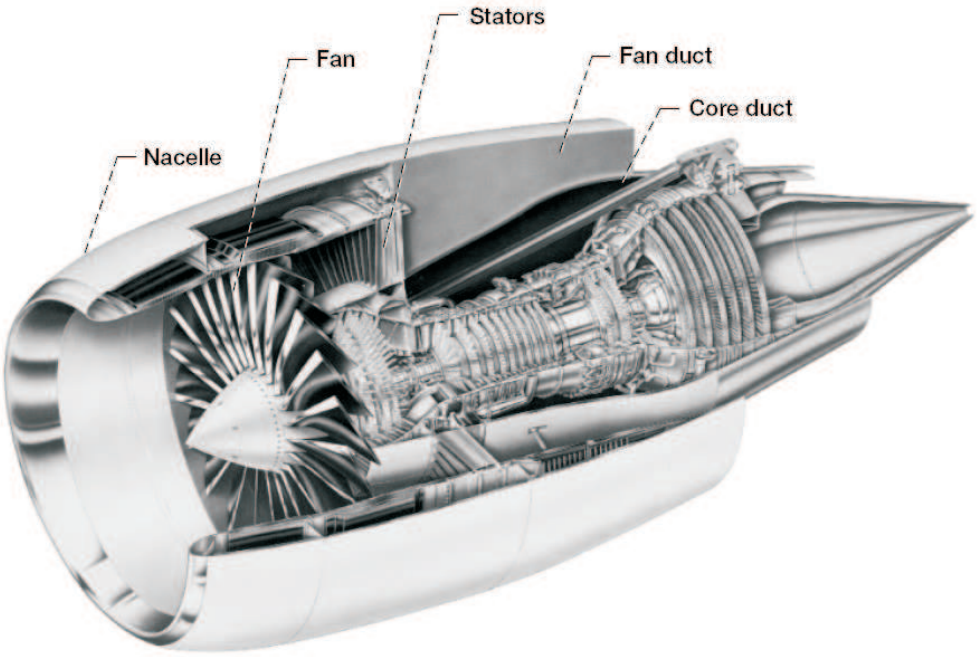

FIGURE 1.2: Modern GE turbofan jet engine, 1970s.

stream is extracted by a turbine to enable the compressor to be self sustaining. The remaining gas is then expelled through a nozzle at the rear of the engine to provide the overall thrust. The compressor and turbine units produce tonal noise as a result of the interaction of the airflow over the rotating and stationary blades, which occur at the blade passing frequency, or BPF, and its harmonics. Another feature of the compressor and turbine associated noise is random aerodynamic noise which is due to the interaction of unsteady flow with the stators, also known as broadband noise, and also rotor self-noise. The burning process also produces random noise of a low order, but the jet of gas propelled through the nozzle to mix with the atmosphere produces is probably the most powerful form of random noise. This is jet noise.

Figure 1.3 shows the noise sources of a turbofan engine and the relative contributions at the inlet and exhaust. The characteristic directions of radiation are rearwards for the jet, turbine and half the fan noise, and forwards for the compressor, and the rest of the fan noise. A breakdown of the noise components of a typical engine during takeoff and approach to landing is shown in figure 1.4. The figure clearly indicates that a large part is played by engine noise. Airframe noise becomes the dominant part of the aircraft

noise during approach.

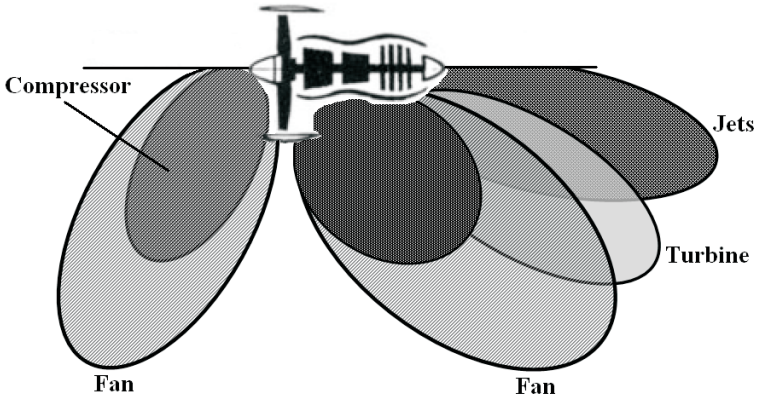

FIGURE 1.3: Typical noise pattern around a turbofan engine

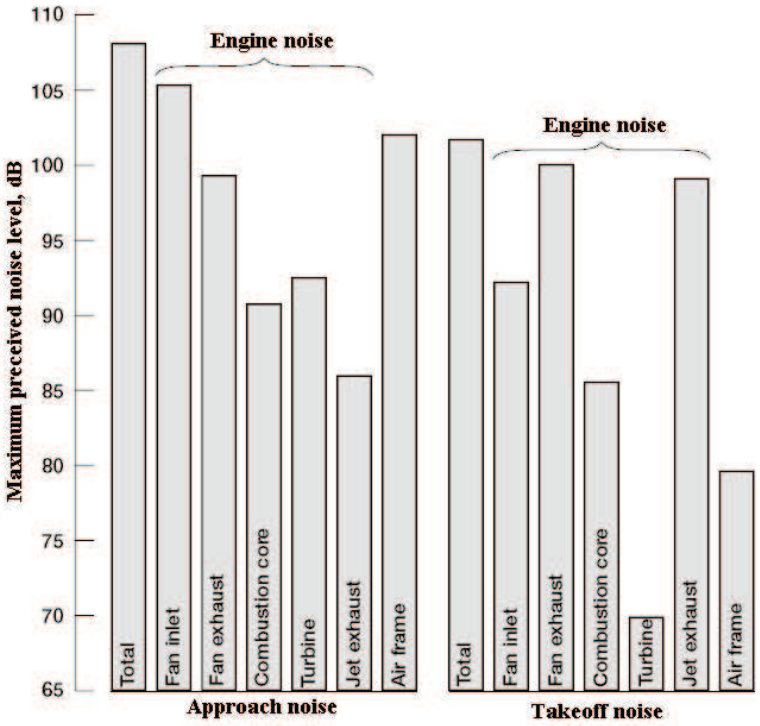

FIGURE 1.4: A breakdown of the noise components of a typical engine during takeoff and approach to landing.

1.2 Jet Noise in Particular

Among all of the aircraft noise sources mentioned above, the jet noise and its prediction has been the subject of continuing interest and studies from the time when the first set

of commercial jets were introduced, and still remains as one of the most complicated problems in aeroacoustics because of the unresolved details of the noise generation mechanism. In 1952 Lighthill published the first of his two papers on aerodynamic sound in the Proceedings of the Royal Society of London [1]. This is discussed in the next section.

1.3 Acoustic Analogies

Lighthill's solution to the jet noise problem, usually referred to as Lighthill's Acoustic Analogy (AA), is actually a rearrangement of the equations of continuity and momentum to give the homogenous acoustic wave operator on the left hand side, and the terms remaining are placed on the right hand side and are viewed as the source terms. In this way the jet is viewed as a volume distribution of quadruple sources that radiate sound into an ambient medium at rest.

Because Lighthill's equation arises from a rearrangement of the Navier-Stokes equation, it is in a strict sense exact. Furthermore, because it has the form of a simple wave equation, a straightforward mathematical solution in terms of a Green's function can always be written down. In practice however, this apparent simplicity makes some difficulties.

The first difficulty with Lighthill's Acoustic Analogy concerns the complexity of the source term, which depends on several aspects of the fluctuating turbulent flow. However, Lighthill showed that a great deal of information is available from the equations despite the fact that the details of the turbulence were not known. Simple turbulence closure models such as the 1-equation mixing length theory of Prandtl give rise to similarity solutions for axisymmetric round jet flows where velocities and lengths are non-dimensionalised using the jet exit velocity and jet diameter. This allows a scaling argument to be made that shows the total acoustic power radiated from an isothermal jet scales as eight powers of the jet velocity U_J.

Another difficulty with Lighthill's Acoustic Analogy concerns directivity. Jet noise is highly directional in nature and there is more than one reason for this. Firstly, the mean flow of the jet can be thought of as convecting the turbulent eddies that constitute the sound sources and this gives rise to convective amplification. Secondly, the sound

produced within the jet must propagate through the jet flow, giving rise to flow acoustic interactions (*i.e.* refraction effect).

While the convective amplification effects can be incorporated within Lighthill's Analogy using suitable Doppler factors applied to the equivalent acoustic sources, the mean flow effects can only be included in a somewhat *ad hoc* way. This phenomenon is commonly referred to as the "refraction effect" and was first observed in experimental evidence found by Atvars *et al.* [2]. The refraction effect can be explained as follows. Once produced by the source, sound waves have to pass through the jet plume in which flow velocity and perhaps temperature vary in the axial and radial direction. This phenomenon is analogous to the Snell's law in optics. The effect depends on the frequency content and wave-length relative to the shear layer width of the jet, and will be even more significant if the sources are deeply buried in a rapidly spreading shear layer. Many attempts have been made to include the refraction effect in the solution to the jet noise problem, but they mostly ended up with sophisticated and unsolvable equations. However, the most satisfying approach, at least from a theoretical viewpoint, is due to Lilley who rearranged the mass and conservation equations to arrive at a third order inhomogeneous wave equation, with the flow-sound interaction effect included in the propagation operator [3]. There have been some efforts to simplify Lilley's equation, but the most cited works are perhaps those of Tester and Morfey [4], and Mani *et al.* [5]. However, the complexity of the problem confines the solution to only low and high frequency asymptotic solutions for simple jet flows.

1.3.1 Traditional Methods of Jet Noise Prediction

One of the strengths of Lighthill's Analogy is that it effectively decouples the acoustic problem from the flow problem and, as discussed above, even modest knowledge about the flow allows scaling laws to be developed. While such laws do not give an absolute prediction for noise, the practical utility of the approach is that careful measurements made on one jet can be used to predict noise from other jets. In the years following Lighthill's theory this was the basis of most jet noise prediction. For example, in the early 1970s Lush [6] made a series of jet noise measurements and developed a comprehensive scaling law for third octave jet noise spectral intensity including convective directivity.

Lush realized that such a scaling law would not predict noise emitted in directions close to the jet axis where it is affected by "cone of silence effects" arising from flow-acoustic interaction, but otherwise the agreement is very good.

Lighthill's U_J^8 law works very well for low Mach number jet flows. Later Ffowcs-Williams investigated scaling law for very high-speed jets [7] and found that acoustic power radiated from such a jet varies as the third power of the jet velocity. Scaling laws turn out to be a bit different when we deal with hot jets, due to the different nature of the source contributing to noise production. Monopole and dipole sources appear to be equally dominant factors in hot jets. Morfey [8] has shown that at low Mach numbers, radiation is associated with dipole volume acceleration, and quadruple volume displacement sources. He then showed that the acoustic power scales as $(\Delta T/T)^2(U_J/c_0)^6$. A Monopole source can also dominate the noise radiation at low Mach numbers in heated jets. Lush and Fisher found that, in this case, the far field intensity varies as $(\Delta T/T)^2(U_J/c_0)^4$ [9].

$$(\Delta T/T)^2(U_J/c_0)^4$$

The latest improvements on scaling laws are reported by Tam [10], and Viswanathan [11]. Tam examined some heated supersonic jets and utilized the scaling law $A(U_J/c_0)/(R/D_J)^2$, where R is the distance of the observer from the jet exit. A and n are two calibrating coefficients which are functions of jet total temperature and microphone azimuthal location $(T_J/T_\infty, \theta)$. Viswanathan has also found that the noise characteristics of unheated and heated jets at every radiation angle can be described in terms of two independent parameters: the total temperature ratio (T_J/T_0) and the velocity ratio (V_J/c_0). The velocity exponent for scaling jet noise is then defined uniquely for each angle and temperature ratio [11].

1.3.2 Developments in Methods of Jet Noise Prediction

While the traditional methods for noise prediction have proved themselves remarkably successful at making predictions from limited knowledge, they are clearly limited by the underlying assumptions about the self similarity of jet flows. This also limits their use

as an aid to engine designers because they are able to predict noise only for jet flows where the underlying source parameters remain largely unchanged. Given the need to reduce jet noise this is a severe shortcoming.

Engine manufacturers are increasingly looking toward novel designs involving features such as chevrons that alter the turbulence characteristics of the flow, or non-axisymmetric flows that may help shield the major noise sources within the jet. If reasonable predictions are to be made for such complex flows a new range of prediction tools is required. However, to offset the increasing difficulty of the problems being posed is the fact that our knowledge of, and ability to predict, turbulent flow fields has increased hugely due to the advent of Computational Fluid Dynamics (CFD).

The application of CFD to jet noise prediction can be achieved in one of two ways. In the first class, the aerodynamic field and the acoustic field are simultaneously calculated by solving the compressible unsteady Navier-Stokes equations. Dealing with this method requires very high numerical resolution due to the large difference in the length scale present between the acoustic variable and flow variables. This approach is computationally demanding and unsuitable for normal design use, but allows for more physical investigations of noise source and propagation mechanisms. Direct Numerical Simulation (DNS) and Large Eddy Simulation (LES) fall into this class.

In DNS, the Navier-Stokes equations are solved for all the scales of the flow, with no turbulence modelling. This requires resolving all spatial and temporal scales of the turbulence which necessitates use of a very fine mesh to capture the smallest eddies of the turbulence, the Kolmogorov scales say. One of the very first DNS calculations of a turbulent jet was performed for a Reynolds number 2000, supersonic jet at Mach 1.92 by Freund *et al.* [12]. However, even in the case of low Reynolds number flows, DNS remains very expensive in terms of computational time. Indeed, in this case, the time step is imposed by the sound velocity, whereas the pressure fluctuations associated with acoustic phenomena are typically at least ten times smaller than the hydrodynamic pressure fluctuations associated with turbulent events, and thousands times weaker than the mean flow that carries them. So, in this situation, a very wide range of scales have to be accurately simulated, leading to very expensive simulations. As a result, DNS can only be used for a small number of academic problems, which nevertheless provide data

of great interest for the understanding of physical phenomena [12, 13, 14].

In LES, the governing equations are the Navier-Stokes equations explicitly filtered in space, and a turbulence model is used to represent the subgrid-scale stress tensor (a comprehensive review can be found in [15, 16]). According to the previous studies on the DNS and LES, the grid requirements of both are difficult to achieve, and their application is limited to some laboratory experiments with typical jet exit Reynolds numbers of about 10^5.

A second class of methods used for applying CFD to jet noise prediction are two step methods that split the solution into different distinct parts, with the flow field being solved separately from the acoustic field. Needless to say, such an approach is essentially a development of Lighthill's work in that the CFD is now used to calculate the equivalent acoustic sources that are then introduced into an acoustic solver. Propagation of the sound can be handled using either Integral methods (Lighthill's Analogy, Kirchhoff integral, Ffowcs-Williams Hawking (FW-H), *etc.*) or Linearized Euler equations (LEE).

More often than not the CFD solver chosen for this type of two step modeling is based on the Reynolds-Averaged Navier-Stokes equations (RANS). Due largely to its inherent speed, this is a popular tool for industry and it is a natural development to use it as the basis for acoustic predictions.

This type of approach was somewhat prefigured by Proudman who, shortly after the appearance of Lighthill's theory, published his work which relates jet noise to the turbulence characteristics of jet flow [17]. According to his method, the total acoustic power in the far field can be found from $\alpha\rho_0 \left(\frac{v}{c_0}\right)^5 \varepsilon$, where c_0, and ρ_0 are the ambient sound speed and the density in the far field, ε designates the dissipation rate of the isotropic turbulence, and the turbulence velocity is defined by $v^2 = 2k/3$, where k is the turbulent kinetic energy. Finally α is a kind of calibrating coefficient that provides an overall estimate of the power of the sources and is expressed in terms of the spatial correlation function of the turbulence.

In fact, Proudman's method is a kind of noise scaling law which links the acoustic power to turbulence values without further ado. As with the original scaling laws of Lighthill it does not provide spectral or directivity information about the noise. Indeed this will be the case with any RANS based method without further explicit modeling of

the acoustic sources, as the CFD does not provide sufficient information.

Perhaps one of the earliest and certainly the best known two-step method is the one developed by Mani, Gliebe and Balsa in the late 1970s (the MGB Method) [5, 18, 19]. These authors employed an empirically derived steady flow prediction to provide the input to an acoustic analogy model based on Lighthill's Analogy and used Lilley's Analogy to derive the flow-acoustic interaction. This method was improved by Khavaran [20, 21] who replaced the empirical basis of the flow prediction with a CFD calculation based on a $k-\varepsilon$ turbulence model. This technique is generally referred to as the Mani-Gliebe-Balsa-Khavaran method (MGBK). One of the first applications of the MGBK method was made by Khavaran and Georgiadis [22] for supersonic elliptic jets. Hamed *et al.* [23] used the method for high bypass coplanar coaxial jets and Barber *et al.* applied the method to axisymmetric multi-stream [24] and high speed jet flows [25] while the mean and turbulence parameters were obtained using the WIND flow solver. Comparison of the MGBK noise prediction for a coaxial jet using different RANS codes was investigated by Koch *et al.* [26]. Frendi *et al.* [27, 28] applied the MGBK methodology to a supersonic jet flow, while a multiple time scale approach was used and results were in acceptable agreement with experimental data. This method was also used for jets with chevron mixers by Koch *et al.* [29] and Engbolm *et al.* [30]. More recently, researchers at the NASA Glenn Research center have been working on further improvement of the MGBK method by including the turbulence anisotropy effect [21], source compactness effect [31], alternative source terms function [31, 32], and also refraction effect [33, 34, 35]. This new refined MGBK package is now called JeNo [36].

In addition to the MGBK method, a number of other RANS-based jet noise prediction methodologies have also been developed and used. Self [37], Self and Bassetti [38] have used a fourth-order space-time velocity correlation model for definitions of source terms and also made use of many length scale definition for the case of isothermal single flow jets. A similar methodology was also applied to isothermal coaxial jets by Page *et al.* [39]. Another RANS-based model has been developed by Tam [40]. According to this method the radiated noise originates from two types of sources, those radiated by fine-scale eddies, and those produced by large-scale ones. The application of this method to other geometries and working condition have also been tested [41, 42, 43]. However, it has been shown that Tam's method is similar to the Acoustic Analogy

method if consistent assumptions are made on the turbulence statistics [44]. It is also worth mentioning here that an alternative approach for the case of noise from a coaxial jet flow, commonly referred to as the four-source model, has been developed by Fisher *et al.* [45, 46] and Preston [47]. This methodology is based upon the fact that the jet stream of a coaxial jet has four distinct regions, and each behave as single stream jets.

An accurate and reliable prediction of jet noise using acoustic analogies requires that the dynamics of the jet flow be accurately modelled. Of particular importance is the spatio-temporal correlation of the Lighthill stress tensor as it will be used directly to evaluate the radiated acoustic field. A limited amount of experimental research has been performed to investigate the aerodynamic and acoustic aspects of jet flows. One of the most famous works is that of Harper-Bourne [48], who tested a low speed jet flow and measured the fourth order and second order two-point space-time correlation using hot wire anemometry. More recently Kerherve *et al.* [49] performed a two-point laser Doppler velocimetry (LDV) measurement for a Mach 1.2 cold supersonic jet to be used for statistical modelling of aeroacoustic source terms. Bridges and Wernet have also conducted a test using particle image velocimetry (PIV) to measure two-point space-time velocity correlations in a hot, high speed jet flow [50].

Subsequent to the work of Mani, Gliebe, Balsa and Khavaran, there has been much interest in improving RANS based two step techniques. One of the most important improvements is that of the source term definition. In addition to the importance of the accuracy of the CFD results and also the acoustic model, it has been shown that there are many factors that play a role in the accuracy of the source term, such as the source model and the defining parameters used to link the source model to the nature of the jet flow plume. Although the model used for the source terms is of great importance, a proper definition of the defining parameters in the source term model, *e.g.* time scale, length scale, and convection velocity, can be even more important. Furthermore, frequency dependency of these parameters is very important as well. Such a dependency was observed before when Fisher and Davis presented their paper in 1963 [51]. Frequency dependency of time scale, length scale, and convection velocity has been also comprehensibly investigated by Harper-Bourne for a low speed ($M_J = 0.18$) jet flow [48]. Morris and Boluriaan [52] and Self [37] have recently implemented this frequency dependence in their statistical noise prediction methodologies, and have shown

that noise prediction improvement is possible if frequency dependent parameters are used. More recently, Kehereve *et al.* [49, 53] have conducted research which shows the frequency dependency of the turbulence properties derived from two-point laser Doppler velocimetry measurements in high speed subsonic jets.

1.4 Objectives of original contributions the Present Work

The central goal of this thesis is to develop a jet noise prediction methodology based on Lighthill's Acoustic Analogy which provides an acceptable level of agreement with measured data and is also computationally feasible. This approach consist of two steps: In the first step one needs to determine the mean and turbulence properties of the flow from Computational Fluid Dynamics analysis (CFD) using the Reynolds Averaged Navier-Stokes (RANS) equations along with a two-equation turbulence model, namely $k-\varepsilon$ or $k-\omega$. The second step requires modeling of the acoustic source terms and noise radiation and propagation mechanisms. The need to define the source terms arises because a steady RANS calculation provides no time dependent quantities required for the acoustic calculation. In particular the turbulent correlations (or equivalent) must be modeled. Although the accuracy of the final prediction depends heavily on the accuracy of both steps, understanding the underlying physics of the noise production and radiation mechanism also has a crucial role in improving noise prediction. The specific objectives of the research are as follows:

1. Provide a mathematical model for jet noise prediction based on an Acoustic Analogy. Lighthill's equation along with Lilley's equation will be derived. In addition, the MGBK method will also be derived to take account of the shear-noise. It will be also shown that using the MGBK method one can also address some other phenomena, such as turbulence anisotropy and source compactness.

2. Provide a general description of different turbulent processes occurring in a jet flow plume. We will then investigate how these processes contribute to the noise production and radiation mechanism. The most important question that arises is whether all turbulence regions are contributing to the noise radiation or whether consideration of a limited number of regions is adequate.

3. Consider frequency dependency of different parameters used in the source term definition, such as time scale, length scale, and convection velocity. Various models will be introduced and their corresponding physical meaning will be explained.

4. Propose and validate a new time scale based upon the turbulent energy transfer rate. How the frequency dependency is taken into account using the new time scale will be discussed. It will also be shown that significant improvement in the noise prediction at low and high frequencies can be obtained using this time scale.

The original contribution in this thesis, to the field of aeroacoustics, is the consideration of various scales in order to better understand the underlying physical mechanisms of jet noise production and propagation. The thesis is aimed to study in depth the most fundamental definitions used in prediction of jet noise, namely time- and length-scale, and their connection to the underlying physics of noise production/propagation mechanism. This involved investigating various time scale and length scale models. The frequency dependency of these parameters have also been carefully studied. Most importantly, a new time scale based on turbulent energy transfer rate has been developed and used for various kinds of jets operating at different conditions. It has been shown that even a simple model using Lighthill's Acoustic Analogy can provide very acceptable results, given that the appropriate time-scales and length-scales are chosen. This thesis provides, for the reader, a convenient collection and outline of the most used jet noise prediction models to date, such as Lighthill, MGBK and models based on the turbulent energy spectrum.

1.5 Outline of the Thesis

This thesis is organized as follows: The mathematical derivation of jet noise radiation is given in Chapter 2. In this chapter Lighthill's Acoustic Analogy is derived and required discussions are provided. In addition, the MGBK methodology is derived and its application discussed. The high frequency solution of Lilley's equation, as suggested by Balsa [54] is also used in the MGBK method. In Chapter 3, different turbulence regions and associated phenomena are explained. Discussions are given for the most important regions responsible for the noise production and radiation mechanism. Chapter

4 concerns the frequency dependency of some of parameters used in the source terms of the Acoustic Analogy, such as time scale, length scale and convection velocity. Various models are introduced. A new time scale based on the turbulent energy transfer rate with inherent frequency dependency will be introduced. In addition to the frequency dependency of the time scale, that of the length scale and convection velocity are also considered by best fitting to the available measured data. Chapter 5 presents numerical results and discussions for noise prediction for the case of unheated and heated subsonic single-stream jets. Comparisons are made between the predicted noise level results using the MGBK method and measured data. The jet noise source distribution is also considered in this chapter. Comparisons of noise prediction and source distribution with experimental data for the case of a coplanar and short-cowl nozzles with experimental data are given in Chapter 6. Predictions are made using the MGBK method.

The details of the RANS CFD analysis are given in Appendix A. This includes a discussion of the grid and turbulence model sensitivity for axisymmetric jet flows. The CFD results are provided for three jet configurations, namely single-flow, coplanar, and short-cowl nozzles, operating at different velocities and temperatures.

Chapter 2

Noise Generation and Radiation Modeling

In mathematics you don't understand things. You just get used to them.

"Johann von Neumann", (1903-1955)

This chapter concerns the mathematical modelling of noise production and radiation from a jet flow and is split into two parts. In the first part, Lighthill's Acoustic Analogy is derived and discussions are provided. This method makes use of the fourth order correlation function when the turbulence is isotropic and it is assumed that noise is dominated by self noise.

The second part of the chapter is devoted to the derivation of the MGBK method which can also take account of the shear-noise. Aside from the shear-noise, source compactness and turbulence anisotropy are also taken into account, which in fact extends the application of the analogy. A list of possible second-order correlation functions, both spatial and temporal parts, is also given in this section.

2.1 Lighthill's Analogy

The fundamental equation that forms the basis of aeroacoustics was developed by Lighthill [1] who introduced his acoustic analogy in 1952 to deal with the problem

of jet noise. The formulation is derived from the Navier-Stokes equation in combination with the equation of mass continuity,

$$\frac{\partial \rho}{\partial t} + \frac{\partial}{\partial x_j}\rho u_j = 0, \tag{2.1}$$

$$\frac{\partial}{\partial t}\rho u_i + \frac{\partial}{\partial x_j}\left(\rho u_i u_j + \delta_{ij} p - e_{ij}\right) = 0, \tag{2.2}$$

where e_{ij} denotes the viscous stress tensor, which can be expressed in terms of the velocity gradient for a Stokesian gas as:

$$e_{ij} = \mu\left(\frac{\partial u_i}{\partial x_j} + \frac{\partial u_j}{\partial x_i} - \frac{2}{3}\delta_{ij}\frac{\partial u_k}{\partial x_k}\right), \tag{2.3}$$

where μ is the fluid viscosity.

Subtracting the space derivative of the momentum equation, (2.2), from the time derivative of the continuity equation, (2.1), one obtains:

$$\frac{\partial^2 \rho}{\partial t^2} - \frac{\partial^2}{\partial x_i \partial x_j}(\rho u_i u_j) = \frac{\partial^2}{\partial x_i \partial x_j}(p\delta_{ij} - e_{ij}) \tag{2.4}$$

The expression is equivalent to:

$$\frac{\partial^2 \rho}{\partial t^2} - \frac{\partial^2}{\partial x_i \partial x_j}(\rho u_i u_j) = \frac{\partial^2}{\partial x_i \partial x_j}(p\delta_{ij} - e_{ij}) + c_0^2\frac{\partial^2 \rho}{\partial t^2} - \frac{\partial^2}{\partial x_i \partial x_j}(c_0^2 \rho \delta_{ij}) \tag{2.5}$$

Equation (2.5) can be rearranged in order to obtained a wave equation on the left-hand side and the acoustic sources on the right-hand side:

$$\frac{\partial^2 \rho}{\partial t^2} + \frac{\partial^2 \rho}{\partial x_i^2} = \frac{\partial^2}{\partial x_i \partial x_j}(\rho u_i u_j) + \frac{\partial^2}{\partial x_i \partial x_j}\left[(p - c_0^2\rho)\delta_{ij}\right] - \frac{\partial^2 e_{ij}}{\partial x_i \partial x_j} \tag{2.6}$$

A decomposition of the flow variable can be introduced:

$$\begin{aligned} p &= p_0 + p' \\ \rho &= \rho_0 + \rho' \end{aligned} \tag{2.7}$$

where the prime denotes the small perturbations from a state where the fluid is at rest with a uniform density ρ_0 and a uniform pressure p_0. Using the above variables in

equation (2.6), one can obtain

$$\frac{\partial^2 \rho'}{\partial t^2} - c_0^2 \nabla^2 \rho' = \frac{\partial^2 T_{ij}}{\partial x_i \partial x_j}, \tag{2.8}$$

which is usually referred to as the Lighthill equation. The T_{ij} term is the Lighthill stress tensor which is given by

$$T_{ij} = \rho u_i u_j + \delta_{ij} \left[(p - p_0) - c_0^2 (\rho - \rho_0) \right] - e_{ij}. \tag{2.9}$$

Mathematically, equation (2.8) is a hyperbolic partial differential equation, which describes a wave propagating at the speed of sound in a medium at rest, on which fluctuating forces are externally applied in the form described by the right hand side of equation (2.8). The equation has the same form of the wave propagation equation that governs the acoustic field produced by a quadrupole source (indicated by the double divergence on the right hand side) in a non-moving medium. It can be shown that for isothermal jet flows, T_{ij} is approximately equal to $\rho u_i u_j$ inside the flow, and approximately equal to zero outside this region. Hence, upon assuming that the density fluctuations are negligible (relative to ρ_0) within the moving fluid, the following approximation to Lighthill's stress tensor can be used

$$T_{ij} \approx \rho_0 u_i u_j. \tag{2.10}$$

So, the right hand side of the Lighthill equation can be treated as a known source term, assuming knowledge of the turbulent flow. It is worth mentioning here that the energy associated with the Reynolds stress term $\rho_0 u_i u_j$ (*i.e.* the aerodynamic source) is much greater than the energy consumed to radiate the sound.

In the absence of any solid boundary the solution to equation (2.8) can be expressed in terms of the free-space Green's function. Hence,

$$\rho'(\mathbf{x},\ t) = \frac{1}{4\pi c_0^2} \int \frac{1}{R} \left[\frac{\partial^2 T_{ij}}{\partial y_i \partial y_j}(\mathbf{y},\ \tau) \right]_{\tau = t - (R/c_0)} d\mathbf{y}, \tag{2.11}$$

where the integration is to range over all y in the volume V where T_{ij} is non-zero, also

$$R = |\mathbf{x} - \mathbf{y}|,$$

is the source to the observer distance. Since the observation location is many wavelengths away from the source position, and also because the observation distance is large compared with the source region dimensions, one can show that [55]

$$\frac{\partial^2}{\partial x_i \partial x_j} T_{ij}(\mathbf{y},\ \tau) \approx \frac{x_i x_j}{c_0^2 x^3} \frac{\partial^2}{\partial t^2} T_{ij}(\mathbf{y},\ \tau) \tag{2.12}$$

Finally, the acoustic pressure can be obtained after substitution of (2.12) in (2.11) and using the far-field pressure-density relation $p' = c_0^2 \rho'$,

$$p'(\mathbf{x},\ t) \approx \frac{1}{4\pi} \frac{x_i x_j}{x^3} \int \frac{1}{c_0^2} \frac{\partial^2 T_{ij}}{\partial t^2}(\mathbf{y},\ t - \frac{R}{c_0}) d\mathbf{y}. \tag{2.13}$$

Accordingly, the average intensity can be determined from the normalized pressure autocorrelation function

$$\Gamma(\mathbf{x}, t) \equiv \frac{1}{\rho_0 c_0} \overline{p'(\mathbf{x}, t) p'(\mathbf{x}, t + \tau)} \tag{2.14}$$

where the overbar notation shows an ensemble average. Finally, using equation (2.13) in (2.14), the normalized pressure autocorrelation function can be obtained from

$$\Gamma(\mathbf{x}, t) = \frac{1}{16\pi^2 \rho_0 c_0^2} \frac{x_i x_j x_k x_l}{x^6} \int \int \overline{\frac{\partial^2}{\partial t^2} T_{ij}\left(\mathbf{y}_1, t_1\right) \frac{\partial^2}{\partial t^2} T_{ij}\left(\mathbf{y}_2, t_2\right)} d\mathbf{y_1} d\mathbf{y_2} \tag{2.15}$$

with

$$\begin{aligned} t_1 &= t - \tfrac{|\mathbf{x} - \mathbf{y}_1|}{c_0}, \\ t_2 &= t + \tau - \tfrac{|\mathbf{x} - \mathbf{y}_2|}{c_0}. \end{aligned} \tag{2.16}$$

It is possible to show T_{ij} is generally a reasonable stationary random function of time [55], so correspondingly the density fluctuations must also be a function of this type. So that [55]:

$$\overline{\frac{\partial^2 T_{ij}(\mathbf{y}_1, t_1)}{\partial \tau^2} \frac{\partial^2 T_{kl}(\mathbf{y}_2, t_2)}{\partial \tau^2}} = \lim_{T \to \infty} \frac{1}{2T} \int_{-T}^{T} \frac{\partial^2 T_{ij}(\mathbf{y}_1, t_1)}{\partial \tau^2} \frac{\partial^2 T_{kl}(\mathbf{y}_2, t_2)}{\partial \tau^2} dt = \frac{\partial^4}{\partial \tau^4} \overline{T_{ij}(\mathbf{y}_1, t_1) T_{kl}(\mathbf{y}_2, t_2)}. \tag{2.17}$$

Some other assumption need to be made, which are not mentioned here for brevity, but they can be found in [55]. However, by substituting (2.13) into (2.14), and by using the far-field assumption ($|\mathbf{x} - \mathbf{y}_1| = x - \frac{\mathbf{x}}{x}.\mathbf{y_1} + O(x^{-1})$) and (2.17), the following relation

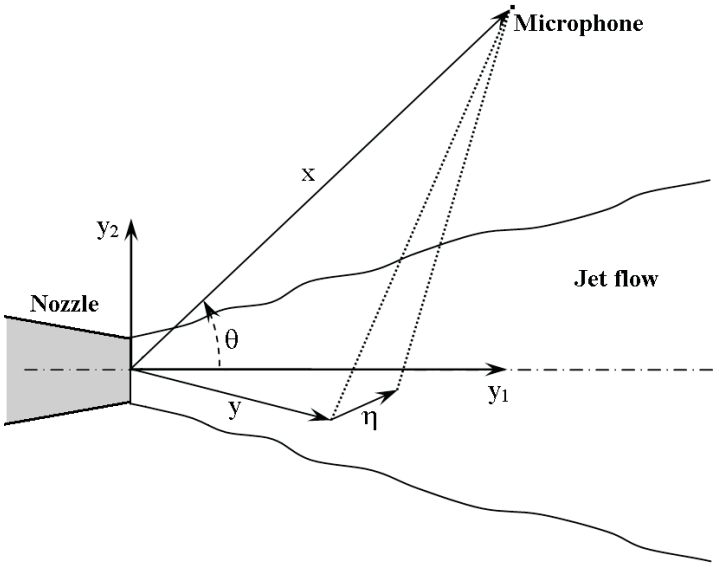

FIGURE 2.1: Coordinate system used in the calculations

can be found

$$\Gamma(\mathbf{x},t)=\frac{\rho_0}{16\pi^2c_0^2}\frac{x_ix_jx_kx_l}{x^6}\int\int R_{ijkl}(\mathbf{y}_1,\boldsymbol{\eta},\tau+\frac{\mathbf{x}}{x}.\frac{\boldsymbol{\eta}}{c_0})d\mathbf{y}_1d\boldsymbol{\eta}, \tag{2.18}$$

where $\boldsymbol{\eta}=\mathbf{y}_2-\mathbf{y}_1$, and R_{ijkl} is the Lighthill stress term correlation function in a fixed reference frame,

$$R_{ijkl}(\mathbf{y}_1,\,\boldsymbol{\eta},\,\tau)=\overline{T_{ij}(\mathbf{y}_1,t)T_{kl}(\mathbf{y}_1+\boldsymbol{\eta},t+\tau)}. \tag{2.19}$$

Upon taking its Fourier transform, the acoustic intensity spectrum can readily be found, as

$$I(\mathbf{x},\,\omega)=\frac{1}{32\pi^3\rho_0c_0^5x^2}\int_{-\infty}^{\infty}\frac{\partial^4}{\partial\tau^4}\int_{\mathbf{y}_1}\int_{\boldsymbol{\eta}}R_{ijkl}(\mathbf{y}_1,\,\boldsymbol{\eta},\,\tau)\,e^{j\omega[\boldsymbol{\tau}-\frac{\mathbf{x}}{x}.\frac{\boldsymbol{\eta}}{c_0}]}d\mathbf{y}_1d\boldsymbol{\eta}d\tau, \tag{2.20}$$

Equation (2.20) can be used to find the sound spectrum as soon as a mathematical model for the correlation function R_{ijkl}, *i.e.* equation (2.19), has been introduced, to allow integration. We will come back to the definition of the above fourth-order correlation function later.

Introduction of moving reference frame. When the acoustic sources are in uniform motion with the eddy convection speed U_c, the space retarded time covariance of T_{ij} is measured in the moving frame. In other words, experimentally the correlation $R_{ijkl}(\mathbf{y}_1, \boldsymbol{\eta}, \tau)$ in a jet flow has a form describing a moving, fluctuating pattern. This can be readily dealt with most neatly by transforming to a reference frame moving with the pattern convection velocity. The following transformation is taken,

$$\boldsymbol{\xi} = \boldsymbol{\eta} - \mathbf{U}_c\tau; \qquad \mathbf{U}_c = (U_1, 0, 0). \tag{2.21}$$

Inserting the new variable, equation (2.21), into equation (2.18), taking the Fourier transform, yields,

$$I(\mathbf{x},\ \omega) = \frac{\omega^4}{32\pi^3\rho_0(1 - M_c\cos\theta)^5 c_0^5 x^2} \int_{-\infty}^{\infty} \int_{\mathbf{y}_1} \int_{\boldsymbol{\xi}} R_{ijkl}^{(m)}(\mathbf{y}_1,\ \boldsymbol{\xi},\ \tau)\ e^{j\omega[(1-M_c\cos\theta)\tau - \frac{\mathbf{x}}{x}\cdot\frac{\boldsymbol{\xi}}{c_0}]} d\boldsymbol{\xi} d\mathbf{y}_1 d\tau, \tag{2.22}$$

where θ is the polar angle of the observer to the jet downstream axis direction. Although the above equation is an alternative form for the power spectral density of equation (2.18), it is more useful since the effects of source convection are more easily brought out. In equation (2.18) the space-time source field correlation is referred to a stationary coordinate frame and is designated R_{ijkl}. In equation (2.22) the same correlation is referred by transformation to a coordinate frame moving with velocity U_c, and is denoted by $R_{ijkl}^{(m)}$.

Before proceeding with the integration, one needs to provide a reasonably accurate estimation of the fourth order cross-correlation function. It has been shown before that the most significant contribution to noise radiation is due to the longitudinal-longitudinal correlation, $R_{1111}^{(m)}(y_1, \xi, \tau)$. This will be denoted by $R^{(m)}$ hereafter for brevity. Many different forms for $R^{(m)}(y_1, \xi, \tau)$ have been considered by various authors and these will be discussed later in section 4.2. For the present, a simple Gaussian correlation function is taken for both temporal and spatial parts [38, 44]. It is given by

$$R^{(m)}(\mathbf{y}, \boldsymbol{\xi}, \tau) = A^2\rho_0^2 v^4 e^{-\left(\frac{\tau}{\tau^A}\right)^2} e^{-\left\{\left(\frac{\xi_1 - U_c\tau}{L_1}\right)^2 + \left(\frac{\eta_2}{L_2}\right)^2 + \left(\frac{\eta_3}{L_3}\right)^2\right\}}, \tag{2.23}$$

where v denotes the characteristic turbulent velocity scale and τ^A and L_1 are correlation

time and longitudinal length scales which will be referred to as the acoustic scales to distinguish them from their $k-\varepsilon$ derived counterparts, which will be referred to as the turbulent scales. In addition, L_2 and L_3 are cross-stream length scales that are proportional to the longitudinal scale, while A is a numerical constant of the order 1 and is a function of Reynolds number (in terms of turbulent velocity and lateral dissipation scale, $\mathrm{Re}_\lambda = \frac{v\lambda_g}{\nu}$). Experimental data show that coefficient A must be in range of 0.58 to 0.7, but closer to 0.7 is more likely to occur [56].

The other factor in (2.22) which needs further explanation is the wavefront direction $\overrightarrow{x}\cdot\overrightarrow{\xi}$. In the geometric far-field of the jet the path difference in equation (2.22) has the simple form

$$\frac{\mathbf{x}\cdot\boldsymbol{\xi}}{x} = \xi_1\cos\alpha + \xi_2\sin\alpha\cos\beta - \xi_3\sin\alpha\sin\beta. \tag{2.24}$$

In order to carry out the integration with respect to ξ, a convenient coordinate transformation has one of the axes ξ_i aligned with vector $\mathbf{k}$, such that $\mathbf{k}.\boldsymbol{\xi} = k\xi_1\cos\alpha$. However, when turbulence is isotropic, the final result should be independent of the direction of wave number k. Assuming that the lateral scales are acoustically compact (*i.e.* turbulence length scale small relative to the acoustic wave-length), after substituting equation (2.23) and (2.24) in equation (2.22), the following relation can be obtained,

$$I(\mathbf{x},\omega) = \frac{A^2\rho_0}{32\pi^3 c_0^5(1-M_c\cos\theta)^5}\frac{\omega^4}{x^2}\int_{\mathbf{y}_1} L_1L_2L_3\tau^A v^4 e^{-\left(\frac{\omega L_1}{2c_0}\right)^2} e^{-\left(\frac{\omega(1-M_c\cos\theta)\tau^A}{2}\right)^2} d^3\mathbf{y}_1. \tag{2.25}$$

Although Lighthill Acoustic Analogy is a rearrangement of the Navier-Stokes equation, there are some assumptions to this formulation that limit its applicability. It is worth listing them here:

1. The sound is radiated into free space.

2. The sound induced by fluid flow is weak (*i.e.*, the backward-interaction of acoustic phenomena on the fluid flow is negligible.) In other words, the fluid flow is not sensitive to the sound induced by the fluid flow, and because of this reason the theory is effectively confined in its application to completely subsonic flows.

3. Taking accounts of the refraction effect using Lighthill's Acoustic analogy is a very difficult task since that must be considered as a part of the source term definition, T_{ij}.

4. Nearly parallel mean flow assumption needs to be used to numerically solve the Lighthill Acoustic Analogy equation.

5. In addition, the integral relation (equation (2.25)) will only give an estimation of the radiated noise from quadruple sources inside the jet flow, and does not account for monopole and dipole sources associated with the mean velocity gradient and density variation.

Lighthill's acoustic analogy is therefore successfully applicable to the analysis of energy "escaped" from subsonic flows as sound, and not to the analysis of the change in character of generated sound which is often observed in transitions to supersonic flow due to high frequency emission associated with shock waves.

2.2 MGBK Method

The simple form of the Lighthill analogy and also the conditions under which it is applicable, limits its application to very special cases. A more general formulation that can be used is the MGBK method. This is an updated version of a noise-prediction program, called "MGB" developed during the 1970s by Mani, Gliebe, and Balsa [5]. These authors provided a comprehensive analysis of the shielding effects of parallel jets when velocity and temperature profiles are functions of the radial variable only. The MGB method was then modified and improved by Khavaran, and is now referred to as MGBK method.

The MGBK method has been used many times for noise prediction of jet flows at different working conditions. One of the most important advantages of the MGBK method is its fast compatibility for any required adjustment to the flow condition or the source term. Source compactness [57], flow anisotropy [57], different shapes of the correlation functions, correlation model separability [31, 32], refraction and shielding effects [58], all have been investigated using the MGBK method. Use of the MGBK method for subsonic jet flows has been numerously reported in the literature [31, 32, 57]. Prediction of radiated noise from supersonic jets has also been studied using the MGBK method [27, 28].

The starting point of this model is the far field approximation of the Lighthill acoustic analogy, as given by Ribner [59],

$$\overline{p^2}(\mathbf{x},\tau) \propto \int_y I_{1111}(\mathbf{y},\tau)(a_{xx} + 4a_{xy} + 2a_{yy} + 2a_{yz})\, d\mathbf{y} \tag{2.26}$$

where the directivity factors a_{xx}, a_{xy}, a_{yy}, and a_{yz} are found from

$$\begin{aligned} a_{xx} &= \frac{\cos^4\ \theta}{(1 - M_c\ \cos\ \theta)^4}, \\ a_{xy} &= \frac{g_s^2 \cos^2\ \theta}{2(1 - M_c\ \cos\ \theta)^2}, \\ a_{yy} &= \frac{3}{8} g_s^4, \\ a_{yz} &= \frac{1}{8} g_s^4. \end{aligned} \tag{2.27}$$

where g_s is the value of the following function at the source point,

$$g^2(r) = \frac{(1 - M_s \cos\theta)^2 (c_0/c_s)^2 - \cos^2\theta}{(1 - M_c \cos\theta)^2}. \tag{2.28}$$

The proportionality factor, I_{1111}, in equation (2.26) is proportional to,

$$I_{1111}(\mathbf{y}, \tau) \propto \frac{1}{R^2}(1 - M_c \cos\theta)^{-1}(1 - M_s \cos\theta)^{-2} \int \frac{\partial^4}{\partial \tau^4} \overline{v_i v_j v_k' v_l'} d^3\mathbf{r} \tag{2.29}$$

where Ω is the observer frequency which relates to the source frequency through [27],

$$\Omega = \omega \sqrt{(1 - M_c \cos\theta)^2 + (\alpha_c k^{0.5}/c_0)^2}, \tag{2.30}$$

where the term $\alpha_c k^{0.5}/c_0$ accounts for the finite life-time of the eddy as it is convected downstream. The constant α_c is found from the measured data to be approximately 0.5.

Regarding the fourth-order correlation function in equation (2.29), it has been shown that for a homogeneous and isotropic turbulent flow, it consist of a sum of second-order velocity correlation [60],

$$\overline{v_i v_j v_k' v_l'} = \overline{v_i v_j}\ \overline{v_k' v_l'} + \overline{v_i v_k'}\ \overline{v_j v_l'} + \overline{v_i v_l'}\ \overline{v_j v_k'}. \tag{2.31}$$

It seems that this formulation was first introduced and experimentally examined by Uberoi [61, 62]. The modelling of the second-order correlation function will be discussed later in section 2.2.1.

Despite the popularity of the Ribner directivity equation, it is correct only when the shielding function, g^2, is positive. In the case of any turning point one needs to modify the directivity terms using Lilley's equation.

Up to this point, the effect of the sound-flow interactions on sound radiation mechanism from quadrupole sources has been considered. As has been shown earlier, in section 2.2, dipole sources, known as shear-noise, can be taken into account using the MGBK method, so one needs also to address the effects of the refraction on sound radiation from dipolar sources. In what follows, the method first developed by Mani *et al.* [5] is used. As before, Lilley's equation for an inviscid flow, linearised about uni-directional transversely sheared mean flow is taken as the basis of the study. This can be written

as,

$$L(p) = c_s^{-2} D^3 p - D\Delta p - \frac{d}{dr}(\log c^2) D\frac{\partial p}{\partial r} + 2\frac{dU}{dr}\frac{\partial^2 p}{\partial x \partial r}$$
$$= \rho D\ \nabla.\nabla.(v_1 v_1 - \overline{v_1 v_1}) - 2\rho \frac{dU}{dr}\frac{\partial}{\partial x}\nabla.(v_1 v_2 - \overline{v_1 v_2}) \tag{2.32}$$

where t denotes time, p is acoustic pressure, v_1, and v_2 are the axial and radial turbulent velocity fluctuations respectively. L is the Lilley wave operator term, and D is the convective derivative, $D = \frac{\partial}{\partial t} + U\frac{\partial}{\partial x}$, and

$$\Delta = \frac{\partial^2}{\partial x^2} + \frac{\partial^2}{\partial r^2} + \frac{1}{r}\frac{\partial}{\partial r} + \frac{1}{r^2}\frac{\partial^2}{\partial \theta^2}. \tag{2.33}$$

The first term on the right hand side of (2.32) denotes the typical quadrupole source term, which is due to the turbulence-turbulence interactions. The second term is attributed to the mean flow and turbulence interaction, or shear noise, which its noise radiation in the absence of refraction can be accounted for by MGBK method. In what follows, Balsa's [54] work for the high frequency Green's function solution for an axisymmetric Lilley's equation is utilized. For a monopole source convecting downstream the jet with convection velocity U_c, the Green's function satisfies:

$$L(G|U_c,\ x) = e^{-j\Omega t}\delta(x - U_c t)\delta(r - r_s)\delta(\phi - \phi_s)/r. \tag{2.34}$$

Let S_M and S_D be the Green's functions to the equations of the self- and shear-noise terms of Lilley's equation:

$$L(S_M|U_c,\ x) = \rho D\left\{e^{-j\Omega t}\delta(x - U_c t)\delta(r - r_s)\delta(\phi - \phi_s)/r\right\}, \tag{2.35}$$

$$L(S_D|U_c,\ x) = -2\rho e^{-j\Omega t}\frac{dU}{dr}\delta(x - U_c t)\delta(r - r_s)\delta(\phi - \phi_s)/r, \tag{2.36}$$

Subsequently, it can be readily shown that

$$S_M = -j\rho\Omega\left(\frac{1 - M_s\cos\ \theta}{1 - M_c\cos\ \theta}\right)G. \tag{2.37}$$

Assuming that $\frac{d^n U}{dr^n} = 0$ for $n \geqslant 2$, a similar relation can be found for a dipole source,

$$S_D = -2\rho\frac{dU}{dr}G. \tag{2.38}$$

It should be noted here that the density gradients are neglected in the derivation of the above relations. The density gradient can produce an additional dipole-like source which was studied by Mani [63]. The following dependency can be readily deduced from the Green's functions of the monopole and dipole sources,

$$\frac{S_D}{S_M} = -j\frac{2dU/dr}{\Omega}\frac{1 - M_c\cos\ \theta}{1 - M_s\cos\ \theta}. \tag{2.39}$$

In order to find G, after using the sequence of Fourier transformations, one finds that equation (2.34) reduces to,

$$\frac{d^2\bar{G}}{dr^2} + \left[\frac{1}{r} + \frac{d}{dr}\log(\frac{c_s}{c_0})^2 + \frac{2s}{k - Ns}\frac{dN}{dr}\right]\frac{d\bar{G}}{dr} + \left[\frac{(k - Ns)^2}{(c_s/c_0)^2} - s^2 - \frac{n^2}{r^2}\right]\bar{G} = \frac{j}{c_0\sqrt{2\pi}}\frac{e^{jn\phi_s}}{Ns - k}\frac{\delta(r - r_s)}{r} \tag{2.40}$$

where $\bar{G}$ is given by,

$$\bar{G} = \frac{e^{j\omega t}}{\sqrt{2\pi}}\int_{-\infty}^{\infty} e^{-jsx}dx \int_{-\infty}^{\infty} e^{jn\theta}Gd\theta, \tag{2.41}$$

$$(-\infty \le s \le \infty,\ n = 0,\ \pm 1,\ \ldots)$$

The first order derivative of $\bar{G}$ in (2.40) can be eliminated by a standard transformation. Defining

$$P = \sqrt{r}\frac{c_s}{c_0}\frac{1}{-k + Ns}\bar{G} \tag{2.42}$$

Equation 2.40 then reduces to

$$P_{rr} + \left\{k^2g^2(r;\sigma) - \frac{n^2 - 1/4}{r^2}\right\}P = \frac{j}{k^2\sqrt{2\pi}}\frac{c_s}{c_0^2}\frac{1}{(1 - N\sigma)^2}e^{jn\phi_s}\frac{\delta(r - r_s)}{\sqrt{r}} \tag{2.43}$$

where $k = \omega/c_0$, $\sigma = s/k$, $N = (U - U_c)/c_0$, and

$$g^2(r;\sigma) = \frac{(1 - N\sigma)^2}{(c_s/c_0)^2} - \sigma^2 \tag{2.44}$$

Looking at the above equations one can deduce that the behaviour of P depends on the algebric sign of g^2. P is oscillatory for $g^2 > 0$, and exponential for $g^2 < 0$. The location in the shear layer where g^2 changes sign is known as the turning point (r_σ). When a negative region exists, fluid shielding of the source is possible and the amount of shielding depends on the proximity of the source with respect to the turning point as

well as the number of turning points. For single flow cold jet, it is reasonable to assume that only one turning point occurs.

By evaluating the axial wave number, σ, at the point of stationary phase, r_σ, equation (2.44) reduces to,

$$g^2(r) = \frac{(1 - M_s \cos\theta)^2 (c_0/c_s)^2 - \cos^2\theta}{(1 - M_c \cos\theta)^2}. \tag{2.45}$$

In case of no turning point, the Green's function can be found as

$$G = \frac{1}{4\pi c_0 kR} \frac{c_s/c_0}{(1 - M_s \cos\theta)^2} \left(\frac{\xi_s}{r_s g_s}\right)^{1/2} e^{j\omega(R/c_0 - t)} e^{jk\left[\int_0^\infty (g - g_\infty)dr - \xi_0 \cos(\phi - \phi_s)\right]} \tag{2.46}$$

where

$$\xi = \int_0^r g dr \tag{2.47}$$

Considering the case in which the shielding function, g^2 has a unique turning point at $r = r_\sigma$ (so that $r_\sigma > r_o$), the solution of the Green's function is given by

$$G = \frac{1}{4\pi c_0 kR} \frac{c_s/c_0}{(1 - M_s \cos\theta)^2} \left(\frac{\xi_s}{r_s f_s}\right)^{1/2} e^{j\omega(R/c_0 - t)} e^{jk\left[\int_{r_\sigma}^\infty (g - g_\infty)dr - jkg_\infty r_\sigma - \xi_0 \cos(\phi - \phi_s)\right]} \tag{2.48}$$

where $f^2 = -g^2$.

After taking the derivatives of the Green's function of each source with respect to the coordinates to make a quadrupole like sources, and then averaging circumferentially with respect to ϕ and ϕ_s, the following equations giving the directivity factors can be obtained

$$\begin{aligned} D_{ij}^{(M)} &= \frac{1}{4\pi^2} \int_{-\pi}^{\pi} \int_{-\pi}^{\pi} \left| \frac{\partial^2 S_M}{\partial x_i \partial x_j} \right| d\phi_s d\phi, \\ D_{ij}^{(D)} &= \left(\frac{2dU/dr}{\Omega} \frac{1 - M_c \cos\theta}{1 - M_s \cos\theta} \right)^2 D_{ij}^{(M)}. \end{aligned} \tag{2.49}$$

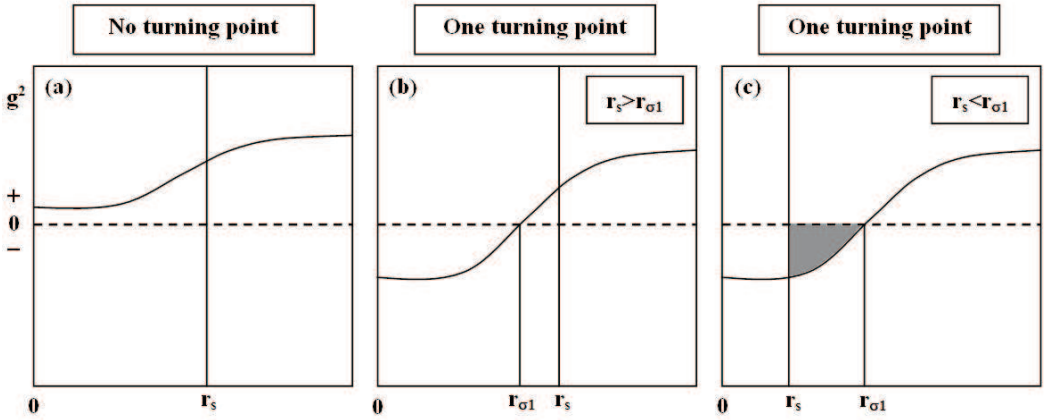

FIGURE 2.2: Position of the turning points. Shaded areas denote shielding of source

and these yields,

$$
\begin{aligned}
D_{11}^{(M)} &= \frac{\cos^4\ \theta}{(1-M_c\ \cos\ \theta)^4}\beta_{xx},\\
D_{12}^{(M)} &= \frac{g_s^2\cos^2\ \theta}{2(1-M_c\ \cos\ \theta)^2}\beta_{xy},\\
D_{22}^{(M)} &= \frac{3}{8}g_s^4\beta_{yy},\\
D_{23}^{(M)} &= \frac{1}{8}g_s^4\beta_{yz}.
\end{aligned}
\tag{2.50}
$$

The shielding coefficients, β_{xx}, β_{xy}, β_{yy}, and β_{yz} depend upon the case encountered in figures 2.2 and 2.3, and Table 2.2. The parameters β_{01}, β_{02}, β_{12} are defined as,

$$
\begin{aligned}
\beta_{01} &= \exp\left\{-2\Omega/c\int_{r_s}^{r_{\sigma 1}}\left|g^2(r)\right|^{1/2}dr\right\},\\
\beta_{02} &= \exp\left\{-2\Omega/c\int_{r_s}^{r_{\sigma 2}}\left|g^2(r)\right|^{1/2}dr\right\},\\
\beta_{12} &= \exp\left\{-2\Omega/c\int_{r_{\sigma 1}}^{r_{\sigma 2}}\left|g^2(r)\right|^{1/2}dr\right\}.
\end{aligned}
\tag{2.51}
$$

In order to better understand the anisotropy effects two parameters are defined, $\beta_c = 1 - \overline{v_2^2}/\overline{v_1^2}$ and $\Upsilon = L_2/L_1$, with v_1 being the stream-wise turbulent velocity, and v_2, and v_3 the cross-stream turbulent velocities. For an axisymmetric jet flow $\overline{v_2^2} \approx \overline{v_3^2}$. In the limiting case of isotropic turbulence they reduce to $\Upsilon = 1$, $\beta_c = 0$. Finally, after finding the directivity coefficients from equation (2.50), the power spectral directivity of

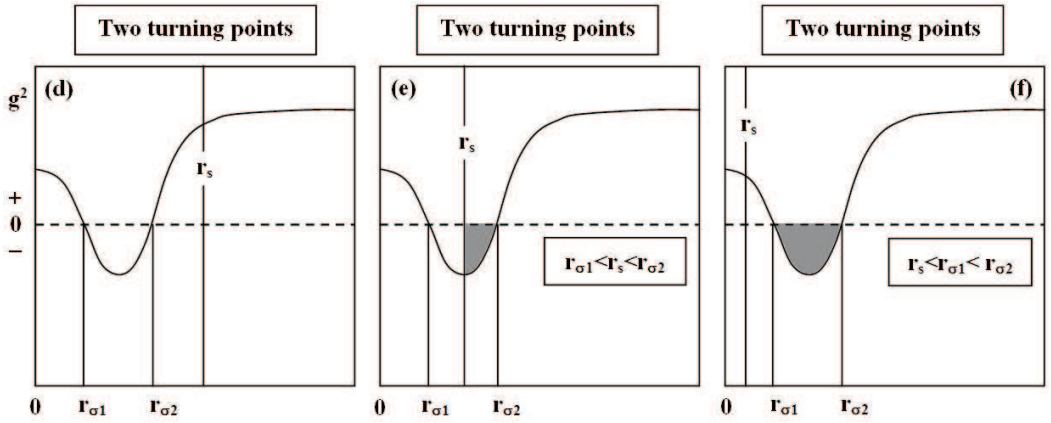

FIGURE 2.3: Position of the turning points. Shaded areas denote shielding of source

Case	β_{xx}	β_{xy}	β_{yy}	β_{yz}
a	1	1	1	1
b	1	1	1	1
c	β_{01}	0	0	0
d	1	1	1	1
e	β_{02}	0	0	0
f	β_{12}	β_{12}	β_{12}	β_{12}

TABLE 2.1: Shielding coefficients β_{ij}.

an axisymmetric jet ($D_{22}^{(M)} = D_{33}^{(M)}$ and $D_{12}^{(M)} = D_{13}^{(M)}$) can be expressed as,

$$I^{Self}(\mathbf{x},\,\theta,\,\omega) = \int_y \int_{-\infty}^{+\infty} \left\{ D_{11}^{(M)} + 2\zeta_1 D_{22}^{(M)} + 4\left(\zeta_2 + 2\zeta_4\right) D_{12}^{(M)} + 2\left(\zeta_3 + 2\zeta_5\right) D_{23}^{(M)} \right\} \Pi_M e^{j\Omega\tau} d\tau d\mathbf{y}, \tag{2.52}$$

$$I^{Shear}(\mathbf{x},\,\theta,\,\omega) = \int_y \int_{-\infty}^{+\infty} \left\{ \zeta_4 D_{11}^{(M)} + \left(\zeta_1 + \zeta_5\right) D_{12}^{(M)} \right\} \Pi_D e^{j\Omega\tau} d\tau d\mathbf{y}, \tag{2.53}$$

where

$$\Pi_M = \frac{(\rho_o/\rho_s)^2}{(4\pi R c_s c_o)^2 (1 - M_s \cos\,\theta)^2 (1 - M_c \cos\,\theta)^2} I_{1111}(\mathbf{y}, \tau), \tag{2.54}$$

$$\Pi_D = \left(\frac{2dU/dr}{\Omega} \frac{1 - M_c \cos\,\theta}{1 - M_s \cos\,\theta} \right)^2 \Pi_M, \tag{2.55}$$

where the weight coefficients, ζ_1, appearing in equation (2.52) and (2.53) are related to the non-isotropic factors through

$$\begin{aligned}
\zeta_1 &= \frac{3}{2}\beta_c^2 + \frac{1}{32}\left[9\left(\Upsilon+\Upsilon^{-1}\right)^4 - 48\left(\Upsilon+\Upsilon^{-1}\right)^2 + 80\right] - \frac{\beta_c}{4}(6-\Upsilon^2+3\Upsilon^{-2}),\\
\zeta_2 &= \frac{1}{8},\\
\zeta_3 &= \frac{1}{8}\left[\frac{3}{4}\left(\Upsilon+\Upsilon^{-1}\right)^4 - 4\left(\Upsilon+\Upsilon^{-1}\right)^2 + 7 - 2\Upsilon^2 + 4\beta_c^2\right] + 2\beta_c(\Upsilon^2-2-\Upsilon^{-2}),\\
\zeta_4 &= \frac{1}{16}(5+2\Upsilon^{-2}-8\beta_c),\\
\zeta_5 &= \frac{1}{2}(\zeta_1-\zeta_3).
\end{aligned} \tag{2.56}$$

Now the self-noise and shear noise can be calculated after integrating this source over the domain and also time.

It is worth mentioning here that aside from the MGBK method which enables us to calculate the self and shear noise components, Jordan and Gervias [64] developed an alternative formulation based on Lighthill's Acoustic Analogy. According to their method the total radiated noise is given by

$$I(\mathbf{x},\,\theta,\,\omega) = \rho(16\pi^2c^5x^2C^5)^{-1}\int_{-\infty}^{\infty}\int_{V_y}\left(D_{ijkl}I_{ijkl}^{(Self)}(\mathbf{x},\mathbf{y},\tau) + D_{ijkl}I_{ijkl}^{(Shear)}(\mathbf{x},\mathbf{y},\tau)\right)e^{j\Omega\tau}d^3\mathbf{y}d\tau. \tag{2.57}$$

Here, $I_{ijkl}^{(Self)}$, and $I_{ijkl}^{(Shear)}$ are the acoustic intensity at x due to a volume of turbulence-turbulence, and turbulence-mean flow disturbances located at the point y, respectively. The self and shear noise terms used in equation (2.57) can be found from:

$$\begin{aligned}
D_{ijkl}I_{ijkl}^{(Self)}(\mathbf{x},\mathbf{y},\tau) \equiv \Bigg[&\cos^4\theta\int\frac{\partial^4}{\partial\tau^4}\overline{v_1^2v_1'^2}d^3\mathbf{r} + 2\cos^2\theta\,\sin^2\theta\int\frac{\partial^4}{\partial\tau^4}\overline{v_1v_mv_1'v_m'}d^3\mathbf{r}\\
&+2\cos^2\theta\,\sin^2\theta\int\frac{\partial^4}{\partial\tau^4}\overline{v_1^2v_m'^2}d^3\mathbf{r} + 3/8\sin^4\theta\int\frac{\partial^4}{\partial\tau^4}\overline{v_m^2v_m'^2}d^3\mathbf{r}\Bigg],
\end{aligned} \tag{2.58}$$

and

$$D_{ijkl}I_{ijkl}^{(Shear)}(\mathbf{x},\mathbf{y},\tau) \equiv 2\left[2\cos^4\theta \int \frac{\partial^4}{\partial\tau^4} UU'\overline{v_1 v_1'}\, d^3\mathbf{r} + \cos^2\theta\ \sin^2\theta \int \frac{\partial^4}{\partial\tau^4} UU'\overline{v_m v_m'}\, d^3\mathbf{r}\right], \tag{2.59}$$

where $m = \{2, 3\}$ denotes the dummy indices.

2.2.1 Second Order Correlation Function

To carry on with the integration of equations (2.52) and (2.53) one needs a model of the correlation function, $\overline{vv'}$. Different types of correlation functions have been examined but this has not been exhaustive and further research is required. The correlation must reflect the underlying physics of the turbulence. The most important features of turbulence, in particular jet turbulence, are its homogeneity, isotropy and axisymmetry. In most of the practical cases it is believed that turbulence can be considered homogeneous. Also, it has been shown that turbulence can be assumed axisymmeric [65, 66], but, while the small scale structures are well approximated as isotropic, this is not so for the large scale turbulence. The correlation function must be derived in a way to include all these characteristics.

An explicit representation form of an axisymmetric tensor $Q_{ij} = \overline{v_i v_j'}$ can be given as [56]:

$$\begin{aligned} Q_{ij} = &\left[\xi_i\xi_j D_r - \delta_{ij}(r^2 D_r + r\mu D_\mu + 2) + \lambda_i\xi_j D_\mu\right] Q_1 \\ &+ \left[\xi_i\xi_j D_r - \delta_{ij}\left\{r^2(1-\mu^2)D_r + 1\right\} + \lambda_i\lambda_j(r^2 D_r + 1) - (\lambda_i\xi_j + \lambda_j\xi_i)r\mu D_r\right] Q_2 \\ &+ \left[-\xi_i\xi_j D_\mu + \delta_{ij}\left\{r^2(1-\mu^2)D_\mu - r\mu\right\} - \lambda_i\lambda_j r^2 D_r + (\lambda_i\xi_j + \lambda_j\xi_i)r\mu D_\mu + \lambda_j\xi_i\right] Q_3, \end{aligned} \tag{2.60}$$

where the unit vector $\boldsymbol{\lambda} = (\lambda_1,\ \lambda_2,\ \lambda_3)$ denotes a principal direction, with r and μ defined as $r^2 = (\boldsymbol{\xi}.\boldsymbol{\xi})$, $(\boldsymbol{\xi}.\boldsymbol{\lambda}) = r\mu$, and the derivatives are defined as,

$$\begin{aligned} D_r &= \frac{1}{r}\frac{\partial}{\partial r} - \frac{\mu}{r^2}\frac{\partial}{\partial\mu}, \\ D_\mu &= \frac{1}{r}\frac{\partial}{\partial\mu}, \end{aligned} \tag{2.61}$$

and scalar functions Q_1, Q_2, and Q_3 are arbitrary functions of the correlation distance vector $\boldsymbol{\xi}$, τ and source location. From the required symmetry of Q_{ij} in its indices it can be shown that Q_3 is a dependent function of Q_1 of the form

$$Q_3 = D_\mu Q_1, \tag{2.62}$$

so that, Q has two independent components. Interchangeability of the indices also requires that [56]

$$(\xi_3 \frac{\partial}{\partial \xi_2} - \xi_2 \frac{\partial}{\partial \xi_3}) Q_i = 0, \qquad (i = 1,\ 2). \tag{2.63}$$

Hence, the correlation function can be found after defining a set of scalars functions compatible with the condition of equation (2.63). At this point the space and time separability of the correlation function has not been considered. By separability is meant the separability of the correlation into two factors each dependent on space or time variables. This will be further discussed in the next section.

Separable Two-Point Correlation

One of the most convenient forms of correlation was suggested by Ribner [59, 67] as:

$$Q_{ij}(r,\ \tau) = \Psi_{ij}(r) g(\tau), \tag{2.64}$$

where, for homogeneous isotropic turbulence the spatial part can be written as [60]

$$\Psi_{ij}(r) = k \left[(f + 1/2r\, f') \delta_{ij} - 1/2 f'\, r_i r_j / r \right], \tag{2.65}$$

and $k = \frac{1}{2}\left(\overline{v_1^2} + \overline{v_2^2} + \overline{v_3^2}\right)$ is the local turbulent kinetic energy, v_1 and $v_{2,3}$ being the stream-wise, and cross-stream (span-wise) turbulent velocities respectively, and f is function of r which can take different forms. Among these the following are commonly

used:

$$f(r) = e^{-\pi\left(\frac{r_1^2}{L_1^2}+\frac{r_2^2}{L_2^2}+\frac{r_3^2}{L_3^2}\right)}, [31, 32] \tag{2.66a}$$

$$f(r) = e^{-\pi\left(\frac{r_1}{L_1}+\frac{r_2}{L_2}+\frac{r_3}{L_3}\right)}, [31, 32] \tag{2.66b}$$

$$f(r) = e^{-\left(\frac{r_1}{L_1}+\frac{r_2^2}{L_2^2}+\frac{r_3^2}{L_3^2}\right)}, [48] \tag{2.66c}$$

$$f(r) = e^{-\sqrt{\left(\frac{r_1}{L_1}\right)^2+\left(\frac{r_2^2}{L_2^2}+\frac{r_3^2}{L_3^2}\right)^2}}, [48] \tag{2.66d}$$

$$f(r) = e^{-\frac{r^2}{L^2}}, [68] \tag{2.66e}$$

where L_1, L_2, and L_3 are length scales in the axial, radial and azimuthal directions respectively, and $L(L_1, L_2, L_3, \overrightarrow{r})$ is defined by [68]:

$$L(L_1, L_2, L_3, \overrightarrow{r}) = \sqrt{\frac{L_1^2 L_2^2 L_3^2 (r_1^2 + r_2^2 + r_3^2)}{L_2^2 L_3^2 r_1^2 + L_1^2 L_3^2 r_3^2 + L_1^2 L_2^2 r_3^2}}, \tag{2.67}$$

These formulations all requires a knowledge of the fluid dynamics and turbulence, which one can obtain by measurement or using a CFD turbulence model, such as RANS. Further details about definition of the length scale will be given in Chapter 3. It is routinely assumed that $L_2 = L_3$ are proportional to L_1, as $\Upsilon = L_2/L_1$. The spatial function models (2.50c) and (2.50d) were introduced by Harper-Bourne [48] who showed that they give a highly acceptable fit with experimental results.

The temporal factor, $g(\tau)$, which gives the temporal decay of the correlation has been modelled in following ways:

$$g(\tau) = e^{-(\frac{\tau}{\tau_0})^2}, [20] \tag{2.68a}$$

$$g(\tau) = e^{-\left|\frac{\tau}{\tau_0}\right|}, [64] \tag{2.68b}$$

$$g(\tau) = e^{-\sqrt{(\sigma/2)^2+(\tau/\tau_0)^2}}, [57] \tag{2.68c}$$

$$g(\tau) = e^{-c_1(\tau/\tau_0)^2-c_2\sqrt{c_3+(\tau/\tau_0)^2}}, [58] \tag{2.68d}$$

where τ_0 is a characteristic time scale of the turbulence, and c_1, c_2, c_3, and σ are empirical constants.

As can be seen, various kinds of temporal functions have been attempted so far. The Gaussian form has been used more than any other, but Khavaran and Krejsa [57] have

developed the last function and have stated that it provides an overall improvement in the predicted spectra at high frequencies compared to the Gaussian model. As with the length scale, some knowledge of turbulence and fluid dynamics is needed for a definition of the time scale. A complete review of the characteristic time scale (τ_0) and length scale (L) come later in section 3.

In all cases, the integration of the temporal part $g^2(\tau)$ over τ, which appears upon substituting (2.64) in (2.52) and (2.53), can be simplified using the following relation

$$\langle G \rangle = \int_{-\infty}^{+\infty} \frac{\partial^4}{\partial \tau^4} g^2(\tau) e^{j\Omega\tau} d\tau = \Omega^4 \int_{-\infty}^{+\infty} g^2(\tau) e^{j\Omega\tau} d\tau. \tag{2.69}$$

The following relations for $\langle G \rangle$ can be found using different $g(\tau)$ functions, listed above. Using a Gaussian function leads,

$$\langle G \rangle = \frac{\sqrt{2\pi}}{2} \tau_0 \Omega^4 e^{-\frac{1}{8}\Omega^2 \tau_0^2}, \tag{2.70}$$

and using the second model (exponential form) yields,

$$\langle G \rangle = \frac{4\tau_0 \Omega^4}{4 + \tau_0^2 \Omega^2}, \tag{2.71}$$

using the third model ($g(\tau) = e^{-\sqrt{(\sigma/2)^2 + (\tau/\tau_0)^2}}$) gives rise to:

$$\langle G \rangle = \sigma \tau_0 \Omega^4 \frac{K_1(\sigma\sqrt{1 + (\Omega\tau_0/2)^2})}{\sqrt{1 + (\Omega\tau_0/2)^2}}, \tag{2.72}$$

where $K_1(.)$ denotes the modified Bessel function of the second kind and first order. Finally, use of the last model with $c_3 = 0$:

$$\langle G \rangle = \sqrt{\frac{\pi}{8c_1}} \tau_0 \Omega^4 \, \mathrm{Re}\{e^{\Xi^2} erfc(\Xi)\}, \tag{2.73}$$

where $\Xi = \frac{c_2 - j(\Omega\tau_0/2)}{\sqrt{2c_1}}$.

Non-Separable Two-Point Correlation

As stated earlier the choice of the correlation function depends only upon the scalar functions Q_1, and Q_2, regardless of whether it is separable or not. The following examples of scalar functions of a non-separable two-point correlation is given in [57]:

$$\begin{aligned} Q_1 &= -\frac{\overline{v_1^2}}{3} e^{-\pi h(\tau)\left\{\xi_1^2/L_1^2+\left(\xi_2^2+\xi_3^2\right)/L_2^2\right\}}, \\ Q_2 &= -\left(\overline{v_1^2}-\overline{v_2^2}\right) e^{-\pi h(\tau)\left\{\xi_1^2/L_1^2+\left(\xi_2^2+\xi_3^2\right)/L_2^2\right\}}, \end{aligned} \tag{2.74}$$

where it is concluded that the separable and non-separable functions would lead to identical results, provided that $h(\tau)$ is chosen carefully [57]. So, at the end, the separability assumption is simply a more convenient way for integrating the source correlation terms.

It can be seen from equations (2.52) through (2.55) that a knowledge of fluid dynamics and turbulence is required to be used as input for the equations. Such information can be obtained using a CFD-turbulence model, such as a RANS $k-\varepsilon$ method. This will provide steady values, such as mean velocity, mean flow strain rate, temperature and sound speed, and also time-averaged turbulence values, such as turbulence kinetic energy, k, turbulence dissipation rate, ε, turbulence production rate, Pr, *etc.* The steady values are used for the definition of the convection factor, C, as well as the flow factor, F, while the turbulence values are mostly used for the definition of the source terms, and particularly for the two-point correlation function. The background theory of turbulence modelling and explanation of the models used in our CFD simulations are all given in Appendix A. The next two Chapters will focus on various aspects of turbulence and noise production and radiation mechanisms, and, accordingly, suggestions will be given for jet noise prediction improvement.

Chapter 3

Turbulence Parameters

> On his death bed, Heisenberg is reported to have said: *When I meet God, I am going to ask him two questions: Why relativity? And why turbulence? I really believe he will have an answer for the first.*

3.1 Introduction

In the previous chapter noise radiation from a turbulent jet flow was considered in a mathematical fashion and it was mentioned that some information about the flow dynamics and the turbulence is required. This information can be easily obtained using any turbulence model, such as RANS and although the accuracy of the information is quite important, the interpretation of the obtained CFD results and the relation to the noise production mechanism is even more important. The most important interpretation to be considered is the appropriate definition of the time and length scales which were left in Chapter 2 to be studied here.

This Chapter gives an overview of the relationships between turbulence and the noise generation mechanism. Once this relationship is well understood, some important characteristics of the turbulence, such as the time scale, length scale and convection velocity will be discussed. In brief, the most important feature of this chapter is the definition of a new time scale and its frequency dependence. It will be shown how the frequency dependency (that is known to give improved noise prediction) arises naturally from

the physics of the turbulence, and without any additional or extraneous mathematical modelling.

Turbulence is essentially random, occurs at high Reynolds number, shows strong intermittency, and is characterized by a wide range of scales (both in space and time). Turbulence parameters, for example velocity, can be written in terms of mean and fluctuating components, as

$$u = U + v. \tag{3.1}$$

The mean-flow and turbulence motions have a number of scales associated with them. We can generally think of turbulence in terms of a cascade: energy enters through a production mechanism at the largest scale and is transferred by a cascade process to smaller scales. At the smallest scale it is dissipated. This is neatly summed up by the well-known quotation:

> *Big whorls have little whorls, which feed on their velocity; and little whorls have lesser whorls, and so on to viscosity.*
>
> "L. F. Richardson, 1922"

What Richardson calls whorls we would call eddies. Roughly speaking an eddy is a region over which the flow is correlated. Large eddies are unsteady and break up into smaller ones and this happens on a characteristic time scale. With the smallest eddies viscosity dominates and the energy dissipates as heat.

As we move through the cascade, the length scale associated with eddies decreases and it is useful to identify different regions. The largest scales are produced by transferring energy form the mean flow and are produced at a length scale characteristic of the macroscopic problem. The larger eddies form what is known as the energy containing region and, as the name suggests, they contain the bulk of the turbulent energy. Hence we expect their typical velocity to be given by $v_0 = (2/3k)^{1/2}$, where k is the turbulent kinetic energy per unit mass. The energy containing range is bounded below by length scale l_E where the inertial subrange begins. As the length scale decreases viscous forces become more important and at l_D the inertial subrange gives way to the dissipation range where viscosity dominates and the energy is dissipated.

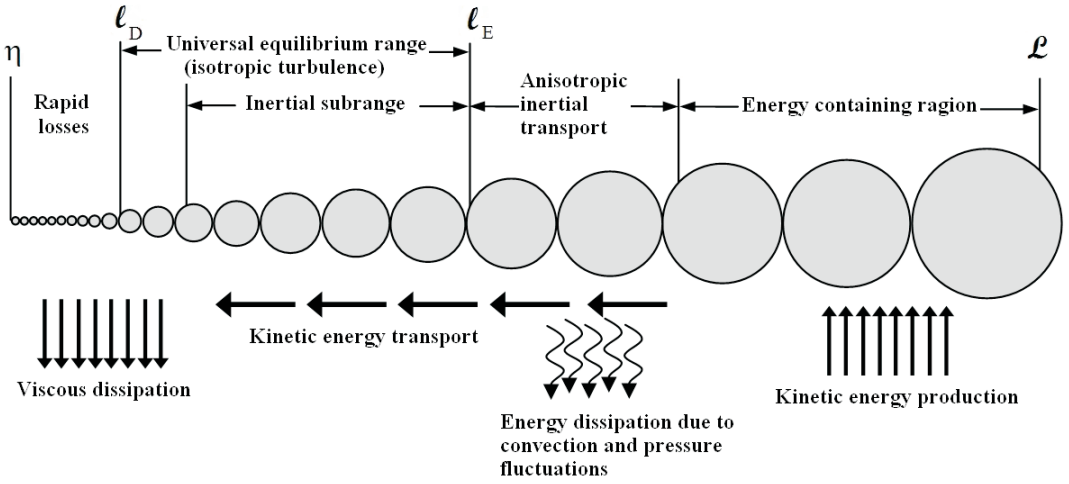

FIGURE 3.1: A schematic of the turbulent eddy cascade for very high Reynolds numbers, after [70]

The inertial and dissipation ranges together form the universal equilibrium range. The importance of this range was recognised by Kolmogorov who postulated that for length scales below l_E the turbulence effectively forgets the details of the production process. More formally, for $l < l_E$ all turbulent flow can be characterized by a universal description. A schematic of the eddy size in a turbulent flow is shown in figure 3.1. Borders between the different mentioned ranges can be roughly approximated using the scales which are more familiar, as [69]

$$\begin{aligned} l_D &= 60\eta, \\ l_E &= \frac{1}{6}L_0, \end{aligned} \tag{3.2}$$

where $\eta = (\nu^3/\varepsilon)^{1/4}$ is the so-called Kolmogorov length scale, and L_0 refers to the largest eddy size of the turbulence that is comparable to the mean flow scales. The next section concerns the most important time- and length scales in the turbulence.

3.2 Turbulence and Important Scales

In order to gain a better understating of the turbulence and its behaviour, it will be instructive to consider in more detail the different scales that exist in a turbulent flow.

In general terms, turbulence scales can be categorized either in terms of the eddy size, or the dominant turbulence phenomenon. These two categories will be studied below.

3.2.1 Turbulence Scales in Terms of The Eddy Size

Regarding the variety of eddy sizes in the turbulence, they generally falls into three typical categories: "***integral scale***", "***Taylor scale***", and "***Kolmogorov scale***". These scales can cover up to ten orders of magnitude difference in length. A general explanation of each scale is given below.

Kolmogorov Length and Time Scale

The smallest scales in a turbulent flow are known as the Kolmogorov scales. At this scale viscosity can be effective in smoothing out velocity fluctuations. These small motions tend to have small time scales, which are statistically independent of the slow large-scales motion and of the mean flow. The following relations provide a reasonable estimation of the Kolmogorov length and time scale in terms of the flow Reynolds number [69]:

$$\begin{aligned} \frac{\eta}{L_0} &\propto (\mathrm{Re}_{L_0})^{-3/4}, \\ \frac{\tau_\eta}{\tau_0} &\propto (\mathrm{Re}_{L_0})^{-1/2}, \end{aligned} \tag{3.3}$$

where $\mathrm{Re}_{L_0} = \frac{k^{1/2} L_0}{\nu}$, with L_0 being the largest eddies of the turbulence are characterized by the length scale, which is comparable to the flow scale L, and k the turbulent kinetic energy.

Dissipation Length and Time Scale (Taylor microscales)

This scale gives a measure of the average dimension of the smallest eddies, at which molecular viscosity dissipates kinetic energy into heat. The longitudinal Taylor microscale can be obtained from

$$\lambda_f = -\frac{1}{2}\left[\frac{\partial^2 f(r)}{\partial r^2}\right]_{r=0}, \tag{3.4}$$

where $f(r)$ is the longitudinal correlation coefficient, and is given by [69]

$$f(r) = \frac{\overline{v_1(\xi_1)v_1(\xi_1 + r)}}{v_1^2}. \tag{3.5}$$

The transverse Taylor macroscale, λ_g, in isotropic turbulence is equal to $\lambda_f/\sqrt{2}$. It is possible to infer that the dissipation length scale gives a measure of the average size (diameter) of those eddies that are principally responsible for dissipation of the turbulent kinetic energy. Furthermore, the following relation with the macroscopic length scales exists [69]

$$\frac{\lambda_f}{L_0} = \sqrt{20}\,\mathrm{Re}_{L_0}^{-1/2}, \tag{3.6}$$

In a similar way, one can define a time scale that gives a measure of the most rapid changes of turbulent velocities, as

$$\tau = -\frac{1}{2}\left[\frac{\partial^2 R(t)}{\partial t^2}\right]_{t=0}, \tag{3.7}$$

where R denotes the Eulerian time correlation of the corresponding velocity signals, given by,

$$R(t) = \frac{\overline{v_1(t')v_1(t'-t)}}{v_1^2}. \tag{3.8}$$

Integral Length and Time Scale

The integral length scale is, to a certain extent, a measure of the longest connection, or correlation distance between the velocities at two points in the shear flow. It can be understood that the fluctuating velocity correlation will be identically zero beyond some finite distance. The longitudinal integral length scale is defined by:

$$\Lambda_f = \int_0^\infty f(r)dr. \tag{3.9}$$

It can also be shown that the transverse length scale Λ_g is half of the longitudinal length scale for isotropic turbulence [56]. A general description of the Taylor and integral length scales is illustrated in figure 3.2.

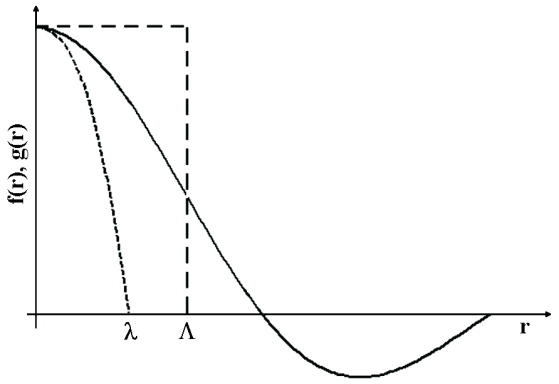

FIGURE 3.2: Estimate of the dissipation and integral lengths

Similar to the integral length scale, the integral time scale can be found from integration of the temporal correlation function R, as

$$\Im = \int_0^\infty R(t)dt, \tag{3.10}$$

and may be interpreted as the longest life for connection in the turbulent behaviour of two fluctuating velocity signals at a fixed point in the flow field but at two instants (Eulerian system).

3.2.2 Turbulence Scales in Terms of The Dominant Physical Phenomenon

Having mentioned most of the possible definitions of the length scale, it can be said at this point that in most of the applications what we mean by the length scale is a measure of the eddy size. The eddy size can be somehow estimated using the shear layer thickness. It has been also principally accepted to use definition $l \propto v^3/\varepsilon$, where v is the fluctuating velocity and $v = k^{1/2}$. This length scale can be assumed to be the scale characterizing the large eddies.

On the other hand, the characteristic time scales of a jet flow, in general, are of three sorts: those related to the development of the whole flow, those associated with the interaction of the mean flow and the turbulence, and finally those that provide a measure of the action of the turbulence on itself. These three scales can be characterized as

"***mean flow strain rate scale***", "***turbulence production scale***", and "***turbulence decay scale***". The time scale associated with the first phenomenon, τ_s, gives an estimate of the rate of change of the mean velocity. The production time scale, τ_p, shows the time needed to produce an amount of energy k at the rate of Pr, and finally, the dissipation time scale, τ_d, gives an estimate of the time to dissipate an amount of energy k at the constant rate ε. These scales are given by,

$$\tau_d \propto (\tfrac{k}{\varepsilon}), \quad \tau_s \propto (|dU/dr|)^{-1}, \quad \tau_p \propto (\tfrac{k}{Pr}). \tag{3.11}$$

The dissipation and production time scales in the universal equilibrium range are roughly equal and are the largest time scales of the turbulence. The strain rate time scale, τ_s, gives an estimate of variation of the mean flow velocity in the radial direction, which is a measure of evolution time of the largest eddies it will be shown that is not of great concern.

3.2.3 Taylor's Hypothesis

Since some of the most important assumptions used in noise modelling are made based on Taylor's hypothesis, it will be worthwhile to spend some time on its definition and also its limitations. According to Taylor's theory, we can relate the spatial correlations to the temporal correlations using a frozen turbulence assumption. In other words, Taylor's hypothesis requires that

$$\frac{\partial}{\partial t} \equiv -U_1 \frac{\partial}{\partial x}, \tag{3.12}$$

where U_1 is a constant mean velocity in the jet flow direction. One can conclude that a proportional relation between the integral time and length scale exists, as [56]

$$\Lambda = U_1 \Im. \tag{3.13}$$

Similarly, it can also be shown that the same relation holds for the Taylor time and length scales [56], as

$$\lambda = U_1 \tau. \tag{3.14}$$

It is generally believed that the accuracy of Taylor's hypothesis depends upon the isotropy of the flow. Grid turbulence, which shows the best consistency with Taylor's hypothesis, has no shear so is very close to isotropic. Anisotropy in the turbulent flow emerges with the appearance of the large eddies in the turbulence, which are absent in grid turbulence, but are important features of free shear flows, where Taylor's hypothesis is known to fail [71].

3.3 Turbulence and Energy Cascade

In the last section different aspects of a turbulent flow were studied in terms of eddy size, and the dominant physical processes. This and the next section will concentrate on the turbulence cascade and the noise production mechanism. The main concern is to understand which of the turbulence regions is the most important contributor to the noise generation mechanism. Once this is understood, we will show how the turbulent energy spectrum can be used for jet noise prediction.

It has been shown that the inertial subrange plays a central role in the noise production mechanism [72, 73, 74], and as we mentioned earlier, energy transfer, or the so-called cascade process, is the most important feature of the inertial subrange. This section gives an introduction to the definitions used for explanation of the energy cascade, such as turbulent energy flux, strain rate, and energy spectrum.

The inertial subrange transfers turbulent energy from the energetic region (energy-containing range), to the dissipation subrange (low-energy). No energy production or dissipation will take place throughout the energy transfer process and a well defined energy flux rate can be defined, see figure 3.1.

Various models are available for describing the behaviour of the energy spectrum in different turbulence regions. Among all of them, Pao's model has been shown to be superior to the other models for mid and high wave-numbers [69],

$$E(\kappa) = \alpha \varepsilon^{2/3} \kappa^{-5/3} e^{-\frac{3}{2}\alpha(\kappa\eta)^{4/3}}. \tag{3.15}$$

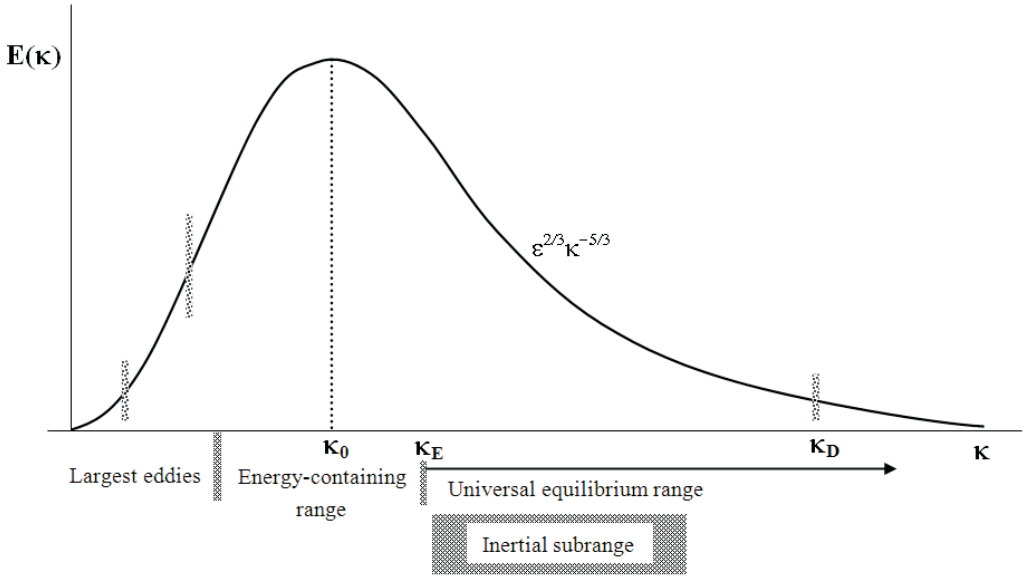

FIGURE 3.3: Turbulence energy spectrum and its different regions

where κ is the eddy wave-number, and the last exponential factor shows the effect of the very small eddies. It will be shown later in Chapter 4 that the appearance of this term is of some importance at high frequencies. Figure 3.3 shows the turbulent energy spectrum in different regions. It can be seen that the spectrum peaks somewhere in the energy containing range, and then exhibits a sharp roll off at higher frequencies.

3.4 Turbulence and the Noise Production Process

We have already introduced different phenomena in a jet shear flow and the scales associated with them. Obviously all of the aforementioned scales are required for a proper clarification of the turbulence and the various processes involved, but one may suggest that not all turbulence scales are involved in the noise production mechanism, and are not therefore of great concern. It has been shown before that the inertial subrange is the most important turbulence region contributing to the intermediate and high frequency parts of the noise spectrum [72, 73, 74]. So, in this section we will concentrate on the role of this region and will also show how one can use the energy spectrum associated with the inertial subrange to calculate the emanated noise.

The inertial subrange is in fact a strain-rate field connecting the most energetic part of the turbulence (Energy-containing range) to the dissipation subrange. It is postulated that the inertial subrange exists when the Reynolds number is high enough to widely separate the energy containing and the dissipation ranges in terms of wave numbers (*i.e.* $\kappa_0 >> \kappa_D$), which is always the case for typical jet flow noise problems. In this case, the inertial subrange can cover a wide range of scales, from very small eddies, as small as 60η, to large vortices of order of $L_0/6$. Thus, the radiated noise from the inertial subrange is, to a large extent, on a par with the total radiated noise from the turbulent flow.

One of the first attempts to emphasis the importance of the inertial subrange in the noise production mechanism has been reported by Meecham [72]. In this work, the sound spectrum behaviour was found as a function of the exponent of the turbulence energy spectrum. He used an algebraic model for the energy spectrum in the inertial subrange, $E(k) \propto \kappa^{-\alpha}$, which is only valid at high frequencies. He finally found that the frequency sound spectrum scales as

$$I(x,\ \omega) \propto x^{-2}\omega^{2-2\alpha}, \tag{3.16}$$

Hence, for a five-thirds law turbulence spectrum $\alpha = 5/3$, the sound intensity will be proportional to $\omega^{-4/3}$, but for $\alpha = 5/2$ turns out to be ω^{-3}. Experimental results for air jets, jet engines, and rockets have shown that the noise spectrum fall off on the high frequency side can scale as ω^{-1} to ω^{-3}, which shows a similar range of exponents. Moreover, it was also shown that the sound intensity diverges for positive exponents of the energy spectrum, $E(\kappa) \propto \kappa^{-\alpha}$, that is consistent with the assumption of applicability of the method for only high frequencies [72].

A more detailed study, which predicts the noise at low frequencies as well as high frequencies, can be carried out if we make use of a more general model for the turbulent energy spectrum in the inertial subrange. The sound intensity magnitude can be related to the turbulent energy spectrum using Lighthill's analogy, and under Taylor's assumption,

$$I(x,\tau) \propto \frac{\partial^4}{\partial\tau^4}\int \kappa^2 Q^2(\kappa,\tau)d\kappa, \tag{3.17}$$

where $Q(\kappa,\tau)$ is a correlation variable. One can use the idea of separating the space and time variables in the space-time correlation function. Thus, in time-stationary, homogeneous isotropic turbulence,

$$Q_{ij}(\kappa,\tau) = Q(\kappa)P_{ij}(\kappa)R(\kappa,\tau), \tag{3.18}$$

where $P_{ij}(\kappa) = \delta_{ij} - \kappa_i\kappa_j\kappa^{-2}$ (κ being wave number). But the temporal part of the space-time correlation function is scale dependent and equation (3.18) can be written as

$$Q(\kappa,\tau) = Q(\kappa)R(\kappa,\tau). \tag{3.19}$$

The single time correlation function $Q(\kappa)$ can be given by

$$4\pi^2 Q(\kappa) = E(\kappa) \propto \begin{cases} \varepsilon^{2/3}\kappa^{-5/3} & \kappa > \kappa_0 \\ E_0(\kappa) & \kappa < \kappa_0 \end{cases}, \tag{3.20}$$

According to the above relations one may deduce that the low frequency noise mainly depends on the driving mechanism of the turbulence acting on large eddies and is strongly dependent on the geometrical aspects of the problem. In a contrary manner, the high frequency noise is characterized by rapid flow fluctuations, and is independent of the driving forces.

On the other hand, it can be shown that the temporal correlation function $R(\kappa,\tau)$ has an inertial subrange similarity form, as

$$R(\kappa,\ \tau) = R(\tau\cdot\Omega(\kappa)), \tag{3.21}$$

where $\Omega(\kappa)$ is determined by the temporal decorrelation mechanism. The decorrelation time Ω^{-1} is in fact a local inertial subrange characteristic. It can take two different forms, depending on whether the correlation is dominated by the local straining (near the dissipation range) or by the nonlocal sweeping (near the energy-containing range). If the inertial subrange is dominated by the sweeping effect of the larger eddies from the energy containing range, $\Omega(\kappa)$ will be an independent property of the inertial subrange and depends on sweeping velocity [73, 74]. In contrast, if the local straining dominates the inertial subrange then $\Omega(\kappa)$ depends only on the inertial subrange properties. Thus,

$\Omega(\kappa)$ can be written as,

$$\Omega(\kappa) \propto \begin{cases} \overline{V} \cdot \kappa & Sweep \\ \varepsilon^{1/3}\kappa^{\alpha} & Strain \end{cases}, \tag{3.22}$$

where $\overline{V}$ denotes the sweeping velocity, which is not a local inertial subrange parameter, and is a property of the larger eddies. Furthermore, Ω defines strain rate and its inverse, Ω^{-1}, represents the eddy turnover time. (It is worth adding here that the small scales close to the energy containing range might be randomly swept by the large eddies. This effect is called "random sweeping", and has been studied by Chen and Kraichnan [75], and Nelkin and Tabor [76])

Finally, after substitution of equation (3.22) in equations (3.20) and (3.21) the radiated sound power under the sweeping hypothesis at low and high frequencies can be found from

$$I(\omega) \propto \begin{cases} \varepsilon^{4/3}\overline{V}^{-1}\kappa_e^{-16/3}\omega^4 & \omega \approx 0 \\ \varepsilon^{-4/3}\overline{V}^{13/3}\omega^{-4/3} & \omega > \overline{V}\kappa_e \end{cases}, \tag{3.23}$$

where $\kappa_e = 0.74l$ is the turbulence spectra peak frequency.

For high Reynolds number, dimensional analysis shows that eddies close but smaller than the energy containing eddies are the key contributors to the radiated acoustic power, so the peak frequency occurs at a frequency slightly higher than those frequencies. So, the peak frequency of the acoustic power is expected to occur around $\omega_0 \propto \overline{V}\kappa_e$. This implies that peak frequency of the turbulence energy is linearly related to the peak frequency of the noise spectrum by a factor of $\overline{V}$.

On the other hand, to capture the acoustic power at relatively higher frequencies, where straining is dominant (*i.e.* near the border of the dissipation range), one can find the following relation after substitution of the second relation of equation (3.22) into (3.17):

$$I(\omega) \propto \omega^{4-(13/3+\alpha)/\alpha}. \tag{3.24}$$

Under the straining hypothesis it can be shown that $\alpha = 2/3$. Substitution of Ω from (3.22) into equation (3.20) and then into (3.17) leads to $I(\omega) \propto \omega^{-7/2}$, which shows a steeper decay than the high frequency prediction given by the sweeping hypothesis. Figure 3.4 shows the behaviour of the acoustic intensity spectrum at different frequencies

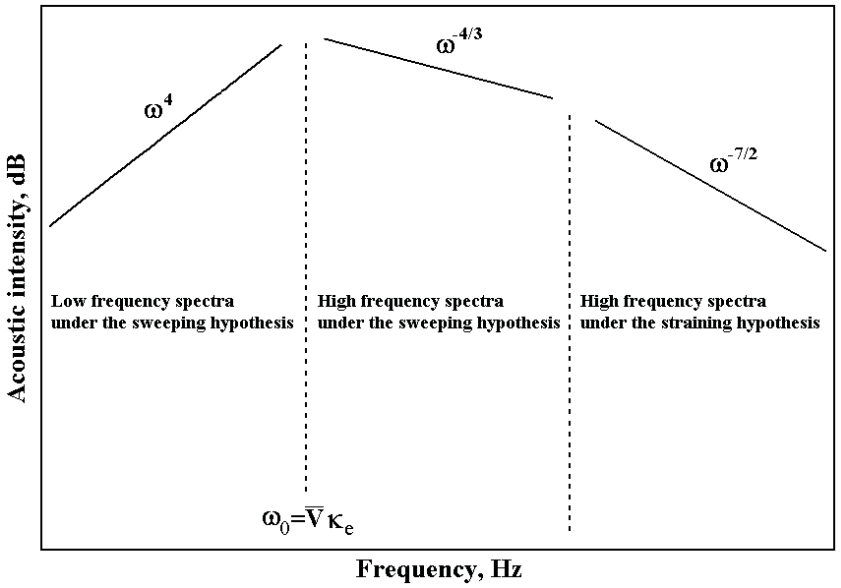

FIGURE 3.4: Behaviour of the sound intensity spectrum in different ranges

bands.

A similar study was also performed by Sarkar and Hussaini [77], who have shown that the noise spectrum at low frequency scales as ω^4, after the peak frequency it behaves as $\omega^{-4/3}$, but this alter and will reach a sharp roll off as $\omega^{-7/2}$. The behaviour of the spectra before the peak frequency reveals that the beginning of the inertial range is mainly dominated by the larger eddies sweeping effect. This effect fades away as the frequency increases and the straining effect entirely dominates the inertial subrange and becomes the most important feature of turbulence. Furthermore, Rubinstein and Zhou [73, 74] have also shown that the Proudman's acoustic power is equivalent to the results obtained under the straining hypothesis, while the assumption made by Lilley is more consistent with the sweeping hypothesis. Proudman's [17] and Lilley's [78] relations for the radiated acoustic power can be found from:

$$I(\omega) \propto \begin{cases} \rho\varepsilon \left(\frac{v}{c}\right)^5 & Proudman \\ \rho\varepsilon \left(\frac{\Omega_0 L}{v}\right)^4 \left(\frac{v}{c}\right)^5 & Lilley \end{cases}, \tag{3.25}$$

where Ω_0 is proportional to the peak frequency of the noise spectrum, and its appearance in the above equation indicates the existence of temporal properties.

3.5 Summary

To conclude this chapter, the most important observations and inferences of the above discussions are listed for future reference:

1. Turbulence is a very complex phenomenon with many scales acting on each other
2. The integral scales represent characteristics of the large eddies, while the Taylor scales corresponds to the inertial scales
3. The inertial subrange of the turbulence spectrum is the principal contributor to the noise production mechanism. The most important feature of this subrange is the energy transfer through vortex stretching
4. The noise production mechanism at low frequencies requires a time scale smaller than the straining mechanism time scale (regarded here as the sweeping time scale). It has been shown that randomly sweeping of the small eddies by slightly larger eddies from the energy containing range is dominant in the low frequency side of the inertial subrange [73, 74].
5. When the sweeping phenomenon dominates the inertial subrange, the appropriate time scale is proportional to κ^{-1}. On the other hand, whenever the local eddy turnover phenomenon is dominant, then the time scale should be proportional to $\propto \kappa^{-2/3}$. Since the wave number and the length scale are inversely proportional, the above deductions can also be rephrased as follows: If the sweeping or straining is dominant in the source region, the time scale describing the temporal behaviour of the source term will be proportional to l and $l^{2/3}$ respectively [79]. This is a very important outcome and will be used later for the definition of a new time scale based on turbulent energy transfer rate.

In the next chapter we shall focus on the most important turbulence parameters used in the noise prediction equations. It must be realized that in dealing with the solution of the acoustic analogy, such as equations (2.52), and (2.53), some parameters are required to be defined, *e.g.* convection velocity, time scale and length scale. These quantities must be found from CFD results hand-in-hand with an understanding of the turbulence and noise production/radiation mechanism. One of the most important issues arising is

the frequency dependency of these parameters which will be comprehensively studied. The above studies will be also used for comparison with what will be found in the next chapter.

Chapter 4

Turbulence Parameters and Frequency Dependency

...it would be better for the true physics if there were no mathematicians on earth.

"Daniel Bernoulli", (1700-1782)

In previous chapters the mathematical modelling of noise radiation from a turbulent jet flow was discussed. This was followed by a discussion of the physical interpretation of the processes involved in the mathematical modelling of variables such as length scale, time scale, and convection velocity. In this chapter we continue this in more detail.

Basic definitions always play an essential role in physics, and aeroacoustics is not an exception. Up until now there have been many articles published discussing different aspects of defining turbulence derived parameters generally used in aeroacoustic problems [48, 53, 80]. Among all of the important aspects the majority of effort is put into the nature of the frequency dependency of the parameters involved. It has been shown that use of frequency dependent parameters improves the final noise prediction. A review of the history of each parameter in the literature, its definitions, and ultimately model for its recent frequency dependent behaviour are given in the following three sections. Utilization of these definitions for jet noise prediction will be left for Chapters 5 and 6, where numerical results and discussions will be given.

4.1 Length Scale

The length scale associated with the turbulence decay rate has been widely used in the literature. It is given by

$$l = c_l \frac{k^{3/2}}{\varepsilon}. \tag{4.1}$$

The frequency dependency of the length scale was first demonstrated by Harper-Bourne [48]. His results indicate that for low frequencies the assumption of a constant length scale is reasonable, but that for higher frequencies a nearly inverse dependence on Strouhal number is obtained, see figure 4.1. Later, Self [37] proposed a frequency dependent model for the length scale based on experimental results presented in [48]. He showed that Harper-Bourne's experimental observations can be fitted into an analytic formula of the form

$$l = c_1 W/(1 + \omega/\omega_c), \tag{4.2}$$

where W is the shear layer width and

$$\omega_c = 2\pi c_2 U_1/W, \tag{4.3}$$

and c_1 and c_2 are calibrating coefficients. An exponential fit to the Harper-Bourne's results was given later by Morris and Boluriaan [52]. The longitudinal length scale was modeled using:

$$l(\omega) = c_l D_J \frac{1 - e^{-c_s St.l/D_J}}{St}, \tag{4.4}$$

where l is the turbulence length scale, equation (4.1), the length scale calibration coefficient is $c_l = 1$, and Strouhal number is defined as $St = fD_J/U_J$. The numerator of the ratio is chosen in such a way that L is constant at low frequencies but then decreases with increasing frequency. According to the authors interpretation, c_s is a factor which determines the transition between the low and high frequency behaviors of the spectrum. In fact, this factor can control both the location of the peak frequency (*i.e.* adjusting the local Strouhal number *i.e.* $\omega l_x/U$), and also to some extent the shape of the spectrum. It was also shown that the low frequency part of the spectrum is much more sensitive to c_s than the high frequency part.

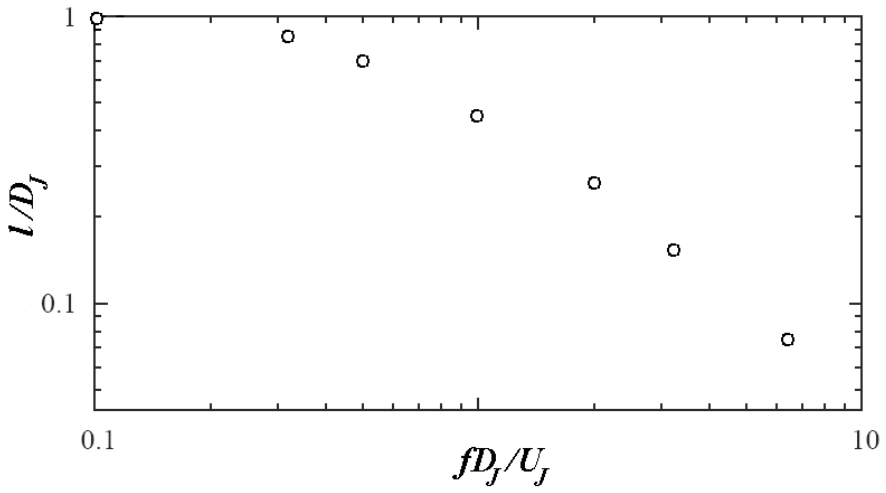

FIGURE 4.1: Frequency dependency of the length scale as measured by Harper-Bourne [48]

Morris and Boluriaan derived a formulation for the radiated noise at 90^o which is based on the Green's function solution of the linearized Euler equations [52], as

$$S(x,\omega) = \frac{\rho_0^2}{18c_\infty^4 R^2} A^2 c_\tau c_l^4 \int_V \frac{k^4 D_J^4 \omega^2 \tau_d^2}{Ul^4 \left(1 + c_\tau^2 l_x^2 \omega^2 / U^2\right) \left(1 + s_d^2\right)^{3/2}} \left[\frac{1 - \mathrm{e}^{-c_s St\, l/D_J}}{St}\right]^4 dy, \tag{4.5}$$

where

$$\begin{aligned} s_d &= \frac{\omega l_x}{U}(1 - M\cos\theta), \\ l_x &= c_l D_J s(\omega)/St, \\ s(\omega) &= 1 - exp(-c_s St l_x/D_J). \end{aligned} \tag{4.6}$$

More recently, Kerherve *et al.* [53] have performed a similar analysis and used the complex coherence function technique for the collected data from high Mach number jet flows ($M_J = 0.75, 0.90$) and found the following frequency dependent model for the length scale

$$l(\omega) = l\frac{\sqrt{1+\alpha^2}}{2} e^{-\frac{\alpha^2 \tau_d^2 \omega^2}{4(1+\alpha^2)}}, \tag{4.7}$$

where l is the integral length scale and $\alpha = \frac{U_c \tau_d}{l}$ is a measure of the isotropy of the turbulence and will be unity under the frozen-turbulence approximation (*i.e.* Taylor's hypothesis).

In summary, one can deduce that despite the fact that it is generally believed that the

length scale is inversely proportional to the frequency of radiated sound, the experimental evidence has shown that this fails at low frequencies. According to the experimental results and analytical relations, the linear proportionality of the length scale and frequency holds as long as the high frequency sources are of interest. In other words, the length scale becomes independent of frequency for large eddies, when anisotropy becomes dominant and Taylor's hypothesis is no longer valid.

4.2 Time Scale

Among all of the possible definitions of the time scale in turbulence the turbulent decay rate is a very common choice, which has been widely used in aeroacoustic prediction as well. It is defined as,

$$\tau_d = c_\tau \frac{k}{\varepsilon}. \tag{4.8}$$

It has been seen before that using this time scale within an aeroacoustics prediction scheme rarely results in good agreement between predicted and measured acoustic spectra over the entire frequency range of interest, with under-prediction at both the high and the low ends of the spectrum, (see for example [37, 38]). This basically means that this time scale has not been capable of providing a physically meaningful interdependence between the turbulence and noise production/radiation mechanism.

Studies have shown that one of the most important weaknesses of the dissipation rate time scale, τ_d, is the lack of frequency dependency and that considering a frequency dependent time scale can make significant noise prediction improvement [39]. There are three different approaches towards taking account of the frequency dependency in the time scale definition: (1) using an *ad-hoc* mathematical model, (2) splitting the whole jet flow domain into smaller regions and associating relevant time scale to each region, and finally (3) the one which makes use of the fact that noise radiation is, to a large extent, governed by the inertial subrange, and tries to find a time scale related to the corresponding dominant phenomenon in the inertial subrange. An explanation of each category is provided below.

Category I, Frequency dependent models: A suggested solution to this problem is motivated by measurements originally reported by Fisher and Davis [51] and later confirmed by those of Harper-Bourne [48] that indicate the acoustic time scale has a frequency dependence. A model to take account of this dependency was suggested by Self [37] and used to capture the 90 degrees spectrum of a single-stream jet using the Lighthill acoustic analogy. Subsequently the model was applied to a co-axial jet [39]. According to this model, the acoustic time scale varies with frequency as

$$\tau(\omega) = c_\tau \frac{2\pi}{c_\omega 2\pi U/l + \omega}, \tag{4.9}$$

where c_τ is a calibrating coefficient that must be obtained empirically, with U being the local mean velocity, and $l = k^{3/2}/\varepsilon$ the turbulent length scale. In simple physical terms, equation (4.8) is equivalent to an assumption that the lifetime of a turbulent eddy is proportional to the local mean shear, while equation (4.9) essentially allow for an enhanced decay rate of those eddies whose characteristic size is comparable to that of the local shear layer width. However, this is a largely qualitative explanation that offers only a partial insight into the underlying physics that determines the exact nature of the dependence of time scale on frequency. While superior to the simple model of equation (4.8), the model described by equations (4.9) shares the assumption that the acoustic time scale depends on the decay of turbulent eddies, *i.e.* that it should be derived solely from a turbulent time scale that is based on the dissipation rate of the turbulent kinetic energy.

Category II, Different subranges (Multiple time scale): As mentioned in Chapter 3, and as is well known in the literature, several different processes operate simultaneously within the jet flow and a characteristic time can be associated with each of them. There appears to be no *a priori* reason to favor one of these time scales over the others, but rather it would seem sensible to assume that the time scale depends foremost on the time scale associated with the physical process that dominates the behavior of the turbulent flow in any particular region of the jet. Thus, according to the discussion in Chapter 3, we are led to consider multiple time scales associated with three physical processes: (1) production of the turbulent energy (energy containing region), (2) action between the

mean flow and turbulence, or strain rate, and (3) dissipation of the turbulent energy (inertial subrange).

Figure 4.2 shows the normalized length scale (U/U_{axis}) of an isothermal $M_J = 0.75$ jet flow inside and outside the jet stream. The figure supports the assumption the jet domain can be split to a finite number of regions over the jet axis (usually two or three). One can readily deduce from the figure that the eddies of equal size are usually aggregated at a specific distance from the jet exit. This characteristic of the jet flow allows the jet domain to be split into a finite number of subranges (usually three: dissipation region, strain-rate region, and production region). Assuming a simple proportional dependence

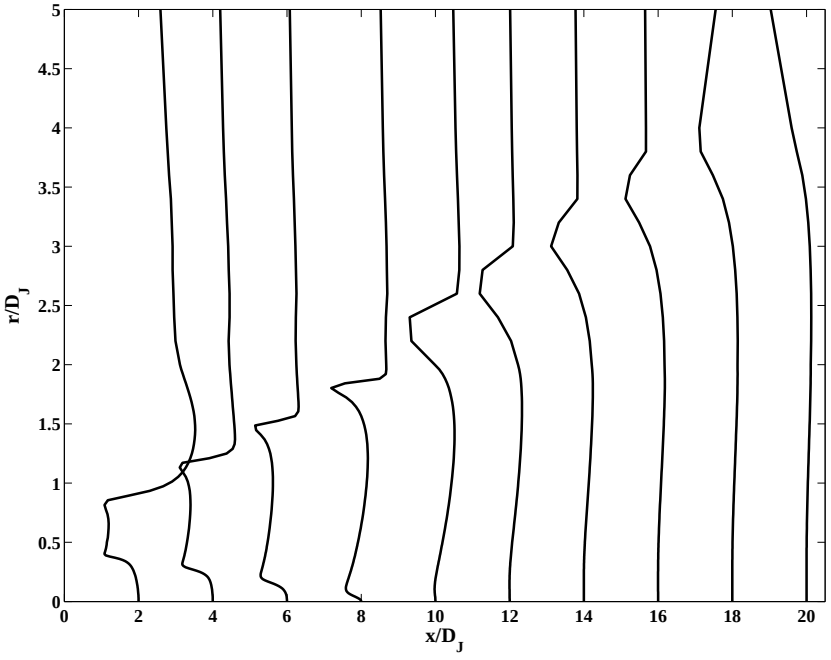

FIGURE 4.2: Normalized length scale (U/U_{axis}) at different axial locations

of the time scale on the corresponding turbulent time scale [27, 28], these will be given by

$$\tau_p = \alpha^I \frac{k}{Pr}, \qquad \tau_s = \alpha^{II} \left| \frac{\partial U}{\partial r} \right|^{-1}, \qquad \tau_d = \alpha^{III} \frac{k}{\varepsilon}, \tag{4.10}$$

where Pr denotes the production rate of turbulent kinetic energy (see for example [28] for a definition of Pr), $|\partial U/\partial r|^{-1}$ is a measure of the local strain rate, and as before, k/ε gives a measure of the turbulent energy decay rate, and α^I, α^{II}, and α^{III} are three empirical coefficients. Each of the three different processes (and hence the corresponding time scale) can be associated with a region of the turbulent jet where it is the dominant

physical process [28, 69]. This is illustrated schematically in Figure 3.1 (although it should be borne in mind that in reality all three physical processes are present everywhere in the jet flow).

According to this method, each time scale should be used for noise prediction of those frequencies radiated from the corresponding region of the jet. This suggests that in order to accurately predict the noise over the entire frequency range some appropriate combination of the time scales defined in equation (4.10) should be used. A model of this type was proposed by Frendi *et al.* [27, 28] in their "dual time scale" model. A suitable generalization to include the effect of all three physical processes operating within the turbulent flow is to assume that the acoustic intensity has the form

$$I_T = \sum_j w_j I_j \,, \qquad j = \{p, s, d\} \tag{4.11}$$

where I_j refers to sound intensity calculated using each of the time scales in (4.10) and w_j are weight parameters that must be determined empirically. An optimization was performed by Frendi *et al.* [27] to determine the three calibration coefficients α^I, α^{II}, and α^{III} and it was found that very good agreement with experimental data over the complete range of frequencies was obtained. Though such a procedure might suggest the essential correctness of the approach, we now have the difficulty of calibrating three different time scale coefficients and corresponding length scales coefficients, and the number of empirical coefficients is raised still further if the weighings (w_j) in equation (4.11) are included.

Category III, Turbulent energy transfer time scale: The difficulties arising with the first two categories of time scale definition, lack of generality and complexity, can be resolved by introducing a time scale that is based on the rate of transfer of turbulent energy between different wave numbers of the turbulent fluctuations. It was shown in section 3.4 that the noise production mechanism is largely governed by the energy transfer phenomenon, which is dominant in the inertial subrange. In what follows we endeavor to find a time scale associated with the inertial subrange. It should, therefore, be based on the turbulent energy transfer rate.

The energy transfer rate at wave number κ can be estimated via $\varepsilon/E(\kappa)$, which shows the rate at which the energy travels through the cascade ($d\kappa/dt$), and $E(\kappa)$ is the energy spectrum of the turbulence. So, the time scale can be found through

$$\tau \propto \int \frac{E(\kappa)}{\varepsilon} d\kappa, \tag{4.12}$$

In order to proceed with the integration, Pao's energy spectrum model, equation (3.15), can be inserted into the above. The integration over wave-number then yields,

$$\tau_T = \alpha^T \tau_d \left(\frac{\Lambda}{l}\right)^{2/3} e^{\frac{3}{2}C(2\pi\frac{\eta}{l})^{4/3}} - \beta^T \tau_\eta Erfi(\frac{3}{2}\alpha(2\pi\frac{\eta}{l})^{2/3}), \tag{4.13}$$

where α^T is now the sole calibrating parameter, Λ denotes the size of the eddy which can be either found from the experimental results or can be estimated from the shear layer thickness), l is again the length scale, given by equation (4.1), C is set to 1.5 [56], $\tau_\eta = \sqrt{\nu/\varepsilon}$ is the Kolmogorov time scale, and $Erfi$ the imaginary error function, defined by

$$Erfi(z) = \frac{2}{i\sqrt{\pi}} \int_0^{iz} e^{-t^2} dt. \tag{4.14}$$

It should be noted here that the exponential factors in the first and second terms of equation (4.13), which depend on the Kolmogorov scales, can be neglected in comparison with the other terms, and allows simplification of (4.13) to the following form

$$\tau_T \approx \alpha^T \tau_d \left(\frac{\Lambda}{l}\right)^{2/3}. \tag{4.15}$$

A comparison of the turbulent energy transfer time scale (4.15), (will be called TET time scale hereafter), and the traditional turbulent decay rate (4.8), (referred to as TDR in the following), is presented in figures 4.3, through 4.5. The eddy size Λ can be estimated using either the shear layer thickness, equation (4.2), or the frequency dependent length scale, equation (4.4) (these two are however equivalent). In this comparison the latter model is used. Comparisons are provided for three Strouhal numbers, $St = 0.1$, 1, and 10. Comparison of each pair of lines (line and line-marker) shows the difference of the TET and the TER time scales at different radial distances from the jet centre-line. It can be seen that the time scale associated with $r = 0$ has a "step jump" around $x = 6D_J$

which is where it crosses the end of the potential core. Similarly $r = D_J$ and $r = 5D_J$ experience such a jump when they pass through the jet shear layer. Results obtained on the centre-line using the two time scales are very similar. The most informative curves are the ones associated with $r = D_J/2$ (across the nozzle lip-line). It can be seen from the figures that the TET time scale provides smaller values than the TDR time scale at high frequencies ($St = 10$). Conversely, at lower frequencies the TDR time scale is smaller than the TDR time scale. In other words, the TET time scale provides smaller values for small eddies and greater value for large eddies. The two curves cross when $\Lambda = l$. This position moves closer to the jet exit as frequency increases. However, as mentioned earlier one can also use a shear layer thickness model in order to estimate the eddies size Λ. In this case the TET time scale depends on the axial position of the source instead of the source frequency.

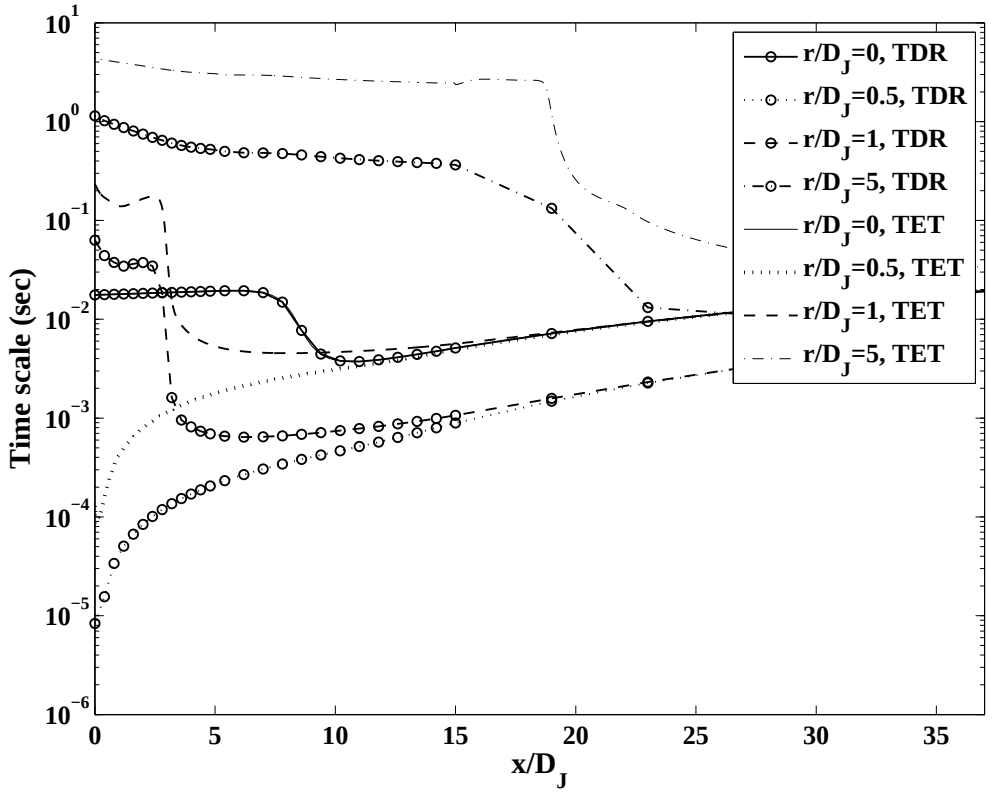

FIGURE 4.3: Comparison of the TET and TDR time scales at different radial locations, $St = 0.1$

Similar results are presented in figure 4.6, but instead of showing time scale versus source position, it is plotted against the corresponding length scale. In the figure each pair of lines starts from the jet exit ($x = 0$) and ends at $x = 50D_J$, and each pair

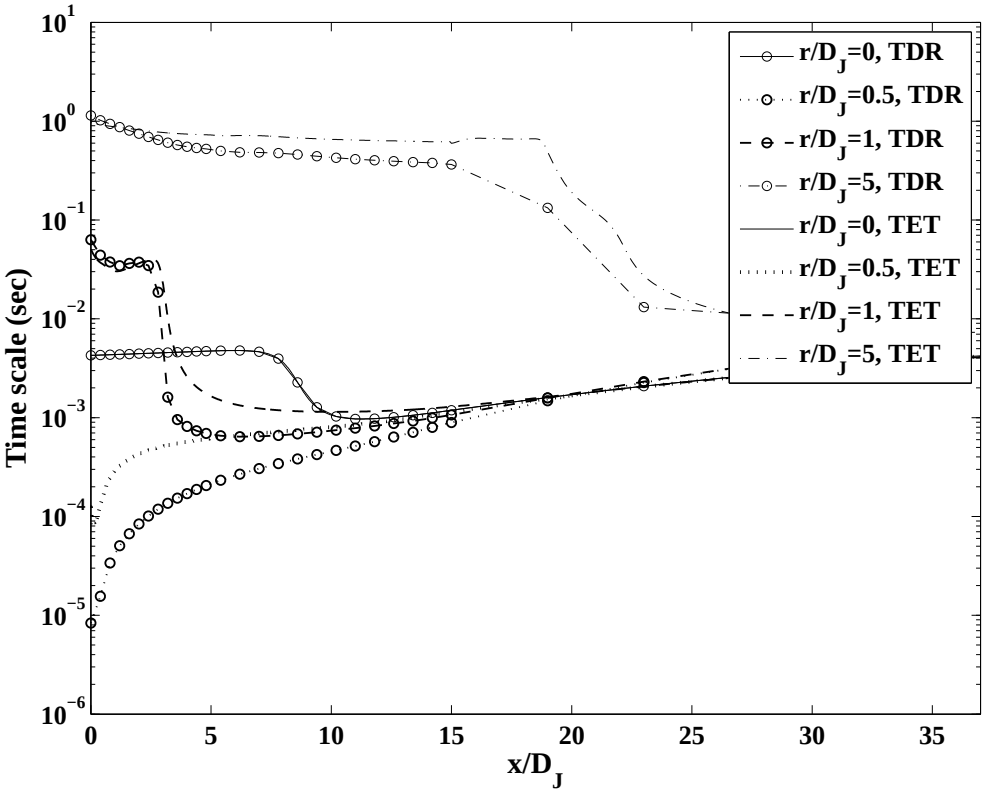

FIGURE 4.4: Comparison of the TET and TDR time scales at different radial locations, $St = 1.0$

corresponds to a radial position. It can be seen from the figure that the lines correspond to $r = 0$ and $r = 2D_J$ turn back on themselves. This turning back corresponds to the step jumps observed in figures 4.3 through 4.5 and arises because of the crossing of the end of the potential core or the jet outer shear layer. As can be observed from the figure, each pair of lines meet each other at $l = \Lambda$ which is also evident from equations (4.13) and (4.15).

The effect of the Kolmogorov factors in equation (4.13) and comparisons with its simplified version, equation (4.15), are presented in figure 4.7. For this case a source with a turbulent dissipation rate $\varepsilon = 2 * 10^{+8} m^2 \sec^{-3}$ is assumed. The new time scale clearly manifests a faster decay as we approach the smaller scales. It is seen that the Kolmogorov scales effect becomes dominant for very small eddies, at which the original new time scale, equation (4.13), falls exponentially and much faster than the simplified version without the viscous dissipation factor. However, it is known that the eddies very close to the Kolmogorov size are not significant contributors to the noise production and

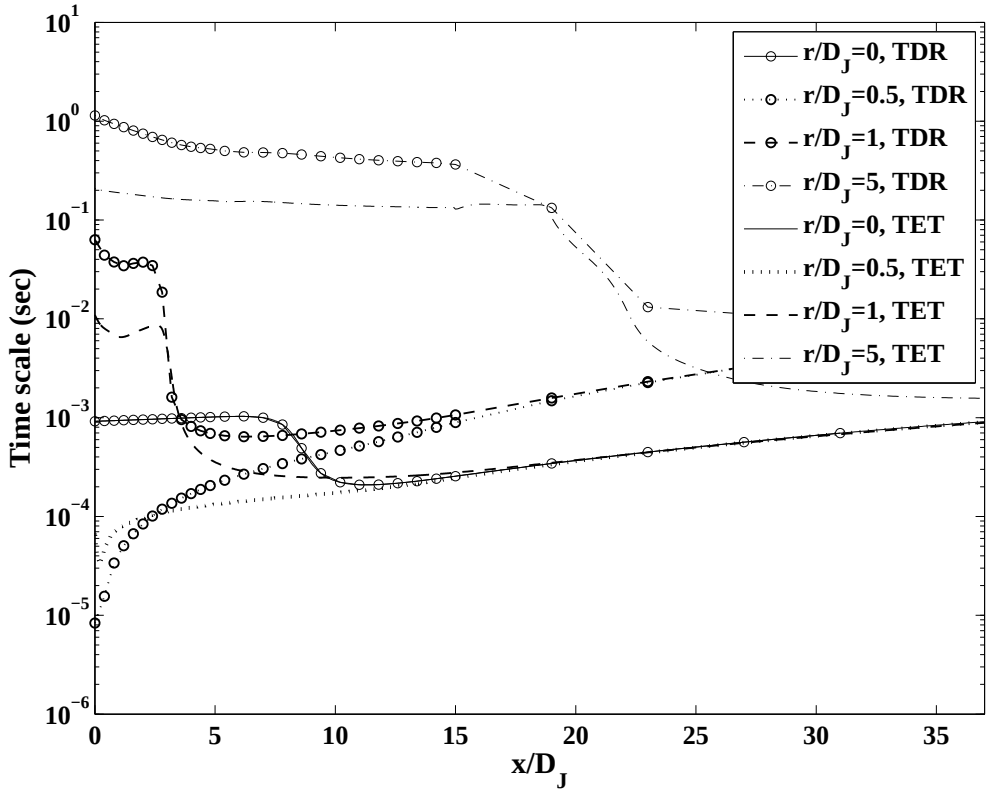

FIGURE 4.5: Comparison of the TET and TDR time scales at different radial locations, $St = 10$

radiation mechanism. So, it is reasonable to only use the simple form of equation (4.15) in our noise prediction codes.

Comparisons of noise prediction using the different time scales and length scales will be given in Chapters 5 and 6, but it is worthwhile mentioning some similarities between the frequency dependent length scale, equation (4.4), and the TET time scale. In the frequency dependent length scale a new coefficient, c_s, has been utilized to firstly adjust the shape of the spectrum, and then set the peak frequency location. The two other factors, c_l, and A are also used to correct the maximum SPL value of the spectrum. In contrast, when using the TET time scale, the multiplier $c_\tau(\Lambda/l)^{2/3}$ determines the position of the peak frequency, and simultaneously corrects the shape of either side of the spectrum. Then, the c_l and A coefficients can be used for SPL adjustments.

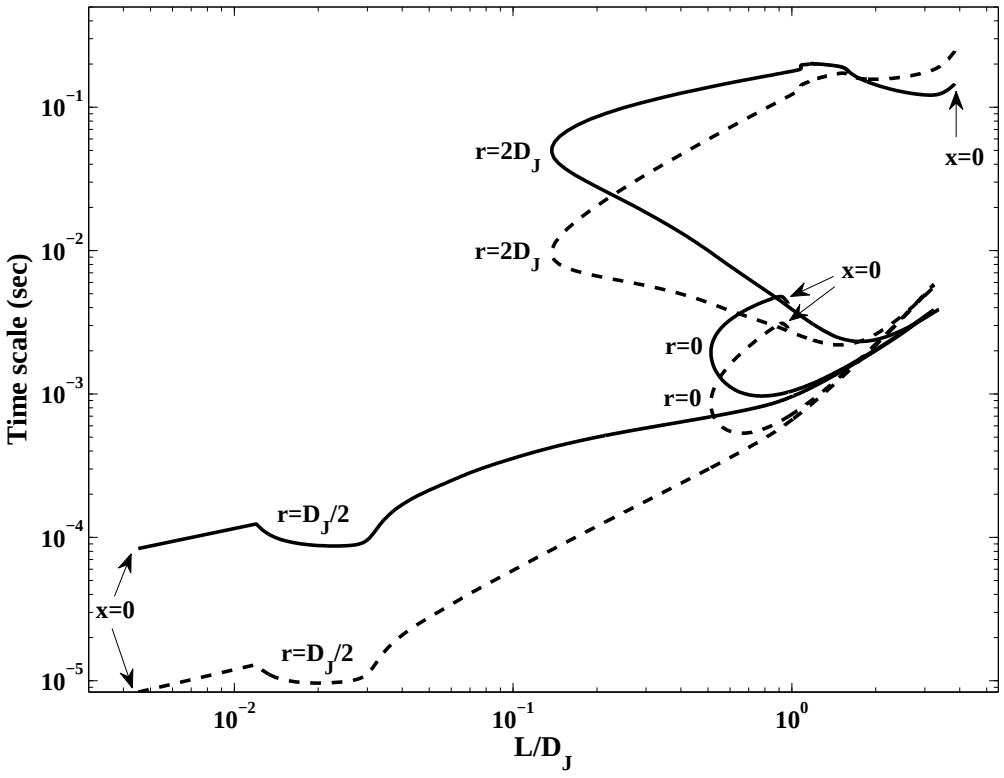

FIGURE 4.6: Comparison of the TET (solid lines) and the TDR time scales (dash lines) at three radial locations ($r = 0$, $D_J/2$ and $2D_J$), $St = 1.0$

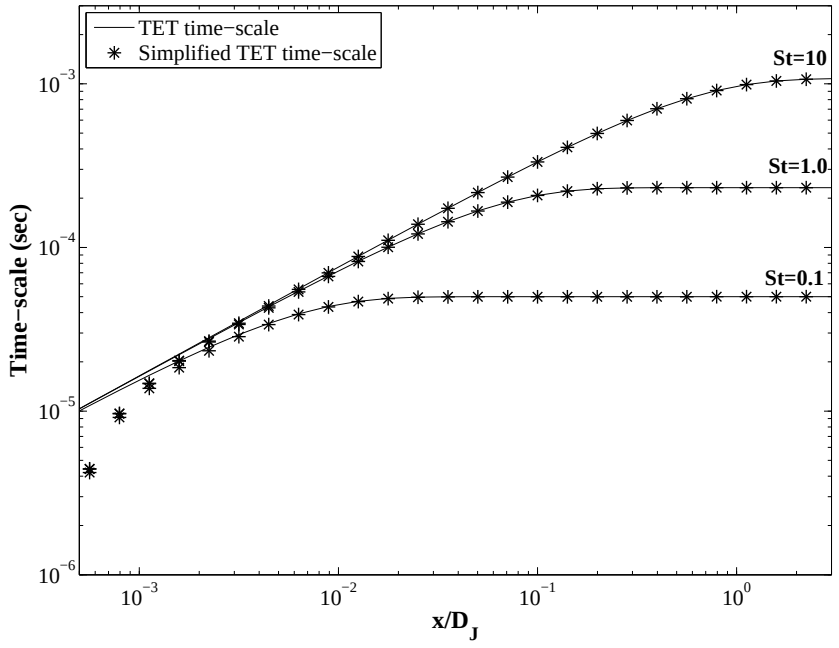

FIGURE 4.7: Effects of the Kolmogorov scales on the TET time-scale

4.3 Convection Velocity

The definition of convection velocity (and accordingly the convection factor) has received comparatively more attention in the literature than those of the time and length scales. The very first experimental researches showed that the convection velocity is roughly equal to $0.62U_J$ [80]. Other works suggested that this coefficient may vary within the jet domain [26, 58, 81]. Furthermore, other research has suggested the frequency dependency of the convection velocity. One of the very first attempts was made by Fisher and Davis [51], who showed that the convection velocity has an intrinsic frequency dependency. This was then confirmed by Akamatsu [82]. Subsequently, Szewczyk reformulated the Doppler factor and constructed a new model in terms of the observation angle and source longitudinal and lateral non-compactness terms [83]. In this method there is a frequency dependence although this was not an overt aim of the authors. Similar studies have been reported in [7, 84] as well.

One of the most important and cited works on the frequency dependency of the convection velocity was conducted by Harper-Bourne, where the results showed that the convection velocity increases gradually with frequency [48]. Although results in [48] are of much interest and have revealed some hidden aspects of turbulence, it should also be noticed that the results are for a Mach 0.18 jet, which can be considered as a very low speed jet. So, its usefulness and applicability for high speed jet flows might be doubtful. More recent work discussing the frequency dependency of the convection velocity is given by Kerherve *et al.* [53], where a complex coherence function technique for the collected data from a high Mach number jet flow is used. It has been shown that the high frequency components are convected with a velocity slightly higher than the local mean velocity, and the classical convection velocity is governed more by the mean flow than by the intrinsic properties of the turbulence.

In summary, two models for the convection velocity can be proposed: one which is based on the local eddy velocity, and other based on a frequency dependency assumption. These two categories are explored further below.

Category I, Convection velocity model based on the local velocity

The convective velocity is usually considered as the phase speed of the largest instabilities, but it was shown that a one-dimensional correlation function does not discriminate between large and small scales and includes therefore contributions from the small scales which are expected to travel with a speed close to the local mean velocity [49, 85, 86]. As a result, the convection velocity is expected to be biased towards the local mean velocity.

Some other investigations have measured the eddy convection velocity in a mixing region. These results generally indicate that the convective velocity varies across the mixing region, but not necessarily with the same rate as the mean velocity changes. Results reveal that the convection velocity decays with increasing distance from the jet axis, while very small changes can be observed moving in the axial direction [80, 81, 87]. It is found that the convection velocity towards the outside extremity of the jet is greater than the local velocity, while this is opposite when the source is located near the flow centre, and the convection velocity does not exceed 90% of the jet exit velocity [49]. This could be interpreted as due to the bias of the smaller scales towards the mean velocity.

The general form of the first model of the convection velocity and also the appropriate weight coefficients has been the subject of a number of works [51, 87]. It is widely believed that the relation must be a function of both jet exit velocity and local characteristics of the flow [32, 55, 80, 81, 88, 89],

$$M_c = aM_{Local} + bM_J, \tag{4.16}$$

where ambient sound speed, c_0, is used as the reference speed of sound, a and b are two weight coefficients and can vary with jet, but generally accepted to be in order of $a = 0.50$, and $b = 0.30$. This model will hereinafter be referred to as "*Mean velocity model*".

Category II, Frequency dependent convection velocity model

In the second model, frequency dependency is also taken into account besides the other flow parameters. The most cited work in this regard is that of Harper-Bourne [48] which is for a Mach 0.18 jet. Harper-Bourne showed that the axial phase convection velocity has a slight increase with frequency, starting from about $0.55U_J$ at $St = 0.1$

and varying to around $0.80U_J$ for $St = 10$, (figure 4.8). Using this information, one can model the convection velocity in terms of frequency and the jet exit velocity, by the analytic form,

$$M_c = AM_J(1 + B\frac{St_{Jet}}{M_J}) \equiv \alpha.\frac{fD_J}{U_J} + \beta.M_J \tag{4.17}$$

This will be referred to as the "Frequency dependent model". The experimental results of [48] were again modeled recently in a logarithmic form by Raizada and Morris [90], as

$$U_c(x,\ \omega) = U_{axis}(x) \cdot [0.056\ \ln(St) + 0.667] \tag{4.18}$$

.

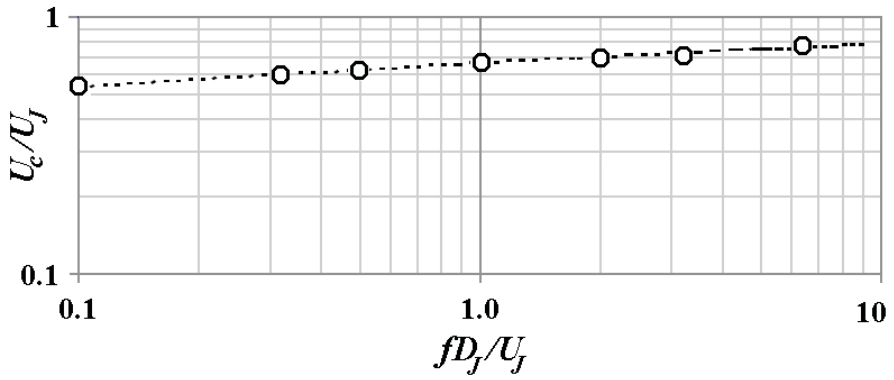

FIGURE 4.8: Frequency dependency of the convection velocity as measured by Harper-Bourne [48]

As mentioned before, the above relations for the time scale, length scale and convection velocity are necessary for the prediction of the radiated noise from a turbulent jet flow. Also, in order to calculate these quantities, one needs to provide some CFD results, which can be achieved using a CFD-RANS turbulence model. As mentioned earlier in Chapter 1, three different nozzles are considered in this study, namely single flow, coaxial and short-cowl nozzle. General descriptions of the geometry, grid, CFD simulations and CFD results can be found in Appendix A. The next two chapters concentrate on some jet noise prediction examples. Chapter 5 concerns prediction of noise radiated from an isothermal/heated single flow jet at different Mach numbers and in Chapter 6 radiation of noise from coaxial and short-cowl nozzles will be studied.

Chapter 5

Numerical Results: Single Flow Jets

As far as the laws of mathematics refer to reality, they are not certain, and as far as they are certain, they do not refer to reality.

"Albert Einstein", (1879-1955)

Introduction

In dealing with the jet noise problem two separate aspects of the problem must be carefully addressed: the turbulent flow simulation and the acoustic problem. A general physical description and the various mathematical models used for these two parts were given in Chapters 2, 3, and 4. In this chapter some comparisons with data will be made using these models. Three kind of nozzles will be used for the simulation of jet noise: single flow, coplanar and short-cowl nozzle. These three nozzles, at different flow speed and temperature conditions have been selected to cover most of the possible and practical jet flow situations, to demonstrate the validity of the approach when the physical application changes. This chapter concentrates on single stream jet flows and numerical results and discussions will be presented for the following cases: Single flow cold jet at three Mach numbers (M_J = 0.6, 0.75, and 0.90) and single flow heated jet at two different velocity and temperature conditions ($T_J = 450K$, $M_J = 0.6$) and

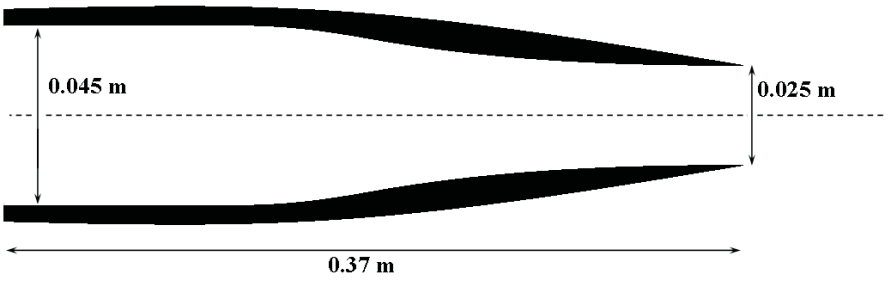

FIGURE 5.1: Nozzle geometry of a single stream nozzle

($600K$, $M_J = 0.75$). The geometry and general dimensional information of the nozzles considered are given in figure 5.1.

Single stream jets are of both theoretical and practical interest. They were used in older commercial jet engines and are still being used in turbojet engines for military aircraft. These nozzles have a comparably simple geometry and are designed to compress and push the flow towards the nozzle exit, resulting in thrust. However, the interaction of the flow coming out from the nozzle and the ambient medium results in a very strong turbulent mixing which is the source of significant aerodynamic noise. In spite of the fact that the application of the single flow nozzle is very limited in comparison with other sophisticated nozzles, their study may provide some useful insights into the understanding of the mechanism of noise radiation from more complex nozzles.

This section is divided into two parts. In the first part, noise radiation from an unheated single-stream jet flow will be considered, and in the second part that of a heated flow is tackled. Jet noise directivity, and the effect of the turbulent energy transfer rate time scale (TET) will be examined in this section.

The MGBK method (equation (2.52)) with the high frequency asymptotic solution of the Lilley equation for the refraction effect (equation (2.50)) are used for the noise prediction. Different turbulence parameters which have been introduced earlier in Chapter 3 will be used and their corresponding effects will be studied. Use of the MGBK method also enables the further investigating of other important features of the turbulence and acoustics, such as the acoustic source non-compactness effect, flow anisotropy effect, *etc.* These effects will also be briefly studied in the present chapter.

In dealing with Lighthill's Analogy or the MGBK method one needs to provide the essential fluid dynamic information of the jet flow. A Reynolds Averaged Navier Stokes (RANS) scheme using a simple modified $k-\varepsilon$ turbulence model has been used for this simulation. Such a solution provides the mean flow parameters (*e.g.* mean velocity, temperature) as well as an estimate of the turbulent kinetic energy and turbulent dissipation rate. This information is then be used for evaluation of the time scale, length scale and the convection velocity. Details of the turbulence modeling and CFD results for all the geometries and conditions presented below are given in Appendix A.

In addition, the acoustic data used in this section for comparison with analytical results are collected from the JEAN project [91, 92, 93, 94]. Experiments for a single stream jet were carried out by Jordan *et al.* at the MARTEL facility at CEAT (Centre d'Etudes Aero-dynamiques et Thermiques), Universite de Poitiers. Far-field acoustic measurements were performed at 30 jet diameters and 50 jet diameters from the jet exit. Results are available from 30 degrees to 150 degrees from the jet downstream axis.

5.1 Unheated Flows

The study of noise generation and radiation from unheated single flow jets is of great importance because of its relatively easier physical interpretation and source modelling. In this case, sources can be, to a large extent, represented by quadrupole source models. On this basis, studies of unheated single flow flows can be very useful and may shed light on understanding the noise generation and radiation mechanisms of more complicated cases.

Noise prediction of high Mach number subsonic flows has been investigated many times and different associated issues have been addressed [38, 39, 44]. In most of these cases, however, the agreement with the experimental data at low and high frequencies is not good. Unlike other works that have tried to resolve the problem through making use of more complex mathematical models or using more sophisticated turbulence modeling methods, in this thesis it is aimed to resolve the problem using physical reasoning derived from knowledge of the turbulence. One can say that this problem arises partly on account of the lack of proper definitions of the basic modelling parameters, such as the

time scale, length scale and convection velocity. The concepts behind the definition of these quantities were reviewed in the last two chapters (Chapters 3 and 4). In this section the new definitions will be used and their effects will be examined for any further enhancements in jet noise prediction. The new time scale (TET) will be used throughout the chapter (unless for the purpose of comparison) and the prediction obtained using it will be compared with those found using other time scales. Furthermore, an explanation will be provided for mismatches that other authors have observed.

5.1.1 Noise Prediction at Ninety Degrees

Prediction of noise at ninety degrees is known to be the simplest to achieve but is none-the-less a very informative task. To begin with, we shall use the Lighthill method, equation (2.25). Convection and refraction effects can be ignored for this case, since the observer is located at ninety degrees and the Doppler factor will be equal to one. The dissipation length scale will be used, equation (4.1), and the length scale ratio is assumed unity, so $l_1 = l_2 = l_3$. Furthermore, the required CFD data for source modelling are found using $k - \varepsilon$ RANS model and the results are presented in Chapter A.

A simulation was performed for a $M_J = 0.75$ jet, using three kinds of time scale: the traditional time scale (TDR), τ_d, as given by equation (4.8); triple time scale (4.10); and the new time scale (TET), τ_T, given by equation (4.13). Figure 5.2 shows the results obtained using each of the time scales. Results are compared with the measured data obtained within the JEAN research programme [64]. It can be deduced from the figure that using the TDR time scale (4.8) can give reasonable agreement with the measured spectra in the vicinity of the peak frequency. This noise is generally associated with the region of the jet just downstream of the end of the potential core where the decay of turbulent energy is the dominant process. However, moving away from this region leads to progressively poorer agreement as other physical processes begin to dominate. In these regions an improved prediction of the noise is obtained by using equations (4.9) to define the time scale, as suggested in [38, 39]. This is because such a model effectively mimics the strain rate time scale and (to some extent) the production time scale which are dominant in regions of the jet away from the end of the potential core. This suggests that in order to effectively predict the noise over the entire frequency range

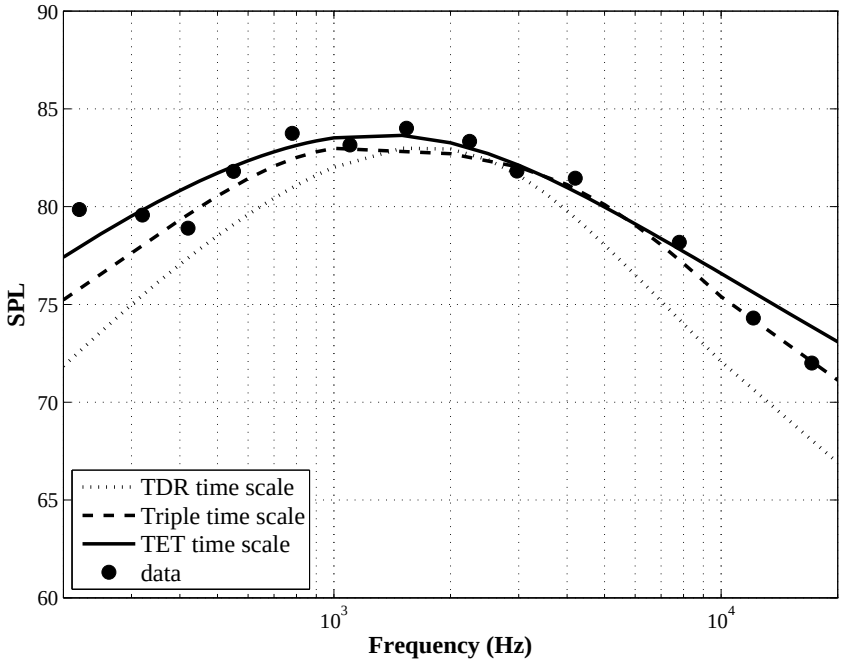

FIGURE 5.2: Comparison of experimental data with predicted spectral density at 90^o to the jet axis using three different time scales and based on the MGBK method (dB re $10^{-12}Pa^2/Hz$): $R = 50D_J$, $M_J = 0.75$, $D_J = 0.05m$.

some appropriate combination of time scales, equation (4.10), should be used. This was first put forward by Frendi *et al.* [28] in their "dual time scale" model. A generalized form to include the effect of all physical processes (usually three) operating within the turbulent flow can be found from:

$$I_T = \sum_j w_j I_j, \qquad j = \{p,\ s,\ d\}$$

where I_j refers to sound intensity calculated using each of the time scales in equation (4.10) and w_j are weight parameters that must be determined empirically. Here, we assumed that all parts contribute equally $w_d = w_s = w_p = 1$, but in [28] it was assumed that $w_d = w_p = 1/2$ and $w_s = 0$. Performing an optimization to determine the three calibration coefficients, α^I, α^{II}, and α^{III} in equation (4.10) would result in very good agreement with experimental data over the complete range of frequencies as is evident from figure 5.2.

Notice that in this combined time scale approach the relation of the time scales is one of simple proportionality. The "effective" dependence on frequency now arises naturally

as the relative importance of different physical processes changes with different areas of the jet flow. Set against this, we now have the difficulty of calibrating three different time scales and corresponding length scales, and the number of empirical coefficients is raised still further if the weighting coefficients (w_j) in last equation are included. These difficulties can be resolved, however, by introducing a time scale that is based on the transfer of energy between different wave numbers of the turbulent fluctuations (TET time scale). A description of this time scale has been given in section 4.2. However, comparison show that the TET time scale provides a very good agreement with the experimental data, whilst the difficulty of calibrating a large number of coefficients, as in the triple time scale is circumvented.

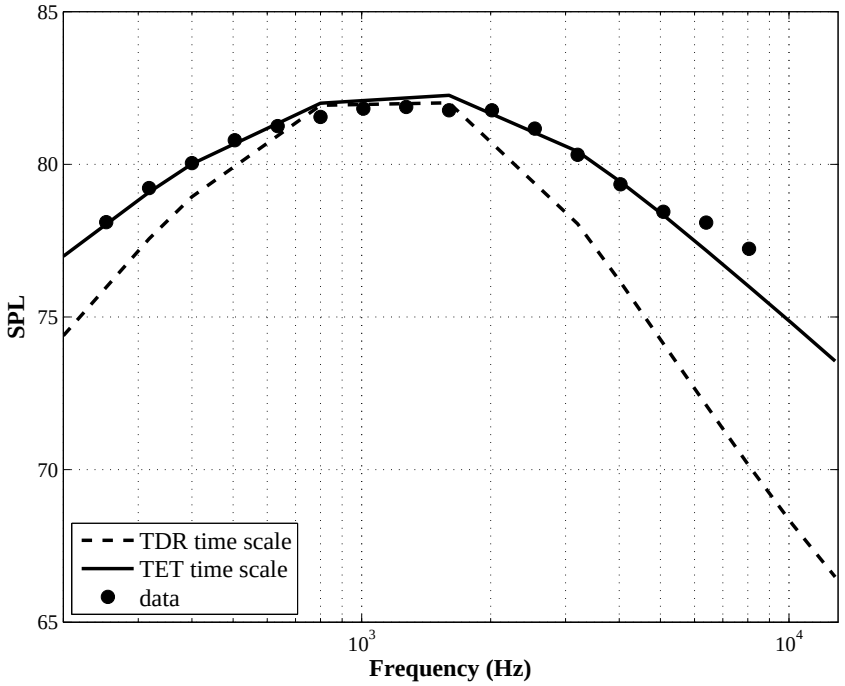

FIGURE 5.3: Comparison of experimental data with predicted spectral density at 90^o to the jet axis using three different time scales and based on the MGBK method: $R = 50D_J$, $M_J = 0.90$, $D_J = 0.05m$.

Simulation has also been performed for a single-flow unheated $M_J = 0.90$ jet. Comparison of the results obtained using the TDR and TET time scales are summarized in figure 5.3. A similar behavior and trend can be observed from this high speed subsonic jet flow to the $M_J = 0.75$ jet. Use of the TDR time scale can result in up to $5dB$ difference at $200Hz$, and $10dB$ difference at $10kHz$, while the results obtained using

the TET time scale follow the experimental data across the entire frequency range of interest (200 Hz-20 kHz).

5.1.2 Directivity Effects

Noise prediction at other angles and directivity effects are also interesting. The MGBK method, equations (2.52) and (2.53), together with the high frequency asymptotic solution of Lilley's equations, (2.50) and (2.51) will be used. In dealing with the directivity factor, equation (2.50) one first need to provide a model for the velocity field inside the jet flow. Although directly using the CFD results in equations (2.52) and (2.53) is possible, it may cause error or unexpected noise because of step-jumps occurring at the potential core or jet shear layer surface. To avoid this a velocity curve-fit has been used to find the turning point location in equation (2.45). The following relation has been found to provide an acceptable fit to the computed CFD data:

$$\begin{aligned} U(x,r) = {} & U_{Jet}H(a-x)H(\frac{D_J}{2a}(a-x)-r)+ \\ & U_{Jet}H(a-x)H(\frac{D_J}{2a}(x-a)+r)sech^2(\left[\frac{D_J}{2a}(x-a)+r\right]/c2)+ \\ & U(x)|_{r=0}\,H(x-a)sech^2(r/c1) \end{aligned} \tag{5.1}$$

where the cylindrical coordinates are denoted by (x,r) $H()$ denotes the Heaviside function, $sech()$ is the Hyperbolic secant function, and other coefficients can be obtained from matching the formulation with the CFD results (see Appendix A). The following values are found for the three jet velocities ($M_J = 0.60, 0.75, 0.90$): for the $M_J = 0.6$ case the coefficients are given by

$$c_1 = 0.114x - 0.0111$$

$$c_2 = 0.0890x + 0.0012$$

$$a = 7.5D_J$$

and for the $M_J = 0.75$ jet flow, we have

$$c_1 = 0.0979x - 0.0101$$

$$c_2 = 0.0890x + 0.0012$$

$$a = 7.5D_J$$

and finally for the $M_J = 0.90$ the following values are found

$$c_1 = 0.11439x - 0.0101$$

$$c_2 = 0.0890x + 0.0012$$

$$a = 7.5D_J$$

The mean velocity and its radial derivative inside the jet flow and corresponding comparisons with the CFD results for the $M_J = 0.75$ jet flow are presented in figure 5.4. It can be seen that the mean velocity model provides a very good level of accuracy at different axial and radial positions. As mentioned before, using such a model instead of the CFD results avoids any numerical errors arising due to the step-jumps or discontinuities happening around the shear layer or potential core surface, which can be usually observed in the CFD results.

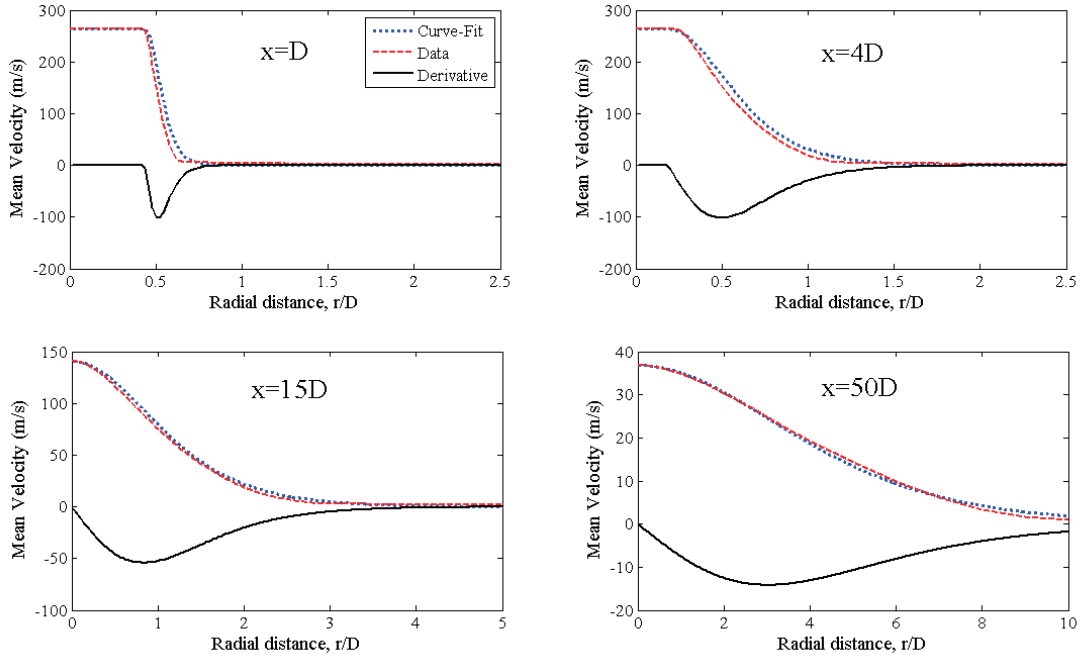

FIGURE 5.4: Velocity curve-fit, $M_J = 0.75$, $D_J = 0.05m$.

For a precise jet noise prediction at small angles, the location of the turning points is of great importance. As discussed previously in section 2.2, turning points occur when the shielding function, g^2, changes sign, equation (2.45), which is:

$$g^2(r) = \frac{(1 - U/c_0 \cos\theta)^2 (c_0/c_s)^2 - \cos^2\theta}{(1 - M_c \cos\theta)^2}. \tag{5.2}$$

Concerning the above relationship, for an unheated flow (c_0/c_s) term is always about unity, so the only effective parameters are the local mean velocity and the observer angle θ. After substitution of the mean velocity from equation (5.1), the turning point location for different observer positions at three different Mach numbers are calculated and are presented in figure 5.5.

As mentioned before in section 2.2, sources radiating from the regions specified in figure 5.5 to an observer inside the cone of silence will suffer an exponential decay. It is worth mentioning in this regard that the last angle at which a source encounters damping is when $\cos\theta^* = \frac{1}{1+U/c_0}$, where θ^* will be called the "cone-angle". Roughly speaking, the last turning point for $M_J = 0.60$, 0.70, and 0.90 jet flows will happen when the observer is located around $\theta^* = 51^o$, 55^o, and 58^o, respectively. Therefore, it can be seen that for any angle greater than the cone-angle (θ^*) the refraction effect can be accounted for by the high frequency approximation with no fear of radiating into the zone of silence. Furthermore, for a single unheated jet flow more than one turning point will never occur.

The damping factor, β_{01}, within the zone of silence can be calculated using the first equation of (2.51). Numerical integration of (2.51-a) is accomplished for the $M_J = 0.75$ jet when the observer is located at $30D_J$. Variation of the damping factor for different frequencies and observer polar angles (θ) can be seen from figure 5.6. Results show that the highest level of damping occurs at high frequencies and for observers in the vicinity of the jet axis. Therefore, it can be deduced that the SPL spectrum for an observer close to the jet axis will experience comparably sharper roll-off after the peak frequency. It can be also seen that less sources encounter damping for larger angles and the damping effect entirely disappears outside the zone of silence, $\theta > \theta^*$.

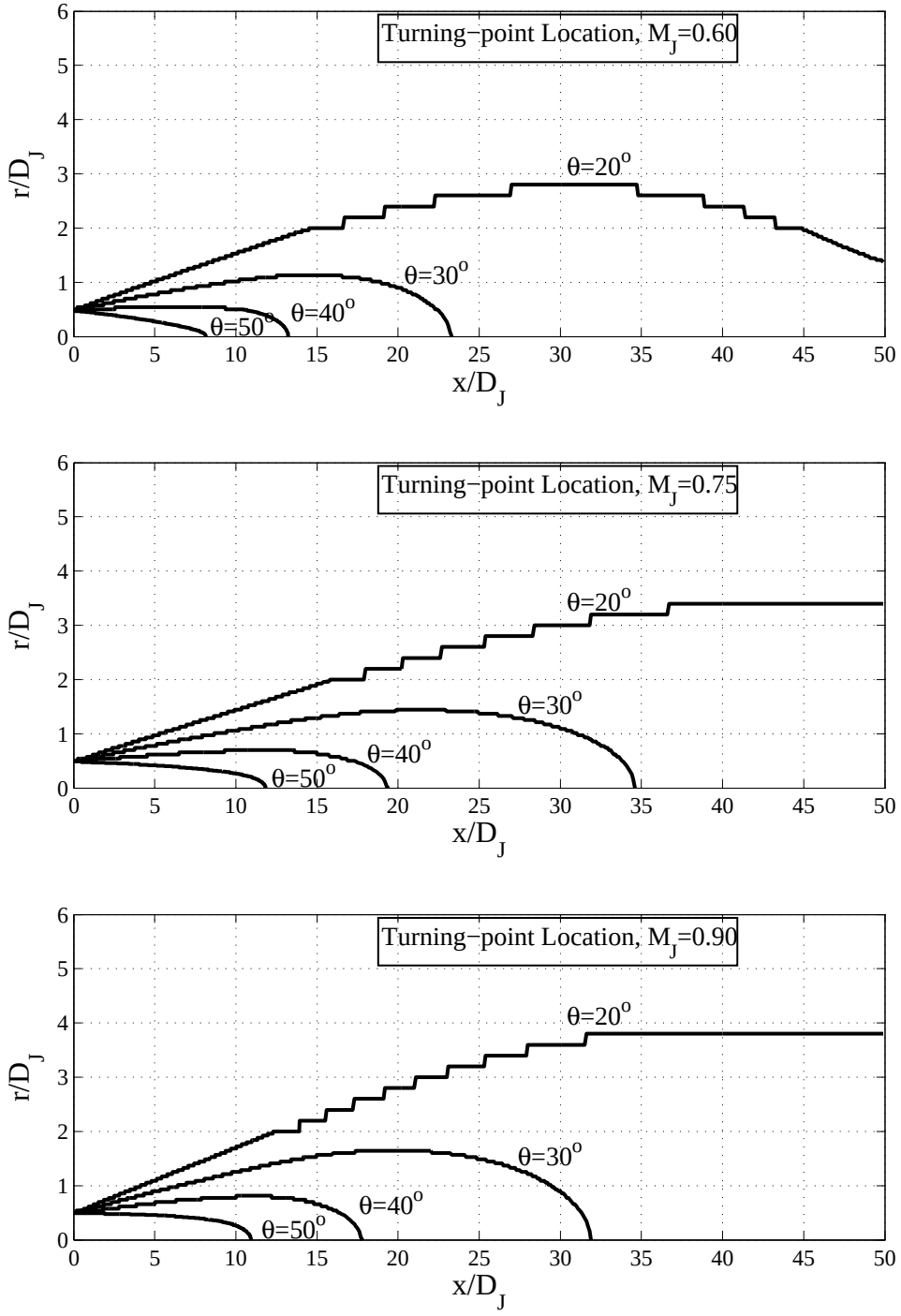

FIGURE 5.5: Turning point location for different observer locations, $D_J = 0.05m$, $R = 50D_J$.

Prediction of the far-field noise directivity using the mathematical models given in section 2.2 is now presented. The turbulent energy transfer time scale (TET), equation (4.15), dissipation length scale, equation (4.1), and the mean velocity model have been used in these predictions. Simulations are performed for $M_J = 0.6$ and $M_J = 0.75$ jet

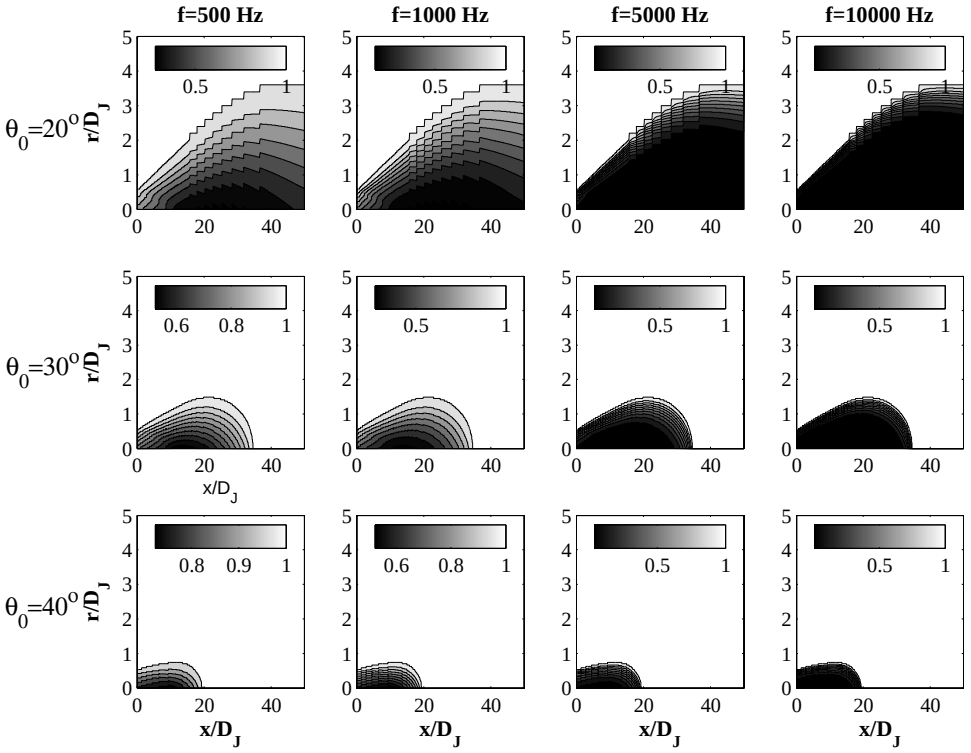

FIGURE 5.6: Damping factor for radiation into the zone of silence; $R = 30D_J$

flows for an observer positioned at $R = 30D_J$ and $50D_J$ from the nozzle exit. Figures 5.7 through 5.10 show comparisons of the numerical results obtained using the TET time scale against the experimental data. In general, an acceptable agreement over all angles between 50 and 130 degrees to the downstream axis for different jet working conditions is achieved. By comparing results with those found by other authors [38], it can be deduced that these results show an improvement compared to those obtained using the time scale defined by equations (4.8) or even (4.9).

However, it is noted that there is still a mismatch between the prediction and data regarding the peak frequency at small angles. It is believed that this discrepancy might have originated from one or more causes.

First, the radiated noise from large eddies is not properly captured, which leads to poor agreement at low frequency range for observers located nearby, and accordingly peak frequency mismatch. The failure to accurately compute the low frequency noises actually stems from the failure of the retarded-time assumption, which is questionable for large eddies since their distance to the observer is sometimes less than what is considered

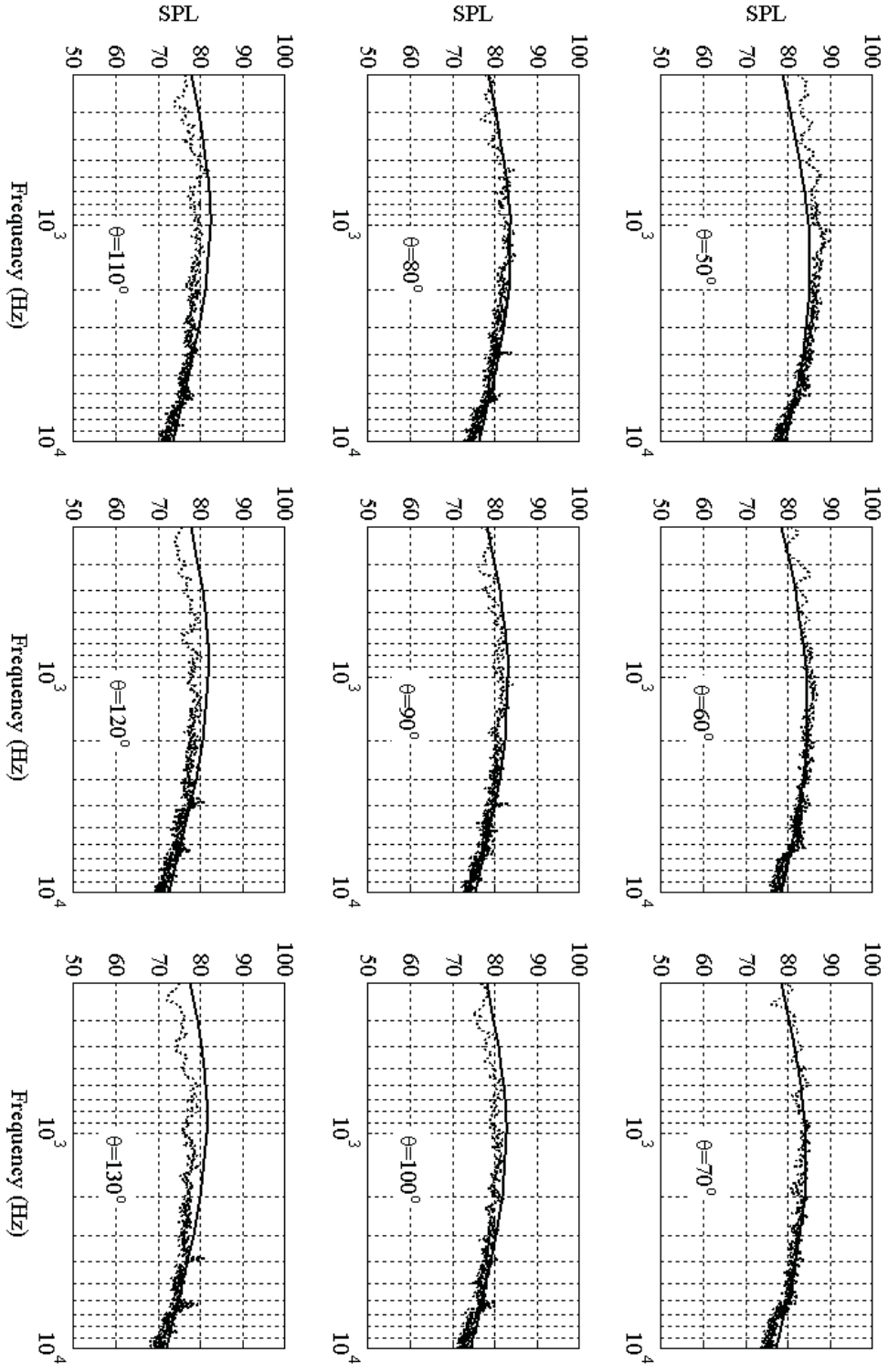

FIGURE 5.7: Comparison of experimental data with predicted spectral density at different angles to the jet axis using energy transfer rate time scale; based on the MGBK formulations for directivity, $R = 30D_J$, $M_J = 0.60$, $D_J = 0.05m$

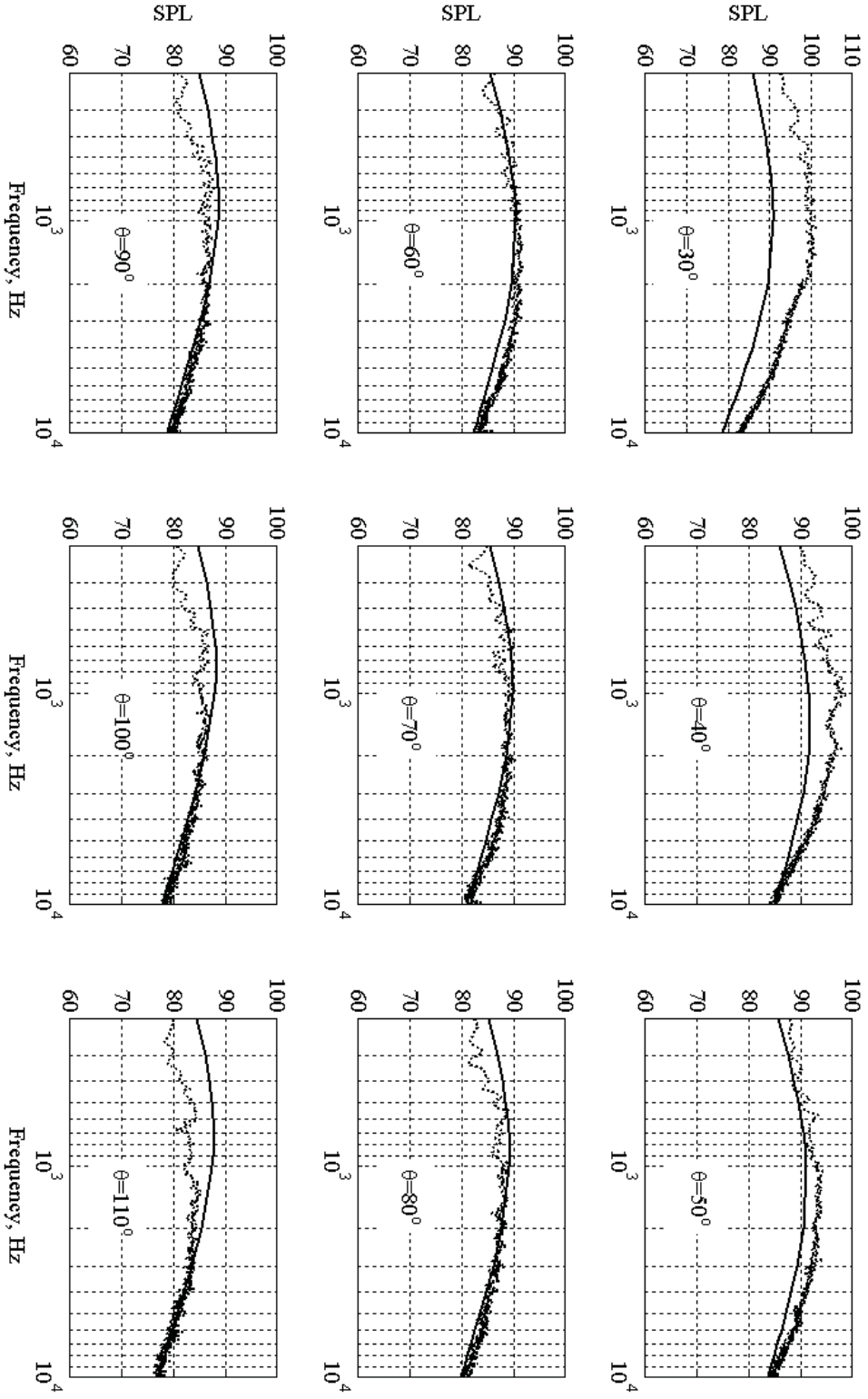

FIGURE 5.8: Comparison of experimental data with predicted spectral density at different angles to the jet axis using energy transfer rate time scale; based on the MGBK formulations for directivity, $R = 30D_J$, $M_J = 0.75$, $D_J = 0.05m$

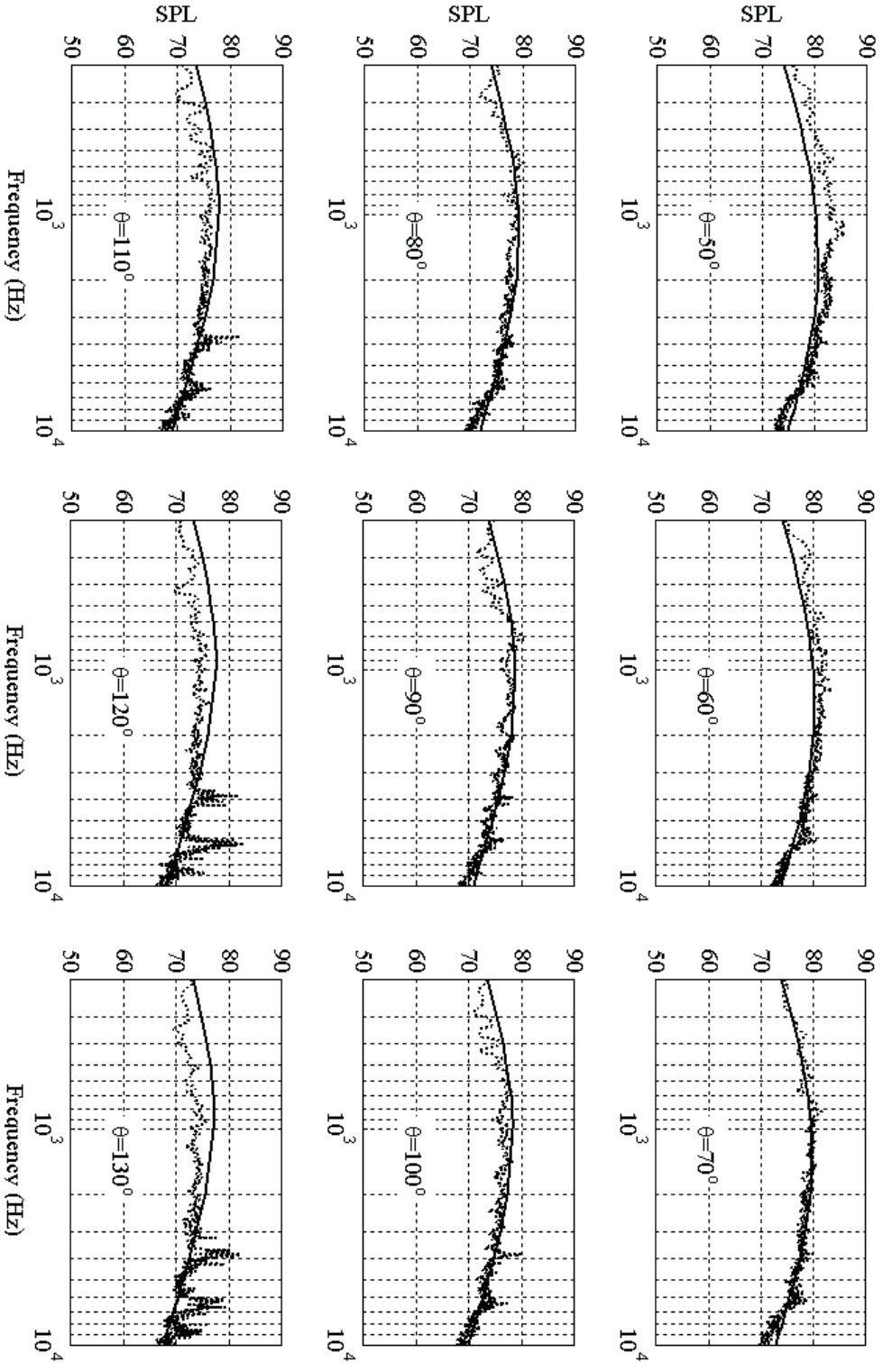

FIGURE 5.9: Comparison of experimental data with predicted spectral density at different angles to the jet axis using energy transfer rate time scale; based on the MGBK formulations for directivity, $R = 50D_J$, $M_J = 0.60$, $D_J = 0.05m$.

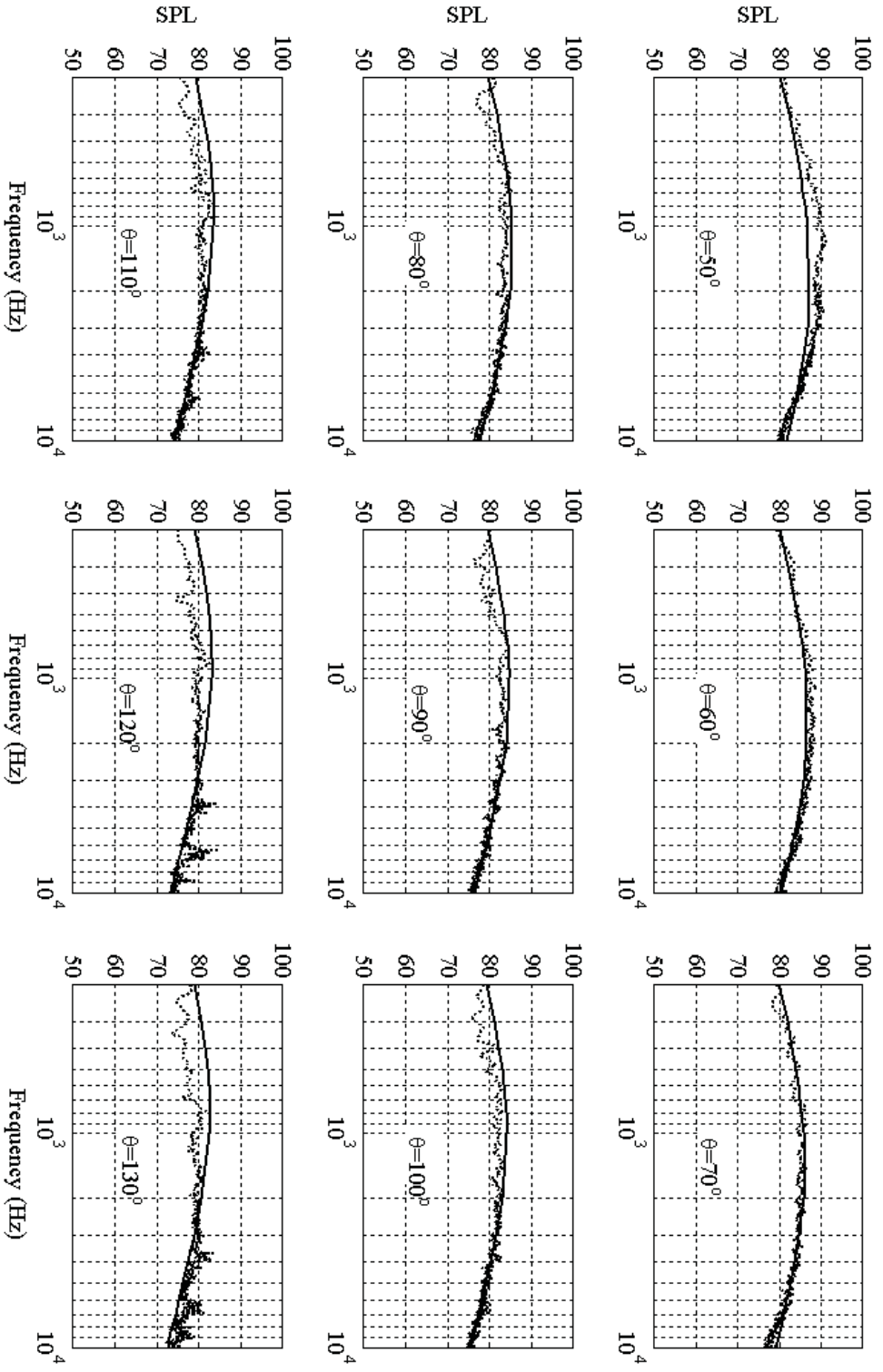

FIGURE 5.10: Comparison of experimental data with predicted spectral density at different angles to the jet axis using energy transfer rate time scale; based on the MGBK formulations for directivity, $R = 50D_J$, $M_J = 0.75$, $D_J = 0.05m$.

as the acoustic far-field. This can be seen from a comparison between the predicted results at $30D_J$ and $50D_J$, figures 5.7 and 5.10. It can be seen that the discrepancy existing at small angles decreases with increasing distance (R). The second possible reason is the use of the high frequency approximated solution of the refraction effect for all frequencies. The third possibility has to do with the definition of the convection velocity. As mentioned before in section 3.4, the peak frequency can be estimated by the eddy-sweeping speed ($\omega_0 \propto \overline{V}\kappa_e$). Thus, the convection velocity value at some particular location has a direct relation with the peak frequency value. Furthermore, it is well understood from the literature that the large eddies are convected downstream at a speed different from the small eddies. This shows that value of the convection speed of the large eddies can play an important role in the accuracy of the noise prediction when the observer is positioned close to the jet axis.

Among the above causes, the first one is thought most likely to be the real reason since it is physically and mathematically justified. The second reason was considered before in [4] and it was shown that although the behaviour of the flow factor at low frequencies is different from that in the high frequency range, the low frequency range is very narrow and can effectively be neglected. So, finally one can conclude that despite of the effect of all of these three causes, the first one is the most important one. However, in order to further examine the correctness of this claim, the effect of using different convection velocity models on the location of the peak frequency will be examined in section 5.1.4.3.

5.1.3 Equivalent Source Location

Location of jet noise sources is a far from trivial problem that is of great importance for both the understanding the noise production and the radiation mechanisms and also for finding new jet noise reduction strategies. According to the nature of jet turbulence it can be readily realized that the high frequency noise sources are mostly aggregated in the vicinity of shear sub-layer, specially where the shear layer is thinner (usually between the nozzle tip and end of the potential core). In contrast, the low frequency sources are associated with larger eddies which are mostly formed in the fully developed region and close to the jet axis. One of the earliest works on this subject was published by Ribner in 1958 [95]. This work was very short and its most important result was that the overwhelming bulk of the jet noise is emitted from first eight to ten diameters, which is regarded as the mixing region. It was found that the sound power distribution in the mixing region is constant, while it is proportional to the reciprocal 7th power of axial distance for the fully developed region. Later, Dyer investigated a similar problem [96] and derived a simple procedure for obtaining axial source distributions in a turbulent jet flow. Upon using this procedure one can find the frequency of the sources as a function of location along the jet axis.

In this section a mathematical model for the jet noise source distribution will be obtained which makes use of the CFD-turbulence results as an input for source modelling. The basis is quite similar to the sound intensity calculation (section 2.1): taking the overall intensity as an integral over the axial extent of the jet,

$$I(R,\,\omega) = \int I_x(\omega)\,dx, \tag{5.3}$$

where $I_x(\omega)$ defines the axial source distribution at each frequency. Since we are only interested in the source distribution from the standpoint of the ninety degrees observer, the following relation can be readily found from Lighthill's equation,

$$I_x(\omega) \propto \int_{-\infty}^{\infty} \int_{\phi=0}^{2\pi} \int_{r=0}^{r_\infty} L_1 L_2 L_3 \tau v^4 e^{-\left(\frac{\omega L_1}{2c_0}\right)^2 - \left(\frac{\omega\tau}{2}\right)^2} e^{-j\omega\tau} dr d\phi d\tau \tag{5.4}$$

Source distributions for an unheated $M_J = 0.9$ jet are presented in Figure 5.11. The

figure illustrates the axial position at which the source location, I_x, peaks at a particular frequency. In other words, maximums of I_x at each frequency are found. The figure shows a comparison of the results obtained using the analytical solution, given by equation (5.4), when the TDR and TET time scales are used with the experimental data [97].

It can be seen that the high frequency sources are aggregated in the vicinity of the jet exit, while the low frequency ones are located further downstream after the potential core. In addition, it can be seen from the figure that using the TDR time scale results in a broader acoustic source regime, while the source domain captured using the TET time scale shows a better agreement with the experimental data. Although some differences between the experimental data and TET results at low frequency range can be observed, the curves slope show that they are sharing the same underlying physical phenomena.

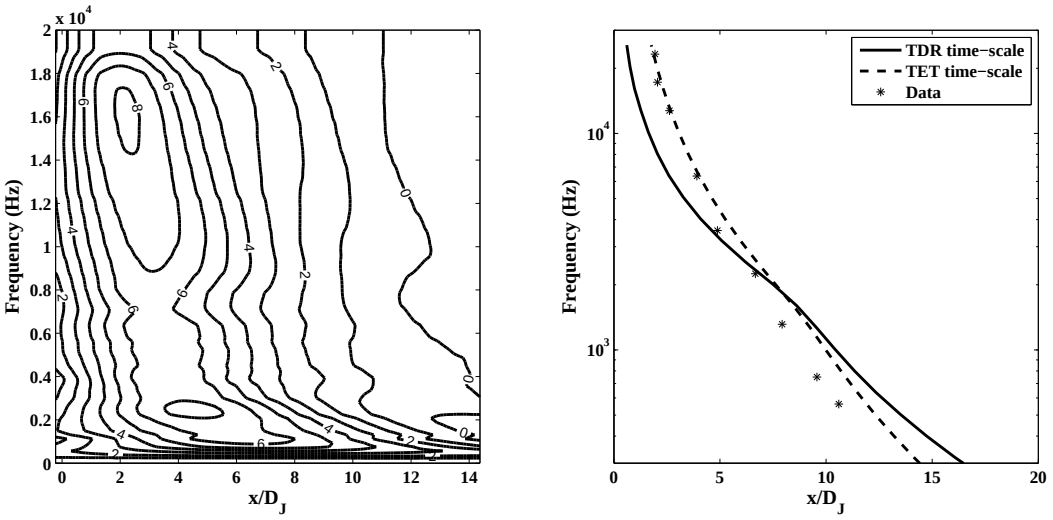

FIGURE 5.11: Source location based on the MGBK method at 90 degrees, $R_r = 50D_J$, $M_J = 0.90$, $D_J = 0.05m$.

Source distributions, I_x, for models based on the TDR time scale, the combined time scale and the TET time scale have been calculated for $M_J = 0.75$ and are shown in figures 5.12 through 5.14. From studying these figures it can be seen that using the dissipation time scale, τ_d, results in a source distribution that is roughly of Gaussian shape for all frequencies. As seen in figure 5.2, using a combination of time scales provides a more realistic results, but Figure 5.13 reveals source distributions that are of a markedly different shape to those observed in real jets [97]. However, using the TET

time scale, τ_T not only leads to a good agreement in the spectra but also reproduces a more physically realistic shape of source distribution, figure 5.14.

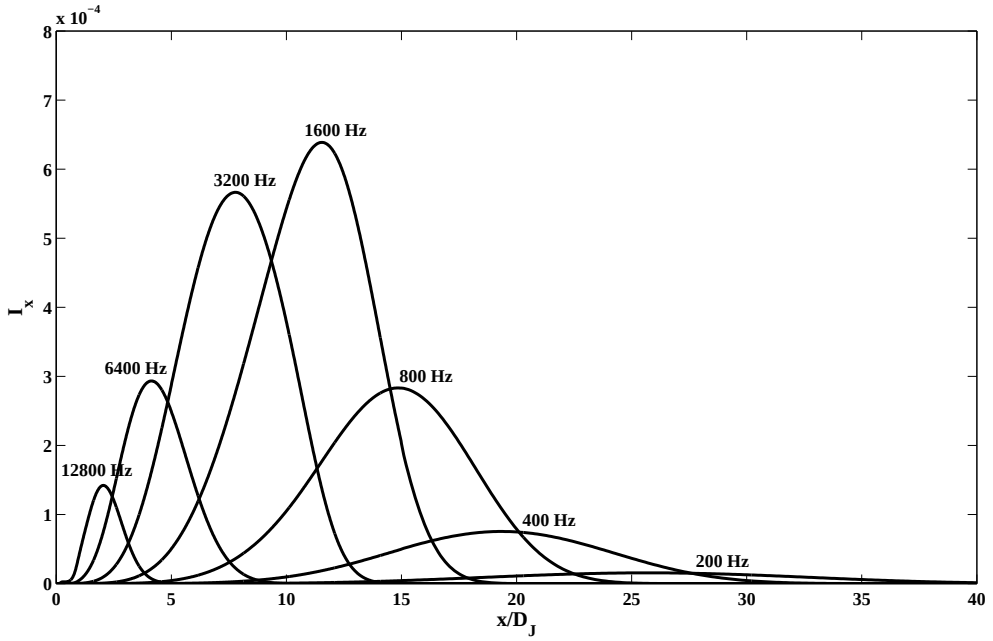

FIGURE 5.12: Predicted noise distribution at each frequency, using dissipation rate time-scale and based on the MGBK method for 90 degrees, $R_r = 50D_J$, $M_J = 0.75$, $D_J = 0.05m$.

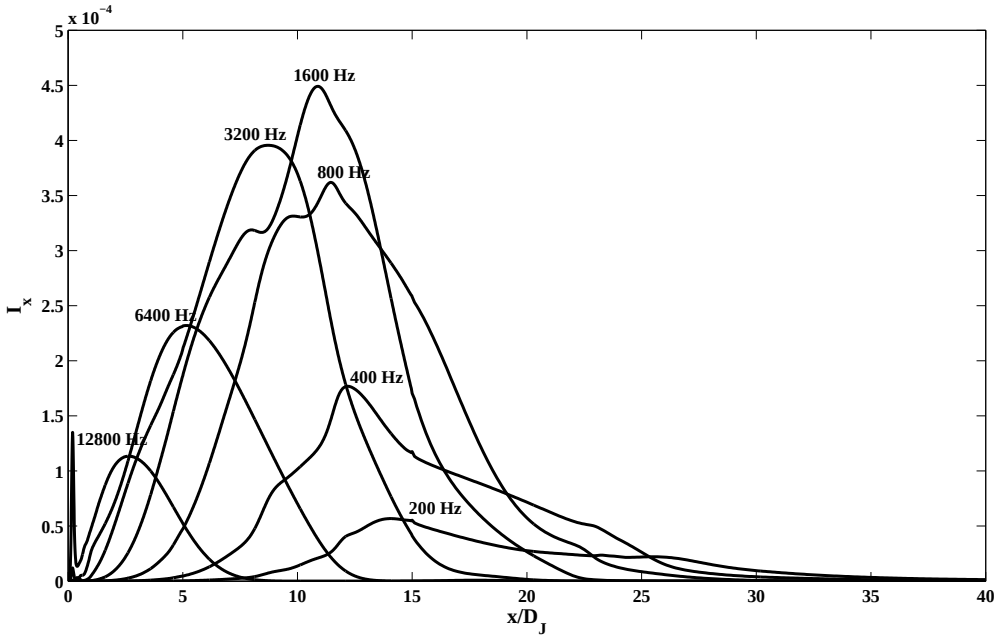

FIGURE 5.13: Predicted noise distribution at each frequency, using combined time-scales and based on the MGBK method for 90 degrees, $R_r = 50D_J$, $M_J = 0.75$, $D_J = 0.05m$.

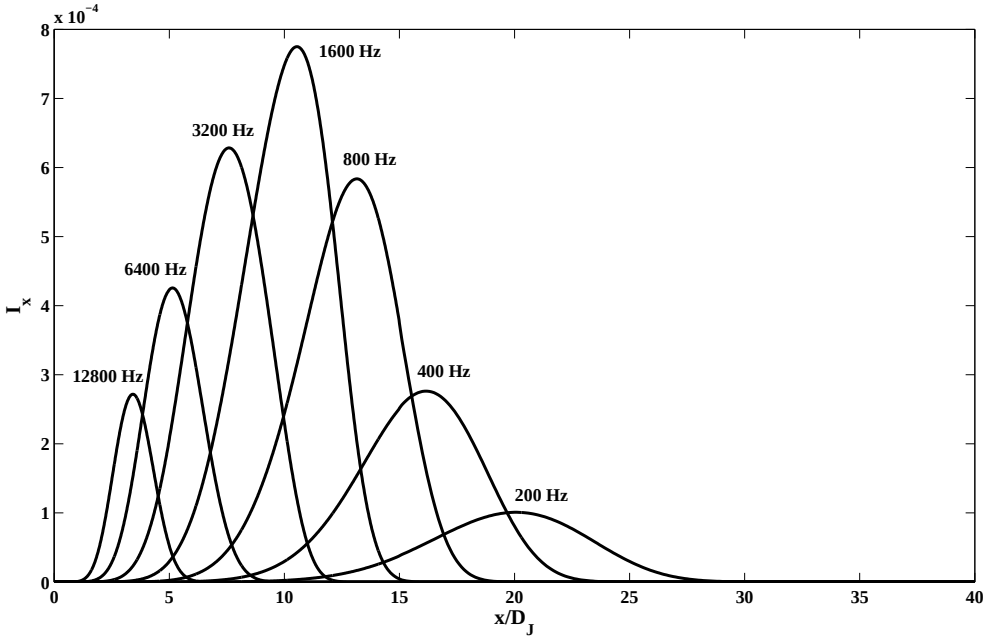

FIGURE 5.14: Predicted noise distribution at each frequency, using energy transfer rate time-scale and based on the MGBK method for 90 degrees, $R_r = 50D_J$, $M_J = 0.75$, $D_J = 0.05m$.

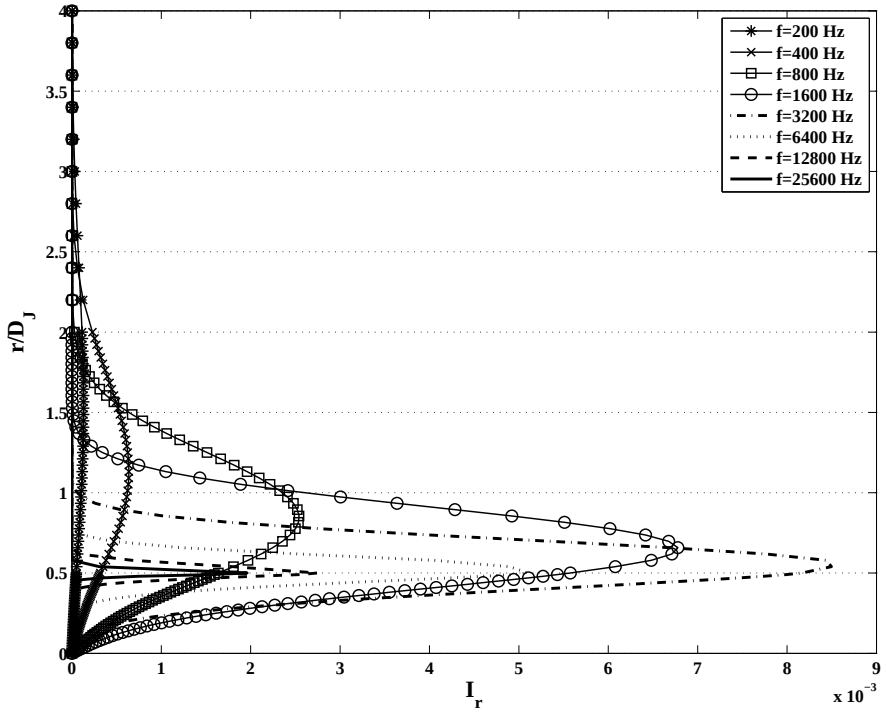

FIGURE 5.15: Radial source distribution based on the MGBK method at 90 degrees using TDR time-scale, $R = 50D_J$, $M_J = 0.90$, $D_J = 0.05m$.

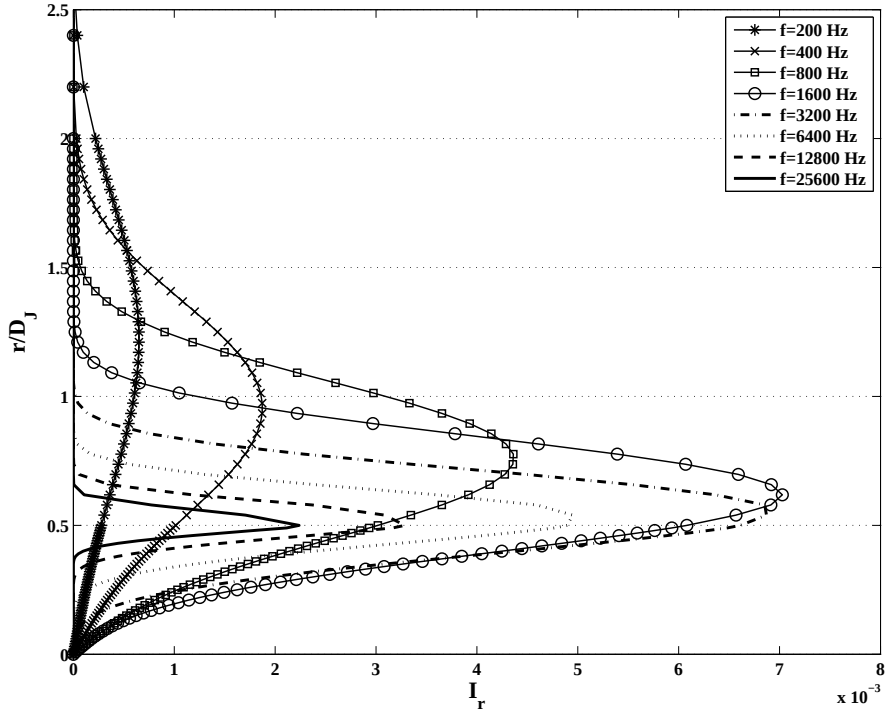

FIGURE 5.16: Radial source distribution based on the MGBK method at 90 degrees using TET time-scale, $R = 50D_J$, $M_J = 0.90$, $D_J = 0.05m$.

Radial distribution of the sources are also considered here, see figures 5.15 and 5.16. It can be seen that using the TDR time scale leads to a wider radial distribution, while the TET time-scale captures all of the sources in the first two diameters from the jet axis. It can also be seen that the high frequency sources are aggregated near the lip-line, whereas the low frequencies further downstream near the jet shear layer. Results also show that the contribution of the high and low frequencies obtained using TET time-scale is higher than when the TDR time-scale is used, which is why using TET time-scale results in a better agreement at these range of frequencies.

5.1.4 Source Compactness, Anisotropy and Convection Velocity

In this section the following issues are addressed: source compactness, turbulence anisotropy and convection velocity. In the first two parts it will be shown how the source compactness and turbulence anisotropy can be taken into account using the MGBK method and how this improves the results. In the last part, two convection velocity models will be introduced (based on experimental evidence) and the goal addressed is the question

raised above regarding the peak frequency mismatch observed for small and large angles comparisons, and its relation to the definition of the convection velocity.

5.1.4.1 Source Compactness

Source compactness is an important issue that can be addressed easily when the MGBK method is used. For a compact eddy, the assumption is made that the eddy size, l, is much shorter than the wave-length of the acoustic disturbance, ($\omega l/c_0 \ll 1$), accordingly the factor $e^{-jk.\xi}$ is set equal to unity. The derivation presented before in section 2.2 was based on this assumption. In order to calculate the effect of source non-compactness, parameters inside the integral over the source domain must be multiplied by the $e^{-jk.\xi}$ factor, see equation (2.18). Khavaran and Bridge investigated this case using different types of correlation function and derived the non-compactness factor (NCF) for each case [31]. Using an exponential function $f(\xi) = e^{-\pi\xi/l}$ leads to

$$NCF(kl) = 20\left(\frac{\pi}{kl}\right)^5 \left[3\tan^{-1}\left(\frac{kl}{2\pi}\right) - 2\frac{kl}{\pi}\frac{5(kl/\pi)^2+12}{\left((kl/\pi)^2+4\right)^2}\right]$$

and for a Gaussian correlation function $f(\xi) = e^{-\pi\frac{\xi^2}{l^2}}$ one finds

$$NCF(kl) = e^{-\frac{\pi}{2}\left(\frac{kl}{2\pi}\right)^2}$$

In order to gain a better understating of the source compactness effect, the axial source distribution, I_x, at each individual frequency is calculated. The Gaussian non-compactness factor is chosen and the resulting distribution amplitudes are normalized so peaks are unity, see figure 5.17. The damping factor due to the refraction phenomenon, which was discussed before, is also included in this figure. Figure 5.17 illustrates the source distribution when the observer is located at $R = 30D_J$ and $\theta = 30^o$. The figure shows that source non-compactness is not a very important issue for low frequencies but its effect becomes more important with frequency.

Looking at the figure one may also deduce that the damping factor increases with frequency, such that most of the radiated energy towards the observer will be diminished in high frequency range. Another interesting point here is the peak position at each frequency. Comparing the noise spectrum, figure 5.8, with the results presented in

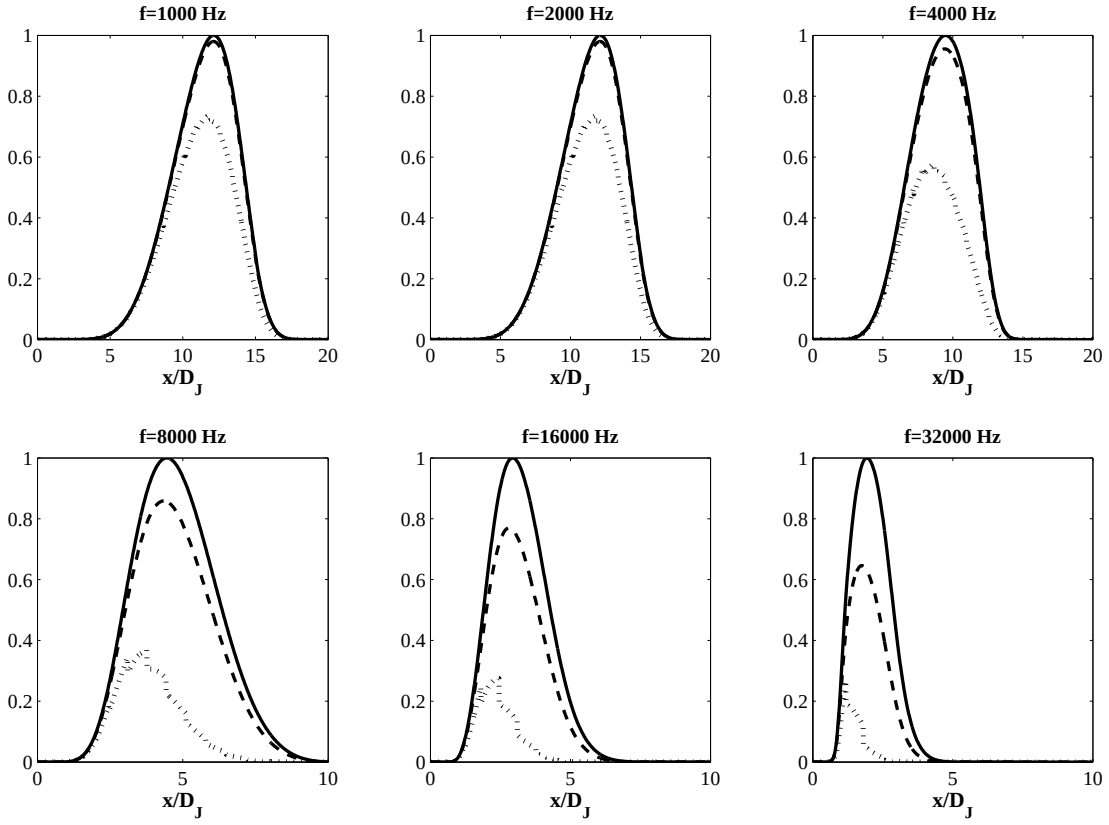

FIGURE 5.17: Predicted noise distribution; $R = 30D_J$, $\theta = 30^o$, $M_J = 0.75$, $D_J = 0.05m$. *Solid line*: neither compactness effect nor damping, *Dashed line*: With compactness effect, no damping, *Dotted line*: with compactness effect and damping

figure 5.17 shows that the most important contributors to the radiated sound at $\theta = 30^o$ are the relatively large eddies aggregated in region of $x \approx 6D_J$ to $x \approx 12D_J$, after the potential core.

A similar simulation is also performed for a microphone at $R = 30D_J$ and $\theta = 40^o$, see figure 5.18. The peak frequency of the spectrum for $\theta = 40^o$ is about $f = 1.5kHz$, and accordingly the most important noise sources are found to be captured in region of $6 < x/D_J < 11$, that means the most important constituents to the noise spectrum have now moved towards the jet exit as the observer recedes from the jet axis. Furthermore, comparison of figures 5.17 and 5.18 show that the damping effect shrinks as the observer angle (θ) increases, and will completely fade at the cone-angle $\theta^* = 54^o$, where there will no longer be any damping.

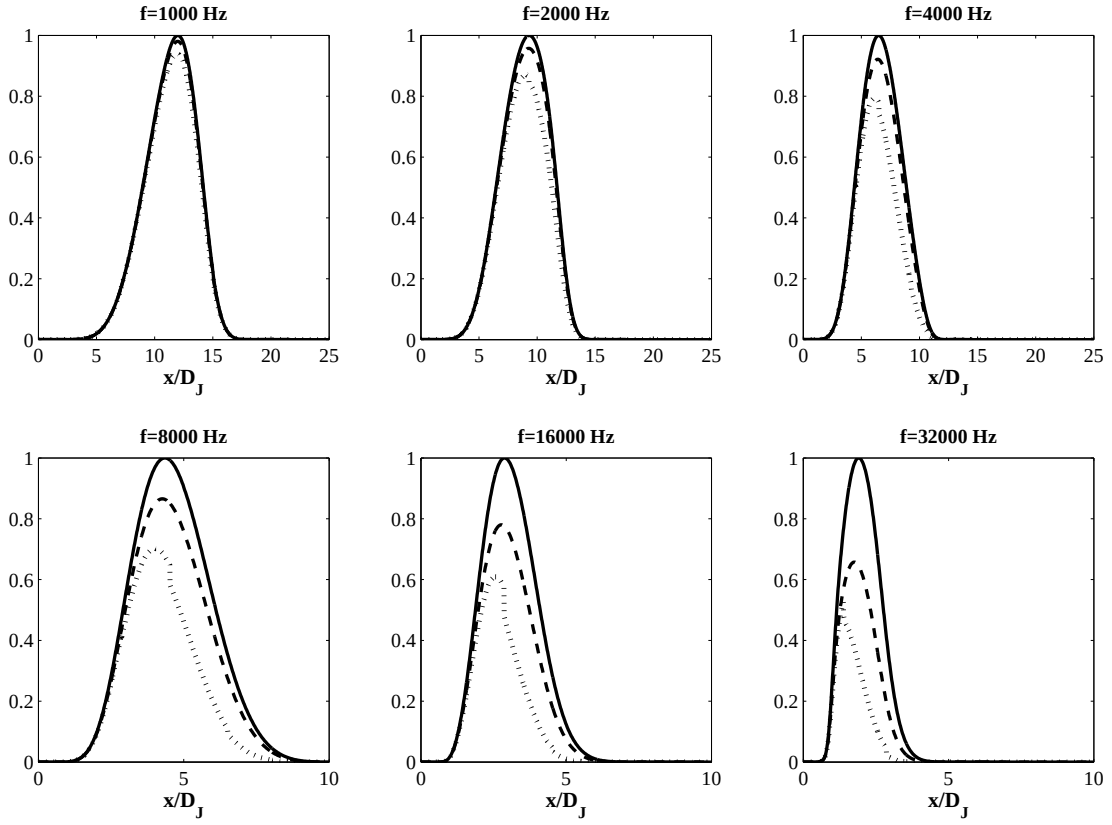

FIGURE 5.18: Predicted noise distribution; $R = 30D_J$, $\theta = 40^o$, $M_J = 0.75$, $D_J = 0.05m$. *Solid line*: neither compactness effect nor damping, *Dashed line*: With compactness effect, no damping, *Dotted line*: with compactness effect and damping

5.1.4.2 Turbulence Anisotropy

In the derivation of sound intensity using Lighthill's Analogy, or the MGBK method, the turbulence was assumed to be isotropic. Strictly speaking, isotropy means independence of orientation and also implies homogeneity (*i.e.* independency of position in space). However, these conditions are only met for special cases, *e.g.* grid turbulence. The importance of the jet turbulence anisotropy and its effects on radiated noise have been emphasized many times [57, 64] and it should be noticed that noise prediction theories derived under the isotropic assumption are only valid for high frequency sources. It has been indicated by Ribner that the non-isotropic structures of the turbulence can have an important effect on the directivity pattern of the narrow band noise at low frequencies [59]. Furthermore, experimental measurements for low subsonic Mach numbers of 0.1 and 0.3 confirmed a high degree of anisotropy among the large eddies [98, 99]. More recent measurements by Zysman *et al.* [100] and Podboy *et al.* [101] for high speed

subsonic and transonic jets have also confirmed such a tendency of turbulence towards anisotropy. Thus, it can be realized that the turbulence isotropy assumption can not be accurate and appropriate supposition for an entire frequency band prediction, and should, in some manner, be added to the solver.

The level of the turbulence anisotropy for axisymmetric turbulence can be estimated through $\beta_c = 1 - v_2^2/v_1^2$. The effect of the length scales ratio can also be studied simultaneously. In this case the ratio of the lateral and longitudinal length scale is defined by $\Upsilon = L_2/L_1$. Figure 5.19 shows the effects of changes in anisotropy level and length scale ratio on the noise spectrum for a $M_J = 0.75$ jet flow when the observer is located at $R = 30D_J$, $\theta = 40^o$.

It is difficult to draw an objective conclusion from the figure, but inserting the above definition into the acoustic intensity equations, (2.57), gives rise to the following factor (multiplying by the sound intensity), which expresses the effect on the noise spectrum,

$$\Upsilon^2(1 - \tfrac{2}{3}\beta_c)^{-13/2}.$$

It can be seen from figure 5.19, and also can be inferred from the above equation that decreasing β_c (*i.e.* closer to isotropy) increases the noise level, simultaneously increasing the length scale ratio also increases the noise level. It should be noted that the above assumption for the anisotropy treats all the frequencies in the same way, which is clearly incorrect as the effect vanishes at sufficiently high frequencies where the turbulence is entirely isotropic. Instead its effect should be maximum at low frequencies. In order to fulfill such a requirement one needs to provide a frequency, or location (or eddy size) dependent model. However, there is a little of experimental data in this regard.

5.1.4.3 Convection Velocity

It has been shown that the convection velocity is frequency dependent as first pointed out many years ago by Fisher and Davis [51], confirmed later by Akamatsu [82] and further experimentally examined by Harper-Bourne and [48] and Kerherve *et al.* [53]. However, the lack of experimental data for the convection velocity at different turbulence scales and for special purposes prevents detailed quantitative comparison, and consequently a kind of trial approach has been used to better investigate the relation between the

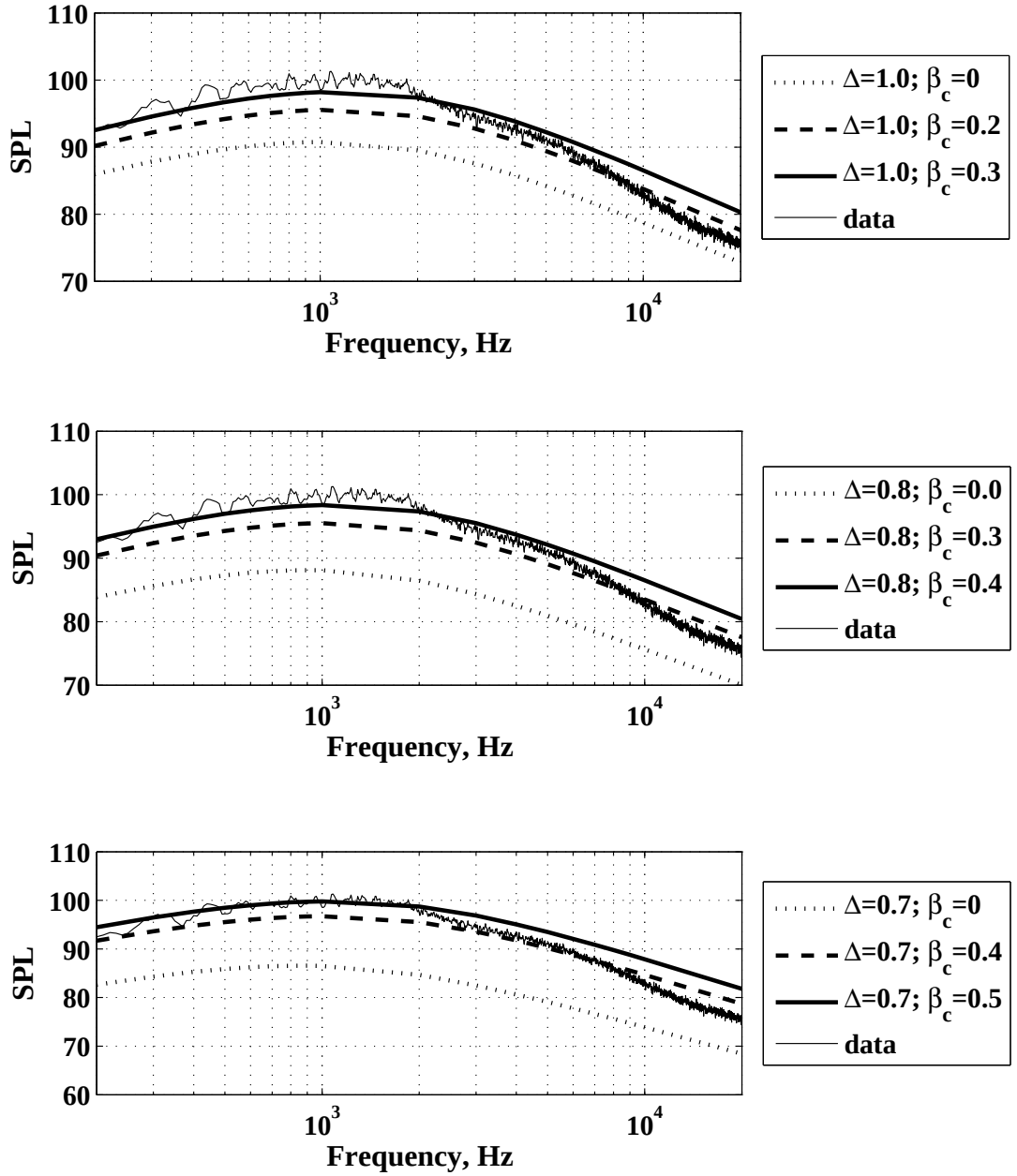

FIGURE 5.19: Effect of turbulence anisotropy on noise spectrum, $\Delta = L_2/L_1$, $\beta_c = 1 - v_2^2/v_1^2$

peak frequency location and the variable convection velocity models which can vary with location or frequency. Two models were introduced in section 4.3: the first model was based on the local mean flow parameters and the second model has a frequency dependent form. In what follows some numerical examples showing the effect of using each model and ascertain whether they can be of any use to lessen the mismatches observed in previous noise results (e.g. figures 5.7, and 5.9) will be given. The two

models are given by:

$$M_c = aM_{Local} + bM_J, \tag{5.5}$$

$$M_c = \alpha.\frac{fD}{U_J} + \beta.M_J \tag{5.6}$$

The first relation will be called the "mean velocity model", and the second one will therefore be referred to as the "frequency dependent model".

Numerical examples are provided to gain a better understanding of the convection velocity by changing the weight coefficients (a, b, and α, β) but keeping them close to the values obtained from the experimental data. Predictions are made at two angles $\theta = 60°$, and $\theta = 140°$ ($R = 50D_J$). The initial values of the weight coefficients can be found from experimental evidence. The first model has been used by many authors [102, 103]. The values used are usually around $a = 0.25$, and $b = 0.50$. In comparison with the first model, there is less data available for the second model. The most referenced work on the frequency dependency of the convection velocity is [48], and according to those results the weight coefficients can be estimated by $\alpha = 0.025$, $\beta = 0.55$.

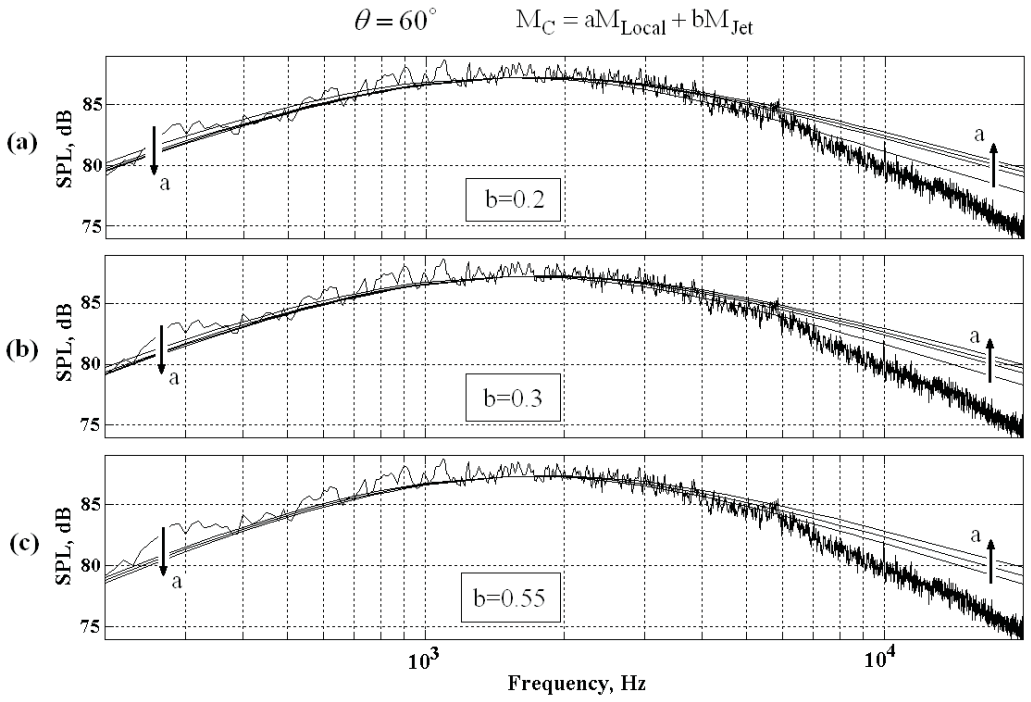

FIGURE 5.20: Power spectral density at $R = 50D_J$, $\theta = 60°$ for a single flow unheated M-0.75 jet, using local dependent convection velocity for **a**) b=0.2; a=0.2, 0.6, 0.7, 0.8, **b**) b=0.3; a=0.2, 0.5, 0.6, 0.7, **c**) b=0.55; a=-0.2, 0, 0.2.

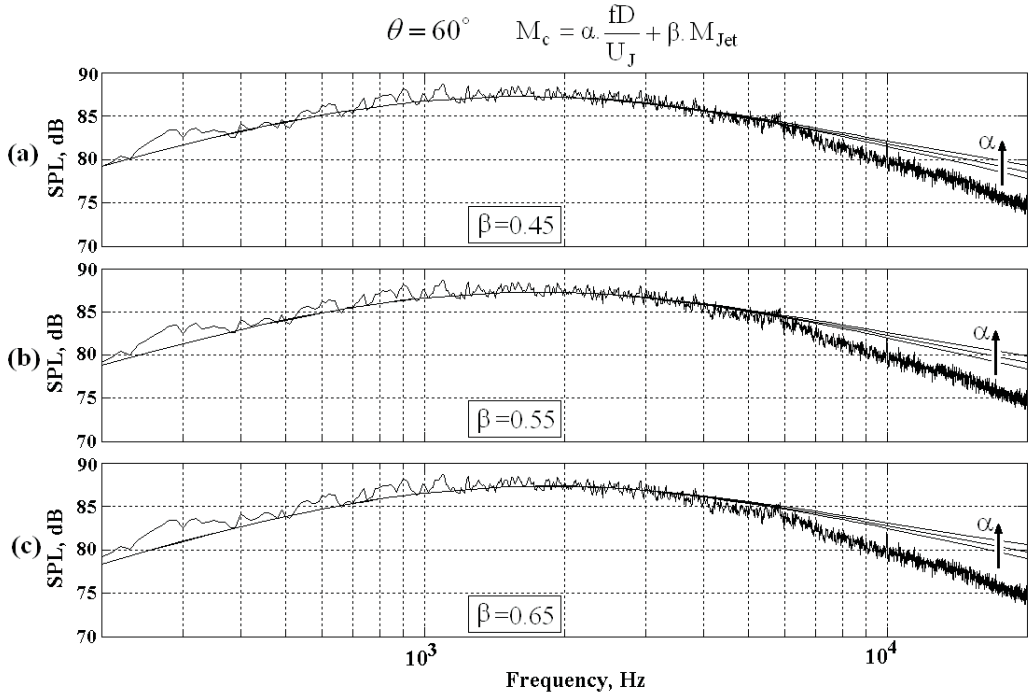

FIGURE 5.21: Power spectral density at $R = 50D_J$, $\theta = 60°$ for a single flow unheated M-0.75 jet, using local dependent convection velocity for **a**) β=0.45; α=-0.025, 0, 0.025, **b**) β=0.55; α=-0.025, 0, 0.025, **c**) β=0.65; α=-0.025, 0, 0.025.

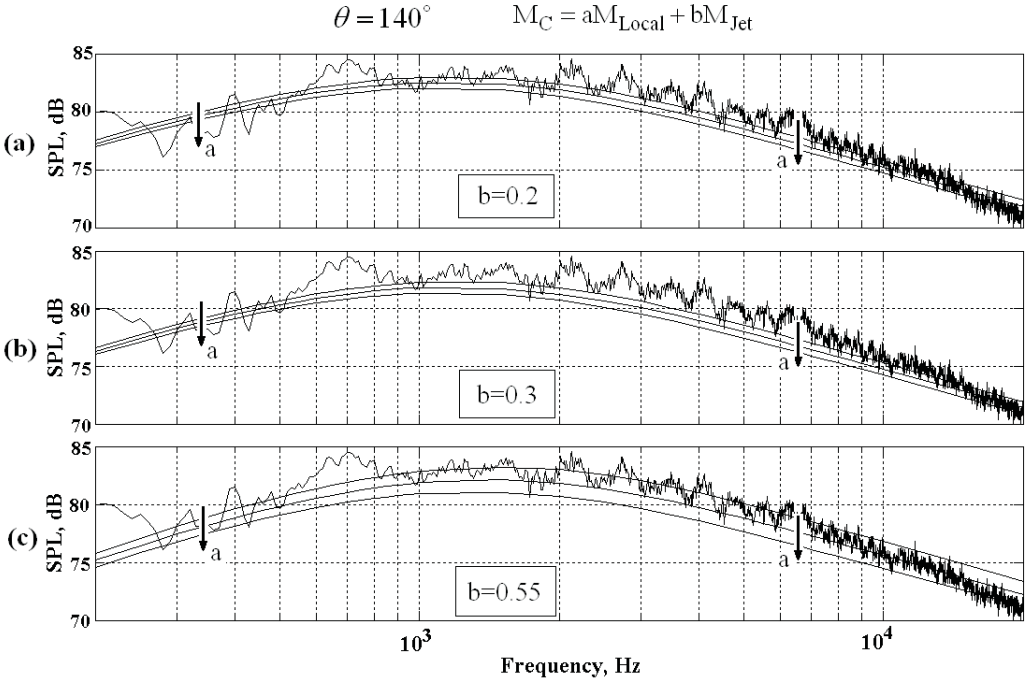

FIGURE 5.22: Power spectral density at $R = 50D_J$, $\theta = 140°$ for a single flow unheated M-0.75 jet, using local dependent convection velocity for **a**) b=0.2; a=0.2, 0.6, 0.7, 0.8, **b**) b=0.3; a=0.2, 0.5, 0.6, 0.7, **c**) b=0.55; a=-0.2, 0, 0.2.

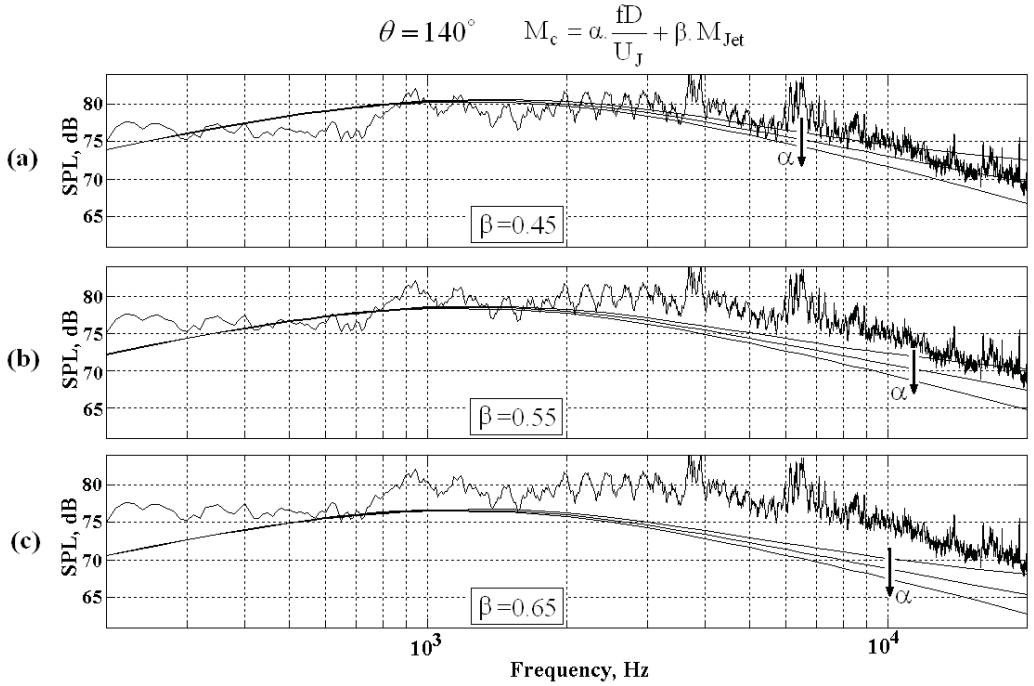

FIGURE 5.23: Power spectral density at $R = 50D_J$, $\theta = 140°$ for a single flow unheated M-0.75 jet, using local dependent convection velocity for **a**) β=0.45; α=-0.025, 0, 0.025, **b**) β=0.55; α=-0.025, 0, 0.025, **c**) β=0.65; α=-0.025, 0, 0.025,.

Exploring figures 5.20 through 5.23 provides the following observations. Comparison of the peak frequency of the experimental results at 140^o (Figures 5.22 and 5.23) with their counterparts (60^o) (figures 5.20 and 5.21) shows that the most important contributors to the radiated noise moves smoothly from the large eddies to the smaller ones as the microphone moves towards the jet exit and happens around 2000 Hz, while that for 60^o is about 1400 Hz. In addition, increasing the jet velocity share in the convection velocity will generally decrease the noise level in the entire spectrum. Increasing the local velocity in the first model also decreases the noise, but changing the coefficient of Strouhal number does not have any significant effect on low frequency noise, while usual trend can be observed again for the high frequencies.

In regard to the effect of the convection velocity on the peak frequency adjustment, it can be seen that for small angles the first model has the merit of shifting the peak frequency to higher frequencies by increasing the convection velocity magnitude, but the frequency dependent form is not able to make any further improvement for this case. Inspection of figures 5.22 and 5.23 also shows that increasing the jet exit velocity share (b) or that of the local velocity (a) shifts the peak frequency to the higher frequencies,

but the spectrum is more sensitive to the jet velocity than the local velocity. One may deduce that the dominant eddies responsible for the sound propagation in this case are slightly smaller than those in energy containing range.

In order to draw a conclusion to the convection velocity discussion it is worth remarking on the best fit found using different models and coefficients. Regarding the local parameter dependency, it can be said that for observers located near the jet axis (*i.e.* downstream), more weight must be given to the local velocity term M_c and less to the jet exit velocity M_J, and as the observer moves upstream (*i.e.* large polar angles), more weight should be given to the jet velocity constituent (b). Regarding the frequency dependent model, the interesting point of using this model is that a very stable and good agreement at small angles (up to 90^o), and in particular for low frequencies can be achieved, but utilizing this model for large angles ($\theta = 140^\circ$) is shown to be inappropriate, as it is not capable of adjusting the peak frequency so as to fit to the experimental data. Finally, it can be understood that neither of the models will perfectly improve the peak frequency location. So, the final inference is that, as mentioned before, the peak frequency mismatch is because of the incapability of the analogy to capture the low frequency noise from close sources.

5.2 Hot Flows

Prediction of radiated noise from a single flow heated jet flow is examined in this section. The same geometry as the previous simulation for the unheated jet is used. The required CFD results for $M_J = 0.60$, $T_J = 450K$ and $M_J = 0.75$, $T_J = 600K$ are found using a Reynolds Averaged Navier Stokes (RANS) scheme with simple modified $k - \varepsilon$ method. The following values are chosen in the modified $k - \varepsilon$ turbulence model: $C_\mu = 0.09$, $C_{\varepsilon 1} = 1.44$ and $C_{\varepsilon 2} = 1.92$. Numerical results of the CFD simulation are presented and discussed in Appendix A.

Once the CFD results are obtained, the source terms can be estimated using the mean flow and turbulence parameters. They will then be used in the MGBK method to find the spectral density function. In all of the predictions of this section the turbulent energy transfer time scale (TET) and the second model of the convection velocity are

used. It must be noted that dipole sources associated with the density gradient are not accounted for in the present prediction. In order to deal with the MGBK method, again we need to find a curve-fit for the mean flow velocity. The curve-fit models presented for the unheated jet flow (equation (5.3)) can also provide an acceptable agreement for hot jet flows. It reads as follows:

$$\begin{aligned} U(x,r) = {} & U_{Jet}H(aD_J - x)H(\frac{aD_J - x}{2} - r) + \\ & U_{Jet}H(aD_J - x)H(\frac{x - aD_J}{2} + r)\,\mathrm{sec}\,h^2(\left[\frac{x - aD_J}{2} + r\right]/c2) + \\ & U(x)|_{r=0}\,H(x - aD_J)\,\mathrm{sec}\,h^2(r/c1) \end{aligned} \tag{5.7}$$

The unknown coefficients of the curve-fit can be found by inspection and matching the relations with the CFD results. The values for the $M_J = 0.60$, $T_J = 450K$ jet are given by,

$$\begin{aligned} c_1 &= 0.0950x - 0.0111 \\ c_2 &= 0.0890x + 0.0012 \\ a &= 7.5 \end{aligned}$$

and for $M_J = 0.75$, $T_J = 600K$ jet following coefficients are found to provide the best fit

$$\begin{aligned} c_1 &= 0.0979x - 0.0101 \\ c_2 &= 0.0890x + 0.0012 \\ a &= 7.5 \end{aligned}$$

Before investigating the density spectral function and directivity figures, it might be useful to know which sources are involved in the radiation of sound into the cone of silence and must be treated in a special way. The region of the sources that are radiating into the cone of silence will be called the "effectively damped area" hereinafter. Figures 5.24, and 5.25 show the location of the turning points of Lilleys equation for different observer angles (by equating equation (2.45) with zero). The following inferences can be deduced. First, the effectively damped area when the observer is located close to the axis ($\theta = 20^o$) becomes larger as the observer distance, R increases (which means for a far observer more sources will be involved and accordingly more sources will suffer

exponential decay). It can also be observed that for larger angles the effectively damped area is not a strong function of the observer distance. Moreover, as it is expected, the damped area shrinks with angle and will entirely fade for angles greater than $\theta = 50^o$. In addition, comparison of the damped area for a hot jet (5.25) and a cold jet, Fig. 5.5, reveals that the damped area for an unheated jet at each angle is larger than its counterpart's. This is due to the further bending of the waves in heated flow because of the density variation. It is also worth mentioning that the edge of cone of silence for a $M_J = 0.75$ unheated jet is $\theta^* = 54^o$, while that for $M_J = 0.75$ hot jet is less than 50^o, which is assigned to the (c_0/c_s) term in equation (2.45), which varies in a hot jet but is approximately unity in an unheated flow.

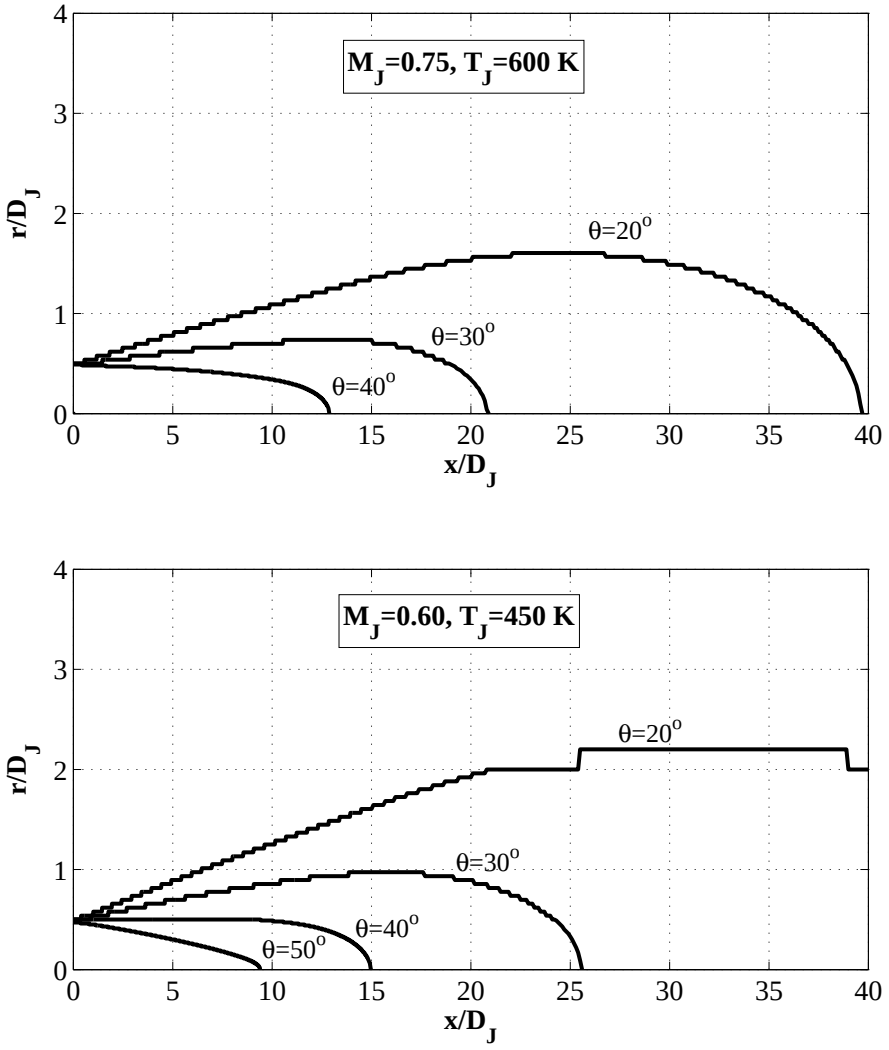

FIGURE 5.24: Turning point location, $R = 50D_J$ $D_J = 0.05m$.

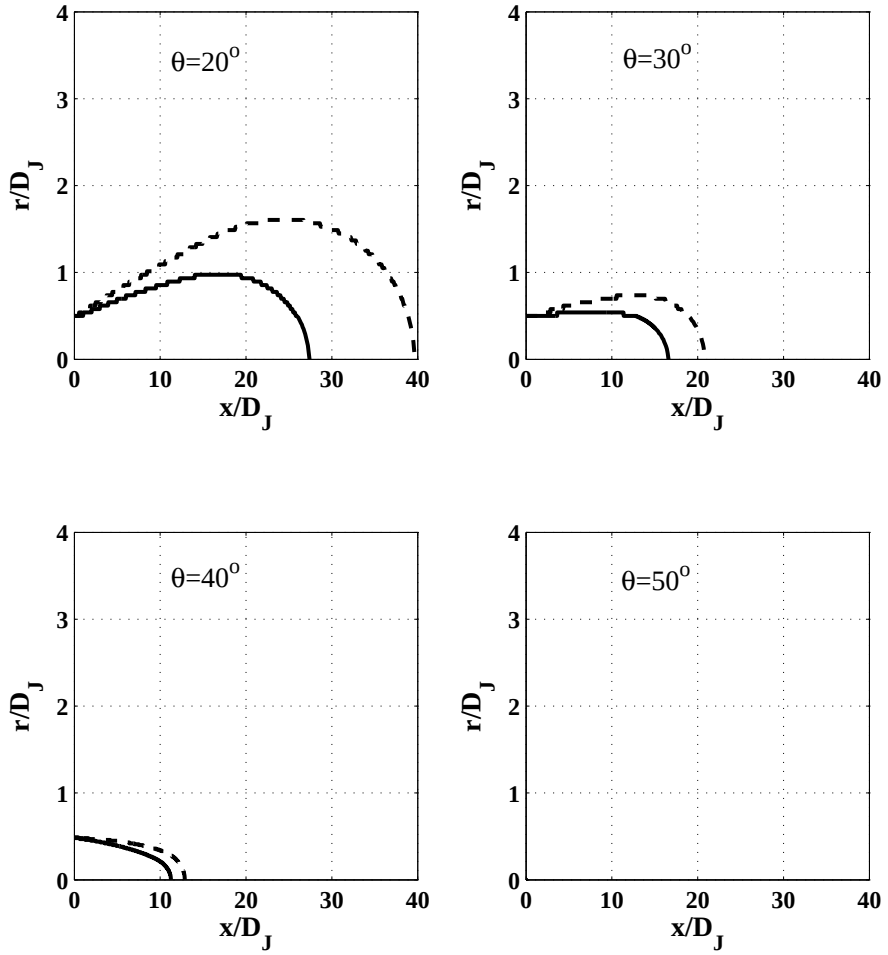

FIGURE 5.25: Turning point location, $M_J = 0.75$, $T_J/T_0 = 2.0$, $D_J = 0.05m$.

Figures 5.27 through 5.28 show comparison of the predicted and measured spectra at different observer angles for different flow and temperature conditions. Results show a very good agreement for most of the angles, except for $\theta = 30^o$ and 40^o at $R = 30D_J$. It was mentioned before by other authors that at high frequencies the prediction at small angles usually shows a larger exponential decay than the measurements (*e.g.* see Figure 6 in [52]). In contrast, it can be seen from the figures 5.27 through 5.28 that both the prediction and the data experience the same exponential decay. This enhancement is believed to be because of using the TET time scale, which has a clear effect on the high frequency noise level. As previously observed, there are some mismatches between the peak frequencies of the predicted results and the data. As explained before, it is believed that these are to a great extent due to the failure of the retarded-time assumption. In other words, the acoustic far-field assumption, which was used for the derivation of the

Acoustic Analogy, is not properly satisfied. This can readily be perceived by comparison of the predictions at $30D_J$ and $50D_J$ (figures 5.17 and 5.18) that the most important contributors to the far-field noise at small angles are the large eddies located $10D_J$ to $15D_J$ downstream of the jet, so the distance between the observer and the contributing sources is sometimes even less than $15D_J$, which is not sufficiently large to be considered far-field.

Comparison of the hot jet results and the unheated jet flow results is interesting and some of help for understanding of noise production mechanism. Comparisons firstly reveal that agreement between the prediction and data becomes poorer with increasing jet temperature T_J. This may have its roots in the differences of noise production mechanisms in each flow. Basically, the MGBK method which is used for our prediction has just accounted for the turbulence-turbulence quadruple and turbulence-mean flow dipole sources which are the most important sources in an unheated flow. However, in a hot flow some other sources may also appear that are due to the variation of the density inside the jet flow. The density associated sources can be modeled as monopole or dipole sources [5]. The contribution of those sources has not been taken into account in this analysis and its consideration needs further investigation.

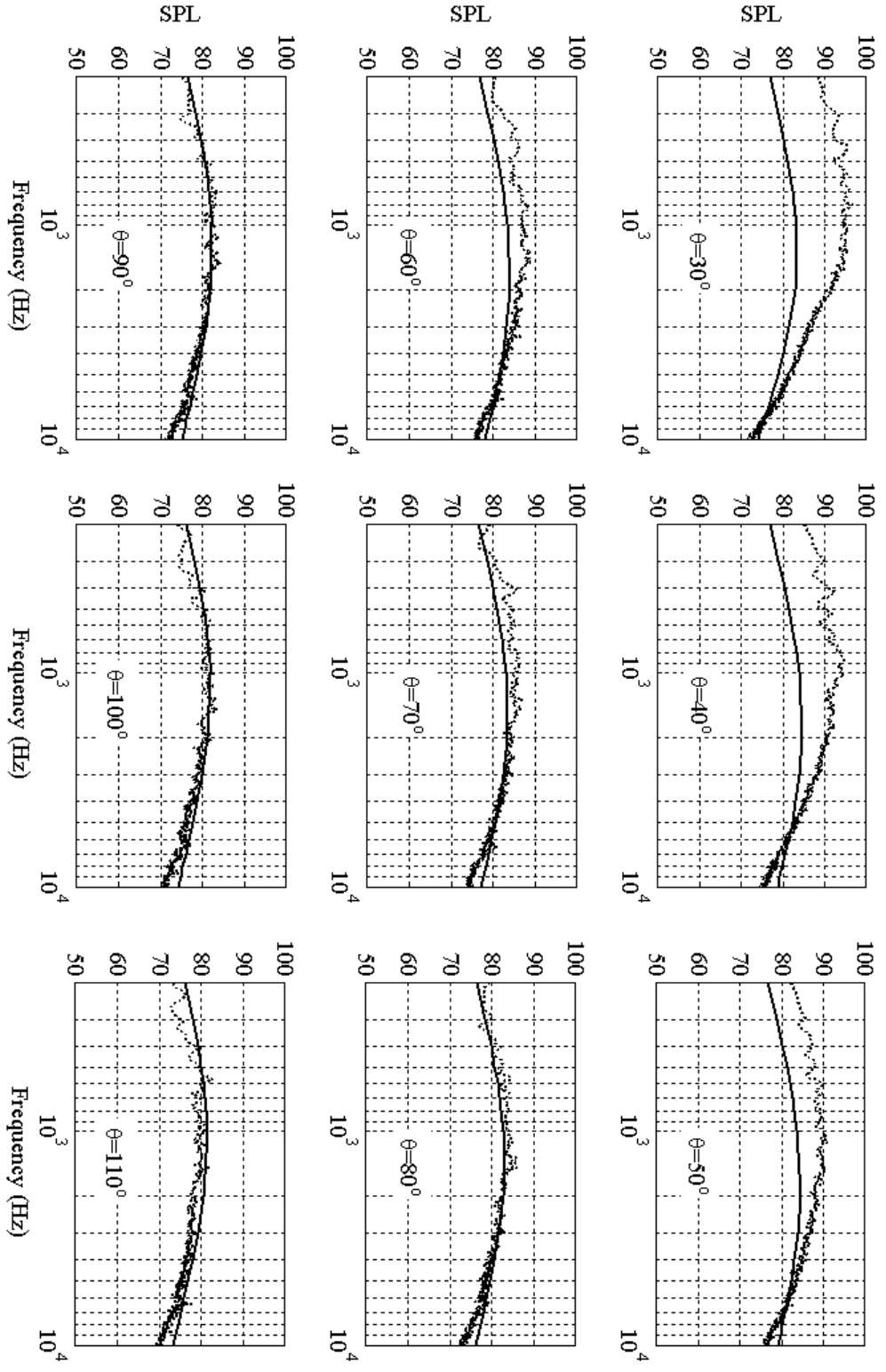

FIGURE 5.26: Comparison of experimental data with predicted spectral density at different angles to jet axis using energy transfer rate time scale; based on the MGBK formulations for directivity, $R = 30D_J$, $M_J = 0.60$, $T_J/T_0 = 2.0$, $D_J = 0.05m$.

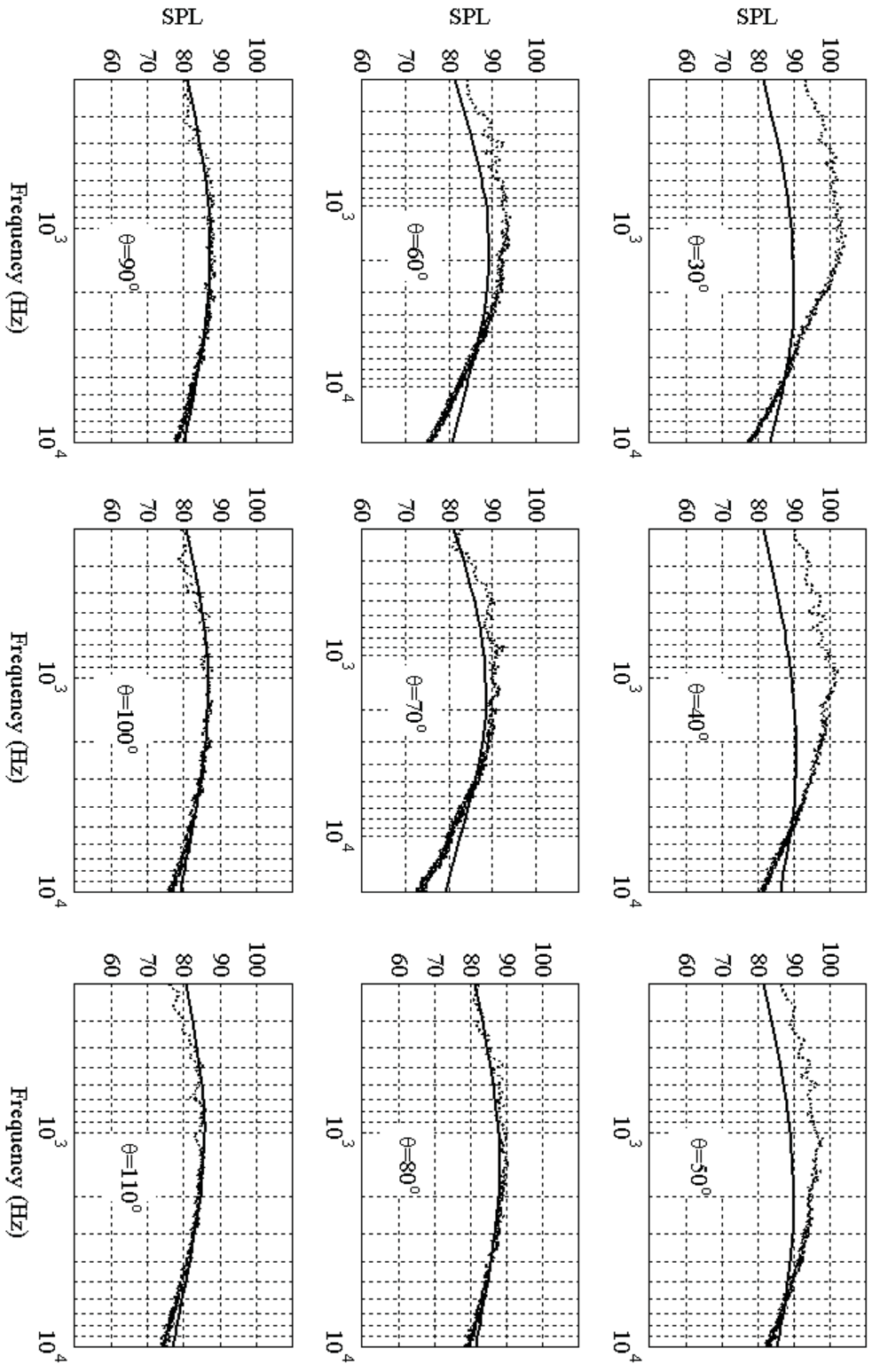

FIGURE 5.27: Comparison of experimental data with predicted spectral density at different angles to jet axis using energy transfer rate time scale; based on the MGBK formulations for directivity, $R = 30D_J$, $M_J = 0.75$, $T_J/T_0 = 2.0$, $D_J = 0.05m$.

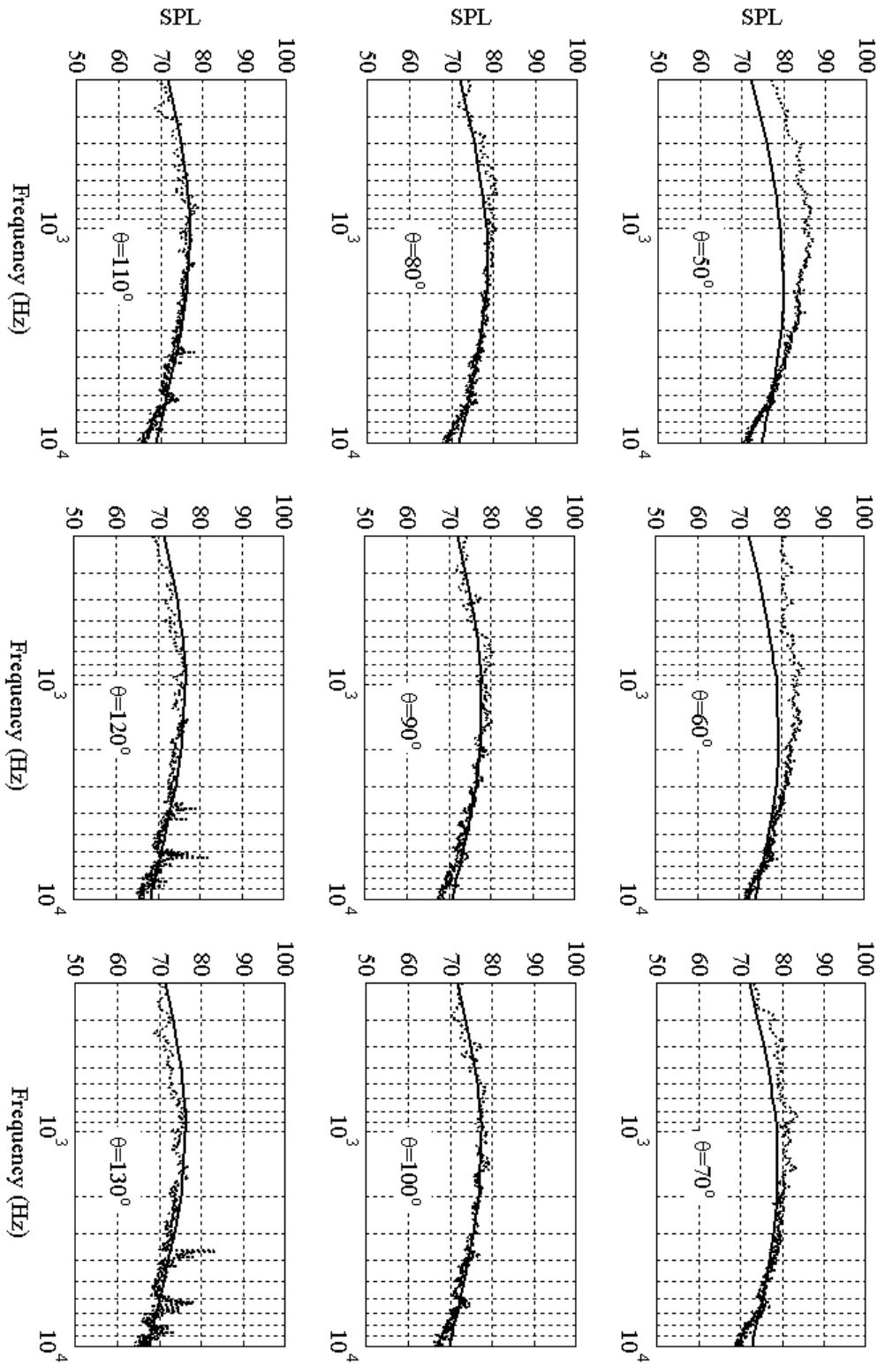

FIGURE 5.28: Comparison of experimental data with predicted spectral density at different angles to jet axis using energy transfer rate time scale; based on the MGBK formulations for directivity, $R = 50D_J$, $M_J = 0.60$, $T_J/T_0 = 1.5$, $D_J = 0.05m$.

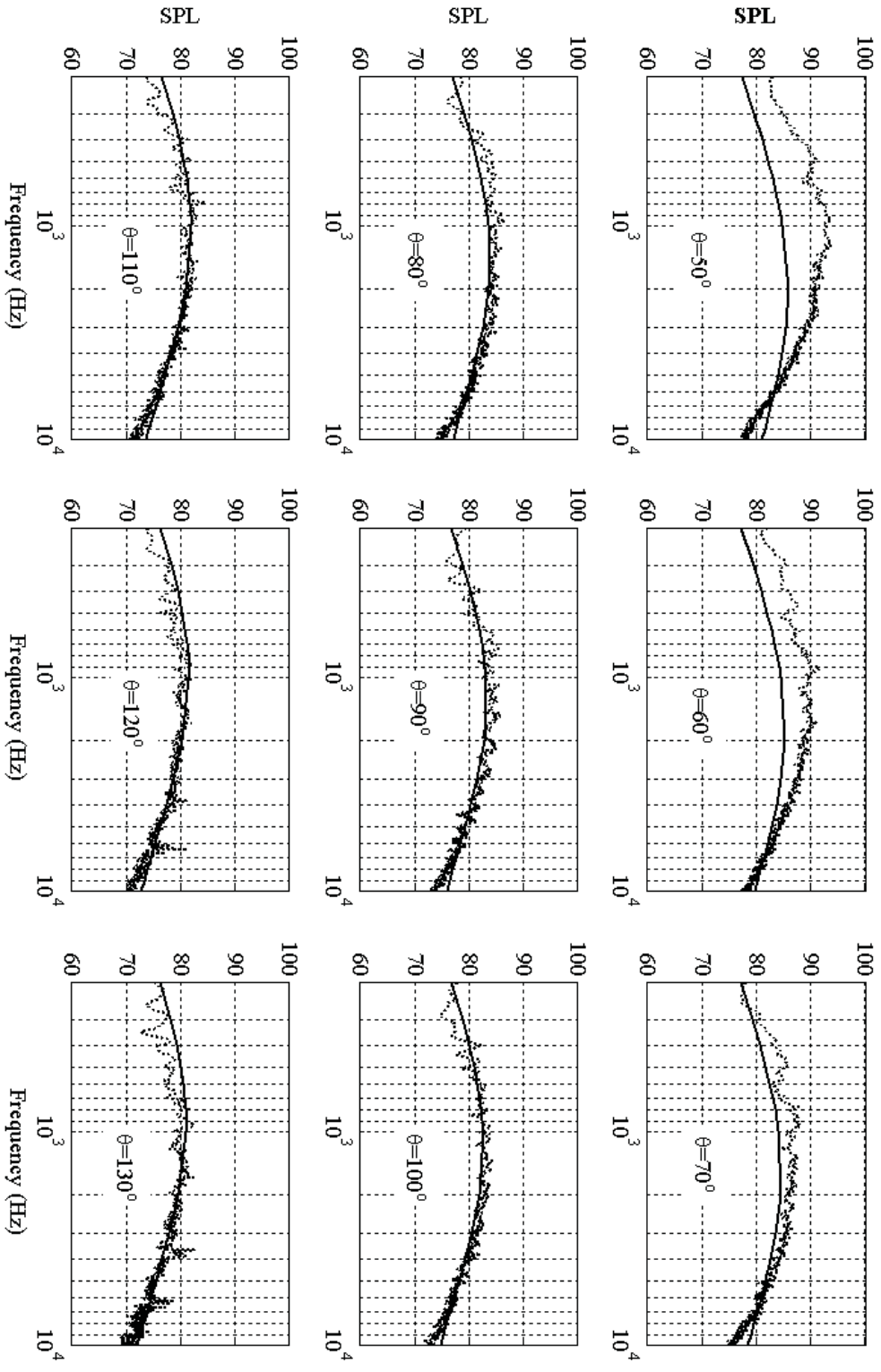

FIGURE 5.29: Comparison of experimental data with predicted spectral density at different angles to jet axis using energy transfer rate time scale; based on the MGBK formulations for directivity, $R = 50D_J$, $M_J = 0.75$, $T_J/T_0 = 2.0$, $D_J = 0.05m$.

Chapter 6

Numerical Results: Dual-Stream Jets

Numerical quantities focus on expected values, graphical summaries on unexpected values.

"John Tukey", (1915-2000)

Introduction

Nowadays commercial jet engines invariably use dual-stream nozzles. These nozzle configurations vary in design complexity depending on the application they are used for, and consist of two exits for flow (bypass jet engines), *i.e.* the primary and secondary nozzles. The primary and the secondary nozzle can have their exits on the same plane, which is called a coplanar jet, or the secondary nozzle can be recessed back relative to the primary nozzle. A popular nozzle design often includes an external plug for the primary nozzle (short-cowl). Furthermore, the nozzle edge can be either smooth or serrated (this being one of the most attractive developments to aid noise reduction). Although the dual-stream nozzle has indisputable aerodynamic advantageous, in turn, they also have significant impact on the intensity and spectral distribution of the noise radiated by the jet. In the context of this section, noise radiation from coplanar and short-cowl nozzles working at different bypass velocity ratios (VR=1, 0.9, and 0.63) will be studied. Jet

noise directivity and the effects of the new time scale will also be addressed. Predictions of the locations of the noise sources inside the jet flow will also be considered.

Comparisons are made with experimental data collected from the CoJeN (Computation of Coaxial Jet Noise) project experiment, which also tackled the CFD and noise radiation prediction of various types of coaxial nozzles at different working velocities and temperatures. The experiments were conducted by many European universities including the ISVR from the University of Southampton .

6.1 Coplanar Jet

In this section, noise radiation from an unheated coplanar jet at three velocity ratios, velocity ratios (VR) 1.0, 0.9, and 0.63 is considered. In the first case flow comes out from the primary and secondary nozzles at $V_p = V_s = 217.2m/s$, and in the second case, $V_p = 240.9m/s$ and $V_s = 217.2m/s$. The diameter of the primary nozzle is $99.5mm$ and the secondary is $200mm$ (figure 6.1). In the third case area ratio is AR=4 ($D_p = 33mm$, $D_s = 75mm$), and the primary and secondary jet velocities are $266.8m/s$, and $168.3m/s$ respectively. The mean flow calculation is performed using Reynolds Averaged Navier Stokes (RANS) and a simple modified $k - \varepsilon$ turbulence model. Further information about the CFD model, computational grid, and domain, and corresponding results can be found in Appendix A.4.3. The MGBK method along with the TET and TDR time

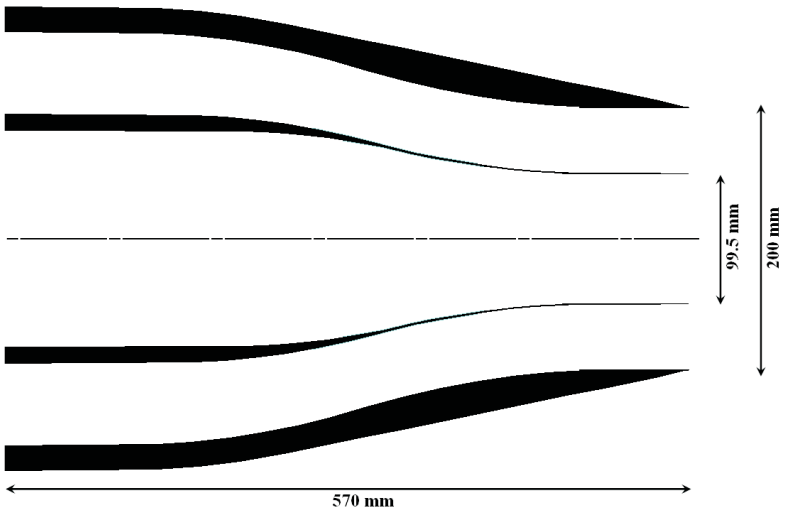

FIGURE 6.1: Coplanar nozzle geometry

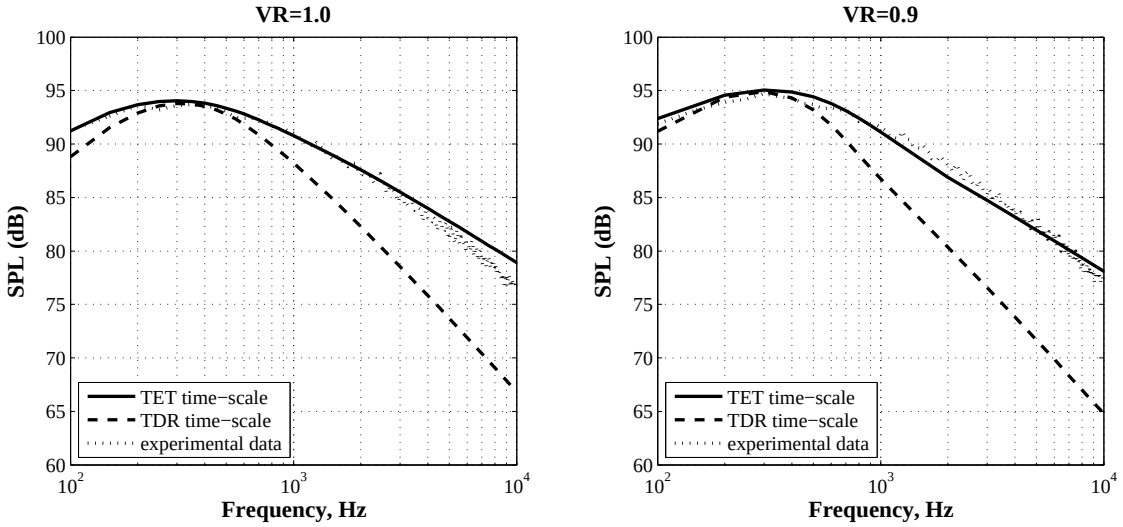

FIGURE 6.2: Noise prediction at 90^o, $R = 65.4D_s$ from a coplanar jet working at VR=1.0, and VR=0.9 using TET and TDR time scales

scales are used for noise prediction at ninety degrees, while the second form of the convection velocity (equation (4.17)), and the dissipation length scale (equation (4.1)) are used for these predictions. Directivity effects will also be studied using Balsa's high frequency solution to Lilley's equation [54], equation (2.49).

Study of noise prediction at ninety degrees is of much theoretical importance, and can help us in understanding the correctness of the mentioned methods. Since for prediction of noise at 90 degrees there is no need to consider the convection and refraction effects, more care can be given to other parameters such as the time scale. The effect of using the TET time scale on the predicted spectrum can be seen in figure 6.2. Predictions are made for the case one ($VR = 1$) and case two ($VR = 0.9$). As before, it can be readily observed that use of the traditional time scale leads to an underestimation at low and high frequencies, while the new time scale has the merit of improving both sides of the spectrum. Furthermore, one may deduce from the similarity of the two spectrums ($VR = 1$, and $VR = 0.9$) that most of contributing sources are those located between the secondary potential core and the outer shear layer. In other words, sound sources located between the primary and secondary potential cores are not of importance.

Jet noise prediction at other angles is also considered here. Microphones are positioned relatively far from the turbulent medium at different angles to the jet axis, as laid out in table 6.1.

TABLE 6.1: Microphone position around the coplanar jet

θ	40	50	60	70	80	90	100	110	120
$R(m)$	11.69	11.74	12.27	12.39	12.64	13.08	13.10	13.21	13.71

To use the MGBK method this requires finding the regions of the jet where sources suffer exponential decay because of radiation into the cone of silence. The turning point locations, equation (2.45), define such a region for each emission angle, see figure 6.3. It can be seen from figure 6.3 that the domain of the sources involved (damped area) decreases with angle and disappears after 50 degrees, which means the critical angle (θ^*) for both of the cases ($VR = 1$, and 0.9) is slightly higher than 50 degrees. It also shows that the damped area increases as the primary velocity V_p increases. According to what was mentioned before in section 2.2, sources inside the damped area will suffer an exponential decay, which is taken into account in our noise prediction using equation (2.50).

As mentioned previously in order to deal with the MGBK method one needs to provide a mathematical formulation for the flow velocity inside the shear layer. The following equation has been used here and an acceptable agreement is obtained,

$$\begin{aligned} U(x,r) = {} & U_p\, H(a-x)H(\tfrac{D_s}{2a}(a-x)-r) \\ & +U_{axis}(x)\; H(a-x)H(\tfrac{D_s}{2a}(a+x)-r)H(r-\tfrac{D_s}{2a}(a-x)) \\ & +U_s\, H(a-x)H(r-\tfrac{D_s}{2a}(a+x))H(\tfrac{D_s}{2a}(a-x)-r) \\ & +U_s H(a-x)H(r-\tfrac{D_s}{2a}(a-x))sech^2\left(\left(r-\tfrac{D_s}{2a}(a-x)\right)/c_2\right) \\ & +U_{axis}(x)\; H(x-a)H(r-\tfrac{D_s}{2a}(a-x))sech^2\left(r/c_1\right) \end{aligned}$$

where $H()$ denotes the Heaviside function, $sech()$ is Hyperbolic secant, and U_{axis} is the flow speed on the jet axis, which can be readily found from CFD results. Other coefficients can be obtained after changing them and comparing with available CFD results. The following are found

$$\begin{aligned} a &= 7.5D_s \\ c_1 &= -0.0101 + 0.0980x \\ c_1 &= 0.00123 + 0.8907x \end{aligned}$$

Using the velocity curve-fit expression, radial derivative of the flow velocity can be readily obtained, as

$$\frac{d}{dr}U(x,r) = -U_s H(a-x)H(r-\tfrac{D_s}{2a}(a-x))tanh\left(\left(r-\tfrac{D_s}{2a}(a-x)\right)/c_2\right)sech^2\left(\left(r-\tfrac{D_s}{2a}(a-x)\right)/c_2\right)$$
$$-U_{axis}(x)\ H(x-a)H(r-\tfrac{D_s}{2a}(a-x))tanh\left(\left(r-\tfrac{D_s}{2a}(a-x)\right)/c_2\right)sech^2\left(\left(r-\tfrac{D_s}{2a}(a-x)\right)/c_2\right)$$

Results are shown in figure 6.4, and 6.5 where the predicted acoustic spectrums are shown for emission angles between 40^o and 120^o; and are compared with measurements. The MGBK method along with Balsa's high frequency asymptotical solution for the refraction effect are used for this predictions. It can be seen that results show an acceptable level of agreement over all observer angles between 40^o to 120^o degrees to the downstream axis. Although there are some discrepancies of the noise at high frequencies for small angles these results are still better than those obtained using the dissipation rate time scale (TDR). Mismatches between the peak frequency of the prediction and experimental data at small and large angles are again interpreted as being due to the failure of the solution to meet the retarded-time condition, as the distance between the effective source region and the observer is relatively small and cannot be considered as being within the acoustic far field. However, the distances used for the CoJeN project are relatively larger than those that were used in the JEAN project and it is noted that the current results show a relatively smaller mismatch than those found for the single-stream jet flow. The other interesting issue is the similarity of VR1.0 and VR0.9 experimental and prediction results. Knowing that the secondary velocity has been kept fixed, this suggests that varying the primary velocity does not have a significant effect on the noise reduction. From an acoustical point of view, this means that the sources embedded between the primary and the secondary potential cores are considerably shielded by the secondary potential core and only the noise sources between the secondary potential core and the outer shear layer are responsible for noise radiation. Further comparison is provided for a VR=0.63, AR=4 coplanar jet (from JEAN database), figure 6.6. As it can be seen results are in good agreement with the measured data except for 40 and 50 degrees, where as mentioned before is because of not properly taking account of the refraction effect.

For further noise reduction, deeper understanding of the physics of noise production is necessary and studying the location of the noise sources can improve our understanding

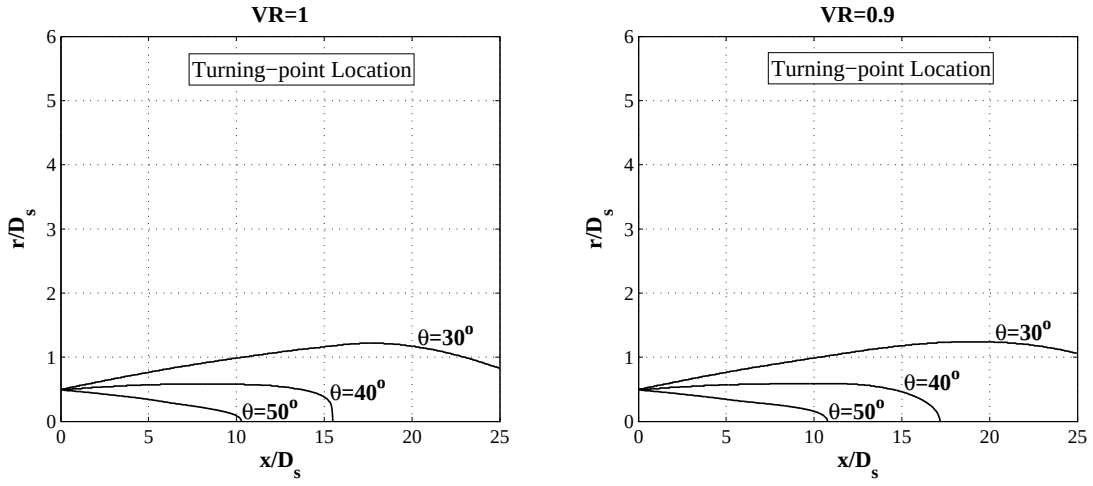

FIGURE 6.3: Turning point location for a dual-stream jet flow; Left figure: velocity ratio 1.0; Right figure: velocity ratio 0.9, using equation (2.45)

of noise production and radiation mechanisms. As mentioned before, in section 5.1.3, the source location, $I_x(R,\omega)$, can be found through the following relation

$$I(R,\,\omega) = \int I_x(R,\omega)\,dx$$

where I_x for an observer located at ninety degrees can be found from,

$$I_x(\omega) \propto \int_{-\infty}^{\infty}\int_{\phi=0}^{2\pi}\int_{r=0}^{r_\infty} L_1L_2L_3\tau v^4 e^{-\left(\frac{\omega L_1}{2c_0}\right)^2-\left(\frac{\omega\tau}{2}\right)^2} e^{-j\omega\tau}drd\phi d\tau$$

Figures 6.7 and 6.8 show the axial locations of peaks of I_x at each frequency when the observer is positioned at $R = 65.4D_S$, and $\theta = 90^o$. Experimental results are obtained from the CoJeN project using a polar array technique. The effects of using two time scales, *i.e.* turbulent dissipation rate (TDR), and turbulent energy transfer rate (TET), are investigated here. The left hand side contour shows the results obtained from experiment, and the right hand side figure shows the comparisons between prediction and data.

Comparisons show that using the TDR time scale gives rise to incorrect estimation of source location particularly at low frequencies, while results found using the TET time scale provides better agreement with the experimental data from 200Hz to 10000Hz. Furthermore, it can be seen that results of the VR1.0 and VR0.9 are very similar. As

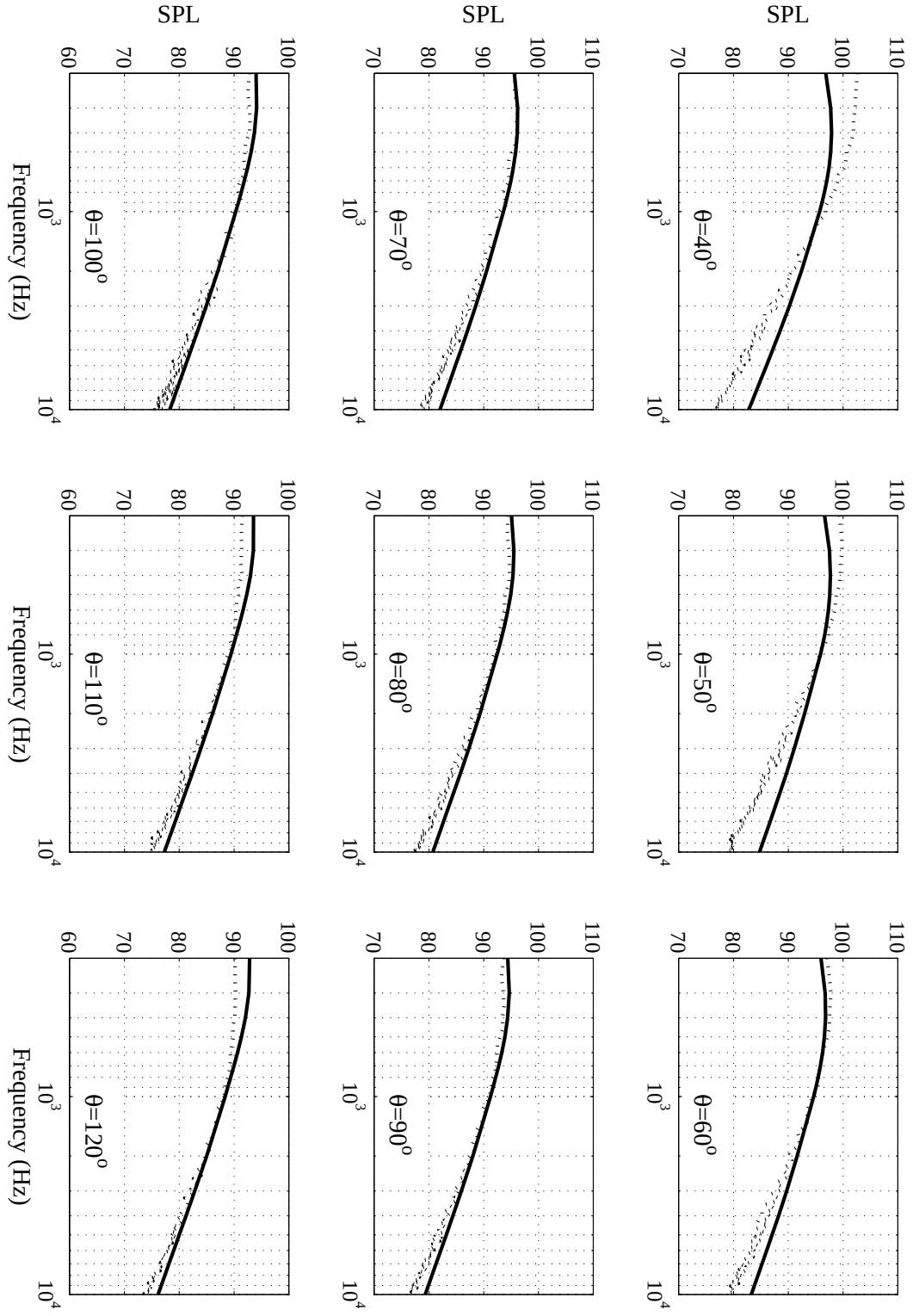

FIGURE 6.4: Comparison of experimental data with predicted spectral density for a coplanar jet at different angles to jet axis using energy transfer rate time scale; based on the MGBK formulations for directivity; VR=1.0

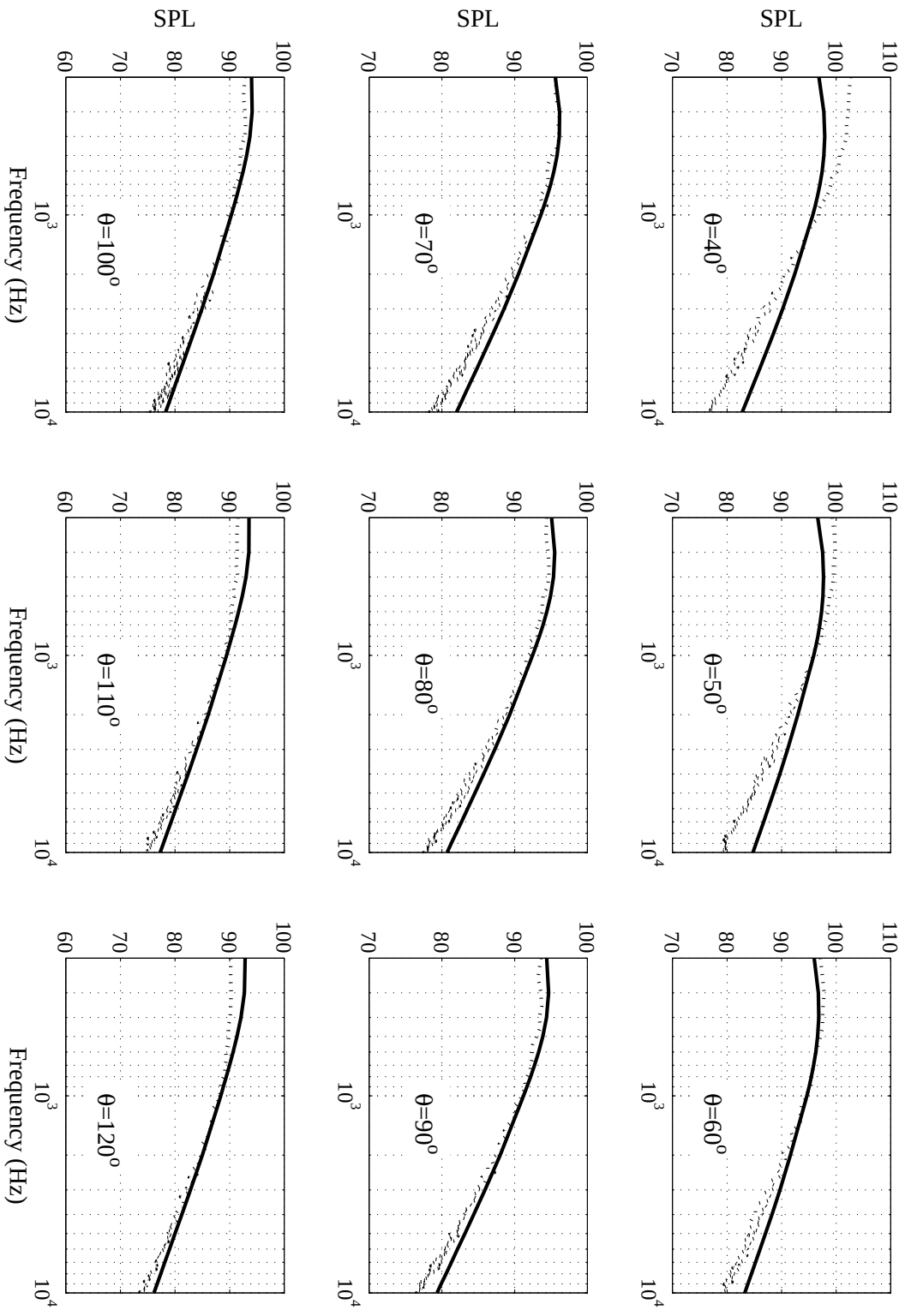

FIGURE 6.5: Comparison of experimental data with predicted spectral density for a coplanar jet at different angles to jet axis using energy transfer rate time scale; based on the MGBK formulations for directivity; VR=0.90

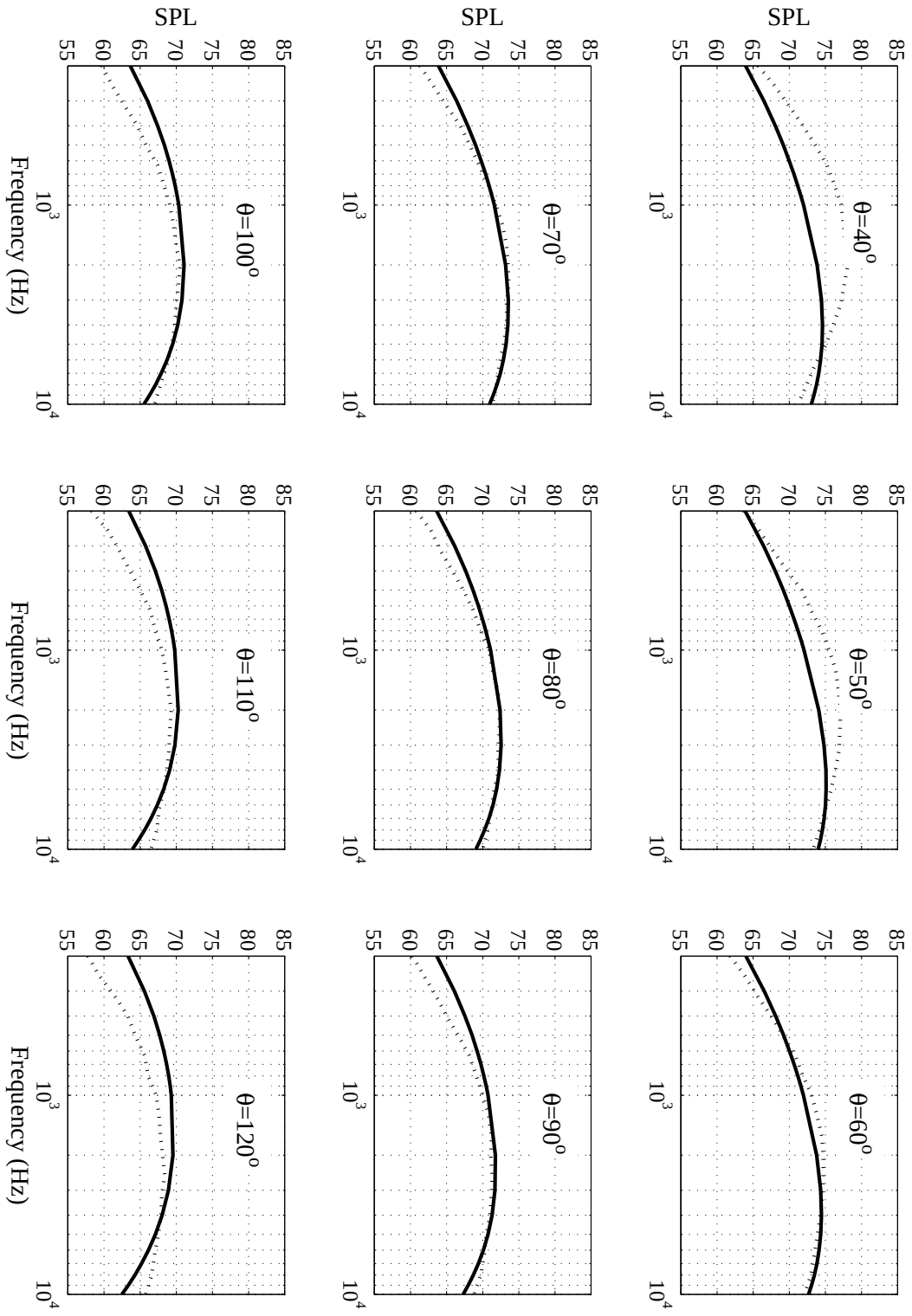

FIGURE 6.6: Comparison of experimental data with predicted spectral density for a coplanar jet at different angles to jet axis using energy transfer rate time scale; based on the MGBK formulations for directivity; VR=0.63, $R_r = 12m$

mentioned above, the interpretation is that increasing the primary flow velocity does not notably change the results (either noise level or source location), because the secondary potential cone is large enough to shield the associated sources.

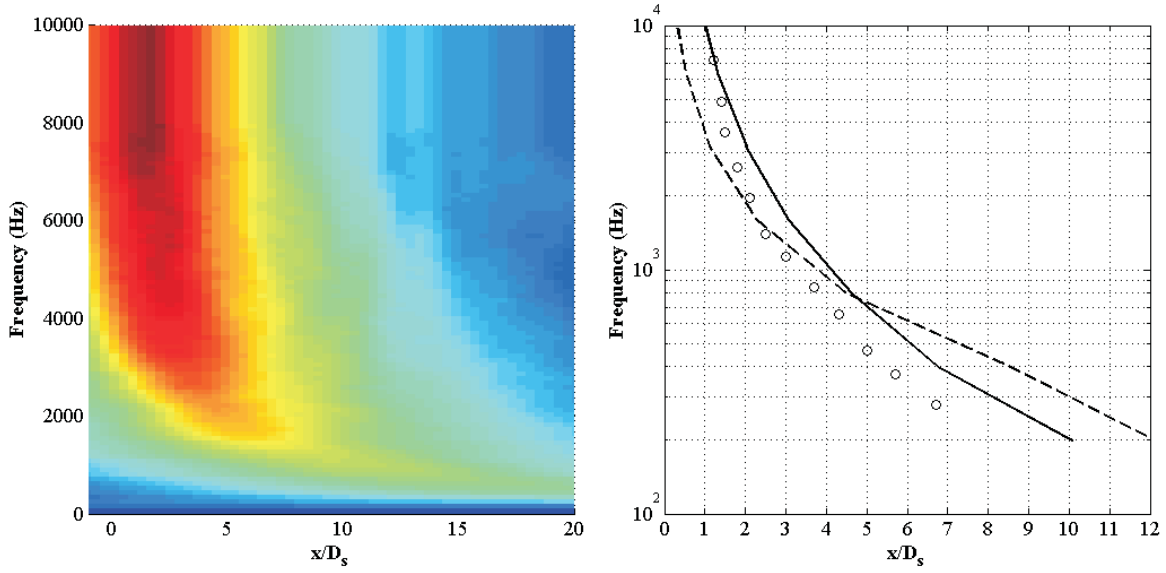

FIGURE 6.7: Source Location, VR=1.0; Left figure: Experimental results; Right figure: (o): data, (- -): TDR time scale, (-): TET time scale

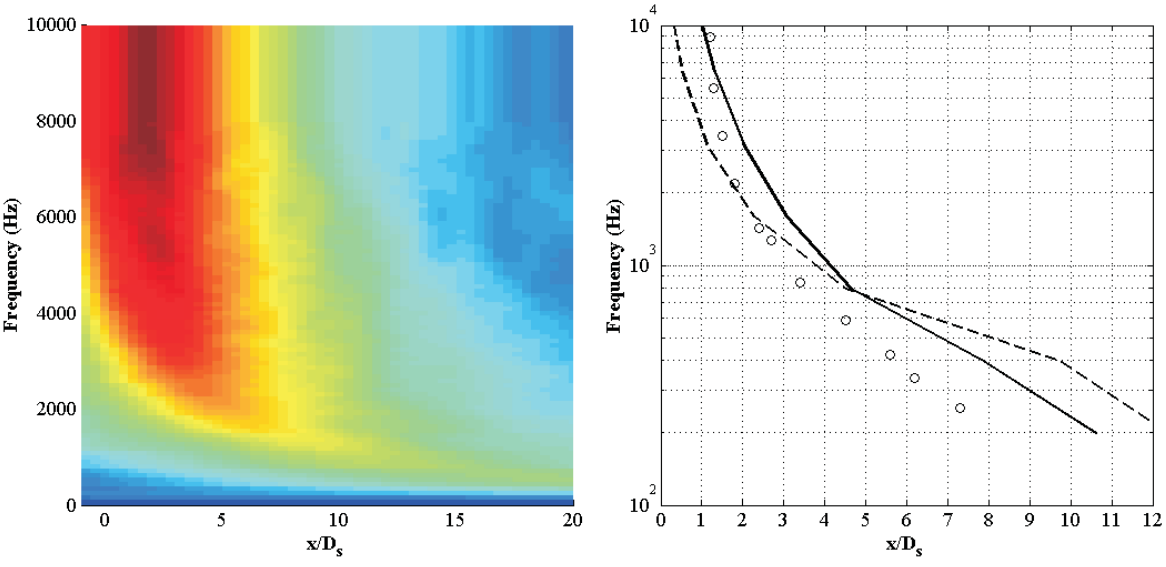

FIGURE 6.8: Source Location, VR=0.9; Left figure: Experimental results; Right figure: (o): data, (- -): TDR time scale, (-): TET time scale

6.2 Short-Cowl Nozzle

The most realistic and practical jet configuration considered in this thesis is the short-cowl nozzle. The nozzle consists of two flow exits and a plug which is installed in the primary nozzle. The basic idea behind use of the plug in this kind of nozzle is to lessen the shock noise and its effects for supersonic applications. The geometry and size of the nozzle used in this section is depicted in figure 6.9. In a similar fashion, the required mean and turbulent values of fluid dynamics are obtained by using a modified $k-\varepsilon$ method. Results are collected and discussed in Appendix A.4.4.

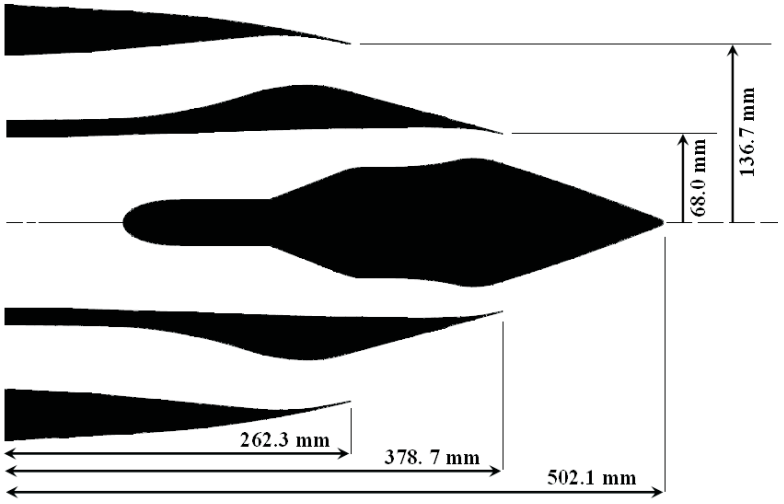

FIGURE 6.9: Short-cowl nozzle geometry

In a similar way as before, we first examine the TET and the TDR time scales by comparing results obtained using them for an observer located at $R = 13.8m$, and 90^o. Two velocity ratios (VR) 1.0 and 0.9 are considered in this section. In the first case, flow comes out from the primary and secondary nozzles at $V_p = V_s = 217.2m/s$, and in the second case, $V_p = 240.9m/s$ and $V_s = 217.2m/s$. Noise prediction is performed using the MGBK method, while the frequency dependent convection velocity, equation (4.17), and dissipation length scales, equation (4.1), are used, see figure 6.10. Comparisons once more show that the TET time scale is superior to its counterpart (*i.e.* TDR time scale). It should be noted that because of the complexity of the geometry it is difficult to account for all of the sources aggregated close to the outer lip. This results in a secondary roll off in the spectrum which occurs beyond $f = 8kHz$, figure 6.10.

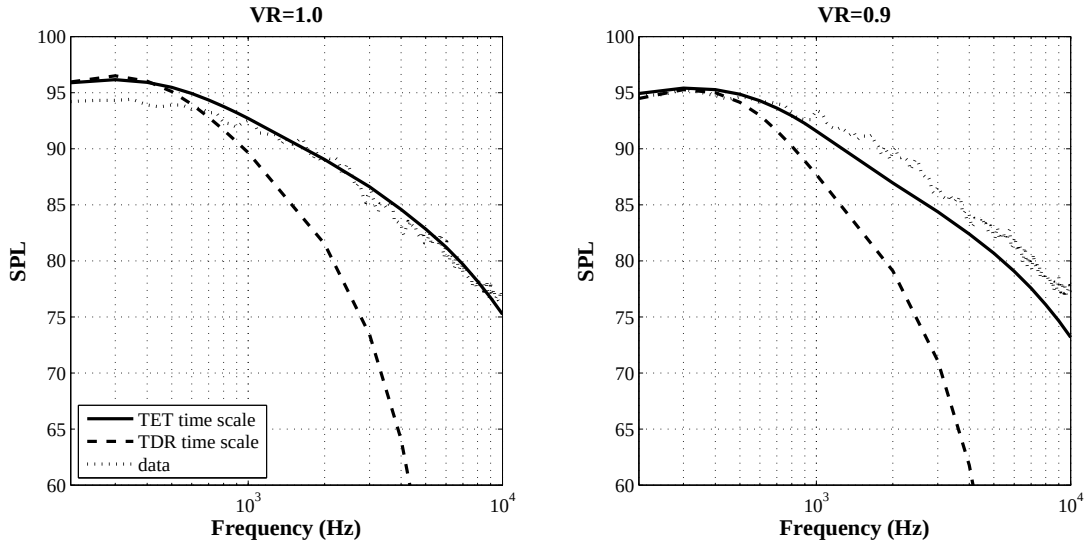

FIGURE 6.10: Noise prediction at 90^o for a short-cowl nozzle at two different bi-pass ratios, VR=1.0, and 0.9

Before exploring the directivity effect turning point locations need to be addressed. Turning point locations can be found by equating equation (2.45) to zero. Figure 6.11 shows the regions where the sources radiating to the observer inside the cone of silence $\theta < \theta^*$ will be treated in a different way. According to the theory of jet noise refraction, this special treatment gives rise to an exponential decay and therefore less high frequency sound radiation to the observer. Comparing results of the short-cowl nozzle with those of a coplanar nozzle, figure 6.3, one can readily deduce that the geometry used for the short-cowl nozzle does not have any significant effect on the size and shape of the effectively damped area. Finding a velocity curve-fit for the flow from a short-cowl nozzle is more difficult than other flows because of the presence of the nozzle after-body. However, a curve-fit similar to the model used for coplanar nozzles, with some simplifications, is used here:

$$
\begin{aligned}
U(x,r) = {} & U_p\, H(a-x)H(\tfrac{D_s}{2a}(a-1.5x)-r)+ \\
& U_p H(a-x)H(r-\tfrac{D_s}{2a}(a-1.5x))sech^2\left(\left(r-\tfrac{D_s}{2a}(a-1.5x)\right)/c_2\right)+ \\
& U_{axis}(x)\; H(-a+x)H(r-\tfrac{D_s}{2a}(a-1.5x))sech^2\left(r/c_1\right)
\end{aligned}
$$

where

$$a = 7.0D_s$$
$$c_1 = -0.0101 + 0.0980x$$
$$c_1 = 0.00123 + 0.8907x$$

Noise radiation to observers at different angles from 40^o to 120^o from jet axis for two different bypass ratios are illustrated in figures 6.12, 6.13. Distance of the observer from the jet exit is the same as those given in Table 6.1. Curves show good agreement with data for most of the angles, except those inside the cone of silence or upstream of the jet exit. Furthermore, as mentioned above, the second roll off which can be observed at high frequencies is because of not taking account of the high frequency sources near the outer shear layer. The mismatches between the peak frequencies are, once again, believed to be due the failure of the assumption made for retarded-time in the solution of the Lighthill equation. However, comparison of results in 6.12, and 6.13 for small angles with those made for single-stream jet, such as figure 5.7, reveals that the mismatch in the current results is smaller. This is not surprising since the present predictions are made at a distance relatively larger than the distance used in the single flow jet test.

Finally, source location is considered. Equation (5.3) along with the TET and TDR

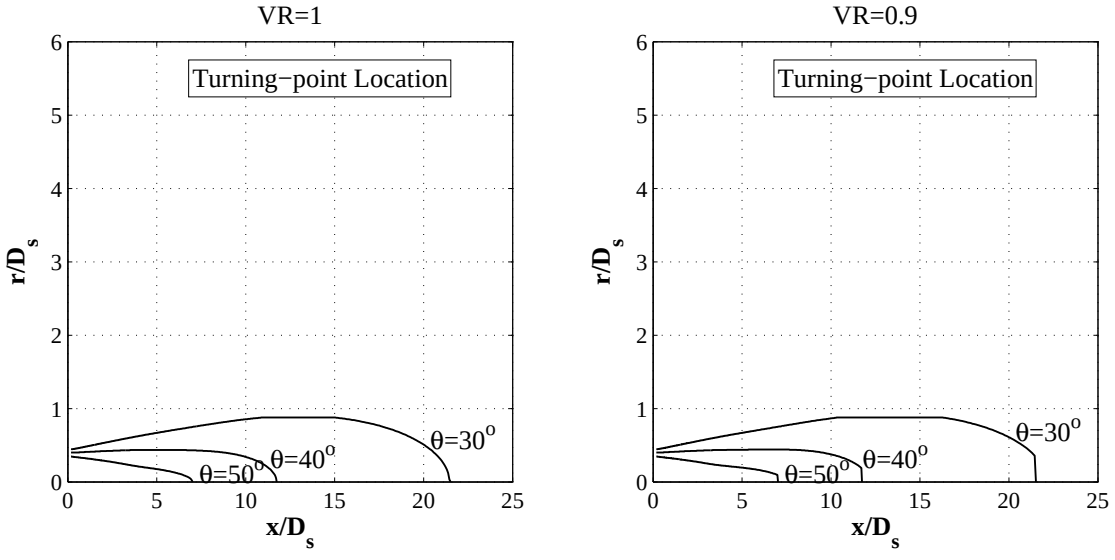

FIGURE 6.11: Turning point location for a short-cowl jet flow at by-pass ratios 1.0 and 0.9; $D_s = 0.2734m$; using equation (2.45)

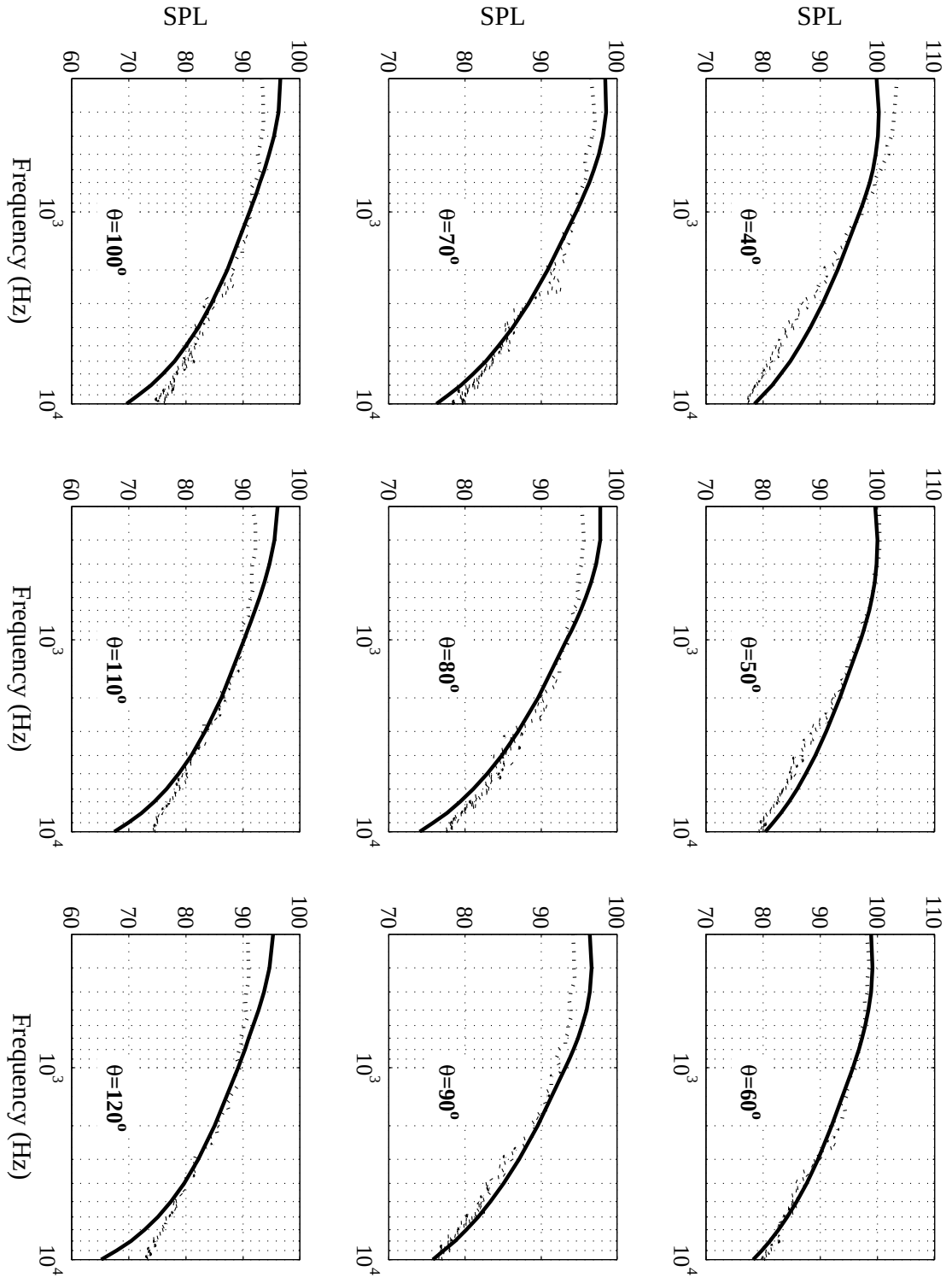

FIGURE 6.12: Comparison of experimental data with predicted spectral density for a short-cowl nozzle at different angles to jet axis using energy transfer rate time scale; based on the MGBK formulations for directivity; VR=1.0

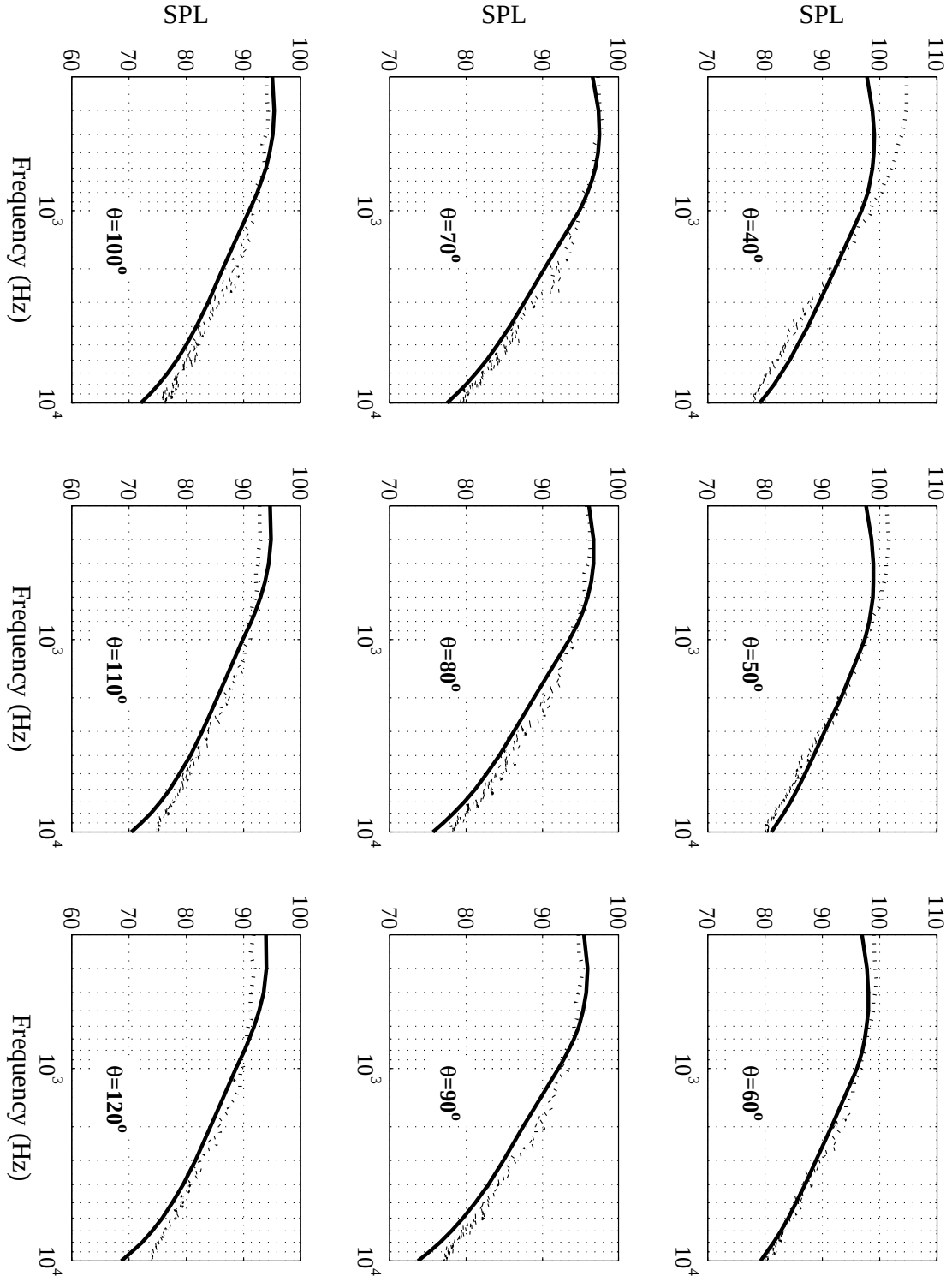

FIGURE 6.13: Comparison of experimental data with predicted spectral density for a short-cowl nozzle at different angles to jet axis using energy transfer rate time scale; based on the MGBK formulations for directivity; VR=0.9

time scale are used for this purpose. Calculations are performed for two working conditions, VR=1.0 and 0.9, as shown in figures 6.14, and 6.15. Results reveal that the agreement obtained using the TET time scale is again much better that using the TDR time scale, particularly at low frequencies. Furthermore, comparison of figures 6.14 and 6.15 with those obtained for coplanar nozzle (figures 6.7 and 6.8), together with the directivity results, shows that changing the primary flow velocity has a more notable effect on the results for the short cowl nozzle than the coplanar one. This is because the secondary flow in a short cowl nozzle starts upstream of the primary flow. In other words, the secondary potential core will not cover all of the sources located between the primary and secondary potential cores, so some of those may contribute to the noise radiation mechanism.

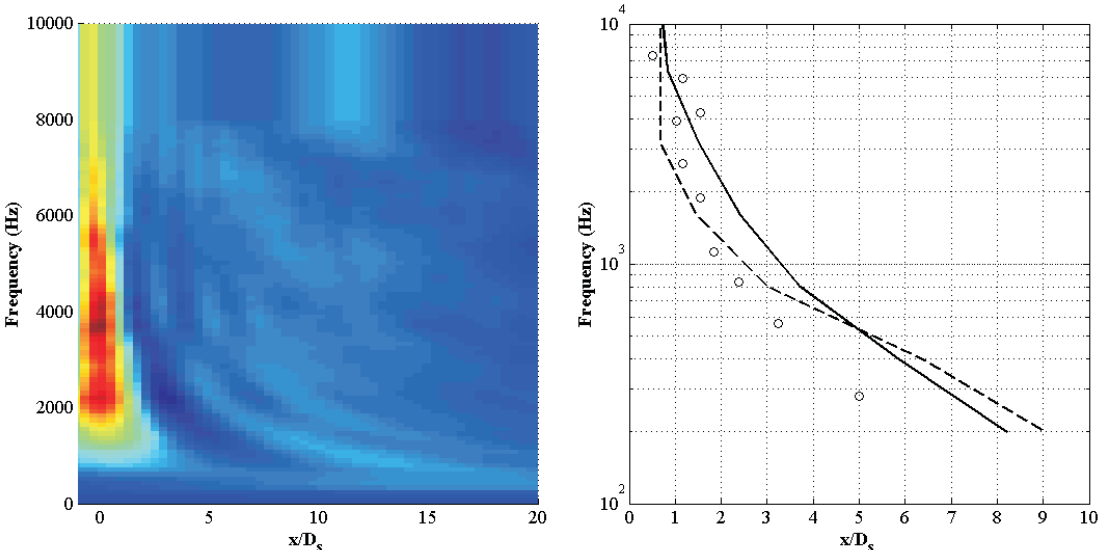

FIGURE 6.14: Source Location, VR=1.0; Left figure: Experimental results; Right figure: (o): data, (- -): TDR time scale, (-): TET time scale

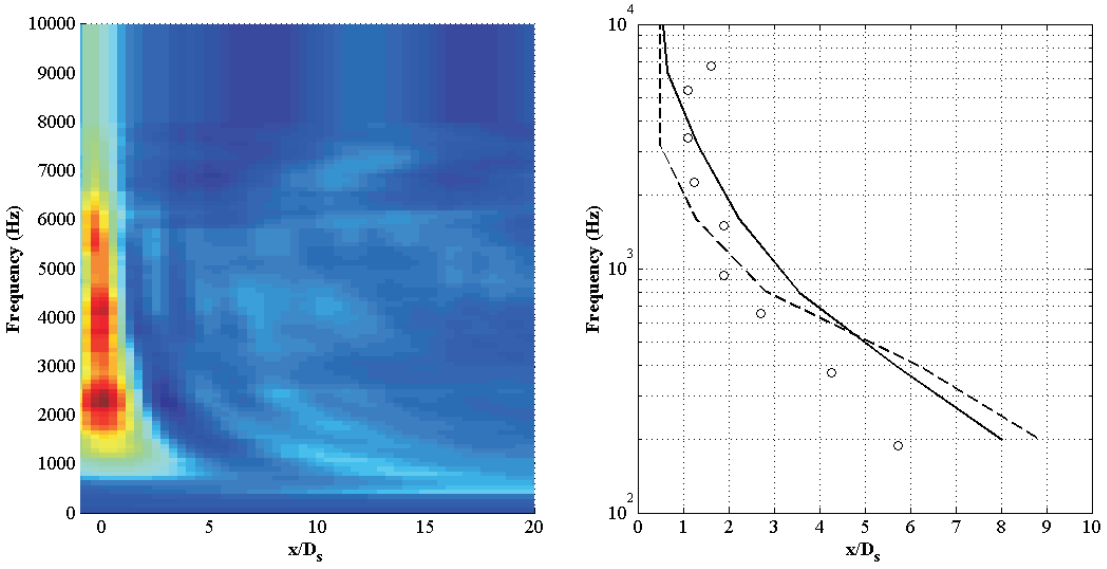

FIGURE 6.15: Source Location, VR=0.9; Left figure: Experimental results; Right figure: (o): data, (- -): TDR time scale, (-): TET time scale

Chapter 7

Conclusion and Recommendations

Please be good enough to put your conclusions and recommendations on one sheet of paper in the very beginning of your report, so I can even consider reading it.

"Winston Churchill", (1874-1965)

7.1 Conclusions

The goal of the current research project is to advance the development of statistical CFD-based jet noise prediction methodologies. This involves first determining the turbulent properties in the jet plume using a RANS CFD model and then supplying those properties to the noise prediction method which is based on Lighthill's Acoustic Analogy or an equivalent model, such as the MGBK method. A derivation was given for Lighthill's Acoustic Analogy and the MGBK method. The sound and mean flow interaction effect is taken into account using Lilley's refraction formulation. Numerical results and discussions are given for the exact numerical solution of Lilley's equation at different Mach numbers and observer angles. In addition, the low and high frequency asymptotic behaviour of the solution is also studied.

As part of the current research effort CFD analysis of jet flows from various nozzles at different working conditions have been modelled. The turbulent and mean flow properties of the jet flow are obtained using a modified $k-\varepsilon$ RANS CFD model. The sensitivity of the results to the grid and also the choice of turbulence model ($k-\varepsilon$, $k-\omega$) are considered. Comparisons of results obtained using $k-\varepsilon$ and the $k-\omega$ have shown that a modified $k-\varepsilon$ model provides a much better self-similarity in the fully developed region than $k-\omega$. Numerical results are provided for three different nozzles: (1) single flow ($T_J = 300K$, $M_J = 0.60, 0.75, 0.90$), ($T_J = 600K$, $M_J = 0.75$), (2) coplanar (VR=0.9, 1.0), and (3) short-cowl nozzle (VR=0.9, 1.0). The mean velocity, turbulent kinetic energy, time scale, and length scale variation inside the jet domain at different radial positions are presented. The potential core length has been found to be about seven diameters long and the shear layer spreading rate is about 6 degrees. Generally speaking, most of the powerful sources are aggregated in the first 20 diameters, while the very high frequency ones are near the jet exit. One can also deduce from the results that the length scale and time scale behave as a linear function of the axial distance beyond $x = 10D_s$, which means the region is dominated by some large eddies. It has been also shown that most of the high frequency sources in coaxial flows are between the secondary potential core and the outer shear layer for the velocity ratios considered. It has been shown that the sources located between the two potential cores are much weaker and are also completely shielded by the secondary potential core, which implies they cannot be of great importance in the process of the noise radiation to an observer located around the jet flow. The convergence of the turbulence quantities, such as the turbulence kinetic energy, beyond $15D_s$ shows that the large eddies govern the dynamics of the flow in that region.

A comprehensive study has been provided for different turbulence scales, associated physical phenomenon, and time and length scale. Turbulence is studied from two standpoints, (1) size of the scales, and (2) dominant physical phenomenon. It is shown that understanding the physics of the turbulence and its connection to the noise production and radiation mechanism can be of great importance. It is also shown that the inertial subrange is the main contributor to the noise production mechanism. However, the inertial subrange shares borders with the dissipation and production regions and therefore eddies there are affected through sweeping and straining. General scaling laws for

radiated noise are provided under the sweeping and straining assumptions.

The main goal of the project has been to investigate the frequency dependency of the defining parameters, *i.e.* time scale, length scale, and convection velocity. Various models based on experimental data and physical reasoning are given. It has been shown that the sources of the same frequency are usually aggregated at almost the same distance from the jet exit. This implies that the frequency dependency can also be modeled using an axial distance or shear layer width dependent relationship. Such relationships, with explicit frequency dependency factor, are provided for the time scale and length scale. However, one of the apparent weaknesses of these types of models is their lack of generality.

It has been shown that one step forward in modelling the frequency dependency of the defining parameters is splitting the shear layer into a finite number of domains (two or three usually) and associating a time scale and length scale to each. Furthermore, a new time scale based on the turbulent energy transfer rate has been introduced which is shown to be capable of improving aerodynamic noise prediction, particularly in the low and high frequency bands. It has also been demonstrated that the known frequency dependence of the timescale no longer needs to be modelled explicitly as it arises as a natural consequence of the underlying physics.

Numerical results and discussion are provided for noise and axial source distribution predictions of single stream flows at different Mach numbers and temperatures. The MGBK method along with the high frequency asymptotic solution of Lilley's refraction equation are used, while most of the aforementioned time scales, length scales, and convection velocities are utilized. Results have shown that the highest level of damping due to the refraction effect occurs at high frequencies and for the observers in the vicinity of the jet axis, which implies comparably sharper roll-off after the peak frequency for the observers near the jet axis. It is shown that despite the difficulties of calibrating various coefficients, using multiple time scales results in very good agreement with experimental data over a wide range of frequencies. In this method the "effective dependence on frequency" arises naturally as the relative importance of different physical processes changes with different areas of the jet flow. It has also been shown that the difficulty of calibrating many coefficients can be overcame by using a time scale based on the

turbulent energy transfer time scale (TET). Noise prediction results obtained using the TET time scale show a very good agreement in the most of the cases with data at ninety degrees as well as other angles, except very small and large angles. A comprehensive discussion is given for causes of the peak frequency discrepancy when the observer is located near the jet axis or behind the jet exit. It is suggested that the one physically and mathematically justified reason is the distance between the low frequency sources and the observer location which is sometimes less than $20D$.

Source location (*i.e.* axial distribution) predictions have also shown the superiority of the energy transfer time scale over the dissipation and multiple time scales approach. Furthermore, the effects of source compactness and turbulence anisotropy are also taken into account and it is shown that their effect can be included in the noise prediction model using a complementary coefficient. Two types of convection velocities (mean velocity model and frequency dependent model) have been also examined. Apart from minor differences their general trend is very similar and no significant improvement has been obtained.

Numerical comparisons are then extended to modern nozzle geometries, *i.e.* coplanar and short-cowl nozzles. Two bypass velocity ratios have been chosen ($VR = 0.9$ and 1.0) ($T_J = 300K$). The jet noise prediction methodology is based upon the MGBK method and high frequency asymptotical solution of Lilley's equation. In general, results have shown that use of the dissipation time scale would lead to an under-prediction at low and high frequencies, while the new time scale (turbulent energy transfer rate) has the merit of improving both sides of the spectrum. It has again been shown that the most important reason of the mismatches between peak frequencies at small and large angles is due to the relatively small distance between the observer position and the jet shear flow, which will finally lead to the failure of the solution of Lighthill's equation to meet the retarded-time assumption. The source location predictions have also shown that using the turbulent energy transfer rate time scale offers better agreement than the dissipation time scale.

7.2 Recommendations for Future Work

When the work contained in this thesis is viewed from a global perspective it becomes clear that there are several avenues for future exploration. The weakest links in the statistical jet noise methodologies lay firstly in the deficiencies in the CFD prediction of the turbulence levels in the jet plume, secondly the understanding the turbulence and its connection with the noise production mechanism, and finally the noise prediction modelling itself. Hence, the recommendations for future research fall into the following categories: (1) CFD, (2) turbulence study, (3) noise prediction modelling.

(1) CFD: The turbulence CFD model used in this thesis is based on 2D axisymmetric RANS $k-\varepsilon$ model. Although the RANS based models provide a very fast solution, comparisons have shown that they are not able to capture the turbulence levels very well. So, any further improvement in jet noise prediction will be subject to obtaining more accurate CFD results.

These improvements could take the form of corrections to existing two-equation turbulence models, such as the variable diffusion correction as investigated by Engblom *et al.* [30], modifications for heated jets referred to as the PAB temperature correction [104], and variable closure coefficients (as shown in this thesis). Furthermore, it has been shown that the $k-\omega$ model provides better agreement in near wall regions. Hence using the Menter shear stress transport (SST) formulation (uses $k-\omega$ near walls and a standard $k-\varepsilon$ model transformed to a $k-\omega$ set for regions away from walls such as in jet mixing regions) might also improve the prediction. Further improvement can also be achieved by applying more advanced Reynolds stress turbulence models. Although RANS CFD analysis is certainly the fastest and most used turbulence model, using more advanced hybrid methods, such as Detached Dddy Simulations (DES) will provide a good chance to improve the quality of the CFD prediction. Although this approach, as well as LES and DNS models, may at this time be computationally expensive for industrial and engineering purposes, it would certainly be a useful validation for improving the present RANS-based noise prediction methods (such as the MGBK method), particularly for low Reynolds number flows.

In order to make further progress with the refraction effect problem, as well as the

noise blockage by the mean flow, for more general types of nozzles (such as serrated and with offset exits) 3D CFD simulation is necessary. As shown in this thesis, the region of highly damped sources (those radiating into the cone of silence) can be found using the CFD results. Finding those three dimensional surfaces (critical angles, θ^*) for non-axisymmetric nozzles will be very useful and can help us to better understand the refraction effect. Furthermore, noise propagation through the shear layer of a non-axisymmetric nozzle is another interesting subject which can be tackled using ray tracing methods which themselves require CFD information. It is generally believed that the noise radiated from the bottom half of the jet flow is mostly blocked and therefore its contribution to the observer located above the jet flow is much less than the noise radiated of the top half of the jet flow. The ray tracing method (or a FEM solution) can provide some useful information on this issue.

(2) Turbulence study: The main purpose of this research work was to show the importance of the turbulence study for jet noise prediction. It has been shown that due to the physics of the jet noise problem, turbulence and noise production and propagation are inherently linked. However, due to the complexity of the problem, statistical jet noise methodologies deals with it as a two-part solution problem (*i.e.* CFD+Acoustic). Therefore, the turbulence study becomes of much importance since it links these two parts, namely CFD and noise prediction modelling. Although some of these studies have been given in this work, such as the turbulent energy transfer time scale, and frequency dependency of parameters, this area is still open for further theoretical and experimental research. The following examples are brought here for instance:

(a) Further developing the idea of the straining and sweeping effects on the inertial subrange and developing more general scaling laws. This will also facilitate understanding of the peak frequency problem and will help to find a non-trial and error method for calibrating the time scale coefficient.

(b) Implementing more advance turbulent energy spectrum models to better show the effect of the anisotropy of velocity fluctuations (to find the turbulent energy transfer rate scales), as [105]

$$
\begin{aligned}
&E(\kappa) \propto \varepsilon_{eff}^{2/3}\kappa^{-5/3}, \\
&\varepsilon_{eff} = \varepsilon\left[1 - 0.60\text{sgn}\left(\tfrac{D\varepsilon}{Dt}\right)(\kappa l_p)^{-2/3}\right]^{3/2},
\end{aligned}
\tag{7.1}
$$

where $l_p = \varepsilon^2 / \left|\frac{D\varepsilon}{Dt}\right|$ characterizes a dynamical property of the turbulent-energy-production process and *sgn* is the sign function.

(c) One of most important weaknesses of the frequency dependent length scale used in this thesis is that it is based on results of a very low Mach number flow ($M_J = 0.16$) [48]. This means that more experimentation needs to be carried out at higher Mach numbers and at different positions within the jet flow.

(d) As mentioned in section 5.1.4.2 the anisotropy effect was included in the noise prediction model using a single parameters, β_c, which treats all the eddies (sources) in the same way. One can readily deduce that such an assumption is not very accurate because the anisotropy effect should entirely vanish at very small scales where Taylor's hypothesis holds. This suggests that the anisotropy model should be frequency or location dependent, increasing (decreasing) with axial distance (frequency). Further investigation requires more experimentation and turbulence study.

(3) Noise prediction modelling: The noise prediction modelling also suffers from various weaknesses. As shown before, noise prediction comparisons are usually made at insufficiently large distances from the jet exit. This is not consistent with the retarded time assumption and will cause the peak frequency mismatch problem for observers near the jet axis. The second weakness is that of dipole and monopole sources arising as a result density variation within the shear layer. It has been shown by Khavaran and Kenzakowski [106] that the implementation of a set of linearized, inhomogeneous Euler equations for heated flows will significantly improve the acoustic predictions at the 90-degree observer angle. Furthermore, development of a 3D statistical noise prediction code along with a 3D ray tracing (or 3D BEM) can be of much help in understanding various noise production and radiation related problems, such as noise blockage, radiation from non-axisymmetric flows, sound-wing interaction, and most importantly, development of new ideas for noise reduction.

Appendix A

CFD Simulation

As previously mentioned in Chapter 2, in order to deal with Lighthill's equation or the MGBK method one needs to provide some information about the mean values and the turbulence characteristics of the flow. Such information will be used for identification of the source terms as well as the description of some phenomena such as convection and refraction. Finding these quantities is quite a straightforward task using commercial software, such as FLUENT. Three nozzles are considered in this thesis: (1) Single-flow nozzle, (2) Coplanar nozzle, and (3) Short-cowl nozzle.

The structure of this chapter is as follows: In section A.1 the most important RANS turbulence models, namely $k-\varepsilon$, and $k-\omega$, are introduced and the corresponding formulations are given. General descriptions of the problem geometry and mesh used for the single flow nozzle is given in section A.2. Section A.3 concerns the grid sensitivity of the solution, as well as the sensitivity of the solution to the choice of the turbulence model. The CFD results used in Chapters 5, and 6 are presented in section A.4. Numerical results for an unheated and heated single flow jet will be given in sections A.4.1 and A.4.2. Section A.4.3 concerns the CFD results of a coplanar nozzle working at different bypass velocity ratios. Finally, section A.4.4 deals with the CFD runs performed for a short-cowl nozzle, which is the most realistic model and very similar to real jet engine nozzles.

A.1 Turbulence Modeling

Three different regimes: laminar, transitional and turbulent, can generally be noticed in a flow field. The flow in the laminar regime is quite smooth, and the adjacent layers of fluid slide past each other in an orderly manner. The change from a laminar flow to a turbulent one, due to the instability of the laminar state, is called transition. In the transition region the initially small disturbances are amplified, areas with concentrated rotational structures are developed and finally the growth and merging of these areas leads to a fully turbulent flow. Most flows encountered in nature as well as in industrial applications are turbulent. However, due to its complexity, our understanding of turbulent flows is still incomplete. Turbulence is characterized by a number of properties. It has been described as a random/irregular motion, both in time and space. The dynamics of turbulence involve a wide range of scales. While the size of the large scales is typically determined by the geometry of the flow, the size of the smallest scale decreases with increasing Reynolds number (Re), and is determined by the viscous dissipation process.

In most turbulent flows it is impossible to resolve all the length and time scales with the computational capacity of today, so one needs to introduce models to simulate some aspects of the flow. Most of the feasible turbulence models are based on statistical approaches where the governing equations of the flow are averaged in time or space. Two-equation Models of turbulence have served as the foundation for much of the turbulence modelling research during the past years. Many kinds of two-equation models, such as $k-\varepsilon$, $k-\omega$, $k-\nu^2$, $k-L$, etc., have been introduced and checked against each other. However, the $k-\varepsilon$ and $k-\omega$ models have received most attention. Here, we shall give the formulation of these two methods, their theoretical differences and finally a numerical comparison of the methods for the problem of subsonic unheated $M_J = 0.75$ round jet.

A.1.1 Mathematical Modelling

The equation governing the mean kinetic energy $\overline{v_i v_i/2}$ of the turbulent velocity fluctuations is obtained by multiplying the Navier-Stokes equations by v_i, taking the time

average of all terms, and subtracting the mean flow energy equation. The final equation of the turbulent energy budget for an incompressible flow, can be found from [69]

$$\frac{\partial k}{\partial t} + U_j \frac{\partial k}{\partial x_j} = \tau_{ij} \frac{\partial U_i}{\partial x_j} - \varepsilon + \frac{\partial}{\partial x_j} \left[\nu \frac{\partial k}{\partial x_j} - \frac{1}{2} \overline{v_i v_j v_k} - \frac{1}{\rho} \overline{p v_j} \right], \tag{A.1}$$

where an overbar is a shorthand for the time average. The quantity ε is the dissipation rate per unit mass and is defined by the following correlation:

$$\varepsilon = \nu \overline{\frac{\partial v_i}{\partial x_k} \frac{\partial v_i}{\partial x_k}}, \tag{A.2}$$

and the specific Reynolds stress tensor is given by

$$\tau_{ij} = -\overline{v_i v_j}. \tag{A.3}$$

Assuming the *Boussinesq* approximation, the specific Reynolds-stress tensor can be found by

$$\tau_{ij} = 2\nu_T S_{ij} - \frac{2}{3} k \delta_{ij}, \tag{A.4}$$

where S_{ij} is the mean strain-rate tensor, and the kinematic eddy viscosity is given by

$$\nu_T = const.\, k^{1/2} l, \tag{A.5}$$

l being turbulence length scale.

Using the DNS results one can show that the turbulent transport and pressure diffusion terms (*i.e.* the last two terms in Eq. A.1) can be approximated as

$$\frac{1}{2} \overline{v_i v_j v_k} + \frac{1}{\rho} \overline{p v_j} = -\frac{\nu_T}{\sigma_k} \frac{\partial k}{\partial x_j}, \tag{A.6}$$

where σ_k is a closure coefficient.

Finally, assuming the latter approximation, equation A.6, and also the Reynolds-stress definition, equation A.1 can be expressed as follows:

$$\frac{\partial k}{\partial t} + U_j \frac{\partial k}{\partial x_j} = \tau_{ij} \frac{\partial U_i}{\partial x_j} - \varepsilon + \frac{\partial}{\partial x_j} \left[\left(\nu + \frac{\nu_T}{\sigma_k} \right) \frac{\partial k}{\partial x_j} \right]. \tag{A.7}$$

To complete the closure of the turbulent kinetic energy equation, it can be supposed that the energy dissipation rate is related to the turbulent kinetic energy and length scale via,

$$\varepsilon = C_D k^{3/2}/l, \tag{A.8}$$

where C_D is a closure coefficient. This method is called a **one-equation model**. The only unknown part of the model is l, which can be estimated from a knowledge of experimental results.

Besides the one-equation method, as indicated at the beginning of section, two-equation models play an important role in RANS simulations. The following two sections provide an overview of the mathematical modelling of the $k-\varepsilon$ and $k-\omega$ models.

A.1.2 $k-\varepsilon$ Method

The most popular two-equation model is the $k-\varepsilon$ model. To formulate the $k-\varepsilon$ model, the idea is to derive an exact equation for ε and also to find the suitable closure approximations for the exact equation governing its behavior given equation (A.1). Although ε can be found by equation (A.2), the precise relation governing it can be derived by applying the following operator to the Navier-Stokes equation:

$$2\nu \overline{\frac{\partial v_i}{\partial x_j}\frac{\partial}{\partial x_k}\left[N(v_i)\right]} = 0, \tag{A.9}$$

where $N(u_i)$ is the Navier-Stokes operator, and is expressed as:

$$N(v_i) = \rho\frac{\partial v_i}{\partial t} + \rho v_k \frac{\partial v_i}{\partial x_k} + \frac{\partial p}{\partial x_i} - \mu\frac{\partial^2 v_i}{\partial x_k \partial x_k}. \tag{A.10}$$

After a considerable amount of algebra, the following equation for ε results [107],

$$\begin{aligned}\frac{\partial \varepsilon}{\partial t} + U_j\frac{\partial \varepsilon}{\partial x_j} = &-2\nu\left[\overline{v_{i,k}v_{j,k}} + \overline{v_{k,i}v_{k,j}}\right]\frac{\partial U_i}{\partial x_j} - 2\nu\overline{v_k v_{i,j}}\frac{\partial^2 U_i}{\partial x_k \partial x_j} \\ &-2\nu\overline{v_{i,k}v_{j,m}v_{k,m}} - 2\nu^2\overline{v_{i,km}v_{i,km}} \\ &\frac{\partial}{\partial x_j}\left[\nu\frac{\partial \varepsilon}{\partial x_j} - \nu\overline{v_j v_{i,m}v_{i,m}} - 2\frac{\nu}{\rho}\overline{p_{,m}v_{j,m}}\right]\end{aligned} \tag{A.11}$$

The new complementary equation derived has increased the number of unknowns and the solution is now even more complicated. Once more, with help of DNS results and

making some approximations, the standard $k-\varepsilon$ model can be written as follows:

$$\frac{\partial k}{\partial t}+U_j\frac{\partial k}{\partial x_j}=\tau_{ij}\frac{\partial U_i}{\partial x_j}-\varepsilon+\frac{\partial}{\partial x_j}\left[\left(\nu+\frac{\nu_T}{\sigma_k}\right)\frac{\partial k}{\partial x_j}\right], \tag{A.12}$$

$$\frac{\partial \varepsilon}{\partial t}+U_j\frac{\partial \varepsilon}{\partial x_j}=C_{\varepsilon 1}\frac{\varepsilon}{k}\tau_{ij}\frac{\partial U_i}{\partial x_j}-C_{\varepsilon 2}\frac{\varepsilon^2}{k}+\frac{\partial}{\partial x_j}\left[\left(\nu+\frac{\nu_T}{\sigma_\varepsilon}\right)\frac{\partial \varepsilon}{\partial x_j}\right], \tag{A.13}$$

$$\nu_T=C_\mu\frac{k^2}{\varepsilon}, \tag{A.14}$$

$$C_{\varepsilon 1}=1.44,\ C_{\varepsilon 2}=1.92,\ C_\mu=0.09,\ \sigma_k=1.0,\ \sigma_\varepsilon=1.3, \tag{A.15}$$

$$l=C_\mu k^{3/2}\Big/\varepsilon, \tag{A.16}$$

where equations (A.15), and (A.16) are the closure coefficients and auxiliary relations respectively. The above system of equations are usually referred to as the RANS $k-\varepsilon$ model.

The $k-\varepsilon$ has been changed and improved in many ways, and the **RNG** $k-\varepsilon$ is known as one of the most well-known changes applied to it. In this model k and ε are still given by equation (A.12) through (A.14), but a modified changeable $C_{\varepsilon 2}$ is defined:

$$C_{\varepsilon 2}=\tilde{C}_{\varepsilon 2}+\frac{C_\mu\lambda^3\left(1-\lambda/\lambda_0\right)}{1+\beta\lambda^3}, \tag{A.17}$$

where $\lambda\equiv\frac{k}{\varepsilon}\sqrt{2S_{ij}S_{ji}}$, and closure coefficients for RNG $k-\varepsilon$ are

$$\begin{gathered}C_{\varepsilon 1}=1.42,,\ \tilde{C}_{\varepsilon 2}=1.68,\ C_\mu=0.085,\\ \sigma_k=0.75,\ \sigma_\varepsilon=0.72,\ \beta=0.12,\ \lambda_0=4.38.\end{gathered} \tag{A.18}$$

A.1.3 $k-\omega$ Method

In most of the two-equation models the turbulent kinetic energy k is taken as one of the variables of the solution, but the second variable needs to be chosen. Different parameters have been examined for this purpose, such as $k-L$, ε, $k-\omega$, $k-\omega^2$, and $k-\tau$. However, $k-\varepsilon$ and $k-\omega$ are the most well-known and used turbulence models. Hence, in this section, the formulation of the $k-\omega$ is presented.

Combining the physical reasoning with the dimensional analysis, Kolomgorov [108] hypothesized the following equation for the specific dissipation rate of ω can be found,

$$\frac{\partial \omega}{\partial t} + U_j \frac{\partial \omega}{\partial x_j} = -\beta \omega^2 + \frac{\partial}{\partial x_j}\left[\sigma \nu_T \frac{\partial \omega}{\partial x_j}\right], \tag{A.19}$$

where β and σ are two closure coefficients. Due to some inherent flaws in this equation, another set of equations are offered to improve the accuracy of the model for free shear flows [107],

$$\frac{\partial k}{\partial t} + U_j \frac{\partial k}{\partial x_j} = \tau_{ij} \frac{\partial U_i}{\partial x_j} - \beta^* k\omega + \frac{\partial}{\partial x_j}\left[(\nu + \sigma^* \nu_T)\frac{\partial k}{\partial x_j}\right], \tag{A.20}$$

$$\frac{\partial \omega}{\partial t} + U_j \frac{\partial \omega}{\partial x_j} = \alpha \frac{\omega}{k} \tau_{ij} \frac{\partial U_i}{\partial x_j} - \beta \omega^2 + \frac{\partial}{\partial x_j}\left[(\nu + \sigma \nu_T)\frac{\partial \omega}{\partial x_j}\right], \tag{A.21}$$

$$\nu_T = \frac{k}{\omega}, \tag{A.22}$$

where the closure coefficients and auxiliary relations are [107]:

$$\alpha = 13/25,\ \beta = \beta_0 f_\beta,\ \beta^* = \beta_0^* f_{\beta^*},\ \sigma = 0.5,\ \sigma^* = 0.5, \tag{A.23}$$

$$\beta_0 = 9/125,\ f_\beta = \frac{1 + 70\chi_\omega}{1 + 80\chi_\omega},\ \chi_\omega \equiv \left|\frac{\Omega_{ij}\Omega_{jk}S_{ki}}{(\beta_0^* \omega)^3}\right|, \tag{A.24}$$

$$\beta_0^* = 9/100,\ f_{\beta^*} = \begin{cases} 1, & \chi_k \le 0 \\ \frac{1+680\chi_k^2}{1+400\chi_k^2}, & \chi_k > 0 \end{cases},\ \chi_k \equiv \frac{1}{\omega^3}\frac{\partial k}{\partial x_j}\frac{\partial \omega}{\partial x_j}, \tag{A.25}$$

$$\varepsilon = \beta^* \omega k,\ l = k^{1/2}/\omega. \tag{A.26}$$

The above formulations are usually referred to as the standard $k - \omega$ turbulence model. In the next section we shall make use of these two RANS turbulence models (*i.e.*, $k - \varepsilon$, $k - \omega$) for the proposed geometry with different grids to investigate the sensitivity of the solution to the grid size and also to the choice of the turbulence model.

A.2 Geometry and Mesh Descriptions

A preliminary single-stream nozzle geometry (D_J=50mm, sharp lip) has been used as a benchmark for the preliminary jet flow calculations. The geometry is depicted in figure A.1.

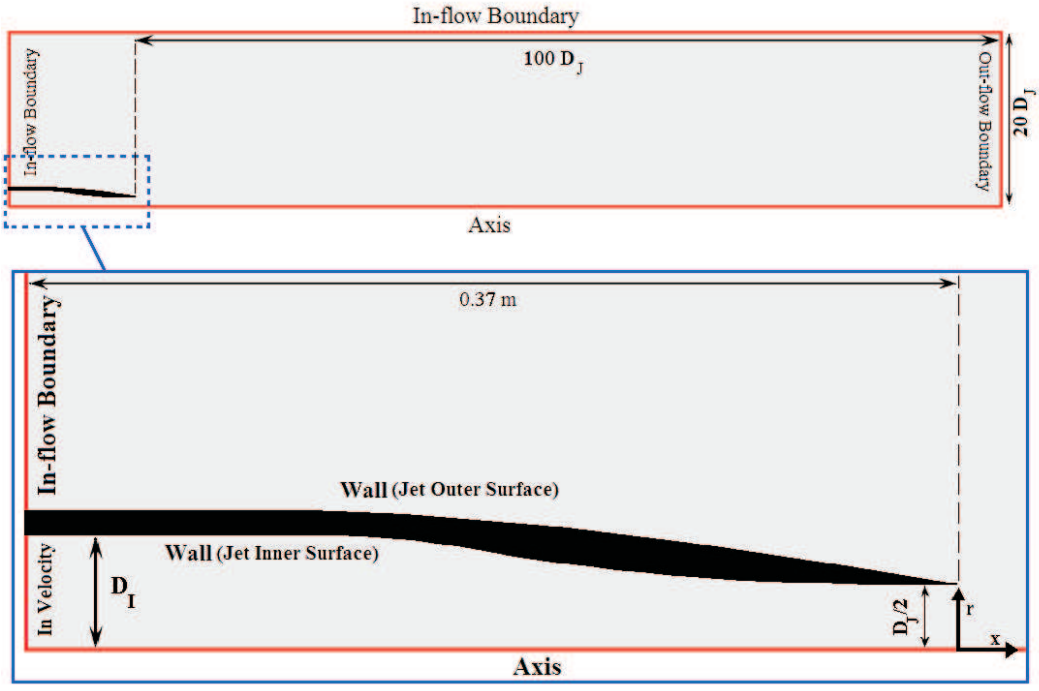

FIGURE A.1: Problem Geometry

The computation domain chosen for the RANS computations consists of an interior nozzle domain, before body domain and jet domain which is extended $100D_J$ axially and $20D_J$ radially. The Gambit software is used to generate the two-dimensional structures and grid. The domain is divided into 27 rectangular sub-domains to make the structural meshing easier. This section concentrates on the simulation of a single flow nozzle. However the simulation process (meshing and boundary conditions) for the coplanar and short-cowl nozzle are carried out in a similar fashion.

In order to solve any boundary value problem, one first needs to specify the boundary conditions. For the cold single flow jet a "velocity-inlet" boundary condition is chosen to simulate the flow of the incompressible fluid through the entrance plane, while for the hot jet a "pressure inlet" boundary condition must be used. In addition to the inlet boundary condition type, two other quantities are required to describe the nature of the turbulent medium at the jet entrance. The hydraulic diameter and the turbulence intensity are chosen for this purpose. The turbulence intensity at the core of a fully-developed duct flow can be estimated from the following formula derived from an empirical correlation for pipe flows:

$$I = 0.16\ (\mathrm{Re}_{D_H})^{-1/8}$$

where D_H denotes the hydraulic diameter, and Re is Reynolds number. For fully-developed internal flows, the hydraulic diameter can be assumed equal to the diameter of the pipe. Additionally, the "Pressure-inlet" and "Pressure-outlet" boundary conditions (that are characterized with a very small turbulent viscosity and intensity) are chosen to replicate the surrounding lines of the computational domain. Furthermore, in order to decrease the computation time, a symmetry boundary condition on the axis is also employed in the current 2D simulation. The FLUENT solutions are obtained by running 10000 iterations using the steady-state coupled solver (implicit), axisymmetric mode, with a second order accuracy.

A.3 Mesh Sensitivity, Near-Field and Self-Similarity Assessment

Many grid sizes have been tested to find the best mesh with respect to the CFD accuracy and also the simulation time. Here, comparisons are presented for two meshes (referred to as the fine and coarse mesh) to examine the grid sensitivity of the CFD simulations. The smallest scales used for the fine mesh is in order of $5 * 10^{-5}m$, with the grid size increasing in the axial and the radial directions. The total number of quadrilateral cells used for the fine mesh is about 200000, while that for the coarse mesh is about 90000. The finest cells are utilized near the outlet of the nozzle and especially close to the nozzle lip, where considerable interaction between the jet flow, solid body, and the surrounding at rest medium occurs. The smallest size for the coarse mesh is $10^{-3}m$, which increases with x and r. Different views of the computational domain using the fine grid mesh can be seen in figure A.2.

An assessment of the grid sensitivity is presented in figure A.3, where contours of the mean velocity for a $M_J = 0.75$ single-flow unheated jet using the coarse and fine grids are presented. Although results show a reasonable agreement near the nozzle exit, they are slightly different further downstream. Hence, due to the good performance of the fine grid, this grid will be used in our future 2D computations. A very similar grid will be used for the coplanar and short-cowl nozzles, which will be explained later.

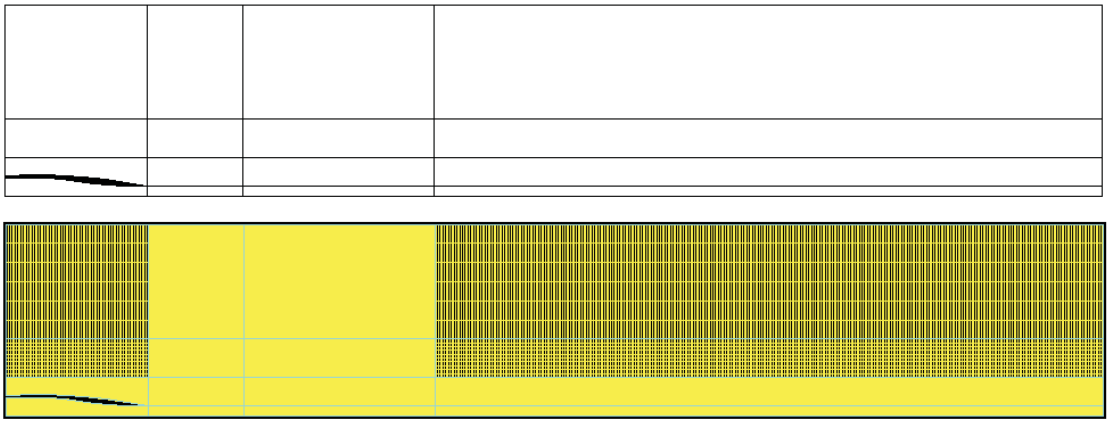

FIGURE A.2: Problem geometry and mesh distribution

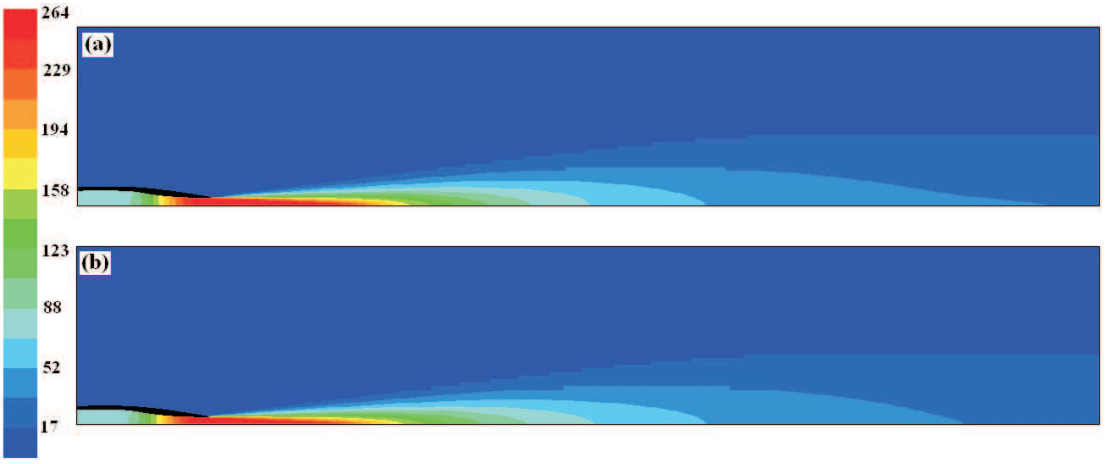

FIGURE A.3: Sensitivity of the CFD results to mesh size; (a) coarse mesh, (b) fine mesh

The sensitivity of the plume mean velocity to the choice of turbulence model is considered for a single flow M0.75 jet. Calculations were performed using Fluent with the standard $k-\omega$ and the modified $k-\varepsilon$ turbulence model. In the modified $k-\varepsilon$ model the $C_{\varepsilon 2}$ factor has been changed from 1.92 to 1.83 in order to reduce the spreading rate from about 0.12 to 0.10, which provides better self-similarity in the fully developed region.

In order to compare the differences of $k-\varepsilon$ and $k-\omega$ models figures A.4 and A.5 are presented. The realizability constraint consists of an eddy viscosity limiter and acts in such a way that the normal Reynolds stress components with the wrong sign (unphysical behaviour) are avoided. Contours of the mean velocity for both models are shown in figure A.4. Results of the $k-\omega$ models shows an extra lobe near the jet exit - from

a physical point these cannot be justified. The results using the $k-\varepsilon$ model are more consistent with what is actually expected from the physics of the problem.

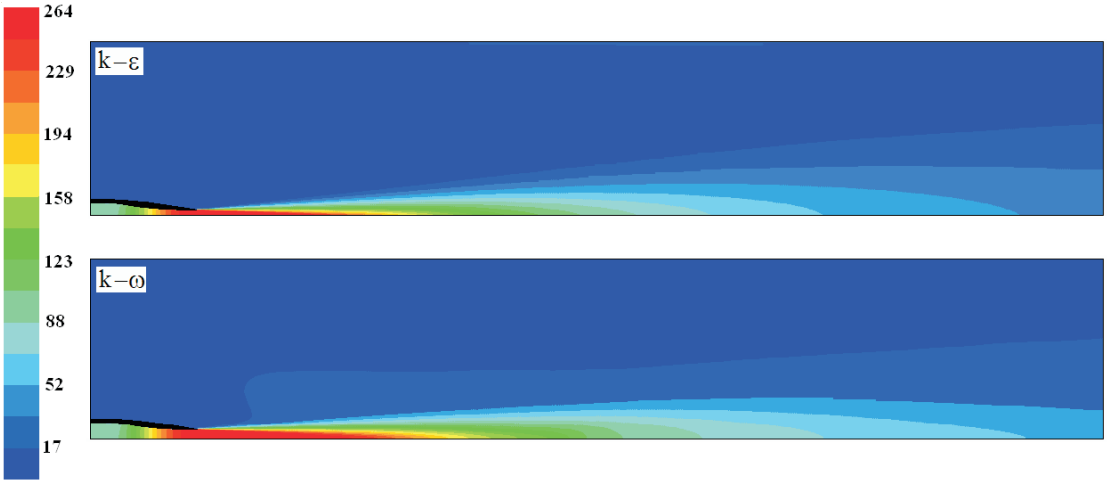

FIGURE A.4: Near-field comparison of $k-\varepsilon$ and $k-\omega$ models

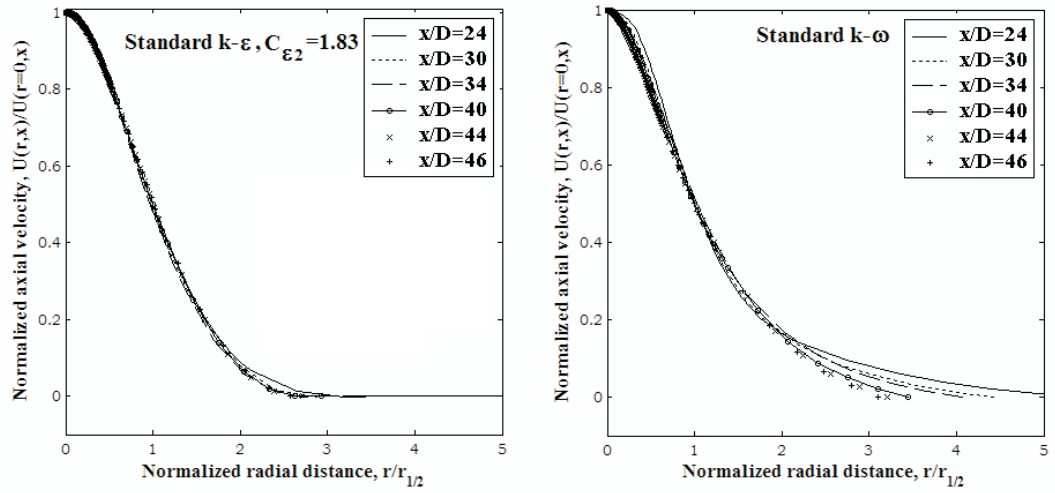

FIGURE A.5: Self-similarity comparisons of $k-\varepsilon$ and $k-\omega$ models (fully developed region)

Another important test to determine the accuracy of the turbulence model for round jet flows is the known self-similarity rule in the fully developed medium. Evidently, a high quality RANS solution must capture this self-similarity. An evaluation of the self-similarity of the computed jet has been made and is presented in figure A.5, for the standard $k-\varepsilon$ turbulence model (with realizability constraint). The self-similarity was checked by plotting various radial profiles with a scaling which should collapse the curves to one single curve. In this scaling $r_{1/2}$ is the half-width of the jet flow width.

The figures show that using a $k-\varepsilon$ turbulence model (with realizability constraint) leads to overlaying of all of the curves. An equivalent evaluation of the $k-\omega$ model is also presented in A.5. It is apparent that the calculated flow field does not capture the self-similarity of the flow.

A.4 Numerical Results and Discussions

Numerical results are presented for three nozzles: (1) Single stream nozzle, (2) Coplanar nozzle, and (3) Short-cowl nozzle. Simulations are performed using the modified $k-\varepsilon$ model with the fine grid introduced earlier.

A.4.1 Unheated Single Flow Jet, M0.75

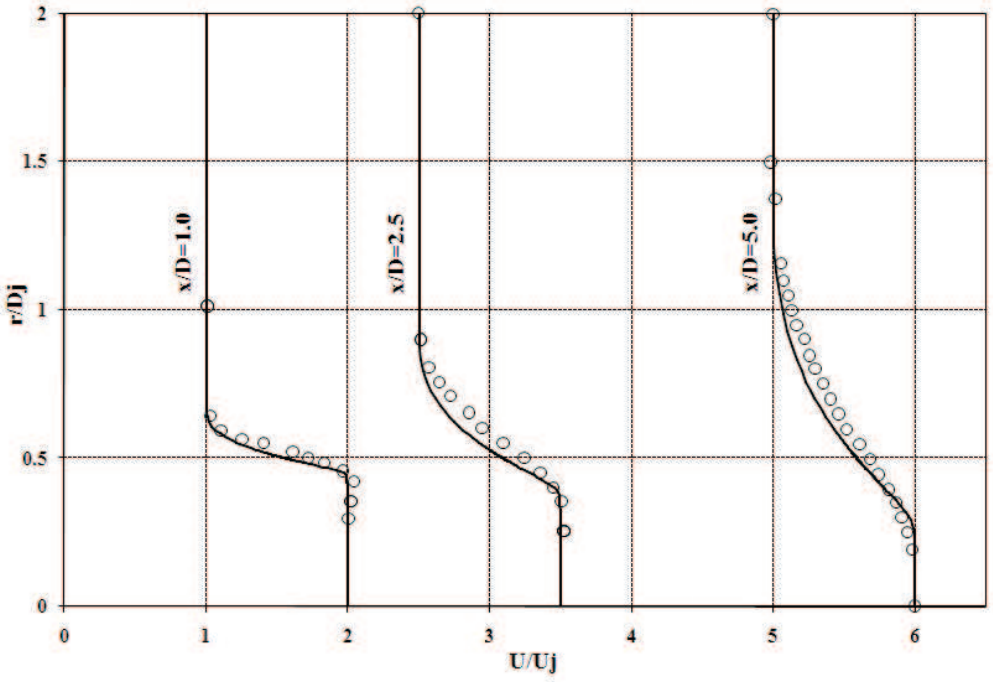

FIGURE A.6: Mean velocity profiles at different axial distances. Solid line:CFD, marker: Measured data

The first CFD simulation is performed for a $M_J = 0.75$ unheated single-stream jet. Figures A.6 through A.10 present the variation of the mean velocity, turbulent kinetic energy, turbulent length scale, and turbulent time scale inside the jet flow. Figure A.6 shows the comparison of the mean velocity with the measured data at three axial

distances ($x = D_J$, $x = 2.5D_J$, and $x = 5D_J$). Comparison shows an acceptable agreement at different jet regions. The turbulent kinetic energy variation and also comparison with measured data along the jet lip-line is presented in figure A.7. The figure clearly illustrates the interactions between the outgoing stream with the lip of the nozzle and the surrounding at rest medium ($r/D_J = 0.5$), which creates a region of high frequency noise sources near the lip ($0 \leq x/D_J \leq 1$). Furthermore, the figure shows that the most important source are located in a region of $0 \leq r/D_J \leq 2$ and $0 \leq x/D_J \leq 20$. Furthermore, comparison shows that the CFD results are in good agreement with the measured data.

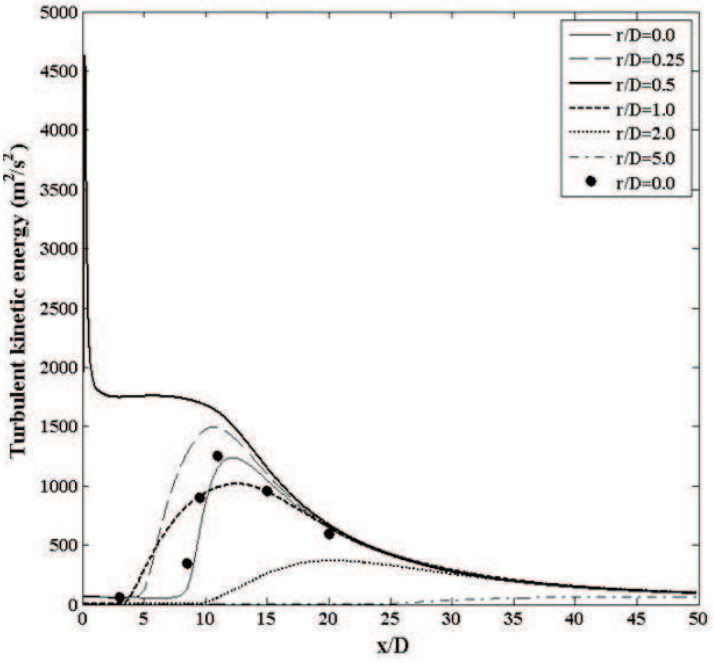

FIGURE A.7: Turbulent kinetic energy; $M_J = 0.75$, unheated single flow jet. Line: CFD, Marker: Measured data

Figures A.9 and A.10 show the turbulent length ($k^{3/2}/\varepsilon$) and time scale (k/ε). The smallest scales can be observed at the nozzle lip, which increase along the jet axis and also the radial direction. The collapse of the length scale and time scale curves on each other regardless of radial position in the downstream region shows that it is dominated by some large structures (big eddies).

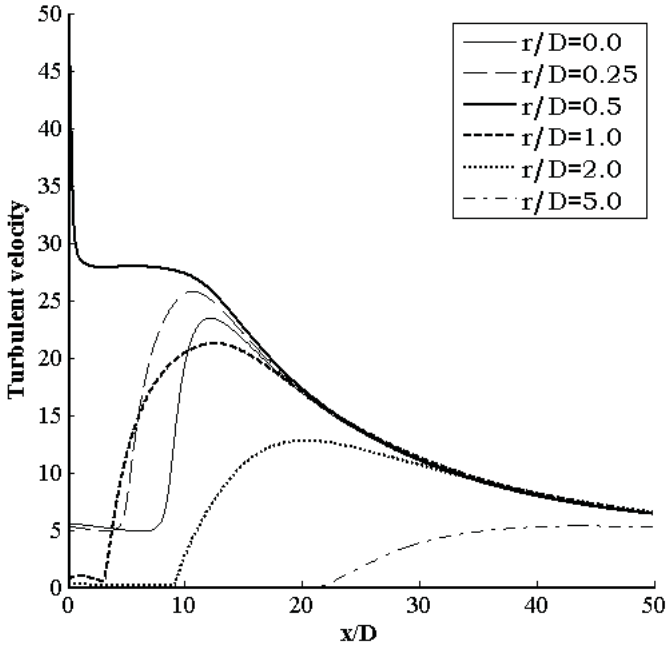

FIGURE A.8: Modeled fluctuating velocity; $M_J = 0.75$, unheated single flow jet

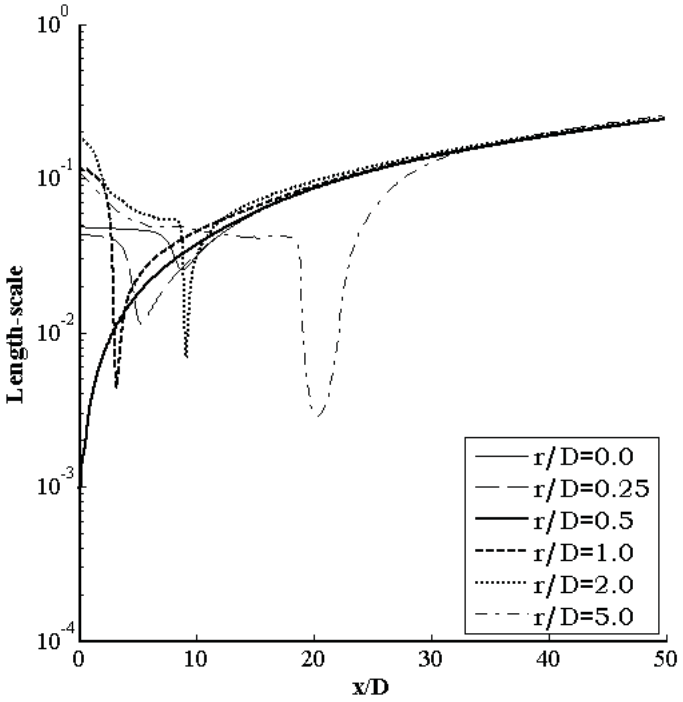

FIGURE A.9: Turbulent length scale ($L = k^{3/2}/\varepsilon$); $M_J = 0.75$, unheated single flow jet

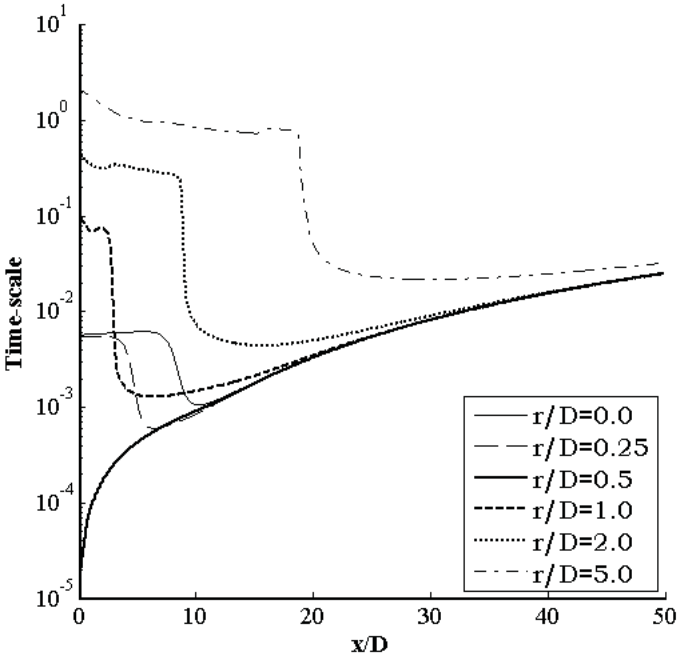

FIGURE A.10: Turbulent time scale ($\tau = k/\varepsilon$); $M_J = 0.75$, unheated single flow jet

A.4.2 Hot Single Flow Jet, $M_{=}0.75$

The FLUENT solutions were obtained by running 10000 iterations using the coupled solver (implicit) with second order accuracy. In addition, the ideal gas law was enabled.

As mentioned in Chapter 2 the mean flow (U, T, c) and turbulent results (k, ε) are needed for noise prediction of a heated single flow jet ($M_J = 0.75$). Again the modified $k - \varepsilon$ method has been used to obtain the required information. The similar fine mesh of the previous simulation is used. The boundary conditions are the same as the previous model, except for the jet inlet surface. Due to the compressibility of the flow at temperature of $T_J = 600K$, a "pressure inlet" boundary condition has been chosen.

The turbulent kinetic energy variations at different radial locations are shown in figure A.11. The trend of the curves is more or less similar to those of the unheated jet, but the magnitude of the values is less than what was found from the unheated jet flow. This implies that we are now dealing with some weaker sources in the hot jet. However the temperature variation inside the jet flow means that some new noise sources should

appear. Comparison with measured data across the centre-line also shows an acceptable level of agreement.

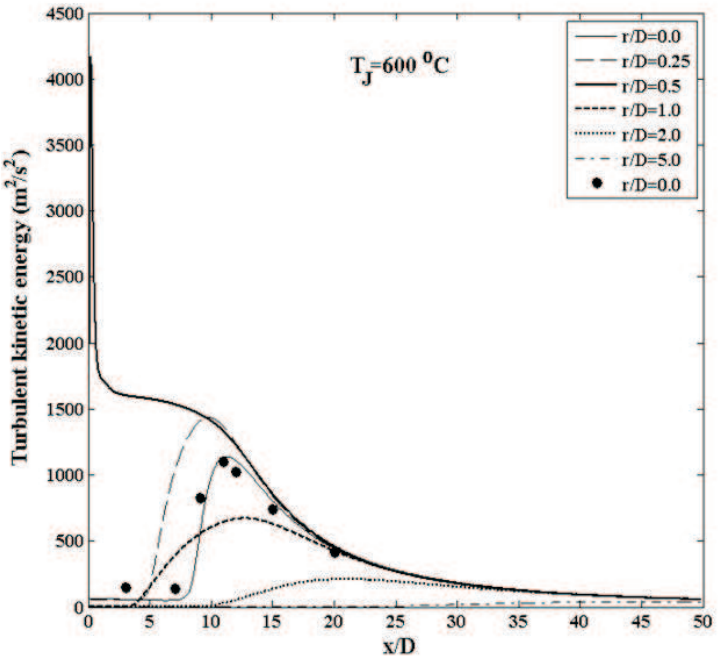

FIGURE A.11: Turbulent kinetic energy; $M_J = 0.75$, $T_J/T_0 = 2$, hot single flow jet, Line: CFD, Marker: Measured data

Temperature variation, and accordingly density and sound speed variation within the jet flow plays a very important role in noise prediction. This particularly effects the refraction and finding the turning point locations, as discussed earlier in section 2.2 (see figure A.12). Finally, the length scale and time scale are calculated and shown in figures A.13 and A.14. Results, in general, are very similar to the unheated jet flow results. There are a few differences inside the potential core and outside the shear layer which are not very important in regard to the noise generation mechanism.

A.4.3 Coplanar Jets

The CoJeN coplanar nozzle has been used in this part of the work. The nozzle geometry is shown in figure A.15. The inner nozzle diameter is $D_p = 0.0995m$ and the secondary diameter is $D_s = 0.200m$. The grid size and its structure is similar to that used for the single flow jet, except that the first row of meshes is repeated for the secondary exit. Two different velocity ratios have been chosen for this simulation. In the first case, the

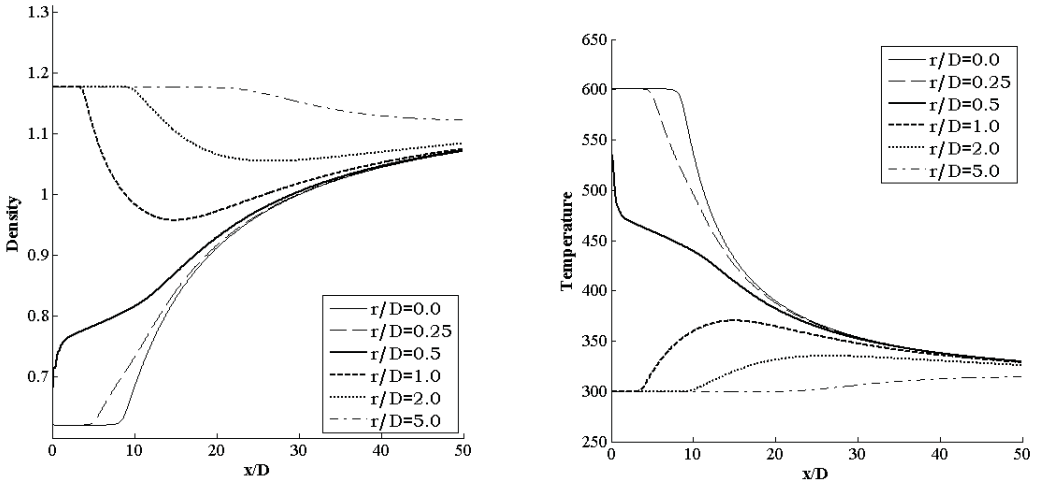

(a) Density; $M_J = 0.75$, $T_J/T_0 = 2$ (b) Temperature; $M_J = 0.75$, $T_J/T_0 = 2$

FIGURE A.12: Density and temperature variation within the jet flow, hot single flow jet

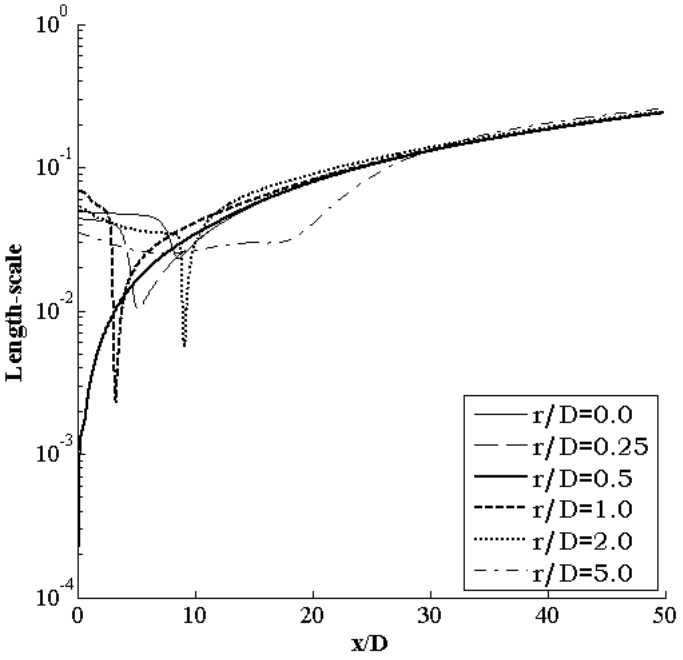

FIGURE A.13: Length scale ($L = k^{3/2}/\varepsilon$); $M_J = 0.75$, $T_J/T_0 = 2$, hot single flow jet

primary velocity is $V_p = 217.2m/s$, and the secondary is $V_s = 217.2$ (velocity ratio is 1), and in the second case $V_p = 240.9m/s$ and $V_s = 217.2$ (VR=0.9).

Figures A.16 to A.17 show the mean velocity and turbulent kinetic energy contours

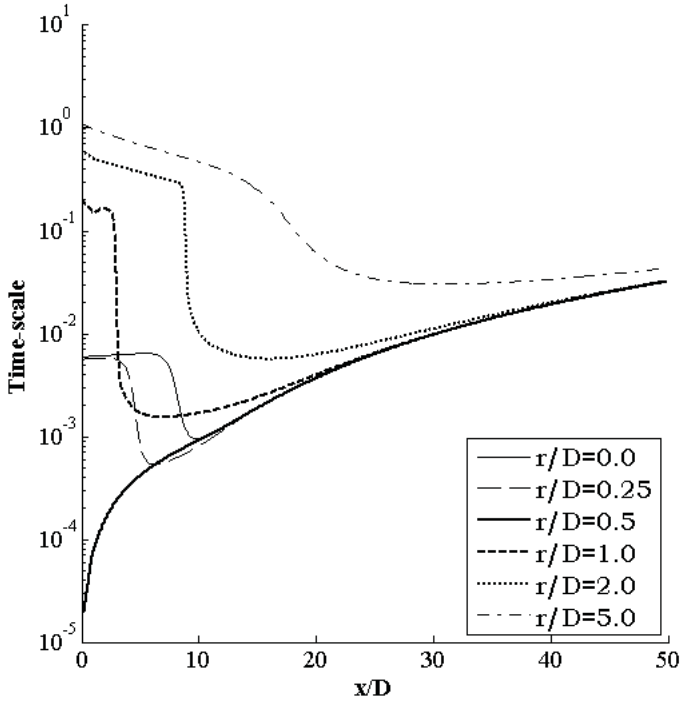

FIGURE A.14: Time scale ($\tau = k/\varepsilon$); $M_J = 0.75$, $T_J/T_0 = 2$, hot single flow jet

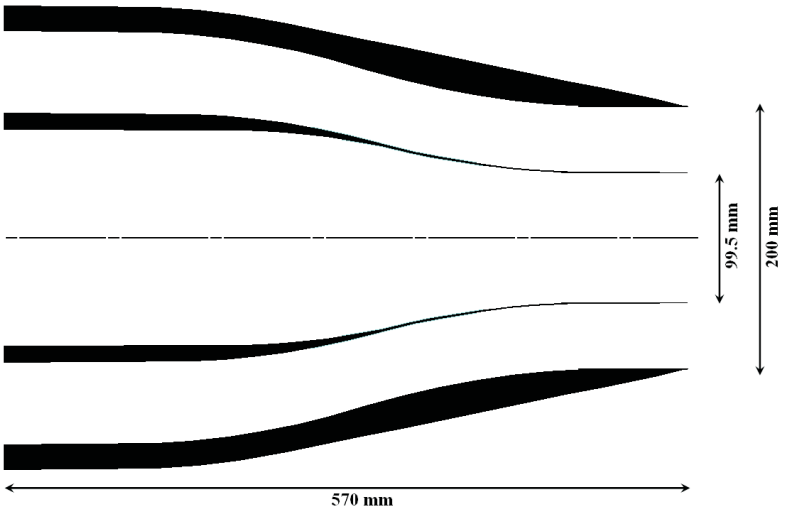

FIGURE A.15: Coplanar nozzle geometry

of $VR = 1.0$. Figure A.16 shows contour of the mean velocity. It can be seen that the potential core extends up to $7D_s$ downstream. Furthermore, the figure shows that the coplanar jet flow in this case behaves very similar to that of a single flow jet. Figure A.17 shows the contour of the turbulent kinetic energy inside the shear layer. It can be seen that the most powerful sources are aggregated close to the secondary lip, while

much weaker sources can be seen near the primary lip. This occurs because the outgoing streams are parallel and with the same speed, so there will be a very weak turbulent interaction between them.

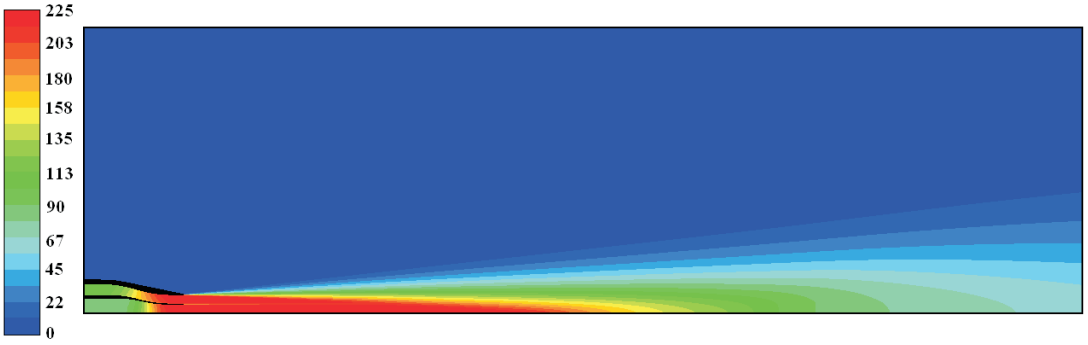

FIGURE A.16: Mean velocity contour of a coplanar nozzle; VR=1

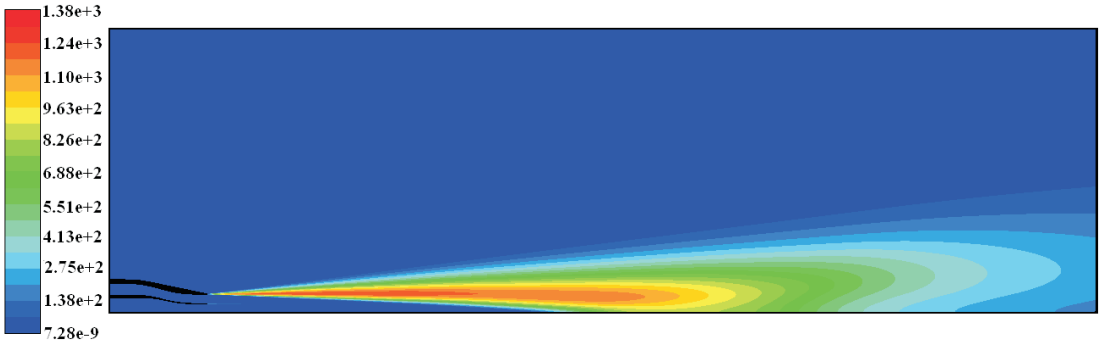

FIGURE A.17: Turbulent kinetic energy contour, coplanar nozzle, VR=1

Figures A.18 and A.20 show the variation of the mean velocity, turbulent kinetic energy, and turbulent scales at different radial positions, respectively. The following inferences can be deduced: (1) The most powerful sources are aggregated in the region of $x < 15D_s$, (2) results overlay on each other after $15D_s$ which means the region is dominated by large scale structures, (3) sources located near the secondary lip ($r = 0.5D_s$) have almost the same source strength up to $x = 10D_s$ where a sharp roll off occurs. Figure A.20 shows the variation of the length scale and time scale at different radial positions. One can deduce that the smallest scales are located near the primary and secondary lips. Furthermore, the overlap of the curves downstream ($x > 15D_s$) shows that this region is mostly occupied by large eddies.

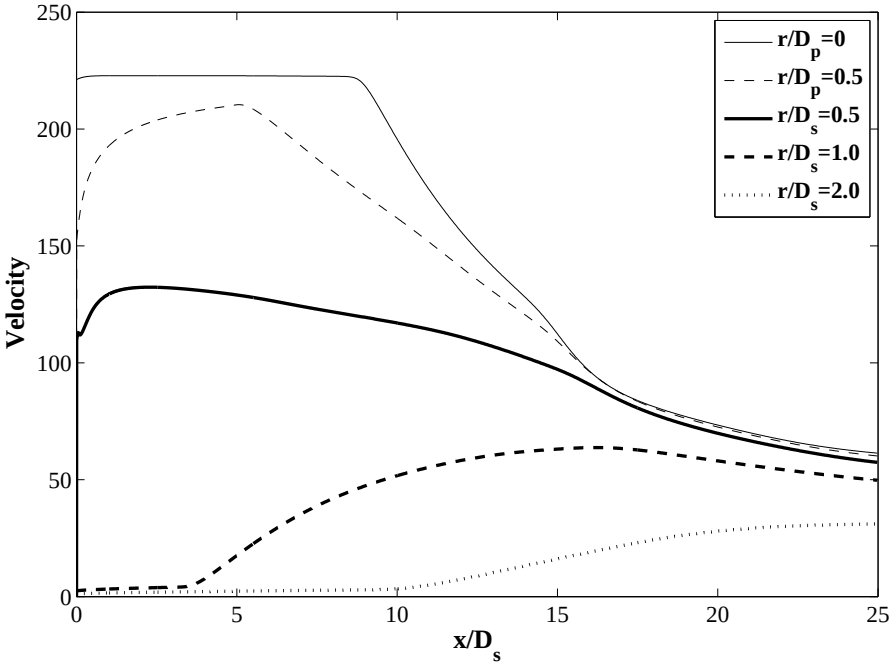

FIGURE A.18: Velocity profile at different radial positions, coplanar nozzle, VR=1

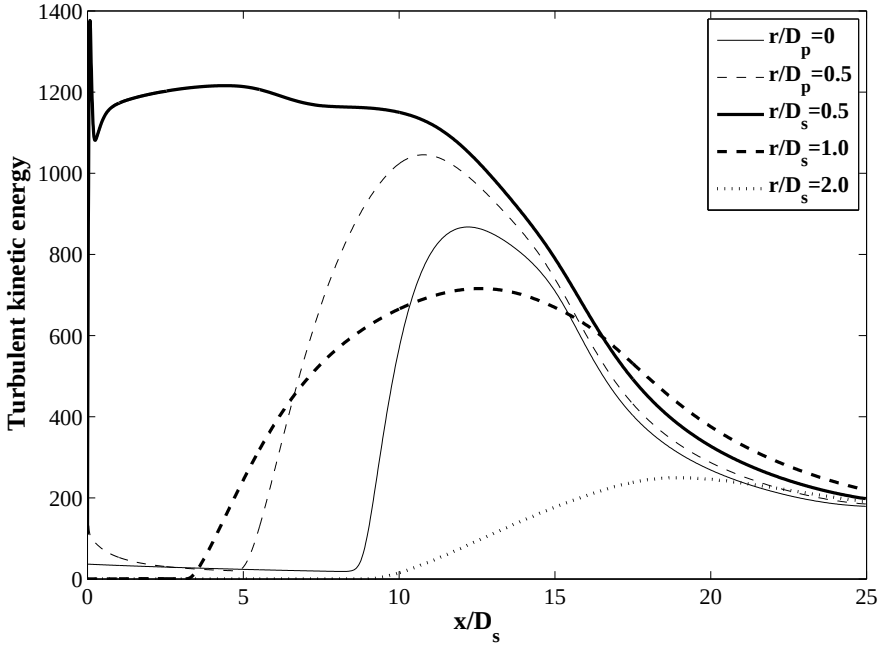

FIGURE A.19: Turbulent kinetic energy, coplanar nozzle, VR=1

Similar figures are also provided for the second bypass velocity ratio case ($VR = 0.9$). It can be seen that results are very similar to $VR = 1$. However the most important difference is the value of the turbulent kinetic energy at $x = 10D_s$, where results of $VR = 0.9$ peaks, while those of $VR = 1.0$ starts to roll off, see figures A.24 and A.19.

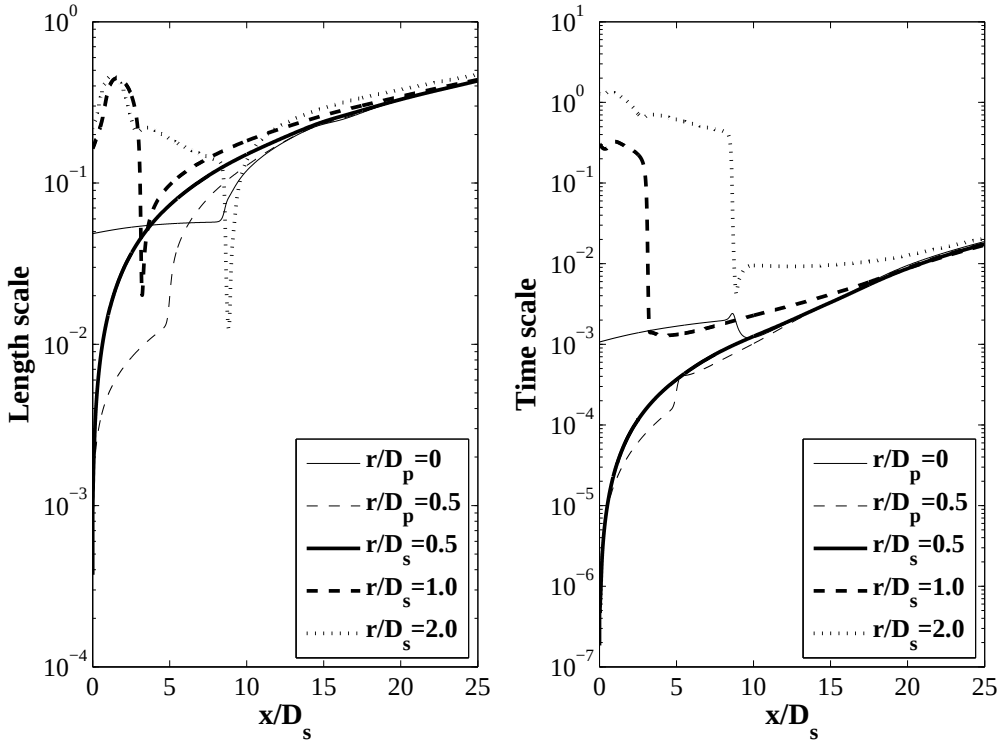

FIGURE A.20: Length scale and time scale, ($L = k^{3/2}/\varepsilon$, $\tau = k/\epsilon$), coplanar nozzle, VR=1

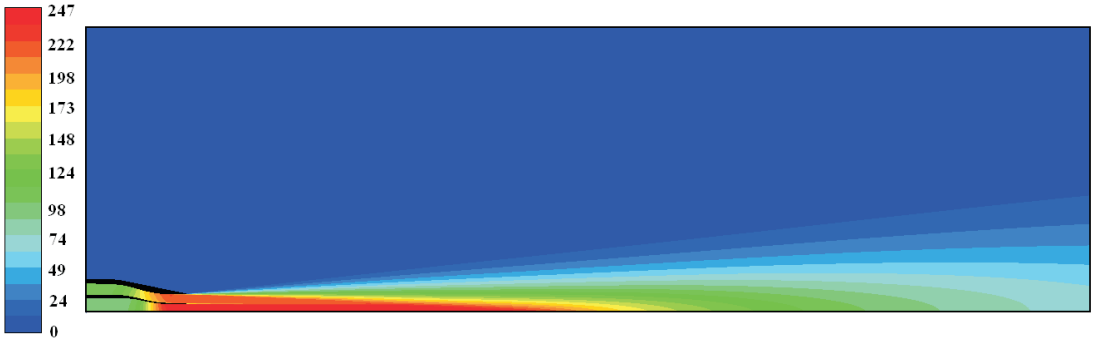

FIGURE A.21: Mean velocity contour, coplanar nozzle, VR=0.9

This causes the appearance of a new group of sources - probably due to the difference of the speed of the outgoing streams which will create a powerful turbulent region. It can also be seen that there is a considerable difference between the magnitude of the source strengths near the secondary lip and the primary lip before $x < 5D_s$. This difference decreases as we move downstream and will completely vanishes after $x = 10D_s$. This means that the curves are related to the same large turbulence structure (*i.e.* eddy).

Figure A.25 shows the variation of the length scale and time scale at various radial

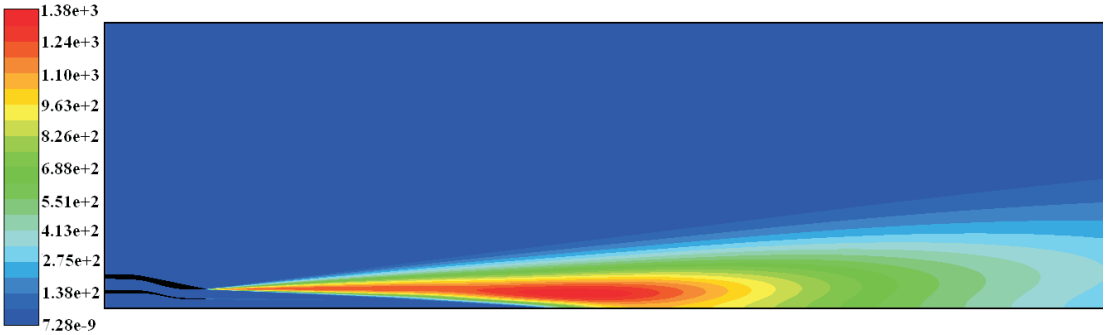

FIGURE A.22: Turbulent kinetic energy contour, coplanar nozzle, VR=0.9

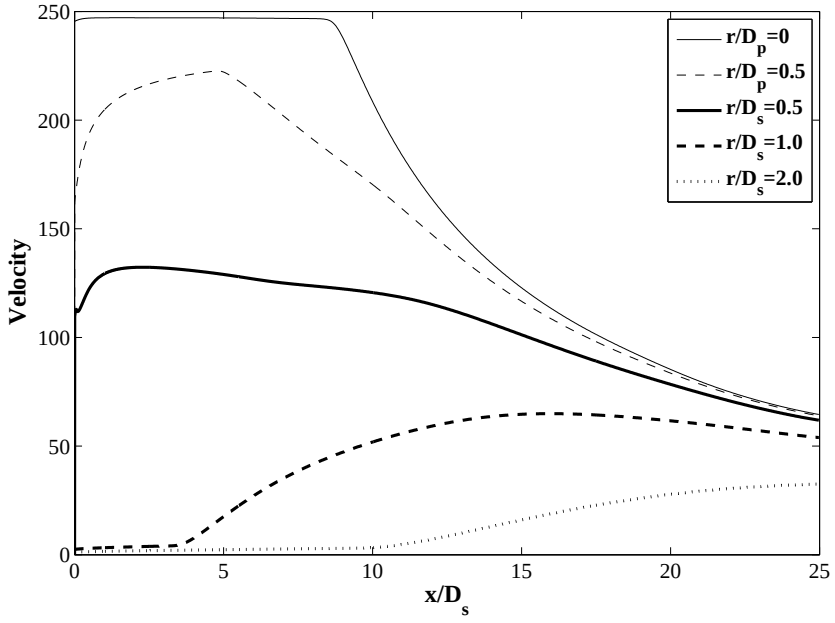

FIGURE A.23: Velocity profile at different radial positions, coplanar nozzle, VR=0.9

positions. The length scale curves are very similar to those of $VR = 1$, but the time scales obtained for $VR = 0.9$ are slightly larger than those of $VR = 1$. Once again, one can readily see from the figures that the curves start to overlay after about $x > 15D_s$, which indicates dominance of the larger scales.

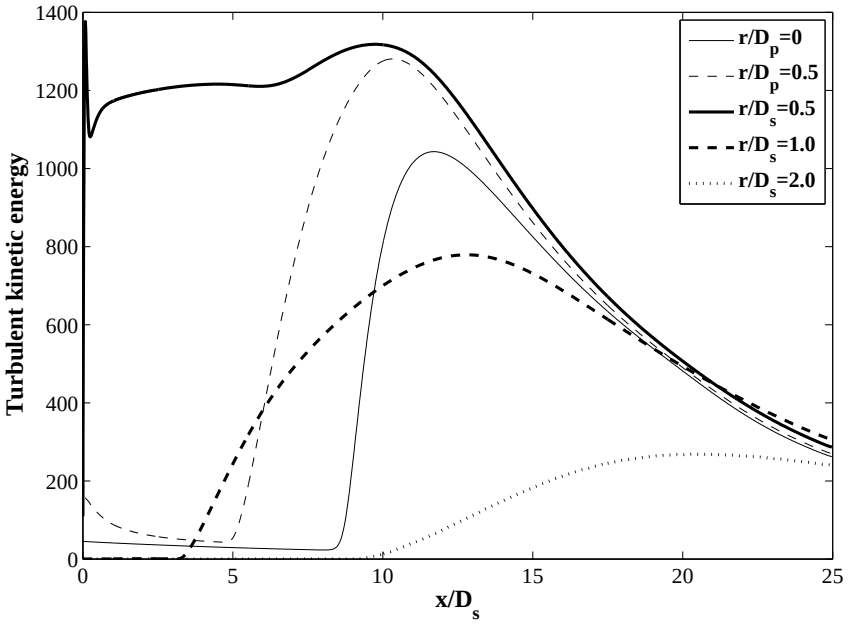

FIGURE A.24: Turbulent kinetic energy, coplanar nozzle, VR=0.9

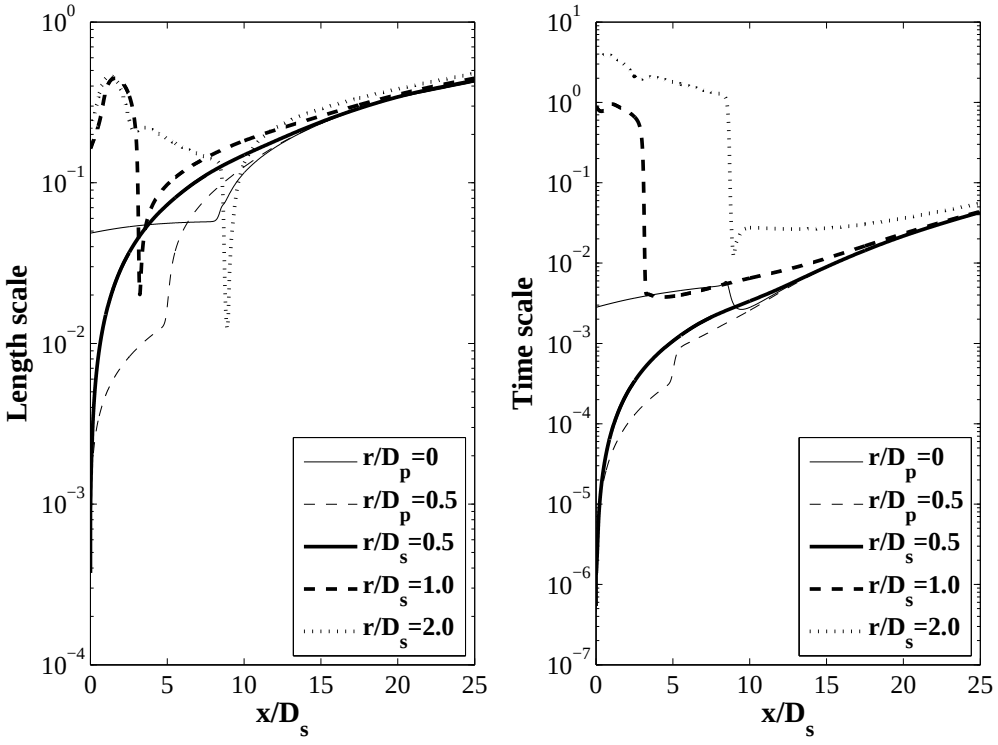

FIGURE A.25: Length scale and time scale, ($L = k^{3/2}/\varepsilon$, $\tau = k/\epsilon$), coplanar nozzle, VR=0.9

A.4.4 Short-Cowl Nozzle

Numerical results are presented for a short-cowl nozzle working at bypass velocity ratios 0.9. The geometry of the nozzle can be seen in figure A.26. The computational domain is extended to $60D_s$ in the axial direction and $25D_s$ in the radial direction. The flow domain consists of 17 regions and a total of 320000 cells have been used for the grid. A "velocity inlet" boundary condition is used at the jet inlet and "pressure inlet" and "pressure outlet" boundary conditions are used at the domain boundaries.

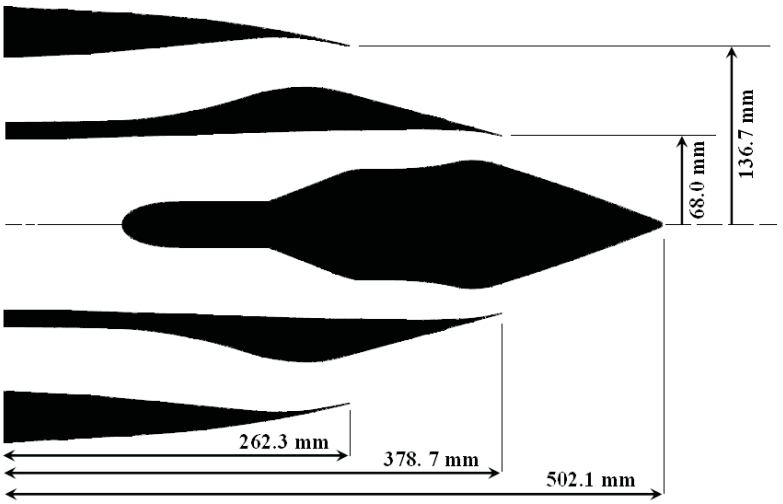

FIGURE A.26: Short-cowl nozzle geometry

Figure A.27 and A.28 shows contours of the mean velocity and turbulent kinetic energy for the first case ($VR = 1$). It can be seen that the primary potential core length is about $7D_s$, and the secondary potential core, due to the curvature of the secondary nozzle, is very short and mixes with the primary potential core very soon after leaving the nozzle exit. The most powerful sources are also mostly aggregated in first ten diameter ($10D_s$) from the jet exit. The interaction between two outgoing flows is very small and no significant turbulent medium emerges between them.

Variation of the mean velocity, turbulent kinetic energy, length scale and time scales are shown in figures A.29 through A.31. The following inferences can be made. Due to the special design of the secondary nozzle, the outgoing flow is pushed downwards, and therefore no powerful source can be seen near the primary nozzle lip. However, results show that most of the powerful sources are in region of $2D_s < x < 15D_s$. This is very different from what has been observed in single stream and coplanar jets, and is

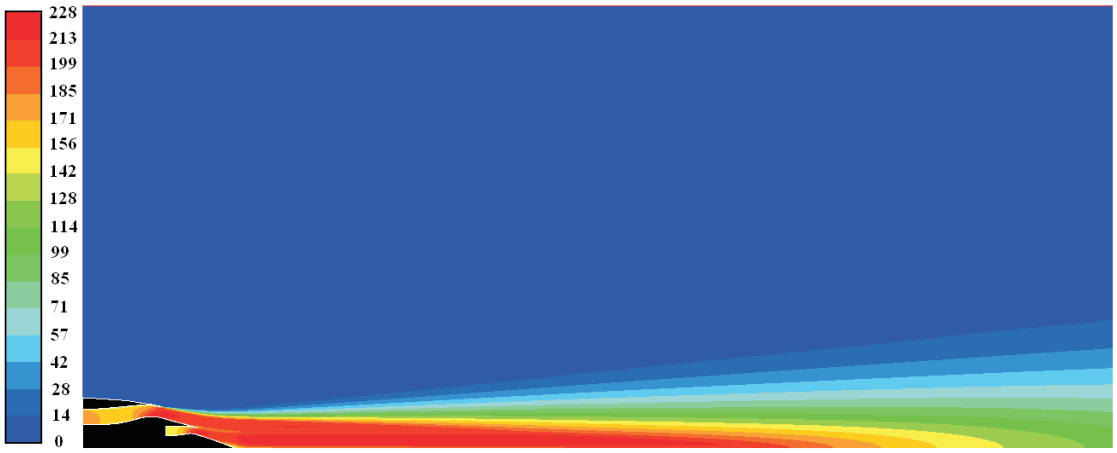

FIGURE A.27: Mean velocity contour of a short-cowl nozzle; VR=1.0

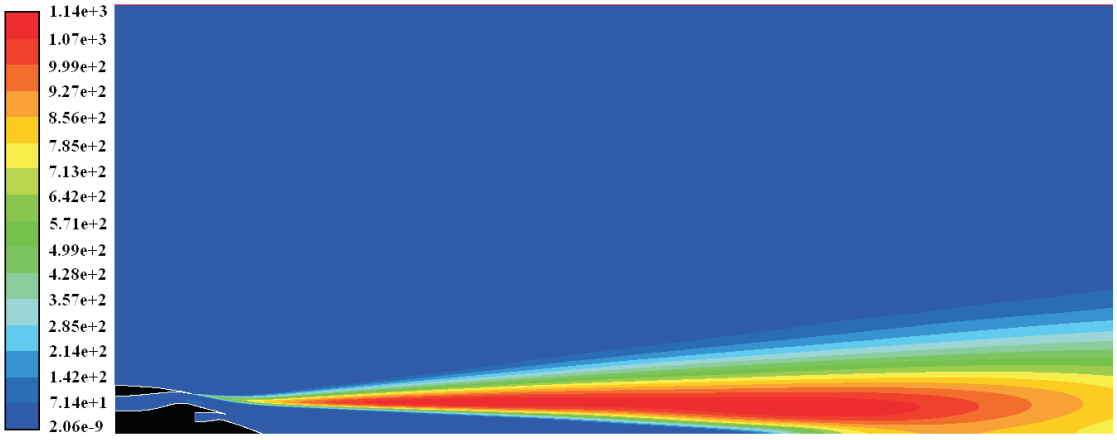

FIGURE A.28: Turbulent kinetic energy contour of a short-cowl nozzle; VR=1.0

because of the design of the short-cowl nozzle. It can be also seen that beyond $15D_s$ the turbulent kinetic energy curves, as well as the length scale and time scale, converge to one single curve across the radial direction. This is because this region is a production rate region and the large eddies govern the dynamic of the flow.

Numerical results of a short-cowl nozzle working at bypass velocity ratio $VR = 0.9$ are presented in figures A.32 through A.36. Figure A.32 shows contour of the mean velocity across the computational domain. Owing to the difference of the stream velocities, two distinct potential cores are now visible. A very small turbulent medium also emerges as a results of the interaction between the two flows, which is however entirely covered by the secondary potential core and will not be of great importance in the noise production mechanism, see figure A.32 and A.33. Figure A.34 shows the variation of the mean velocity at various radial locations. Figure A.35 illustrates the behaviour of the turbulent

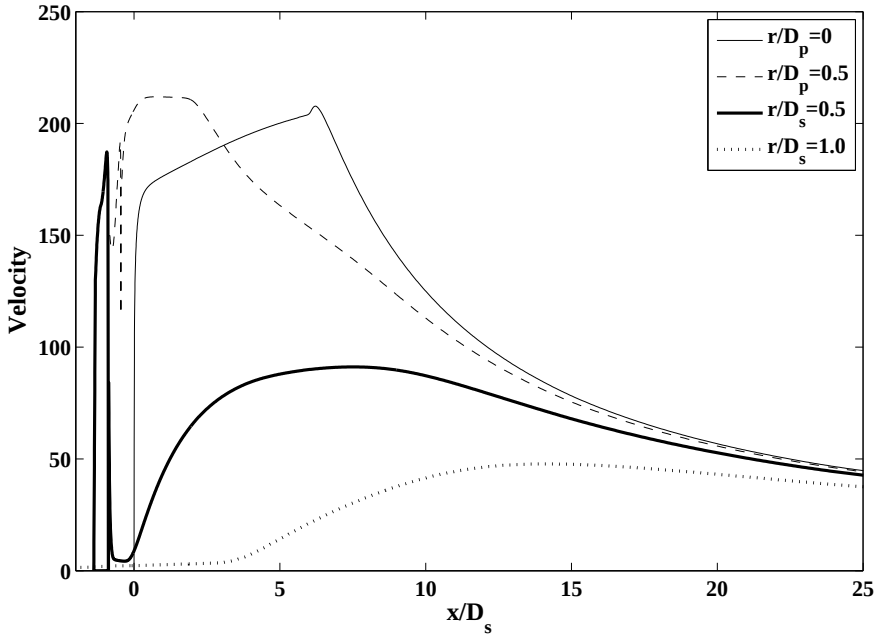

FIGURE A.29: Mean velocity variation, short-cowl nozzle, VR=1.0

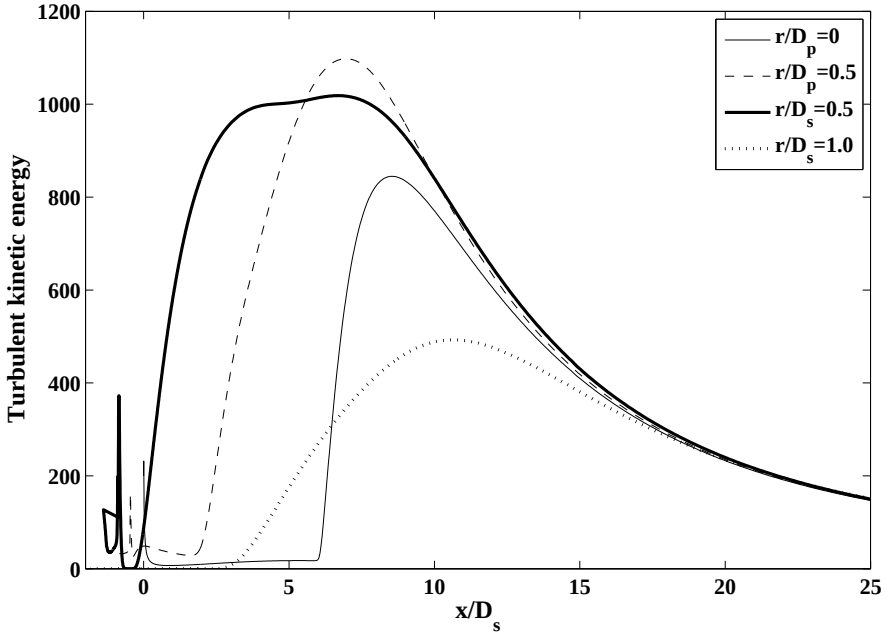

FIGURE A.30: Turbulent kinetic energy variation, short-cowl nozzle, VR=1.0

kinetic energy inside the jet flow at different radial distances. By comparing figure A.35 with A.30, one can also deduce that the sources appearing in the second case are slightly more powerful than those observed in the first case (VR=1). It can be also seen that the length scale behaves as a linear function of axial distance beyond $x = 10D_s$. In order to further examine the correctness of the presented results, another comparison

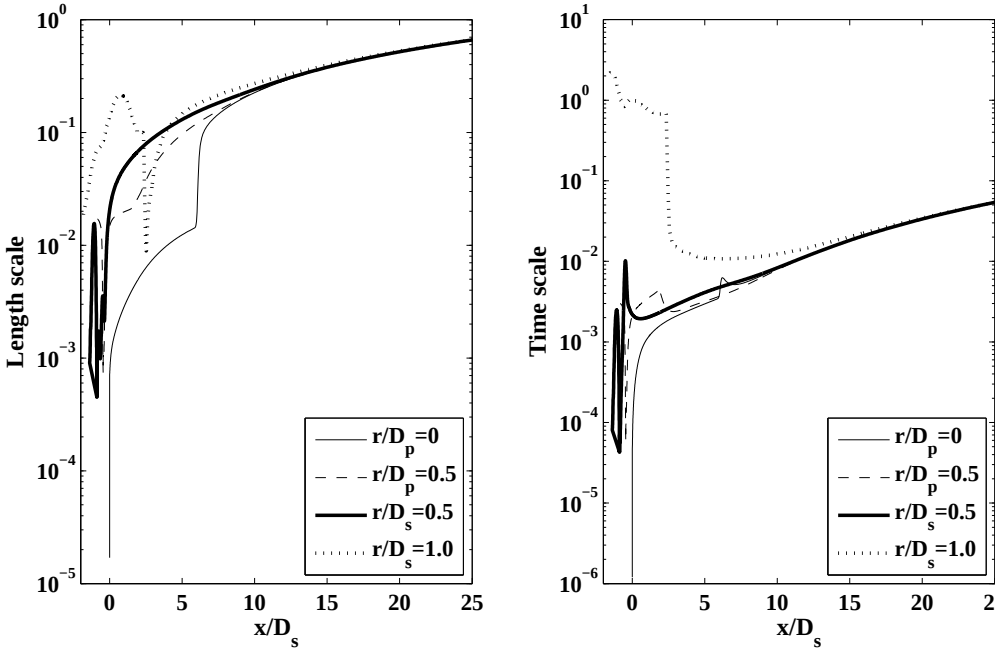

FIGURE A.31: Length scale and time scale variation, short-cowl nozzle, VR=1.0

with measured data is presented. Figure A.37 illustrates the comparison of the CFD for a $VR = 0.63$, $T_p = 850K$ short-cowl nozzle with the measure data at three different axial distances. As it can be seen, results are generally in good agreement.

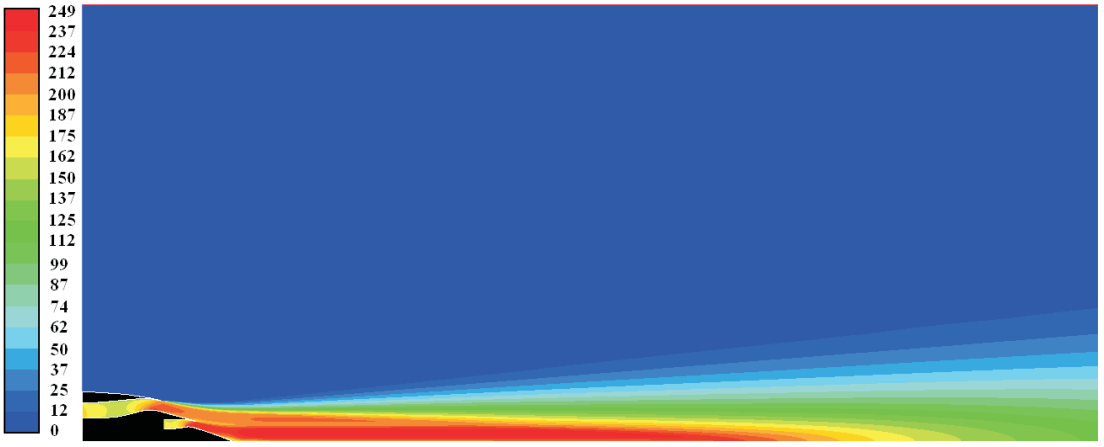

FIGURE A.32: Mean velocity contour of a short-cowl nozzle, short-cowl nozzle, VR=0.9

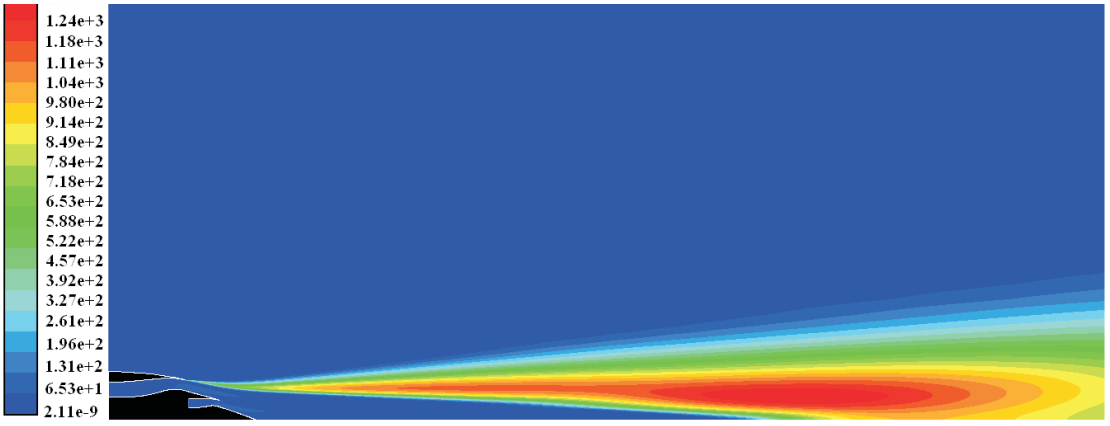

FIGURE A.33: Turbulent kinetic energy contour of a short-cowl nozzle, short-cowl nozzle, VR=0.9

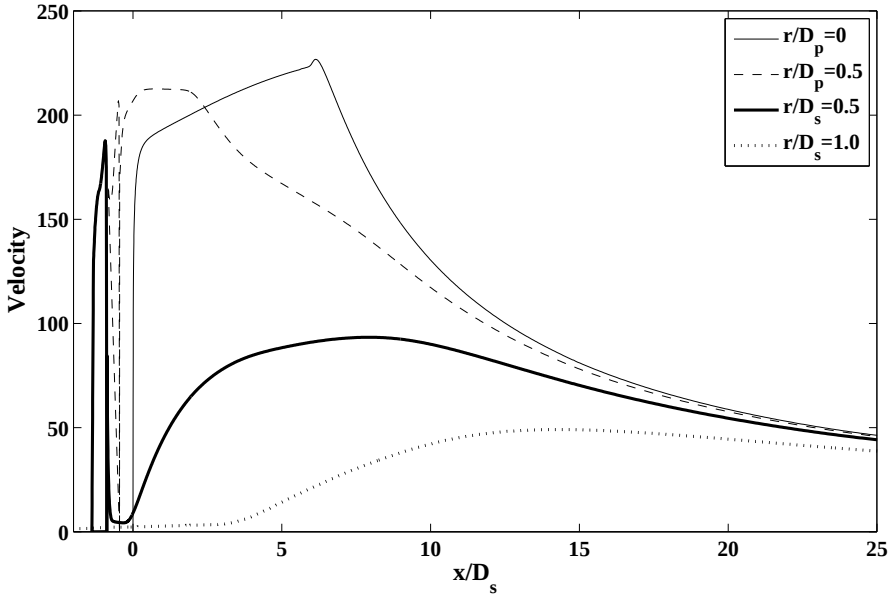

FIGURE A.34: Mean velocity variation, short-cowl nozzle, VR=0,9

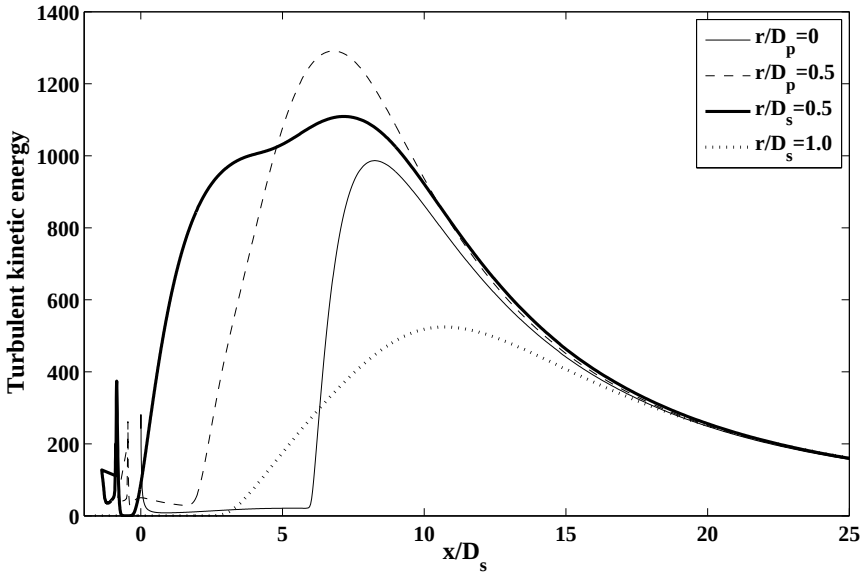

FIGURE A.35: Turbulent kinetic energy variation, short-cowl nozzle, VR=0.9

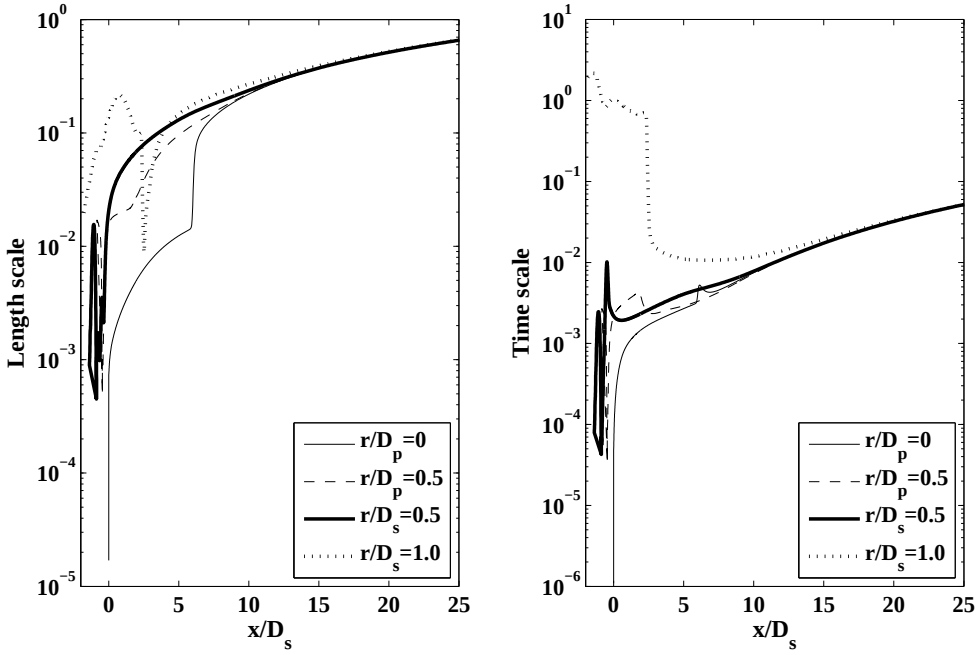

FIGURE A.36: Length scale and time scale variation, short-cowl nozzle, VR=0.9

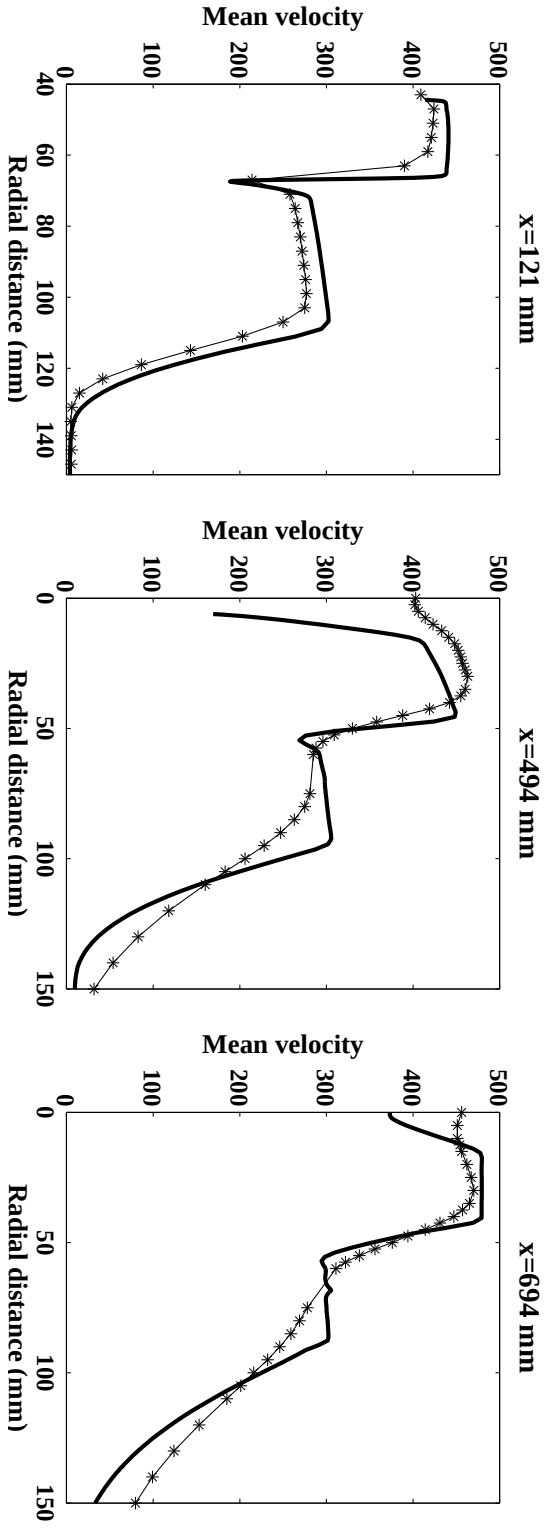

FIGURE A.37: Comparison of the mean velocity with measured data, VR=0.63, $T_p = 850K$. Solid line: CFD, Marker: Measured data

Bibliography

[1] M. J. Lighthill. On sound generated aerodynamically: I General theory. *Proc. R. Soc. Lond. A*, 211.

[2] J. Atvars, L. K. Schubert, and H. S. Ribner. Refraction of sound from a point source placed in an air jet. *Journal of Acoustical Society of America*, 37:168–170, 1965.

[3] G. M. Lilley. The generation and radiation of supersonic jet noise. vol. IV-Theory of turbulent generated jet noise, noise radiation from upstream source, and combustion noise, part III: Generation of sound in a mixing region. *Air Force Aero Propulsion Lab., AFAPL-TR-72-53*, 1972.

[4] B. Tester and C. Morfey. Developments in jet noise modeling-theoretical predictions and comparisons with measured data. *Journal of Sound and Vibration*, 46(1):79–103, 1976.

[5] R. Mani, T. F. Balsa, and P. R. Gliebe. High-velocity jet noise source location and reduction. *Task 2, Federal Aviation Administration Report, FAA-RD-76-II*, 1978.

[6] P. A. Lush. Measurements of subsonic jet noise and comparison with theory. *Journal of Fluid Mechanics*, 46:477–500, 1971.

[7] J. E. Ffowcs Williams. The noise from turbulence convected at high speed. *J. Roy. Soc. London A*, 225:469–503, 1963.

[8] C. L. Morfey. Amplification of aerodynamic noise by convected flow inhomogeneities. *J. Roy. Soc. London A*, 225:469–503, 1973.

[9] P. A. Lush and M. J. Fisher. Noise from hot jets. *AGARD Conference Proceedings CPP*, 131:12–1–12–8, 1973.

[10] C. K. W. Tam. Dimensional analysis of jet-noise data. *AIAA*, 44:512–522, 2006.

[11] K. Viswanathan. Improved method for prediction of noise from single jets. *AIAA*, 45:151–161, 2007.

[12] J. B. Freund, S. K. Lele, and P. Moin. Direct numerical simulation of a Mach 1.92 turbulent jet and its sound field. *AIAA*, 38(11):2023–2031, 2000.

[13] J. B. Freund. Noise sources in a low-Reynolds-number turbulent jet at Mach 0.9. *Journal of Fluid Mechanics*, 438:227–305, 2001.

[14] J. L. Stromberg, D. K. McLaughlin, and T. R. Troutt. Flow field and acoustic properties of a Mach number 0.9 jet at a low Reynolds number. *Journal of Sound and Vibration*, 72(2):159–176, 1980.

[15] A. Uzun. *3-D large eddy simulation for jet aeroacoustics.* PhD thesis, Purdue University, 2003.

[16] N. Andersson. *A study of Mach 0.75 jets and their radiated sound using large-eddy simulation.* PhD thesis, Chalmers University of Technology, 2003.

[17] I. Proudman. The generation of noise by isotropic turbulence. *J. Roy. Soc. London*, A214:119–132, 1952.

[18] T. F. Balsa and P. R. Gliebe. Aerodynamics and noise of coaxial jets. *AIAA*, 15:1550–1558, 1977.

[19] T. F. Balsa. The acoustic field of sources in shear flow with application to jet noise: Convective amplification. *Journal of Fluid Mechanics*, 79:33–47, 1977.

[20] A. Khavaran, E. A. Krejsa, and C. M. Kim. Computation of an axisymmetric convergent-divergent nozzle. *Journal of Aircraft*, 31:603–609, 1994.

[21] A. Khavaran. Role of anisotropy in turbulent mixing noise. *AIAA*, 37:832–841, 1999.

[22] A. Khavaran and N. Georgiadis. Aeroacoustics of supersonic elliptic jets. *AIAA 1996-0641*.

[23] A. Hamed, A. Khavaran, and S. Lee. The flow and acoustic predictions for a high bypass ratio exhaust nozzle. *AIAA 1998-3257*.

[24] T. J. Barber, L. M. Chiappetta, and S. H. Zysman. An assessment of jet noise analysis codes for mulitstream axisymmetric and forced mixer nozzles. *AIAA 1996-0750*.

[25] T. J. Barber, A. Nedungadi, and A. Khavaran. Predicting the jet noise from high speed jets. *AIAA 2001-0819*.

[26] L. D. Koch, J. Bridges, and A. Khavaran. Flowfield comparisons from three navier-stokes solvers for an axisymmetric separate flow jet. *AIAA 2002-0672*.

[27] A. Frendi, W. D. Dorland, T. Nesman, and T. S. Wang. A jet engine noise measurement and prediction tool. *Journal of Acoustical Society of America*, 112(1):2036–2042, 2002.

[28] A. Frendi, T. Nesman, and T. S. Wang. On the effect of time scaling on the noise radiated by an engine plume. *Journal of Sound and Vibration*, 256:969–979, 2002.

[29] L. D. Koch, J. Bridges, and A. Khavaran. Mean flow and noise prediction for a separate flow jet with chevron mixers. *AIAA 2004-0189*.

[30] W. A. Engblom, A. Khavaran, and J. Bridges. Numerical predictions of chevron nozzle noise reduction using wind-mgbk methodology. *AIAA 2004-2979*.

[31] A. Khavaran and J. Bridges. Modelling of fine-scale turbulence mixing noise. *Journal of Sound and Vibration*, 279:1131–1154, 2005.

[32] A. Khavaran, J. Bridges, and J. B. Freund. A parametric study of fine-scale turbulence mixing noise. *AIAA 2002-2419*.

[33] D. W. Wundrow and A. Khavaran. On the applicability of high-frequency approximation to Lilley's equation. *Journal of Sound and Vibration*, 272:793–830, 2004.

[34] M. E. Goldstein, A. Khavaran, and R. E. Musafir. Jet noise predictions based on two different forms of Lilley's equation, part 1: Basic theory. *NASA-TM-2005-213829-Part 1.*

[35] M. E. Goldstein, A. Khavaran, and R. E. Musafir. Jet noise predictions based on two different forms of Lilley's equation, part 2: Acoustic predictions and comparison with data. *NASA-TM-2005-213829-Part 2.*

[36] A. Khavaran, J. Bridges, and N. Georgiadis. rediction of turbulencegenerated noise in unheated jets: Part 1, jeno technical manual (version 1.0). *NASA TM-2005-213827.*

[37] R. H. Self. Jet noise prediction using the Lighthill acoustic analogy. *Journal of Sound and Vibration*, 275:757–768, 2004.

[38] R. H. Self and A. Bassetti. A RANS based jet noise prediction scheme. *AIAA 2003-3325.*

[39] G. J. Page, J. J. McGuirk, M. Hossain, R. H. Self, and A. Bassetti. A CFD coupled acoustics approach for coaxial jet noise. *AIAA 2003-3286.*

[40] C. K. W. Tam and L. Auriault. Jet mixing noise from fine-scale turbulence. *AIAA*, 37:145–153, 1999.

[41] C. K. W. Tam, N. N. Pastouchenko, and L. Auriault. Effect of forward flight on jet mixing noise from fine-scale turbulence. *AIAA*, 39(7):1261–1269, 2001.

[42] C. K. W. Tam and N. N. Pastouchenko. Noise from fine-scale turbulence of non-axisymmetric jets. *AIAA*, 40(3):456–464, 2002.

[43] C. K. W. Tam, N. N. Pastouchenko, and K. Viswanathan. Fine-scale turbulence noise from hot jets. *AIAA*, 43(8):1675–1683, 2005.

[44] P. J. Morris and F. Farassat. Acoustic analogy and alternative theories for jet noise prediction. *AIAA*, 40:671–680, 2002.

[45] M. J. Fisher, G. A. Preston, and W. D. Bryce. A modelling of the noise from simple coaxial jets part i: With unheated primary flow. *Journal of Sound and Vibration*, 209(3):385403, 1998.

[46] M. J. Fisher, G. A. Preston, and C. J. Mead. A modelling of the noise from simple coaxial jets part ii: With heated primary flow. *Journal of Sound and Vibration*, 209(3):405–417, 1998.

[47] G. A. Preston. *Modelling of Sound Source Regions for the Prediction of Coaxial Jet Noise*. PhD thesis, Institute of Sound and Vibration Research, University of Southampton, 1996.

[48] M. Harper-Bourne. Jet near field noise prediction. *AIAA/CEAS 2002-2554*.

[49] F. Kerherve, P. Jordan, Y. Gervais, J. C. Valiere, and P. Braud. Two-point laser doppler velocimetry measurements in mach 1.2 cold supersonic jet for statistical aeroacoustic source model. *Experiments in Fluids*, 37:419–437, 2004.

[50] J. Bridges and M. P. Wernet. Measurements of the aeroacoustic sound source in hot jets. *AIAA 2003-3130*.

[51] M. J. Fisher and P. O. A. L. Davies. Correlation measurements in a non-frozen pattern of turbulence. *Journal of Fluid Mechanics*, 18:97–116, 1963.

[52] P. J. Morris and S. Boluriaan. The prediction of jet noise from CFD data. *AIAA/CEAS 2004-2977*.

[53] F. Kerherve, J. Fitzpatrick, and P. Jordan. The frequency dependence of jet turbulence for noise source modelling. *Journal of Sound and Vibration*, 296:209–225, 2006.

[54] T. F. Balsa. The far field of high frequency convected singularities in sheared flows, with an application to jet noise production. *Journal of Fluid Mechanics*, 74:193–208, 1976.

[55] M. E. Goldstein. *Aeroacoustics*. McGraw-Hill, New York, 1976.

[56] J. O. Hinze. *Turbulence*. D C W Industries, New York, 1975.

[57] A. Khavaran and E. A. Krejsa. On the role of anisotropy in turbulent mixing noise. *AIAA 1998-2289*.

[58] A. Khavaran. Refraction and shielding of noise in non-axisymmetric jets. *AIAA 1996-1780*.

[59] H. S. Ribner. Quadrupole correlation governing the pattern of jet noise. *Journal of Fluid Mechanics*, 38:1–24, 1969.

[60] G. K. Batchelor. *The Theory of Homogeneous Turbulence*. Cambridge University Press, Cambridge, 1999.

[61] M. S. Uberoi. *Journal of Aeronautics Science*, 20, 1953.

[62] M. S. Uberoi. *Natl. Adisory Comm. Aeronaut. Tech. Notes*, 3116, 1954.

[63] R. Mani. The influence of jet flow on jet noise, Part 2. The noise of heated jets. *Journal of Fluid Mechanics*, 73:779–793, 1976.

[64] P. Jordan and Y. Gervias. Modeling self and shear noise mechanisms in inhomogeneous, anisotropic turbulence. *Journal of Sound and Vibration*, 279:529–555, 2005.

[65] G. K. Batchelor. The theory of axisymetric turbulence. *Proc. Roy. Soc. Lodon, A*, 186:480–502, 1946.

[66] S. Chandrasekhar. The decay of axisymmetric turbulence. *Proc. Roy. Soc. Lodon, A*, 203:358–364, 1950.

[67] H. S. Ribner. Theory of two-point correlations of jet noise. *NASA TN D-8330*, 1976.

[68] M. Billson. *Computational techniques for turbulence generated noise*. PhD thesis, Chalmers University of Technology, 2004.

[69] S. B. Pope. *Turbulent Flows*. Cambridge University Press, Cambridge, 2003.

[70] T. L. Thatcher, D. J. Wilson, E. E. Wood, M. J. Craig, and R. G. Sextro. Pollutant dispersion in a large indoor space: Part 1- scaled experiments using a water-filled model with occupants and furniture. *Indoor Air*, 14:258–271, 2004.

[71] C. Tong and Z. Warhaft. Passive scalar dispersion and mixing in a turbulent jet. *Journal of Fluid Mechanics*, 292:1–38, 1995.

[72] W. C. Meecham and G. W. Ford. Acoustic radiation from isotropic turbulence. *Journal of Acoustical Society of America*, 30:318–322, 1958.

[73] R. Rubinstein and Y. Zhou. Time correlation and the frequency spectrum of sound radiated by turbulent flows. *ICASE report*, NAS1-19480, 1997.

[74] R. Rubinstein and Y. Zhou. The frequency spectrum of sound radiated by isotropic turbulence. *Physics Letters A*, 267:379–383, 2000.

[75] S. Y. Chen and R. H. Kraichnan. Sweeping decorelation in isotropic turbulence. *Physics of Fluids A*, 1(12):2019–2024, 1989.

[76] M. Nelkin and R. Tabor. Time correlation and random sweeping in isotropic turbulence. *Physics of Fluids A*, 2:81, 1990.

[77] R. Sakar and M. Y. Hussaini. Computation of the sound generated by isotropic turbulence. *ICASE Report 93-74*, 1993.

[78] G. M. Lilley. The radiated noise from isotropic turbulence revised. *NASA-ICASE Report No. 93-75*, 1993.

[79] T. Sanada and V. Shanmugasundaram. Random sweeping effect in isotropic numerical turbulence. *Physics of Fluids A*, 4(6):1245–1250, 1992.

[80] P. O. A. L. Davies, M. J. Fisher, and M. J. Barratt. The characteristics of the turbulence in the mixing region on a round jet. *Journal of Fluid Mechanics*, 15(3):337–367, 1963.

[81] J. A. B. Wills. On the convection velocities in turbulent shear flows. *Journal of Fluid Mechanics*, 20(3):417–432, 1964.

[82] K. Akamatsu. Phase velocity measurement in turbulent flow. Master's thesis, ISVR, University of Southampton, 1972.

[83] V. M. Szewczyk. *The role of flow acoustic interaction in jet noise studies.* PhD thesis, ISVR, University of Southampton, 1978.

[84] H. S. Ribner. Aerodynamic sound from fluid dilatations, A theory of sound from jet and other flows. *University of Toronto, UTIA Rept. 86, AFOSR TN 3430*, 1962.

[85] D. Papamoschou and A. Bunyajitradulya. Evolution of large eddies in compressible shear layers. *Physics of Fluids*, 9(3):756–765, 1997.

[86] G. L. Brown and A. Roshko. On density effects and large scale structure in turbulent mixing layers. *Journal of Fluid Mechanics*, 64:775–816, 1974.

[87] G. S. Elliot, M. Samimy, and S. A. Arnette. The characteristics and evolution of large-scale structures in compressible mixing layers. *Physics of Fluids*, 7(4):864–876, 1995.

[88] J. D. Koch, J. Bridges, C. Brown, and A. Khavaran. Numerical and experimental determination of the geometric far field for round jets. *NASA/TM-2003-212379*.

[89] E. A. Krejsa and N. H. Saiyed. Characteristics of residual mixing noise from internal fan/core mixers. *NASA-107395, AIAA 1997-0382*.

[90] N. Raizada and P. J. Morris. Prediction of noise from high speed subsonic jets using an acoustic analogy. *AIAA 2006-2596*.

[91] P. Jordan, Y. Gervais, J. C. Valiere, and H. Foulon. Final results from single point measurements. project deliverable D3.6, JEAN-EU 5th Framework Program, G4RD-CT-2000-00313. Laboratoire d'Etude Aerodynamiques, Poitiers. 2002.

[92] P. Jordan, Y. Gervais, J. C. Valiere, and H. Foulon. Results from acoustic field measurements. project deliverable D3.6, JEAN-EU 5th Framework Program, G4RD-CT-2000-00313. Laboratoire d'Etude Aerodynamiques, Poitiers. 2002.

[93] P. Jordan and Y. Gervais. Modeling self and shear noise mechanism in anisotropic turbulence. *AIAA/CEAS 2003-8743*.

[94] O. Power, F. Kerherve, J. Fitzpatrick, and P. Jordan. Measurements of turbulence statistics in high subsonic jets. *AIAA/CEAS 2004-3021*.

[95] H. S. Ribner. Strength distribution of noise source along a jet. *Journal of Acoustical Society of America*, 30:876, 1958.

[96] I. Dyer. Distribution of sound sources in a jet stream. *Journal of Acoustical Society of America*, 31:1016–1022, 1959.

[97] J. Battaner-Moro. Report on automated source breakdown for coaxial and single jet noise measurements. *ISVR internal report no. 03/10*, 2003.

[98] I. S. F. Jones. Fluctuating turbulent stresses in the noise-producing regions of a circular jet. *Journal of Fluid Mechanics*, 36:529–543, 1969.

[99] P. Bradshaw, D. H. Ferriss, and R. F. Johnson. Turbulence in the noise-producing regions of a circular jet. *Journal of Fluid Mechanics*, 19:591–624, 1964.

[100] S. H. Zysman, L. M. Chiappetta, N. H. Saiyed, and G. G. Podboy. Flowfield measurement and analysis of a 1/7-scale mixed flow exhaust system model. *AIAA 1995-2744*.

[101] G. G. Podboy, J. E. Bridge, N. H. Saiyed, and M. J. Krupar. Laser doppler velocimeter system for subsonic jet mixer nozzle testing at the NASA Lewis aeracoustics propulsion Lab. *AIAA 1995-2787*.

[102] A. Khavaran and E. A. Krejsa. Refraction of high frequency noise in an arbitrary jet flow. *AIAA 1994-0139*.

[103] A. Khavaran and J. Bridges. Modeling of turbulence generated noise in jets. *AIAA 2004-2983*.

[104] N. J. Georgiadis, D. A. Yoder, and W. A. Engblom. Evaluation of modified two-equation turbulence models for jet flow predictions. *AIAA*, 44(12):3107–3114, 2006.

[105] A. Yoshizawa. Nonequilibrium effect of the turbulent-energy-production process on the inertial-range energy spectrum. *Physical review E*, 79(5):4065–4071, 1994.

[106] A. Khavaran and D. C. Kenzakowski. Progress toward improving jet noise predictions in hot jets. *AIAA 2007-0012*.

[107] D. C. Wilcox. *Turbulence Modeling for CFD*. McGraw-Hill, LA Canda, CA, 1993.

[108] A. N. Kolmogorov. Equation of turbulent motion of an incompressible fluid. *Izvestia Academy of Science, USSR, Physics*, 6(1,2):56–58, 1942.